



Strojniški vestnik

Journal of Mechanical Engineering

no. **1-2**

year **2024**

volume **70**

tolerancing

ISO standard

geometrical
product
specification

verification

Strojniški vestnik – Journal of Mechanical Engineering (SV-JME)

Aim and Scope

The international journal publishes original and (mini)review articles covering the concepts of materials science, mechanics, kinematics, thermodynamics, energy and environment, mechatronics and robotics, fluid mechanics, tribology, cybernetics, industrial engineering and structural analysis.

The journal follows new trends and progress proven practice in the mechanical engineering and also in the closely related sciences as are electrical, civil and process engineering, medicine, microbiology, ecology, agriculture, transport systems, aviation, and others, thus creating a unique forum for interdisciplinary or multidisciplinary dialogue.

The international conferences selected papers are welcome for publishing as a special issue of SV-JME with invited co-editor(s).

Editor in Chief

Vincenc Butala

University of Ljubljana, Faculty of Mechanical Engineering, Slovenia

Technical Editor

Pika Škraba

University of Ljubljana, Faculty of Mechanical Engineering, Slovenia

Founding Editor

Bojan Kraut

University of Ljubljana, Faculty of Mechanical Engineering, Slovenia

Editorial Office

University of Ljubljana, Faculty of Mechanical Engineering

SV-JME, Aškerčeva 6, SI-1000 Ljubljana, Slovenia

Phone: 386 (0)1 4771 137

Fax: 386 (0)1 2518 567

info@sv-jme.eu, <http://www.sv-jme.eu>

Print: Demat d.o.o., printed in 240 copies

Founders and Publishers

University of Ljubljana, Faculty of Mechanical Engineering, Slovenia

University of Maribor, Faculty of Mechanical Engineering, Slovenia

Association of Mechanical Engineers of Slovenia

Chamber of Commerce and Industry of Slovenia,

Metal Processing Industry Association

President of Publishing Council

Mihael Sekavčnik

University of Ljubljana, Faculty of Mechanical Engineering, Slovenia

Vice-President of Publishing Council

Matej Vesenjāk

University of Maribor, Faculty of Mechanical Engineering, Slovenia

International Editorial Board

Hafiz Muhammad Ali, King Fahd U. of Petroleum & Minerals, Saudi Arabia

Josep M. Bergada, Politechnical University of Catalonia, Spain

Anton Bergant, Litostroj Power, Slovenia

Miha Boltežar, University of Ljubljana, Slovenia

Filippo Cianetti, University of Perugia, Italy

Peng Cheng, Virginia State University, USA

Franco Concli, University of Bolzano, Italy

J.Paulo Davim, University of Aveiro, Portugal

Igor Emri, University of Ljubljana, Slovenia

Imre Felde, Obuda University, Faculty of Informatics, Hungary

Aleš Hribnik, University of Maribor, Slovenia

Soichi Ibaraki, Kyoto University, Department of Micro Eng., Japan

Julius Kaplunov, Brunel University, West London, UK

Iyas Khader, Fraunhofer Institute for Mechanics of Materials, Germany

Jernej Klemenc, University of Ljubljana, Slovenia

Milan Kljajin, J.J. Strossmayer University of Osijek, Croatia

Peter Krajnik, Chalmers University of Technology, Sweden

Janez Kušar, University of Ljubljana, Slovenia

Gorazd Lojen, University of Maribor, Slovenia

Edgar Lopez, University of Istmo, Mexico

Darko Lovrec, University of Maribor, Slovenia

Thomas Lübben, University of Bremen, Germany

Trung-Thanh Nguyen, Le Quy Don Technical University, Vietnam

Tomaž Pepelnjak, University of Ljubljana, Slovenia

Primož Podržaj, University of Ljubljana, Slovenia

Vladimir Popović, University of Belgrade, Serbia

Franci Pušavec, University of Ljubljana, Slovenia

Mohammad Reza Safaei, Florida International University, USA

Silvio Simani, University of Ferrara, Italy

Marco Sortino, University of Udine, Italy

Branko Vasić, University of Belgrade, Serbia

Arkady Voloshin, Lehigh University, Bethlehem, USA

General information

Strojniški vestnik – Journal of Mechanical Engineering is published in 6 double issues per year.

Institutional prices include print & online access: institutional subscription price and foreign subscription €100,00 (the price of a single issue is €10,00); general public subscription and student subscription €50,00 (the price of a single issue is €5,00). Prices are exclusive of tax. Delivery is included in the price. The recipient is responsible for paying any import duties or taxes. Legal title passes to the customer on dispatch by our distributor. Single issues from current and recent volumes are available at the current single-issue price. To order the journal, please complete the form on our website. For submissions, subscriptions and all other information please visit: <http://www.sv-jme.eu>.

You can advertise on the inner and outer side of the back cover of the journal. The authors of the published papers are invited to send photos or pictures with short explanation for cover content.

We would like to thank the reviewers who have taken part in the peer-review process.



Cover:

The geometrical product specifications (GPS) are, in addition to material specifications, a key component of effective planning and production of mechanical products as well as communication between partners in these processes. The principles and basic rules for precise and unambiguous specification of all requirements are embodied in a series of ISO GPS standards.

Image Courtesy:

Photo by https://unsplash.com/@risto_kokkonen?utm_
Adapted by Pika Škraba

ISSN 0039-2480, ISSN 2536-2948 (online)

© 2024 with Authors.

SV-JME is indexed / abstracted in: SCI-Expanded, Compendex, Inspec, ProQuest-CSA, SCOPUS, TEMA. The list of the remaining bases, in which SV-JME is indexed, is available on the website.

The journal is subsidized by Slovenian Research and Innovation Agency.

Strojniški vestnik - Journal of Mechanical Engineering is available on <https://www.sv-jme.eu>.

Contents

Strojniški vestnik - Journal of Mechanical Engineering
volume 70, (2024), number 1 2
Ljubljana, January February 2024
ISSN 0039-2480

Published every two months

Papers

| | |
|---|-----|
| Samo Zupan, Robert Kunc: Overview of Principles and Rules of Geometrical Product Specifications According to the Current ISO Standards | 3 |
| Zhengfang Li, Xudong Di, Zhengyuan Gao, Zhiguo An, Ling Chen, Yuhang Zhang, Shihong Lu: Improvement of the Dimensional Accuracy of a Ti-6Al-4V Ripple Disc During Electric Hot Incremental Sheet Forming | 20 |
| Ireneusz Zagóski, Monika Kulisz, Anna Szczepaniak: Roughness Parameters with Statistical Analysis and Modelling Using Artificial Neural Networks After Finish Milling of Magnesium Alloys with Different Edge Helix Angle Tools | 27 |
| Tat-Khoa Doan, Trung-Thanh Nguyen, An-Le Van: Multi-performance Optimization of the Rotary Turning Operation for Environmental and Quality Indicators | 42 |
| Xin Tian, Guangjian Wang, Yujiang Jiang: A New Calculation Method for Instantaneous Efficiency and Torque Fluctuation of Spur Gears | 5 |
| Grzegorz Struzikiewicz: Investigation of the Titanium Alloy Turning Process with Prime A Tools under High-Pressure Cooling Conditions | 7 |
| Berat Gürçan Şentürk, Mahmut Cüneyt Fetvacı: A Modified Approach to the Rack Generation of Beveloid Gears | 8 |
| Oktay Adıyaman: Investigation on the Application of Worn Cutting Tool Inserts as Burnishing Tools | 92 |
| Reviewers 2023 | 102 |

Overview of Principles and Rules of Geometrical Product Specifications According to the Current ISO Standards

Samo Zupan*¹, Robert Kunc

University of Ljubljana, Faculty of Mechanical Engineering, Slovenia

The article provides an overview of the philosophy of geometrical product specifications (GPS), which are, in addition to material specifications, a key component of effective planning and production of mechanical products as well as communication between partners in these processes. The principles and basic rules for precise and unambiguous specification of all requirements are embodied in a series of ISO GPS standards. It includes standards that describe the required accuracy of geometrical features of size and geometrical tolerances. An overview of the fundamental principles and rules imposed by the current ISO GPS standards and their content was carried out. This includes a description of the organization of the ISO GPS system and a summary of the content of the more relevant standards, which have recently undergone multiple revisions. The ISO GPS standards are based on the duality principle of specification and verification. In the present research, we focused primarily on geometrical specifications, while omitting the parallel pillar of verification, which, according to the ISO GPS matrix model, contains an even greater number of standards that define this area in more detail.

Keywords: ISO standard, geometrical product specification, geometrical dimensioning and tolerancing, principles, rules, size, tolerance, verification

Highlights

- Overview of the organization of ISO geometrical products specification (GPS) standards and the fundamental principles and rules given in the current editions of these standards.
- Specification of the accuracy of linear and angular sizes of geometrical features and other dimensions in technical documentation.
- Specification of the accuracy of geometrical features of workpieces.
- General tolerances for size and geometry.
- Other important ISO GPS standards.

0 INTRODUCTION

Geometrical product specifications are, in addition to material specifications, a key part of the information necessary for effective design, planning, production, and monitoring of products throughout their lifecycle. This is especially true for mechanical products, namely components or assemblies of various machines and devices. Individual components must display appropriate characteristics of different parts of their geometry, which are primarily surfaces, but also the lines and points on these surfaces, viewed in a three-dimensional (3D) or two-dimensional (2D) space (technical drawings). These basic building blocks are generally referred to as geometrical features. Depending on the purpose and function of components in assemblies, different features play more or less important roles in ensuring that components are assembled into sets and perform their tasks (main tasks and sub-functions).

Mechanical engineers have been managing this issue by setting tolerances, which are defined in various standards and whose values depend on the functional analyses of the roles of individual components and assemblies in the common function of a machine or

device. These tolerances need to be determined and specified in the technical documentation of individual components (traditionally in workshop drawings).

In the present day, the process of developing and planning mechanical products is shifting towards specifying all geometrical requirements already in the phase of virtual CAD modelling of products; model based definitions (MBD). Logically, all necessary specifications (tolerances) regarding permissible deviations from the theoretically exact geometry (TEG), as specified in virtual models, are added to the virtual models at this stage. Since this information is non-geometrical or geometrically and visually hard to detect, a system of principles, rules and symbols is needed that can record such information easily and, above all, completely unambiguously either in CAD product models (adding appropriate attributes such as comments and symbols) and/or, at a later stage, in technical product drawings (primarily 2D workshop drawings).

Globally, two standard systems have been established in this area for practical use:

- ASME standards (ASME Y4.5 and others),
- ISO system of standards for the area of geometrical product specifications (GPS).

*Corr. Author's Address: University of Ljubljana, Faculty of Mechanical Engineering, Slovenia, samo.zupan@fs.uni-lj.si

Over the past 20 years, the ISO GPS system has been adopted as a set of national standards by most European countries as well as by many other countries and associations. During this period, many new standards have been created, many have been updated, and the dynamics of updating continues in line with the development of manufacturing technologies as well as quality control technologies (verification – measurement).

This paper will briefly describe the current state of the ISO standards system for GPS, its starting points, key general principles, and rules. Certain innovations will be described that either break away or significantly differ from previous practices, or else provide clear definitions of previously non-existent principles and rules. One of the main concepts and goals of the GPS standards is the completeness of definitions in technical documentation and complete unambiguity of specifications.

Currently, there are not many book sources available that would systematically and extensively discuss the area and be in line with the current state. Since the dynamics of verification, updating, and adoption of new ISO standards in this field has been relatively high over the past two decades, all sources are quickly becoming obsolete. Nevertheless, the following should be mentioned: [1] to [5] and [6] to [12].

1 ORGANIZATION AND BASIC PRINCIPLES OF ISO GPS STANDARDS

Numerous ISO standards determining the basic principles, rules and symbolic language that concerns the method of technical product specifications are divided into a group of standards relating to technical product documentation (TPD), which is overseen by Technical Committee 0 (ISO/TC 0), and a group of standards on GPS, which is overseen by Technical Committee 23 (ISO/TC 23). The TPD group comprises a set of standards that lay down the basics of displaying technical products in various technical drawings: principles and rules for displaying products in 2D projections of spatial objects, technical fonts, carriers of technical drawings, equipment for making drawings, etc.

The group of GPS standards is extensive and sets out principles and rules for recording geometrical product specifications that are not merely visual and therefore require an agreed and coordinated symbolic language. According to ISO terminology, this symbolic language helps to prepare clearer and more understandable descriptions of various operations

used to compose different operators. In practice, this means clear and unambiguously defined sequences of procedures (operations can simply be called recipes) which lead to clear and complete specifications of geometrical requirements for selected geometrical features (explicit requirements) or generally for all features that are not explicitly marked. A similar statement, but possibly with different operators, can be applied to the other fundamental pillar of GPS, i.e. verification [1], [5], [13] and [14]. Every specification of geometrical requirements inevitably leads to appropriate verification, and ISO GPS unambiguously links this according to the principle of duality.

Most of our review content consists of chapters and standards from the narrower area of GPS, called in the American Society of Mechanical Engineers (ASME) geometrical dimensioning and tolerancing (GD&T). The content can be divided into the following summarized points that apply to the geometrical features that make up a workpiece:

- basic principles and rules of GPS;
- features of (linear and angular) size and distance and orientation dimensions (linear and angular) and their tolerances;
- specifications of geometrical tolerances (GT) that are independent of other features of the product:
 - form GTs of lines and surfaces;
- specifications of GTs that depend on other product features (require definitions of references, i.e., datums):
 - orientation GTs of lines and surfaces,
 - location GTs of points, lines and surfaces,
 - runout GTs of lines and surfaces;
- datums (references necessary for the specification of orientation, location, and runout of GTs);
- surface conditions that are visually hard to recognize and are limited by way of permissible:
 - roughness,
 - waviness,
 - primary profile (sum), and
 - specified limitations of local surface defects;
- specifications regarding the allowed conditions of theoretical sharp edges, which are the mathematical boundaries between surfaces.

All GTs are divided into two classes according to the basic definitions of tolerance zone type and shape:

- line GT and 2D tolerance zones, and
- surface GT and 3D tolerance zones.

According to the ISO philosophy, the geometrical features to which geometrical tolerances can be applied and which also affect the correct interpretation

of the specification and the appropriate product verification operations are divided into:

- **integral** features, which are individual features that can be physically touched by measuring means during the verification process (individual external surfaces, lines or points);
- **derived** features, which cannot be directly touched, but are mathematically determined from adjacent symmetrical integral features (median or statistically median points, lines, and surfaces).

Features of size (FoS) hold a special status in GPS, in particular as regards the specification and verification of GTs. The definition includes external surfaces (shafts) and internal surfaces (holes), all with their associated characteristic dimensions (e.g., diameter, distance between two parallel surfaces) and the size tolerances of the measured dimensions. In assembling workpieces with such characteristics, various fits (clearance, interference and transition) are formed, which are key to determining the possibility of assembly and functional properties of assemblies. To ensure the appropriate precision of the orientation and location of these FoS's which crucially affect the possibility of assembly and functioning, the corresponding geometrical tolerances are typically specified. However, these tolerances are usually not applied to integral features, but to derived features (axes or median planes) of such FoS. This approach enables the use of additional "material" requirements; maximum material requirement (MMR), least material requirement (LMR), reciprocity requirement (RPR), which also allows systematic use of classic mechanical fixed gauges, (MMR), known in many industrial environments and languages as "calibres", or at least virtual fixed gauges, (LMR).

All definitions of geometrical tolerances in ISO standards are by default based on the principle that during verification each extracted point of a feature (integral feature) or each mathematically derived point (derived feature) must be within the defined tolerance zone (either 2D or \mathbb{D}). In practice, this is commonly known as the "classical" definition of tolerances, or "the worst-case tolerance". With new or additional indications for geometrical tolerances, the specification can be modified in such a manner that the entire mathematically defined feature (i.e., associated feature), which is determined by appropriate operations (e.g., mathematically ideal surface envelope at the maximum or minimum material amount, Gaussian or Chebyshev (minimax) associated line or surface, etc.), must be within the tolerance zone. We arrive at such a feature by using appropriate operations on

the cloud of extracted points on the real surface of the product (operations: extraction, filtration, association, collection, construction).

By stating an appropriate explicit requirement in the documentation, every dimensional and geometrical tolerance can also be defined as a statistical tolerance. This part is not addressed in the ISO GPS standards. In principle, this means that only a certain percentage of extracted or derived feature points determined as a result measurements during verification must be within the tolerance zone. In practice, it turns out that the use of statistical tolerances and tolerance analyses is still not as common and widespread as anticipated and possible [12].

1.1 Organization of ISO GPS Standards

ISO standards for geometrical product specifications are organized into a matrix [13] which roughly presents their content and purpose. The standards are divided into three main groups:

- 1 Fundamental standards: determine common starting points, default principles, and rules;
2. General standards: essential for practical engineering use, contain special rules and symbolic language;
- 3 Complementary standards: important other standards for comprehensive geometry management (e.g., standards on machine elements).

Global standards (the category has been removed from ISO 48 205 edition [13]): a former category that contained definitions, concepts and terminology that were not necessary for everyday practical engineering work (but certainly for the management, organization, software solution programmers, etc.). Standards which were formerly classified as global GPS standards have either been withdrawn or can be categorized as fundamental or general GPS standards.

Additionally, certain documents lie outside the scope of the ISO GPS system but are necessary for verification (e.g., International System of Units (SI units), International vocabulary of metrology (VIM), Guide to the expression of uncertainty in measurement (GUM).

The GPS matrix system was first defined in 1995 and revised in ISO 48 205 [13]. It is classified among the fundamental standards and is important for understanding the entire system. Another key fundamental standard is ISO 85 2011 [14], which was thoroughly revised and supplemented in this last revision and provides key concepts, principles,

and rules for correctly understanding and using GPS standards. In brief, the most important principles can be summarized in the following points:

- Invocation principle; if one part of the ISO GPS system is explicitly used in a drawing, the entire ISO GPS system applies.
- Hierarchy principle; according to this principle, rules in a standard at a higher hierarchy level (fundamental, global, general, complementary) apply unless a standard at a lower level explicitly gives a different rule.
- Definitive drawing principle; all requirements must be indicated on the drawing, in the documentation referenced on the drawing or in the contract, and it cannot be expected that requirements that are not indicated will be fulfilled.
- Feature principle; the component consists of features with natural (mathematical) boundaries and – unless otherwise specified – each GPS specification applies to the entire indicated feature and only to this one feature.
- Independency principle; unless otherwise specified, each GPS specification for a feature or a relation between features must be fulfilled independently of all other requirements in the specification. This is an important principle compared to some other standards (previous and existing), which by default have a certain connection (dependency) between different specifications (e.g., Rule # in ASME Y4.5 – the envelope rule).
- Decimal principle; in GPS all numbers are considered exact (trailing and leading zeroes of non-specified decimal numbers).
- Default principle; a default rule is a rule that applies when nothing else is specified.
- Reference condition principle; defines the conditions under which the GPS specifications apply to the component (reference temperature defined, clean workpiece, etc.).
- Rigid workpiece principle; all specifications apply to the component in the free state, i.e., without influence from external forces including the force of gravity.
- Functional control principle; GPS is based on the idea that the function of a component only depends on the material properties and the geometrical properties of the component.
- General specification principle; general tolerances only apply to characteristics for which there is no individual (explicit) specification. An individual

specification can be more or less restrictive than the general tolerance.

- Responsibility principle; in GPS, specifications and verifications are not considered as either completely correct or completely wrong. Instead, they are evaluated on their level of uncertainty and/or ambiguity (Correlation and Specification ambiguity and Measurement uncertainty).

Decision rules for verifying conformity or nonconformity with specifications are very important and are stated in a multi-part standard ISO 425 [15] and [16], especially in 1st part, 2017 edition. These rules distribute the combination of the specification ambiguity, which is the responsibility of the designer, and the measurement uncertainty, which is the responsibility of the party proving conformance or non-conformance. The relevant principle is discussed in the paper in next Subclause 2.

1.2 Duality Principle in ISO GPS Standards

The principle of duality is one of the most important principles and states that each geometrical specification (basic pillar) is followed by an appropriate verification (parallel pillar). We determine the specification using appropriate specification operators, which shall sequentially clearly and unambiguously lead to the definition of the geometrical characteristic. Specifications can be composed of the following operations [2], [5] and [58]:

- **Partition** separates the feature(s) involved in the specification;
- **Extraction** defines a set of points that is the digital representation of a feature;
- **Filtration** suppresses certain wavelengths in the surface;
- **Association** defines an ideal feature (without form error) from a set of extracted points on surface of real part (with form error);
- **Collection** considers a number of features as one entity;
- **Construction** defines new ideal features from two or more ideal single features;
- **Evaluation** defines a numeric value from one or more features. The evaluation is always the last operation in a recipe.

Each product can be represented using different types of product spatial virtual models, on which the necessary operations for specification can also be determined and observed:

- **Nominal** model: a mathematically geometrically ideal CAD model of product surfaces without any defects or deviations, indicating geometrical specifications;
- **Skin** model: a surface model of a product that includes possible geometrical and dimensional deviations;
- **Real** model: a model that represents surfaces using clouds of extracted (measured) points on the surfaces (integral features) of the real product.

Verification is also defined using an appropriate operator composed of a correct sequence of verification operations. It is therefore necessary to take into account correlation and specification ambiguity, as well as measurement uncertainty which is inevitable and must be appropriately determined or estimated based on the measuring devices and procedures used. This means that due to measurement equipment limitations, methods and procedures, verification does not necessarily follow the operations given in the specifications. However, it is necessary to correctly consider measurement uncertainty when evaluating the result.

Table 1. ISO GPS standards matrix [13] (simplified example for ISO 1101)

| | Chain Links | | | | | | |
|---------------------------|----------------------------------|---|---|---|---|---|---|
| | A | B | C | D | E | F | G |
| Size | | | | | | | |
| Distance | | | | | | | |
| Form | • | • | • | | | | |
| Orientation | • | • | • | | | | |
| Location | • | • | • | | | | |
| Run-out | • | • | • | | | | |
| Profile surface texture | | | | | | | |
| Areal surface texture | | | | | | | |
| Surface imperfections | | | | | | | |
| specification | verification | | | | | | |
| A Symbols and indications | D Conformance and nonconformance | | | | | | |
| B Feature requirements | E Measurement | | | | | | |
| C Feature properties | F Measurement equipment | | | | | | |
| | G Calibration | | | | | | |

Therefore, standards define the specification and verification of a geometrical characteristic as the ordered set of operations. A specification operation is an operation that is formulated using only mathematical or geometrical expressions or algorithms, or both. These are step-by-step and sequential steps that can be defined mathematically and descriptively as a kind of recipe that leads us to the desired result. Individual steps in this recipe are

called operations and the ordered set of operations is the operator.

The principle of duality is also taken into account in the matrix of the standard chain, which divides this matrix into two pillars: the specification column and the verification column (Table 1). The matrix is composed using seven chain links (A to G columns) and currently nine geometrical properties in the chain of standards, which ensure clear definitions of the content of GPS standards. Each ISO GPS standard can regulate the content that belongs to one or more chain links from A to G in this matrix, which is clearly marked in all GPS standards.

Most ISO standards from the GPS group (currently about 44) relate to the product verification pillar (measuring equipment and methods, measurement uncertainty, etc.). In this paper, we will limit ourselves to standards governing the specification of geometrical characteristics, [13] to [67], which must be followed by verification. Similarly, we will also omit the broad field of surface property specifications (roughness, waviness, primary profile - ISO 21920:2021 [46] to [48]) and edges (ISO 3207 [49]) and corresponding verifications (several ISO standards).

2 TOLERANCE OF LINEAR AND ANGULAR DIMENSIONS

The old division of specifications used to control the accuracy of dimensions indicated on workshop drawings and the geometrical properties of a product was unrefined and unclear, distinguishing only between

- tolerances of linear and angular dimensions, and
- geometrical tolerances.

There was no clear correlation regarding the purpose of linear dimensions, or whether they represent the FoS or the position or orientation of a feature in space. Furthermore, it was not clearly defined whether an angular dimension could represent a characteristic size of a feature or only its orientation. The rules for defining the geometrical characteristics of features (form, orientation, location) have always been clearer, but still incomplete.

The ISO 4405 standard [17] to [19] belongs to the group of general GPS standards and now clearly defines in three parts the tolerances of linear and angular dimensions, typically representing the size of shafts and holes (Parts 1 and 3 FoS: circle, cylinder, pair of prismatic surfaces, cone, pair of pyramidal surfaces, etc.) and what are other linear and angular dimensions that are not classified as "size". In the second part, the standard gives recommendations on

tolerancing for features associated with these linear and angular dimensions (location and orientation GT – Part 2).

ISO 4405 -1 2006 [17] defines the default definition of linear size (Table 2, Fig. 1) and determines various other special specification operators for the linear size of shafts and holes (FoS). The default definition of size is still, as before, any possible distance between two opposing points (LP) on features (surface/s) lying on the same normal, passing through the derived line or plane (axis or median plane).

Table 2. Linear/angular size specification modifiers

| | Modifier | Linear Sizes [17] |
|--------------------------|----------|---|
| Local linear sizes: | (LP) | Local two-point size (default size) |
| | (LS) | Local size defined by sphere |
| Global linear sizes: | (GG) | Least-squares association criterion |
| | (GX) | Maximum inscribed association criterion |
| | (LP) | Minimum circumscribed assoc. criterion |
| Calculated linear sizes: | (GC) | Minimax (Chebyshev) association criterion |
| | (CC) | Circumference diameter |
| | (CA) | Area diameter |
| | (CV) | Volume diameter |
| | Modifier | Angular Sizes [19] |
| Local angular sizes: | (LC) | Two-line angular size with minimax association criterion (new default size) |
| | (LG) | Two-line angular size with least squares association criterion |
| Global angular sizes: | (GC) | Global angular size with least squares association criterion |
| | (CC) | Global angular size with minimax association criterion |
| | Modifier | Statistical linear/angular sizes [17] and [19] |
| Rank-order sizes: | (SX) | Maximum size |
| | (SN) | Minimum size |
| | (SA) | Average size |
| | (SM) | Median size |
| | (SD) | Mid-range size |
| | (SR) | Range of sizes |
| | (SQ) | Standard deviation of size |

However, the standard now fully defines many other possible operators on how to determine the linear size of a feature. These methods (operators) are divided into four groups: local sizes (2), global sizes (4), calculated sizes (3), and statistical sizes (7 rank order linear sizes).

The ISO 4405 3 2006 [19] default specification operator for angular size is the “two-line angular size”

with minimax association criterion (Table 2, Fig. 2). The standard determines additional specification modifiers for the angular size of shafts and holes (FoS). The default definition of angular size is now different (see Fig. 4 in ISO 4405 3 [19]) from what it used to be (the angle between two envelope lines in the cross-sectional plane easily measured with mechanical protractors) and is determined by the mathematical “minimax” (Chebyshev) rule, which represents a mathematical definition of the profile line from the cloud of measured points and can be significantly different from the ones with envelope lines. The standard now fully defines other possible modifiers for determining the angular size of a feature divided into three groups: local angular sizes (2) and global angular sizes (2), which also include statistical sizes (7 rank order angular sizes).

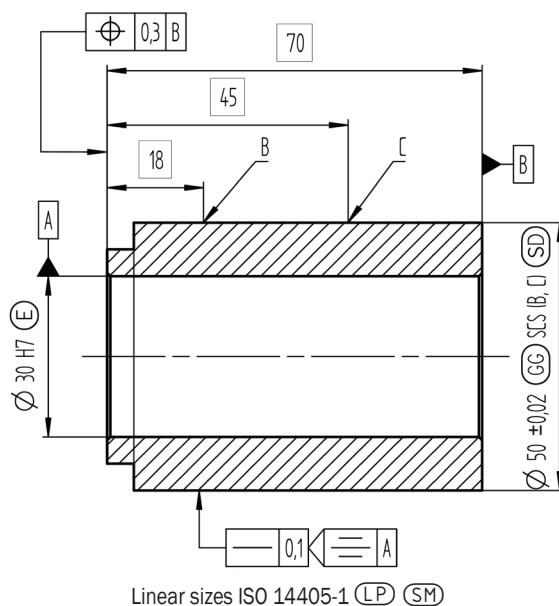


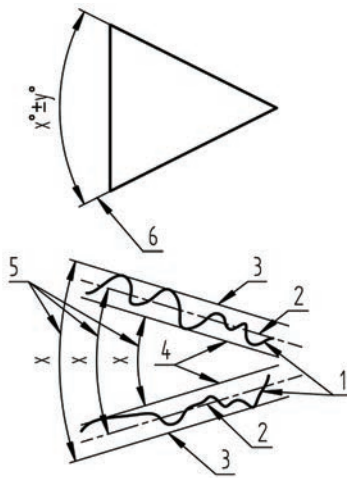
Fig. 1. Example of explicit size specification and alternate defaults

The standard introduces numerous new symbols that specify which operator (definition) applies to individual size measurements or generally to all size measurements on a product that does not have an explicit modifier (alternate defaults specified with the indication of ISO 4405 [17] and [19] and the appropriate modifier).

Tolerances of linear and angular dimensions are indicated on drawings or models according to the dimensioning rules (ISO 129-1:2018 [21]) as:

- upper limit deviations (ULD) and lower limit deviations (LLD) from the nominal dimension;
- upper limit sizes (ULS) and lower limit sizes (LLS);

- the ISO tolerance code of the internal or external size according to ISO 281200 (only linear dimensions) [23].



Angular sizes ISO 14405-3 (C)

Notes:

1 real feature, 2 associated feature with minimax criterion without material constraint, 3 assoc. feature with minimax criterion with outside material constraint, 4 assoc. feature with minimax criterion with inside material constraint, 5 two-line angular size, and 6 angular dimension

Fig. 2. Example of default angular size definition (Chebyshev)

According to the rules given in ISO 4405 it is possible to use other operators of linear or angular size throughout the entire tolerance range (interval), or different types for the upper and lower limit sizes (Fig. 1). As new global size operators can affect both the size and shape of FoS, correlations between different specifications are created with such use, breaking the principle of independence. During verification, in this case it is necessary to perform various measurements that produce an interconnected result. This is similar to considering the well-known envelope principle (E) when dimensioning the size of shafts and holes. Although according to the ISO GPS philosophy, the envelope principle is not implicit (as it is in ASME Y4.5 - Rule \mathbb{M}), it is still often useful and represents a connected requirement for the ideal form of shafts and holes in a state where the product contains the maximum amount of material (MMS). It is also important to know that the envelope principle is no longer automatically included if we use ISO encoded tolerances of size for shafts and holes, but the envelope requirement always needs to be added explicitly or generally for all shafts and holes on the product (Fig. 1).

The operators that determine the definitions of statistical sizes are the same for linear and angular

size measurements and represent typical statistical estimators, which are mainly used when defining statistical tolerances and also when defining statistical indexes in statistical process control (SPC). The calculation of statistical estimators is simple in size measurements, as the actual measurements are themselves independent scalar statistical variables. However, the use of these operators in size specifications does not automatically imply the adherence to statistical tolerance criteria for verifying these measurements. The documentation must state explicitly and unambiguously that a certain dimension must be verified using the principles of statistical tolerancing.

Caution should also be exercised when performing tolerance analyses, as the known methods do not necessarily include the adapted rules from the existing standards. The same applies to software tools, for which it is generally difficult to determine the standards with which they fully comply.

ISO 4405 2:2008 [18] lays down guidelines for specifying tolerances or dealing with other linear or angular dimensions that do not represent size, in terms of specification unambiguity. This refers to dimensions that represent:

- various linear distances between features that are not between two opposite points;
- linear dimensions that represent the distance between two different integral features;
- rounding radii;
- angular dimensions representing orientation between two different features (reference and feature).

The use of dimension tolerances (using limit deviations, limit dimensions, or ISO tolerance code) can be ambiguous in these cases and is not recommended. Only suitable geometrical tolerances should be used for all such geometrical characteristics.

3 GEOMETRICAL TOLERANCES

The principles and rules governing the narrower area of GPS, known in ASME as GD&T, are regulated by numerous ISO standards. Over the past 0 to 5 years, many new standards have been adopted, and many existing ones have undergone fundamental revisions, enabling new ways of specifications that were previously undefined. In the far past, many of them were probably adopted from ASME standards, but later they evolved in ISO along a slightly different path. Nevertheless, both systems are very close and

similar, with a few significant differences [4], [5] and [11].

Several individual standards from the former global ISO GPS group are essential for a comprehensive and in-depth understanding of the concepts, which we will not discuss in detail ([25] and [58] to [65]). Below described are the essential standards for everyday practical use which belong to the group of general standards.

GTs are organized into four groups depending on what geometrical characteristics they specify and thus control for the selected feature (Table 3):

- form,
- orientation,
- location, and
- runout.

Table 3. Geometrical tolerances (groups, symbols) [24]

| Group | Symbol | Tolerance, tolerance zone, datums (Yes/No) |
|-------------|--------|--|
| Form | — | Straightness, 2D or 3D ¹ , No |
| | ▭ | Flatness, 3D, No |
| | ○ | Roundness, 2D, No |
| | ⊘ | Cylindricity, 3D, No |
| | ⤿ | Line profile, 2D, No |
| | ⤿ | Surface profile, 3D, No |
| Orientation | // | Parallelism, 3D ² , Yes ³ |
| | ⊥ | Perpendicularity, 3D ² , Yes ³ |
| | ∠ | Angularity, 3D ² , Yes ³ |
| | ⤿ | Line profile, 2D, Yes |
| Location | ⤿ | Surface profile, 3D, Yes |
| | ⊕ | Position, 3D, Yes ⁴ |
| | ⊙ | Concentricity or Coaxiality, 3D, Yes ⁴ |
| | ≡ | Symmetry, 3D, Yes ⁴ |
| Run-out | ↗ | Circular runout, 2D, Yes ⁵ |
| | ↗↗ | Total runout, 3D, Yes ⁵ |

1 for median axes
 2 generally 3D, can be converted to 2D with additional modifiers
 3 single datum or system of 2 datums (block at least 4 to 5 degree of freedom (DoF))
 4 full datum system (block 6 DoF)
 5 datum/datum system must establish an axis of rotation

The first three groups of GTs include tolerances, which, along with size tolerances (according to ISO 4405 [17] and [19]), can fully control (supervise) the basic geometrical characteristics of rigid bodies: their size, permissible form deviations, orientation, and location in \mathbb{D} space. Given these characteristics, the geometry in \mathbb{D} space is fully defined. GTs are organized hierarchically: their requirements are

increasing, which means that costs increase as well. Therefore, economic logic dictates that we choose the largest tolerance zones for location GTs, smaller for orientation, and the smallest for form GTs.

Table 4. Additional GT symbols (modifiers) – excerpt from ISO 1101 [24] and ISO 1660 [34]

| Symbol | Description |
|--|--|
| Combination specification elements | |
| CZ | Combined zone |
| SZ | Separate zones |
| Unequal zone specification elements | |
| UZ | Specified tolerance zone offset |
| Constraint specification elements | |
| OZ | Unspecified linear tolerance zone offset (offset zone) |
| VA | Unspecified angular tolerance zone offset (variable angle) |
| Associated toleranced feature specification elements | |
| Ⓢ | Minimax (Chebyshev) feature |
| Ⓣ | Least squares (Gaussian) feature |
| Ⓝ | Minimum circumscribed feature |
| Ⓣ | Tangent feature |
| Ⓧ | Maximum inscribed feature |
| Derived toleranced feature specification elements | |
| Ⓐ | Derived feature ¹ |
| Ⓟ | Projected tolerance zone |
| Toleranced feature identifiers | |
| UF | United feature |
| LD | Minor diameter |
| MD | Major diameter |
| PD | Pitch diameter |
| ↔ | Between |
| Ⓢ | All around (profile) |
| Ⓣ | All over (profile) |
| Auxiliary feature indicators | |
| ACS | Any cross-section |
| SCS | Specified cross-section |
| ⊞ | Intersection plane indicator |
| ⊞ | Orientation plane indicator |
| ← | Direction feature indicator |
| ⊞ | Collection plane indicator |

¹ alternate indication of median axes and planes as toleranced feature

The basic standard is ISO 101 207 [24], which sets out the basic rules and symbols for using geometrical tolerances for form, orientation,

location, and runout. The standard defines 4 different geometrical tolerances (cf. Table 3), which can be applied to integral or derived features (median lines or surfaces of FoS), and can have \mathbb{D} or 2D tolerance zones.

Depending on the type of GT, numerous additional tolerance symbols (modifiers) can be used which unambiguously define the shape and size of the tolerance zone and determine whether the principle of independence or other correlations applies between individual parts of the zone. Geometrical tolerances for form and profile are defined in detail in separate standards.

The default definition of all GTs is that all extracted (measured) [25] points on the toleranced feature of the real product must be within the boundaries of the tolerance zone. However, before assessing (verifying) whether the feature is within the tolerance zone, it is now possible to use various mathematical procedures on the cloud of these points, such as various filtering and association of ideal mathematical features according to the selected mathematical definition (e.g., tangent plane, envelopes, Gaussian or Chebyshev line or surface; Table 4). By default, the assessment is carried out using the default definition of tolerancing (also known as “worst-case tolerance”), but it can also be carried out according to the statistical principle. In this case, however, certain issues arise, which will be discussed later.

3.1 Form GTs

Form GTs are basically determined in the widely used ISO 10 1 [24] standard and defined in more detail in specific standards (straightness (2D) [30], and [31], flatness (3D) [32] and [33], roundness (2D) [28] and [29] and cylindricity (\mathbb{D}) [26] and [27]). They can control deviations from the ideal form for elementary geometrical features (straight line, flat surface, circular line, and cylindrical surface). However, they cannot control their size, orientation, and location. The group of form tolerances also includes line profile and surface profile [34] tolerances, when used without references (datums).

3.2 Orientation GTs

Orientation GTs (parallelism, angularity, and perpendicularity [24]) are also primarily intended for elementary geometrical features (straight lines, flat surfaces) and mainly control the orientation relative to the reference (datum). In principle, one datum

is enough, but for repeatability of measurements, it is recommended to use two datums. According to the basic definition, all three orientation GTs have \mathbb{D} tolerance zones, but with the use of appropriate additional indicators, they can be converted into 2D zones (tolerances apply independently for individual lines on surface feature). The theoretically exact orientation of the feature must be specified using the Theoretical Exact Dimension (TED) in the datum system. Orientation GTs cannot control the size of the features and their locations in space, but they can indirectly (secondarily) control the form, although this is not their primary purpose.

3.3 Location GTs

Location GTs (position, concentricity or coaxiality, and symmetry) are primarily intended for derived FoS features (axes, median planes) and control their location in the coordinate system, which is determined by the reference system (datums). According to ISO, these tolerances can also be used to control individual integral features (lines, planes). By default, these tolerance zones are three-dimensional (\mathbb{D}), and the theoretically exact location of the characteristic must be dimensioned using TED in the datum system. The datum system must be complete and lock all degrees of freedom (DoF) of movement of rigid bodies (three translations and three rotations). The sequence of single datums in the datum system (primary, secondary, and tertiary) allows for the reproducible establishment of these datum coordinate systems and therefore reproducible measurements. Except for the size of the selected feature, location GTs control all geometrical characteristics: primarily the location, indirectly (secondarily) the orientation, and indirectly (tertiary) the form.

The position tolerance (ToP) has historically been the most frequently used geometrical tolerance (over 60%). The reason for this is that the position of the FoS is critical to ensure the assembly of components (production and maintenance economics) and often also has a significant impact on the function of the assemblies. This tolerance is mostly used to control the position of median axes or median planes of shafts and holes (FoS). Such usage also meets the condition for the application of additional material requirements (MMR, LMR, RRP), which further can reduce production and control costs with the use of fixed gauges.

3.4 Material Requirements

Material requirements can be used with location tolerances and orientation tolerances, and even with certain form tolerances (straightness, rarely flatness), when these are applied to derived features (median axes and planes) of FoS. Details on material requirements are regulated by the ISO 2692:2021 standard [35] (Table 5).

Table 5. Additional GTs modifiers - ISO 2692 [35] and ISO 10572 [50]

| Symbol | Description |
|---|--|
| Material condition specification element [35] | |
| (M) | Maximum material requirement (MMR) |
| (L) | Least material requirement (LMR) |
| (R) | Reciprocity requirement (RPR) |
| State specification element [50] | |
| (F) | Free state condition (non-rigid parts) |

All material requirements mean a certain interconnection of the tolerance of the size dimension of the FoS and geometrical tolerance, thereby eliminating the principle of independence. With these requirements, potential increases in the deviation of the geometrical characteristic may occur when the size of the FoS (shaft or hole) approaches the opposite limit size at which the product with this FoS contains the maximum (MMR) or minimum (LMR) possible amount of material. This increase is called a “bonus” tolerance (originating from the tolerance of the linear size dimension of the FoS).

The reciprocity requirement (RPR) is an additional requirement, which may be used together with the maximum material requirement (MMR) and the least material requirement (LMR) in cases where it is permitted — taking into account the function of the tolerated feature(s) — to enlarge the size tolerance when the geometrical deviation on the actual workpiece does not take full advantage of, respectively, the maximum material virtual condition or the least material virtual condition.

The reciprocity requirement (RRP) is less well-known in practice and is rarely used. The permitted increase in the size tolerance, however, arises from the specified value of the tolerance zone of the used GT.

The MMR and LMR requirements can also be used for datums if these are also derived FoS (axes, median planes). Such use brings an additional bonus to the size of the GT tolerance zone, which is called “datum shift” (as it arises from the tolerance of the linear size dimension of the datum FoS). The logical

and correct use of the MMR requirement for both the controlled FoS and the datum FoS at the same time allows the manufacture and use of complex entirely mechanical verification control devices (gauges) of fixed size (calibres), with which we quickly check the appropriateness of geometrical characteristics according to the principle of “accepted or rejected”.

All material requirements can reduce production costs in serial production. However, caution is needed when the characteristics being tolerated are key to assembly or function, as they increase the total tolerance and thus possible variations in the geometrical and/or size characteristic between the limit values (greater scatter), which development engineers must take into account.

3.5 Profile GTs

The two geometrical tolerances of the profile (line and surface profile) are added to each of the basic three groups of tolerances for controlling form, orientation, and location.

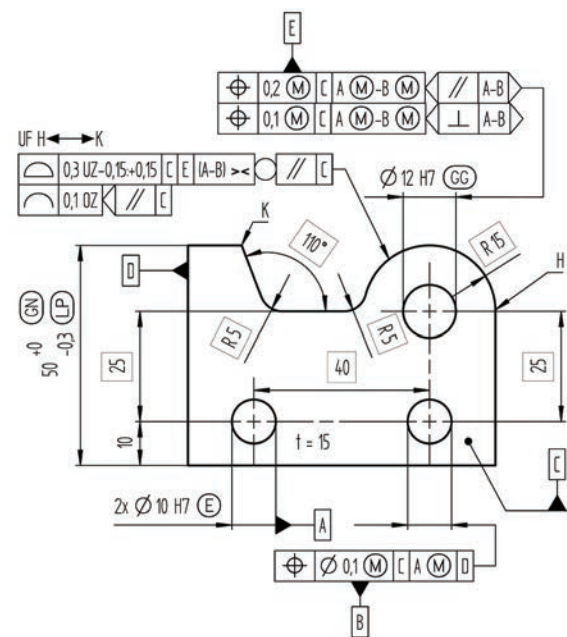


Fig. 3. Example of complex GT specifications (ISO GPS system)

These two tolerances rank among some of the most universal GTs and can control almost anything through an appropriate use of additional indicators and datums (Fig. 3). Therefore, profile GTs are becoming, along with the position tolerance, the most widely used GTs and are also well suited to the modern methods of geometry control and measuring equipment, which allow measurement of the absolute

coordinates of each point on geometrical features. All these possibilities are detailed in the rules of the ISO 6: 2017 standard [34], which has been thoroughly updated compared to the previous edition. In the future, with all the changes and innovations, these two tolerances will undoubtedly joint the position tolerance in the group of the most commonly used GTs.

3.6 Runout GTs

The geometrical tolerances for circular runout and total runout are still categorized in a separate group, even though by definition, they allow control over the form, orientation, and position of the tolerated feature. The definitions of both tolerances are based on the characteristic rotational movement of many machine elements or their features and were used for verification even before the GDT system was even regulated in various standards. In the past, the methods were known under the names “full indicator reading” (FIR) and “total indicator reading” (TIR).

When using runout tolerances, the following rules apply:

- Both tolerances can only be used for integral features, never for derived features (median lines and planes).
- In this case, a datum or datum system is mandatory as it establishes a clear rotational axis around which we must physically rotate the tolerated feature in its entirety (θ°) or in a restricted area in which this feature is defined. In principle, we can also rotate the measuring probe around the axis of this feature.
- The measuring probe used to extract points on the feature during verification must constantly touch, or slide along, this feature.
- The movement of the probe in the direction of the normal line on the feature or in the direction that must be clearly specified (using the appropriate additional tolerance indicators or modifiers) is compared with the specified width of the tolerance zone.

The circular runout tolerance means measurement in a cross-sectional plane that is normal to the rotational axis, the tolerance zone is two-dimensional (typically, a circular ring). The measurement of the circular runout deviation over the entire surface is carried out when moving along the rotational axis; each measurement is independent of the others.

The total runout tolerance involves the same method of measurement, except that during

measurement we move the cross-sectional plane along the rotational axis so that we cover the entire surface, and the measurements are dependent on each other. Therefore, the tolerance has a D tolerance zone (rotational volumetric ring).

Both runout tolerances represent the control of form and orientation, and in special cases, also the position of the tolerated feature. However, they generally do not control size. Verification is effective but generally requires special measuring equipment, which is usually only available in workshops that produce characteristic “rotational” products in series. In principle, we can achieve similar effects with the alternative use of other geometrical tolerances.

3.7 Datums and Datum Systems

References or datums are key to all GT with which we control the location and/or orientation of geometrical features, and to runout tolerances. With the help of datums, we create a global and/or local coordinate system, within which the tolerance zone of GT is precisely positioned and oriented (Table 6). The rules for specifying and practically establishing datums, and thus reference coordinate systems, are described in detail in ISO 5459:2011 [36].

Table 6. Symbols and additional datum indicators - excerpt from ISO 5459 [36]

| Symbol | Description |
|--|---|
| Datum features and datum target indicators | |
| | Datum feature indicator (capital letters A, B, C, AA, etc.) |
| | Single datum target frame |
| | Moveable datum target frame |
| | Datum target point |
| | Datum target lines, borders... |
| Datum modifiers symbols (excerpt) | |
| [PD] | Pitch diameter |
| [MD] | Major diameter |
| [LD] | Minor diameter |
| [ACS] | Any cross section |
| [ALS] | Any longitudinal section |
| [CF] | Contacting feature |
| [DV] | Variable distance (for common datum) |
| [PT] | (situation feature of type) Point |
| [SL] | (situation feature of type) Straight line |
| [PL] | (situation feature of type) Plane |
| >> | For orientation constraint only |
| | Projected tolerance zone (for secondary or tertiary datum) |
| | Least material requirement |
| | Maximum material requirement |

Datums are stated on technical drawings or models (MBD) which display the TEG and whose sizes correspond to the dimensioned nominal dimensions. Datums can be individual (e.g., A) or common (e.g., A-B), and both types can form datum systems.

However, for verification, datums need to be established from the real geometry features of the product with all possible and permissible errors. One of the principles is that it is appropriate to first ensure, using the form and orientation GTs, that these features also have suitable quality (flatness, straightness, etc.) after manufacturing. A Cartesian coordinate system is most easily created with three planar datums that are orthogonally oriented to each other, but other combinations are also possible. Such a datum system locks all degrees of freedom of movement (three translations, three rotations) of a rigid body, which is a necessary condition when needing to control all geometrical features, primarily with location. When only orientation needs to be controlled, it is enough that four or five degrees of freedom are locked. When using datum systems, the sequence (primary, secondary, tertiary) in the tolerance frame is crucial as it also allows for repeatable insertion of the product into the gauge, thus ensuring repeatable and comparable measurements.

Datums for verification can be established using mechanical measuring tools and accessories (tables, support elements, etc.). At least one suitable primary datum system defined on the product should be of such a type that it can be used to position products in measuring devices. The primary single datum in the datum system should ideally support the weight of the product.

Datums can also be established mathematically from clouds of measured points. In doing so, various operations previously described in the characteristic specifications can be used to determine a proper mathematical feature from a cloud of points that will be used to establish the datum. The current standard allows for the use of operations similar to those applicable for toleranced features (filtering [24], ISO 6 [37] series, associations, etc.). It also offers several ways to limit the extent of features used for datums (datum targets). If a derived feature (e.g., an axis) is chosen for an individual datum, it is also possible to use material requirements and the appropriate simulation of the datum (e.g., with fixed mechanical aids in the case of MMR). It can also be set which characteristics each datum can be used for and which degrees of freedom it should lock.

All these possibilities are foreseen in the current version of the standard, which today allows for an unambiguous definition of practically useful datums based on the state of measurement technology. Various additional requirements (modifications) that need to be taken into account are typically written in the definition and use datums with appropriate indicators written in square brackets (e.g., [CF], [DV], [VA], etc. Fig. 4) and new symbols used on the drawing or 3D model (e.g., movable datum targets).

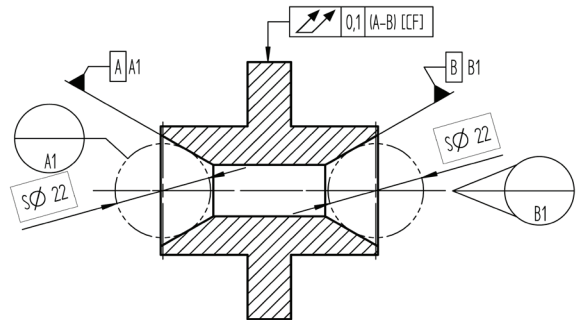


Fig. 4. Example of datum system specification using a movable datum target and contacting feature [CF]

3.8 General Tolerances

The general principles of ISO GPS (ISO 85 [14]) also include the general specification principle and the definitive drawing principle. The first speaks to the fact that for each product it is possible to explicitly specify every one of its characteristics, while the second indicates that general specifications (dimension tolerances, GT, surface conditions, edge states) must be determined for all characteristics without explicit specifications. The second principle speaks to the fact that we cannot demand the executor (workshop) to make anything that is not unambiguously defined on the drawing in an explicit or general way.

General specifications are therefore a very important part of technical documentation. In ISO GPS, this issue is regulated with a series of general standards, which must be appropriately listed or used in the documentation:

- ISO 22038 2021 [38] is a new standard that sets out the principles and rules on how to specify general dimensional tolerances and general geometrical tolerances on documentation. It is recommended that this standard is explicitly mentioned in the documentation and that it is detailed within this mention whether the general tolerances are:

- linear size dimension tolerances;
- angular size dimension tolerances; or
- geometrical tolerances (it recommends the exclusive use of surface profile tolerance with a complete reference system of plane datum system; R, S, T).

| |
|---|
| <p>General tolerances ISO 22081</p> <p>Linear size:</p> <ul style="list-style-type: none"> - ISO 8062-3 – DCTG 10 – RMAG E ☉¹ - ISO 2768-m ☉² <p>Angular size: ±0,15°</p> <p>Geometrical tolerances:</p> <ul style="list-style-type: none"> - ISO 8062-4 ☉ 2,7 R S T (P8) ☉³ - ☉ 1,0 R S T ☉ |
| <i>Title block</i> |
| <p>Notes</p> <p>¹ molded condition ☉</p> <p>² final machined ☉</p> <p>³ general datum system must be specified on drawing</p> |

Fig. 5. Example of general tolerances specification [38]

Each of these can be determined individually and with their own constant values or own table for a larger size range, or we can refer to another appropriate standard in which the values are already determined according to the selected quality class defined in this standard.

- ISO 2768-1:1989 [39] is the basic standard for general tolerances of linear and angular dimensions (sizes) of products, which are mainly produced using cutting technologies (machining). Typically, the permitted deviations depend on the size of the dimension (eight intervals from 0.5 mm to 100 mm) and on the required quality (four classes: fine, medium, coarse, and very coarse). As with all general tolerances, the tolerance interval is centred around the nominal value of the dimension. This, of course, means that dimensions controlled by general tolerances are entirely unsuitable for forming various fits between parts (shafts and holes), as the fit is impossible to predict. The second part of this standard governed certain general geometrical tolerances and was outdated and therefore withdrawn in 2021
- ISO 803 [40] to [43] specifies general specifications for castings made from metal alloys. The standard is issued in several parts and regulates vocabulary, rules, general tolerances for

linear dimensions (DCTG in 6 quality grades), general geometrical tolerances (GCTG – surface profile tolerance based on the full general datum system R, S, T in 5 grades) and sizes of required machining allowances for subsequent mechanical processing (RMAG in 0 quality grades). The size measurement interval is in sub-intervals up to 0,000 mm, and the corresponding quality levels depend on the type of material and casting technology.

- ISO 2045 208 [44] is a standard that sets general tolerances for general plastic castings and is very similar to ISO 803 in principles and rules. However, it also provides guidance on product acceptability conditions and allows the selection of suitable specifications that correspond to the chosen type of material and plastic casting technology. The standard is issued under the auspices of ISO/TC 6 SC 2.
- ISO 13920:2023 [45] is a standard that sets general tolerances for length and angle measurements as well as form and orientation (flatness, straightness, parallelism), and positions of parts of welded constructions. The standard is issued under the auspices of ISO/TC 44/SC 0 and is conceptually somewhat different from what is presented in the current principles and rules of ISO GPS. It focuses on the main errors that occur in welding technology.

4 OTHER GPS STANDARDS

In addition to the standards described earlier in the paper, it is necessary to mention several commonly and widely used standards and specific ISO GPS standards from the group of general geometrical specification standards which are less frequently used but contain certain useful and effective principles and rules.

- ISO 16792:2021 [66] is a standard that falls into the TPD group and operates under the auspices of ISO/TC 0. However, it is inextricably linked with the group of GPS standards as it sets out the principles and rules on how to specify geometrical specifications in accordance with the MBD philosophy directly in 3D CAD models of products.
- ISO 10579:2010 [50] is a global GPS standard that sets out principles and rules for tolerancing parts that are not rigid and deform during verification under the influence of gravity differently in different orientations.

- ISO 21920:2021 [46] to [48] is a new standard in three parts that sets out profile specifications for the texture and condition of surfaces (roughness, waviness) and replaces ISO 02, which has been withdrawn.
- ISO 3 :207 [49] is a standard under the auspices of ISO/TC 0 that specifies allowable conditions (“chamfering or rounding”) of sharp edges (external and internal) that are modelled as ideal.
- Less frequently used standards include, for example, standards used to specify and control certain characteristics on workpieces produced using special technological processes (e.g., castings [51]), local and limited imperfections on surfaces [52], conical and pyramidal (wedge) shapes [53] to [56], patterns [57] etc.
- ISO 20170:2019 [67] is a new and important standard from the group of fundamental ISO GPS standards. It describes principles and tools to control a manufacturing process in accordance with a GPS specification. For this purpose, a set of one or more complementary, independent characteristics (size, form, orientation, and location characteristics independent to each other) that correlate to the manufacturing process parameters and to the manufacturing process coordinate system established from the manufacturing datum system are used. This standard describes the concept of decomposition of the macro-geometrical part of the GPS specification. It does not cover the micro-geometry, i.e., surface texture. The objective of the decomposition is to define correction values for manufacturing control or to perform a statistical analysis of the process. In order to carry out SPC, it is inevitable to monitor the selected and most influential size dimensions and also geometrical tolerances on the basis of calculated statistical process capability indices (such as C_p , C_{pk} , etc.), and not merely based on verification whether the tolerated features are within the tolerance zone or not (classic tolerance definition). For size dimensions, which behave as independent scalar statistical variables during verification, these indices are easy to calculate (also with the help of new statistical operators of size definition according to ISO 4405). However, geometrical tolerances can be complex specifications (operations) that cannot be mathematically represented by a single scalar statistical variable. For SPC, it is necessary to mathematically

decompose each GT into a list (vector) of scalar statistical components. This standard is the first to provide clear starting points, a mathematical basis (geometrical transformations), methods and rules for this decomposition. In this way, each geometrical specification can be fully monitored according to the principles of SPC.

5 CONCLUSIONS

This paper provides an overview of the philosophy of geometrical product specifications which is embodied in the ISO series of GPS (ISO/TC 23) standards. The principles and basic rules for clear and unambiguous specification of all requirements related to the geometrical features of products are divided into fundamental, general and complementary ISO GPS standards.

A clear and unambiguous geometrical specification which belongs to the basic pillar of GPS enables unambiguous product verification based on the principle of duality, thus facilitating the negotiation and communication process between the parties, i.e., the client and the supplier, in the process of designing and manufacturing mechanical products.

In the last two decades, ISO has made comprehensive and significant progress in this area, with many standards being amended and improved. The regulated specification of geometrical requirements with innovations in standards also enables a clear and unambiguous definition of necessary operations in verification, which better correspond to modern measurement methods and measurement technology based on the absolute measurement of the location of individual points in the cloud of extracted points on geometrical features of real products (CMM, optical and laser scanning, etc.).

Since these are important basics of technical communication, users should be well acquainted with them. This is often not the case, as it is a rather extensive topic with many novelties and frequent changes, causing considerable effort and thus problems for practical users in training. Due to the vast and varied scope of standards, engineers find it difficult to keep up with their dynamics in practice. Another issue is the accessibility, or the cost, of standards for users. This causes numerous problems since the communication between partners (client and supplier) often does not occur on the same basis.

In this paper, we focused primarily on geometrical specifications and the standards that regulate the geometry and sizes of products. There

are also novelties in the field of surface texture and edge state specifications, which are mentioned but not explained in detail. Likewise, the entire parallel pillar of verification is omitted from the discussion. According to the ISO GPS matrix, the verification pillar contains an even larger number of standards that regulate verification in more detail.

8 REFERENCES

- [1] Nielsen, H.S. (2012). *The ISO Geometrical Product Specifications Handbook*, ISO/Danish Standards, International Organization for Standardization, Geneva.
- [2] Charpentier, F. (2012). Handbook for the geometrical specification of products, The ISO-GPS standards.
- [3] Krulikowski, A. (2015). ISO GPS Ultimate Pocket Guide (A companion to ISO 1101:2012 and related Geometrical Tolerancing Standards), 2015 Effective Training Inc. an SAE INTERNATIONAL company, from www.etinews.com, accessed on 2023-08-06, DOI:10.4271/pd027104.
- [4] Henzold, G. (2020). *Geometrical Dimensioning and Tolerancing for Design, Manufacturing and Inspection: A Handbook for Geometrical Product Specification Using ISO and ASME Standards*, 3rd ed., Butterworth-Heinemann, Oxford, DOI:10.1016/B978-0-12-824061-8.00006-2.
- [5] Tornincasa, S. (2021). *Technical Drawing for Product Design, Mastering ISO GPS and ASME GD&T*, 1st ed. Springer, Cham, DOI:10.1007/978-3-030-60854-5.
- [6] Płowucha, W., Jakubiec, W., Humienny, Z., Hausotte, T., Savio, E., Dragomir, M., Bills, P., Marxer, M., Wisła, N., Mathieu, L. (2014). Geometrical product specification and verification as toolbox to meet up-to-date technical requirements. *The 11th International Scientific Conference Coordinate measuring technique*.
- [7] Moroni, G., Petrò, S., Polini, W. (2017). Geometrical product specification and verification in additive manufacturing. *CIRP Annals*, vol. 66, no. 1, p. 157-160, DOI:10.1016/j.cirp.2017.04.043.
- [8] Shakarji, E.P., Srinivasan, C.M. (2018). A brief analysis of recent ISO tolerancing standards and their potential impact on digitization of manufacturing. *Procedia CIRP*, vol. 75, p. 11-18, DOI:10.1016/j.procir.2018.04.080.
- [9] Vakouftsis, C., Mavridis-Tourgelis, A., Kaisarlis, G., Provatidis, C.G., Spitas, V. (2020). Effect of datum system and datum hierarchy on the design of functional components produced by additive manufacturing: a systematic review and analysis. *The International Journal of Advanced Manufacturing Technology*, vol. 111, p. 817-828, DOI:10.1007/s00170-020-06152-6.
- [10] Humienny, Z. (2021). State of art in standardization in the geometrical product specification area a decade later. *CIRP Journal of Manufacturing Science and Technology*, vol. 33, p. 42-51, DOI:10.1016/j.cirpj.2021.02.009.
- [11] Humienny, Z. (2021). Can ISO GPS and ASME tolerancing systems define the same functional requirements? *Applied Sciences*, vol. 11, no. 17, art. ID 8269, DOI:10.3390/app11178269.
- [12] Walter, M.S.J., Klein, C., Heling, B., Wartzack, S. (2021). Statistical Tolerance Analysis-A survey on awareness, use and need in German industry. *Applied Sciences*, vol. 11, no. 6, art. ID 2622, DOI:10.3390/app11062622.
- [13] ISO 14638:2015. *Geometrical product specifications (GPS) – Matrix model*. International Organization for Standardization, Geneva.
- [14] ISO 8015:2011. *Geometrical product specifications (GPS) – Fundamentals – Concepts, principles and rules*. International Organization for Standardization, Geneva.
- [15] ISO 14253-1:2017. *Geometrical product specifications (GPS) – Inspection by measurement of workpieces and measuring equipment – Part 1: Decision rules for verifying conformity or nonconformity with specifications*. International Organization for Standardization, Geneva.
- [16] ISO 14253-2:2011. *Geometrical product specifications (GPS) – Inspection by measurement of workpieces and measuring equipment – Part 2: Guidance for the estimation of uncertainty in GPS measurement, in calibration of measuring equipment and in product verification*. International Organization for Standardization, Geneva.
- [17] ISO 14405-1:2016. *Geometrical product specifications (GPS) – Dimensional tolerancing – Part 1: Linear sizes*. International Organization for Standardization, Geneva.
- [18] ISO 14405-2:2018. *Geometrical product specifications (GPS) – Dimensional tolerancing – Part 2: Dimensions other than linear or angular sizes*. International Organization for Standardization, Geneva.
- [19] ISO 14405-3:2016. *Geometrical product specifications (GPS) – Dimensional tolerancing – Part 3: Angular sizes*. International Organization for Standardization, Geneva.
- [20] ISO 128-1:2020. *Technical product documentation (TPD) – General principles of representation – Part 1: Introduction and fundamental requirements*. International Organization for Standardization, Geneva.
- [21] ISO 129-1:2018. *Technical product documentation (TPD) – Presentation of dimensions and tolerances – Part 1: General principles*. International Organization for Standardization, Geneva.
- [22] ISO 286-1:2010. *Geometrical product specifications (GPS) – ISO code system for tolerances on linear sizes – Part 1: Basis of tolerances, deviations and fits*. International Organization for Standardization, Geneva.
- [23] ISO 286-2:2010. *Geometrical product specifications (GPS) – ISO code system for tolerances on linear sizes – Part 2: Tables of standard tolerance classes and limit deviations for holes and shafts*. International Organization for Standardization, Geneva.
- [24] ISO 1101:2017. *Geometrical product specifications (GPS) – Geometrical tolerancing – Tolerances of form, orientation, location and run-out*. International Organization for Standardization, Geneva.
- [25] ISO 14406:2010. *Geometrical product specifications (GPS) – Extraction*. International Organization for Standardization, Geneva.
- [26] ISO 12180-1:2011. *Geometrical product specifications (GPS) – Cylindricity – Part 1: Vocabulary and parameters of*

- cylindrical form. International Organization for Standardization, Geneva.
- [27] ISO 12180-2:2011. *Geometrical product specifications (GPS) – Cylindricity – Part 2: Specification operators*. International Organization for Standardization, Geneva.
- [28] ISO 12181-1:2011. *Geometrical product specifications (GPS) – Roundness – Part 1: Vocabulary and parameters of roundness*. International Organization for Standardization, Geneva.
- [29] ISO 12181-2:2011. *Geometrical product specifications (GPS) – Roundness – Part 2: Specification operators*. International Organization for Standardization, Geneva.
- [30] ISO 12780-1:2011. *Geometrical product specifications (GPS) – Straightness – Part 1: Vocabulary and parameters of straightness*. International Organization for Standardization, Geneva.
- [31] ISO 12780-2:2011. *Geometrical product specifications (GPS) – Straightness – Part 2: Specification operators*. International Organization for Standardization, Geneva.
- [32] ISO 12781-1:2011. *Geometrical product specifications (GPS) – Flatness – Part 1: Vocabulary and parameters of flatness*. International Organization for Standardization, Geneva.
- [33] ISO 12781-2:2011. *Geometrical product specifications (GPS) – Flatness – Part 2: Specification operators*. International Organization for Standardization, Geneva.
- [34] ISO 1660:2017. *Geometrical product specifications (GPS) – Geometrical tolerancing – Profile tolerancing*. International Organization for Standardization, Geneva.
- [35] ISO 2692:2021. *Geometrical product specifications (GPS) – Geometrical tolerancing – Maximum material requirement (MMR), least material requirement (LMR) and reciprocity requirement (RPR)*. International Organization for Standardization, Geneva.
- [36] ISO 5459:2011. *Geometrical product specifications (GPS) – Geometrical tolerancing – Datums and datum systems*. International Organization for Standardization, Geneva.
- [37] ISO 16610-1:2015. *Geometrical product specifications (GPS) – Filtration – Part 1: Overview and basic concepts*. International Organization for Standardization, Geneva.
- [38] ISO 22081:2021. *Geometrical product specifications (GPS) – Geometrical tolerancing – General geometrical specifications and general size specifications*. International Organization for Standardization, Geneva.
- [39] ISO 2768-1:1989. *General tolerances – Part 1: Tolerances for linear and angular dimensions without individual tolerance indications*. International Organization for Standardization, Geneva.
- [40] ISO 8062-1:2007. *Geometrical product specifications (GPS) – Dimensional and geometrical tolerances for moulded parts – Part 1: Vocabulary*. International Organization for Standardization, Geneva.
- [41] ISO/TS 8062-2:2013. *Geometrical product specifications (GPS) – Dimensional and geometrical tolerances for moulded parts – Part 2: Rules*. International Organization for Standardization, Geneva.
- [42] ISO 8062-3:2023. *Geometrical product specifications (GPS) – Dimensional and geometrical tolerances for moulded parts – Part 3: General dimensional and geometrical tolerances and machining allowances for castings using \pm tolerances for indicated dimensions*. International Organization for Standardization, Geneva.
- [43] ISO 8062-4:2023. *Geometrical product specifications (GPS) – Dimensional and geometrical tolerances for moulded parts – Part 4: Rules and general tolerances for castings using profile tolerancing in a general datum system*. International Organization for Standardization, Geneva.
- [44] ISO 20457:2018. *Plastics moulded parts – Tolerances and acceptance conditions*. International Organization for Standardization, Geneva.
- [45] ISO 13920:2023. *Welding – General tolerances for welded constructions – Dimensions for lengths and angles, shape and position*. International Organization for Standardization, Geneva.
- [46] ISO 21920-1:2021. *Geometrical product specifications (GPS) – Surface texture: Profile – Part 1: Indication of surface texture*. International Organization for Standardization, Geneva.
- [47] ISO 21920-2:2021. *Geometrical product specifications (GPS) – Surface texture: Profile – Part 2: Terms, definitions and surface texture parameters*. International Organization for Standardization, Geneva.
- [48] ISO 21920-3:2021. *Geometrical product specifications (GPS) – Surface texture: Profile – Part 3: Specification operators*. International Organization for Standardization, Geneva.
- [49] ISO 13715:2017. *Technical product documentation – Edges of undefined shape – Indication and dimensioning*. International Organization for Standardization, Geneva.
- [50] ISO 10579:2010. *Geometrical product specifications (GPS) – Dimensioning and tolerancing – Non-rigid parts*. International Organization for Standardization, Geneva.
- [51] ISO 10135:2007. *Geometrical product specifications (GPS) – Drawing indications for moulded parts in technical product documentation (TPD)*. International Organization for Standardization, Geneva.
- [52] ISO 8785:1998. *Geometrical Product Specification (GPS) – Surface imperfections – Terms, definitions and parameters*. International Organization for Standardization, Geneva.
- [53] ISO 1119:2011. *Geometrical product specifications (GPS) – Series of conical tapers and taper angles*. International Organization for Standardization, Geneva.
- [54] ISO 2538-1:2014. *Geometrical product specifications (GPS) – Wedges – Part 1: Series of angles and slopes*. International Organization for Standardization, Geneva.
- [55] ISO 2538-2:2014. *Geometrical product specifications (GPS) – Wedges – Part 2: Dimensioning and tolerancing*. International Organization for Standardization, Geneva.
- [56] ISO 3040:2016. *Geometrical product specifications (GPS) – Dimensioning and tolerancing – Cones*. International Organization for Standardization, Geneva.
- [57] ISO 5458:2018. *Geometrical product specifications (GPS) – Geometrical tolerancing – Pattern and combined geometrical specification*. International Organization for Standardization, Geneva.
- [58] ISO 17450-1:2011. *Geometrical product specifications (GPS) – General concepts – Part 1: Model for geometrical*

- specification and verification*. International Organization for Standardization, Geneva.
- [59] ISO 17450-2:2012. *Geometrical product specifications (GPS) – General concepts – Part 2: Basic tenets, specifications, operators, uncertainties and ambiguities*. International Organization for Standardization, Geneva.
- [60] ISO 17450-3:2016. *Geometrical product specifications (GPS) – General concepts – Part 3: Toleranced features*. International Organization for Standardization, Geneva.
- [61] ISO 17450-4:2017. *Geometrical product specifications (GPS) – Basic concepts – Part 4: Geometrical characteristics for quantifying GPS deviations*. International Organization for Standardization, Geneva.
- [62] ISO 22432:2011. *Geometrical product specifications (GPS) – Features utilized in specification and verification*. International Organization for Standardization, Geneva.
- [63] ISO 25378:2011. *Geometrical product specifications (GPS) – Characteristics and conditions – Definitions*. International Organization for Standardization, Geneva.
- [64] ISO 18391:2016. *Geometrical product specifications (GPS) – Population specification*. International Organization for Standardization, Geneva.
- [65] ISO 21204:2020. *Geometrical product specifications (GPS) – Transition specification*. International Organization for Standardization, Geneva.
- [66] ISO 16792:2021. *Technical product documentation – Digital product definition data practices*. International Organization for Standardization, Geneva.
- [67] ISO 20170:2019. *Geometrical product specifications (GPS) – Decomposition of geometrical characteristics for manufacturing control*. International Organization for Standardization, Geneva.

Improvement of the Dimensional Accuracy of a Ti-6Al-4V Ripple Disc During Electric Hot Incremental Sheet Forming

Zhengfang Li¹ – Xudong Di² – Zhengyuan Gao^{3*} – Zhiguo An³ – Ling Chen⁴ – Yuhang Zhang¹ – Shihong Lu⁵

¹ Kunming University, School of Mechanical and Electrical Engineering, China

² Jianghuai Automobile Group Co., Ltd., Passenger Car Research Institute of Technology Center, China

³ Chongqing Jiaotong University, School of Mechatronics and Vehicle Engineering, China

⁴ Kunming University, Office of Science and Technology, China

⁵ Nanjing University of Aeronautics and Astronautics, College of Mechanical & Electrical Engineering, China

The edge warpage of a Ti-6Al-4V ripple disc is a major forming defect during electric hot incremental forming, which can lead to a significant dimensional error. In this paper, a novel manufacturing method, namely the combination of electric hot incremental forming and electrically assisted sizing, has been proposed to improve the forming defect. The effect of process parameters on forming fracture was analysed in detail, and then an optimal combination of process parameters was obtained to ensure the successful forming of a Ti-6Al-4V ripple disc. On this basis, a sizing device and a sizing current were separately designed and analysed to eliminate the warpage defect of Ti-6Al-4V ripple discs. According to the experimental result, Ti-6Al-4V ripple discs can be satisfactorily fabricated through the method proposed.

Keywords: incremental sheet forming, electric hot forming, electrically assisted sizing, edge warpage, ripple disc

Highlights

- A novel forming process that combines electric hot incremental forming and electrically assisted sizing of Ti-6Al-4V ripple discs is proposed to fabricate the part.
- The suitable current value is obtained to fabricate Ti-6Al-4V ripple discs in electric hot forming.
- The effect of main forming parameters, such as feed rates and step size, on the forming quality of the part is analysed in detail.
- A sizing device and a sizing current are separately designed and analysed to improve the forming accuracy of Ti-6Al-4V ripple discs.

0 INTRODUCTION

The formability of materials is enhanced during incremental sheet forming, and the lower forming accuracy of parts is also obtained due to the local forming characteristics, namely that the forming region between the tool and the sheet has a springback with the removal of the tool; consequently, the application of this technology can be restricted. To solve this problem, various efforts, in Taguchi desirability function analysis [1], process optimization [2], optimal forming strategies [3], grey relation analysis [4], and considering tool deformation [5], are executed to improve the forming accuracy of parts. The sum of clamping, non-clamping, and final errors is the manufacturing error of parts in incremental sheet forming and it is often less than or equal to ± 3 mm according to the study of Oleksik et al. [2]. Currently, auxiliary support, path compensation, and process optimization are separately adopted to reduce the fabricating error of parts [6] to [9]. Although some assistant forming schemes [10] are proposed to enhance the dimensional accuracy of parts in the forming process, the manufacturing cost is increased due to the fact that the complexity of the whole

process can be improved. Therefore, the latter two methods remain major ways of enhancing the forming quality of parts during incremental sheet forming.

The deformation mechanism of materials is more complex in electric hot incremental forming (EHIF), and the effect factors of dimensional accuracy are mainly process parameters, thermal expansion, and residual stress [11]. Saidi et al. adopted the cartridge heater to fabricate the part of titanium alloy Ti-6Al-4V below the recrystallization temperature [12]. Xu et al. adopted the self-lubricating method to improve the surface quality of TA1 sheet [13]. Mohanraj et al. proposed a thermal model to predict the forming region temperature during the electric heating incremental sheet forming [14]. Wu et al. further analysed the characterization of material flow for the hot incremental sheet-forming process of dissimilar sheet metals [15]. Ajay adopted the optimal method of process parameters to improve the forming quality of titanium alloy in incremental sheet forming [16]. Fan et al. [17] employed a composite process, namely reverse drawing and EHIF, to enhance the axial forming accuracy of parts with Ti-6Al-4V. On this basis, Ambrogio et al. [18] further adopted an energy density function to analyse the energy level of

different alloys, such as AA2024-T3, AZ31 B-O, and Ti-6Al-4V alloys, and then the mapping relationship between forming angle and minimum energy level was established. Furthermore, Skjoedt et al. [19] and Shi et al. [20] separately proposed a modified spiral forming path to enhance the manufacturing accuracy of parts.

According to the above studies, some typical parts, such as cone and square cone, are adopted to analyse the optimal method of dimensional accuracy [21] to [23]. However, the heteromorphic part, namely a ripple disc, is still rarely reported in recent studies, and its forming defect, namely that is obtained due to the interaction between residual stress and thermal expansion, is shown in Fig. 1. In this paper, a novel manufacturing method, the combination of EHIF and electrically assisted sizing (EAS), was proposed to improve forming defects of the ripple disc. The effect of process parameters on forming fracture was analysed in detail, and then an optimal combination

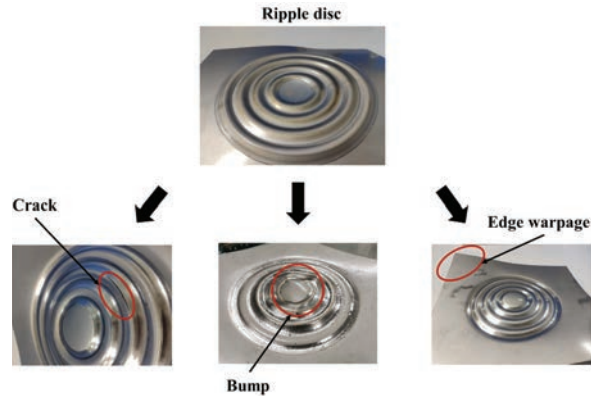


Fig. 1. Forming defects of a ripple disc

of process parameters was obtained to ensure the successful forming of Ti-6Al-4V ripple discs. On this basis, a sizing device and a sizing current were separately designed and analysed to eliminate the warpage defect of Ti-6Al-4V ripple discs. The

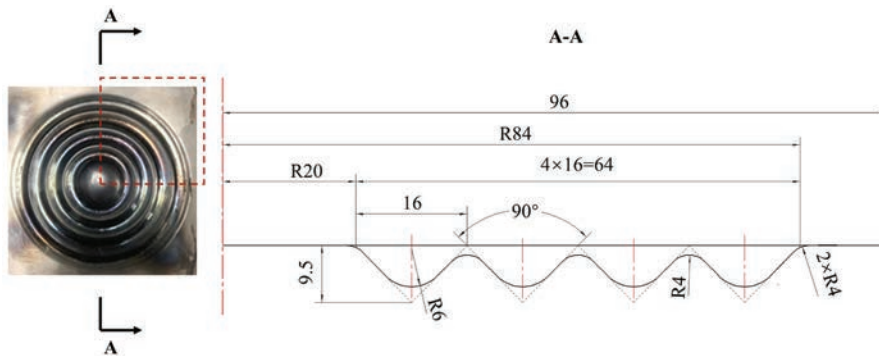


Fig. 2. Sketch of the forming profile of parts; units in mm

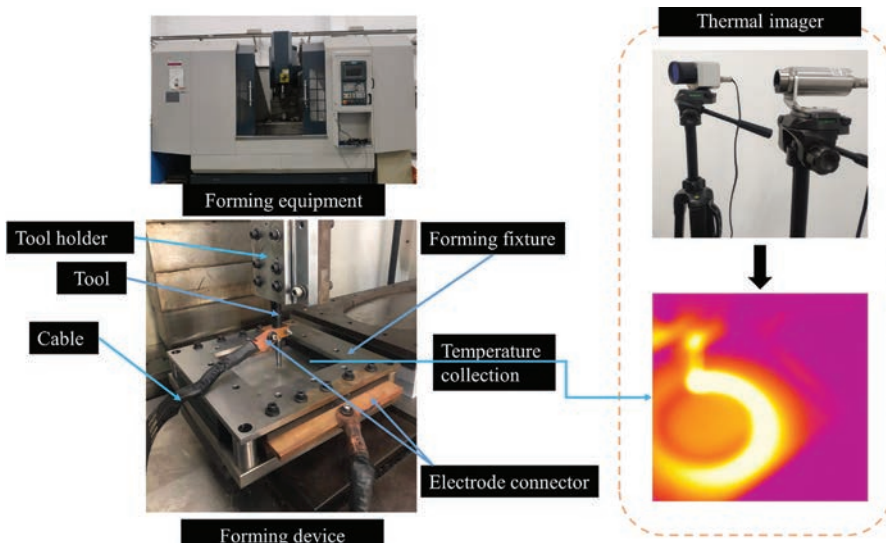


Fig. 3. The test setup of the ripple disc in EHIF

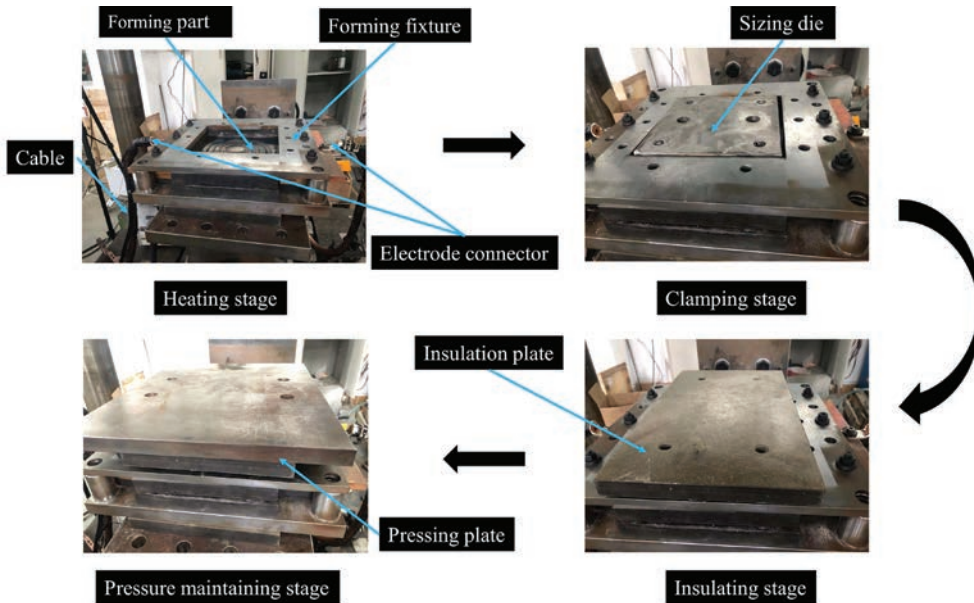


Fig. 4. The sizing process of the ripple disc

proposed novel method can be used to rapidly fabricate the ripple disc for the aerospace field and be also further expanded to the forming of other similar parts for other fields, such as the automotive industry, biomedicine, rail transit, and the like.

1 METHODS

A ripple disc with Ti-6Al-4V titanium alloy is fabricated to analyse the effect of forming and sizing process parameters on forming quality, the dimension of which is shown in Fig. 2. The part with 0.8 mm thickness is fabricated in a numerical control machine (Producer: LNC Technology CO., Ltd., Taiwan; Type: LNC-M00; Machine range: 400 mm for x -axis, 00 mm for y -axis, and 00 mm for z -axis). Meanwhile, a direct-current power (current range of 0 A to 00 A) and a thermal imager (Producer: Shenzhen Cemp Technology Co., Ltd., China; Type: PIM - PI0x; Range: $-20\text{ }^{\circ}\text{C}$ to $00\text{ }^{\circ}\text{C}$; Error: $\pm 0.1\text{ }^{\circ}\text{C}$) are separately adopted to provide the heat and to collect temperature for the forming region, which is shown in Fig. 3

The warpage defect of parts remain, and then an electrically assisted sizing process, as shown in Fig. 4, is designed to improve the forming defect. The four stages (i.e., heating, clamping, pressure-maintaining, and insulating) are designed in the sizing process, in which the last three stages are used to ensure the

sizing force and the sizing time, and the first stage is used to provide a reliable sizing temperature.

2 EXPERIMENTAL

2.1 Electric Hot Incremental Forming Experiments

Fig. 5 shows the forming strategy of ripple disc, and the two stages are adopted to fabricate the part. The first forming path is designed to obtain the lateral wall of ripple disc, and the opposite wall is fabricated according to the second forming path. Meanwhile, some process parameters, such as current, feed rate and step size, are selected to analyse the forming quality of ripple disc, and the corresponding experimental scheme is shown in Table 1. In the sizing stage, the heating method, namely electrically assisted integral heating, is different from the local heating method of forming stage. Therefore, a high-power

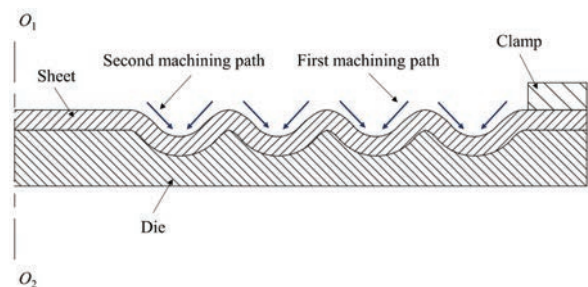


Fig. 5. The forming strategy of the ripple disc

pulse power (current range of 0 A to 600 A) is adopted to realize the integral heating of sheet metal. Current values from 2200 A to 600 A are separately used to heat the sheet, and the max holding time is 5 min in order to reduce the oxidation phenomenon of Ti-6Al-4V titanium alloy.

Table 1. The forming experimental scheme of the ripple disc

| No. | Current [A] | Feed rate [mm/min] | Step size [mm] |
|-----|-------------|--------------------|----------------|
| 1 | 75 | 900 | 0.2 |
| 2 | 202 | 900 | 0.2 |
| 3 | 220 | 900 | 0.2 |
| 4 | 350 | 900 | 0.2 |
| 5 | 220 | 300 | 0.2 |
| 6 | 220 | 1500 | 0.2 |
| 7 | 220 | 900 | 0.4 |
| 8 | 220 | 900 | 0.6 |

2.2 Electrically Assisted Sizing Experiments

The reference annealing temperature of Ti-6Al-4V titanium alloy is 600 °C to 650 °C, and the keep-warm time is 6 min to 240 min in the traditional annealing process. In the electrically assisted sizing process, five current values, (2200 A, 2400 A, 2600 A, 2800 A, and 3000 A) are designed according to the traditional annealing process, and the isothermal surface of parts is viewed as a saturated temperature of the annealing process, as shown in Fig. 6. The corresponding saturated temperatures are 563.7 °C, 593.6 °C, 623.5 °C, 653.3 °C, and 683.1 °C, respectively. Meanwhile, the heating time for the electrically assisted sizing process should be less than the keep-warm time of the traditional annealing process due to the high-temperature oxidation defect of Ti-6Al-4V titanium alloy. Therefore, 0 min, 5 min, 20 min, 25 min, 60 min, and 5 min are respectively used to analyse the change of *h*, in which *h* is the warpage height of the part edge.

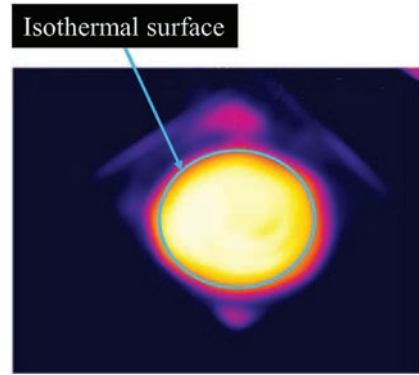


Fig. 6. The thermal imaging photo of the isothermal surface of parts

3 RESULTS AND DISCUSSION

3.1 Effect of Current Intensity on Forming Quality

Four experimental groups (no. 1 to no. 4) are adopted to analyse the effect of current intensity on forming quality according to Table 1. The height (*h*) of the warpage is viewed as a major forming defect, and the crack and the bump are further used to estimate the feasibility of the parameters designed. Fig. 7 shows the effect of current intensities on forming defects, and the value of *h* increases with the increase of current intensity when the current intensity is less than 200 A. Meanwhile, the value of *h* is basically unchanged in the range of 202 A to 350 A, the springback is significant under the action of 75 A current, the crack is obtained under the action of 202 A current, and the bump is acquired under the action of 600 A current. According to the above analysis, the springback is a major defect when the current intensity is lower, and the interaction of thermal stress and springback is a major factor when the current value is greater than 200 A, in which the thermal stress is a main inducing factor of forming defects. Therefore, the current of

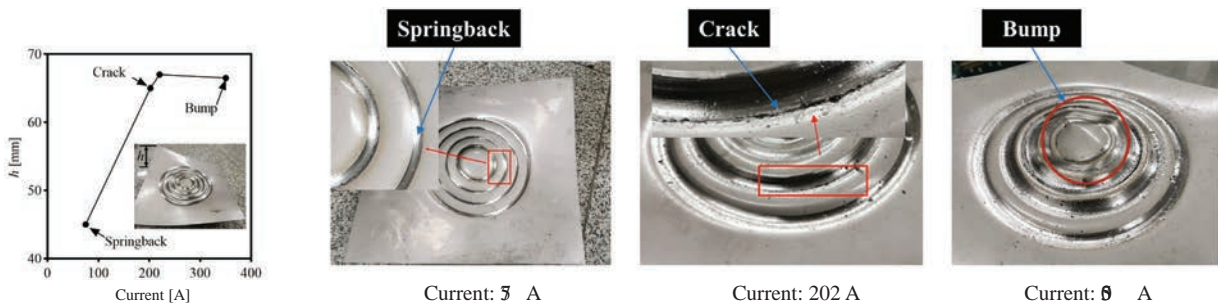


Fig. 7. The effect of current intensity on forming defects

220 A is a suitable current parameter in the EHIF of ripple disc.

3.2 Effect of Feed Rates on Forming Quality

Fig. 8 shows the effect of feed rate on forming quality, in which the warpage of parts is both existent under the action of each feed rate. Meanwhile, the bump is obtained at the centre of parts when the feed rate is 300 mm/min, which is caused due to the effect of thermal stress. The springback is significant under the action of 1500 mm/min feed rate because a large deformation resistance is obtained due to the fact that the forming temperature is lower than the other two experiments. Therefore, a feed rate of 900 mm/min is selected to fabricate the part according to the above analysis.

3.3 Effect of Step Size on Forming Quality

Based on the current of 220 A and the feed rate of 900 mm/min, three step sizes (0.2 mm, 0.4 mm, and 0.6 mm) are separately used to analyse the forming quality of parts. Fig. 9 shows the effect of step size on forming quality, and the warpage of parts is still obtained in the three experiments. Meanwhile, the forming part

would produce a crack under the action of 0.4 mm and 0.6 mm, and the crack increases with the increase of step size. The contact area between tools and sheets increases with the increase of step size, which leads to the actual forming temperature being less than the temperature planned. Therefore, the plasticity of materials is reducing with the increase of step size, and then the crack defect is easily obtained when the step size is large.

3.4 Improvement on Warpage Defect

According to the aforementioned analysis, the combination of process parameters (220 A, 900 mm/min, and 0.2 mm) is adopted to obtain a ripple disc without crack- and bump-defect. However, the warpage defect of the parts remains, and then an electrically assisted sizing process is adopted to eliminate the defect.

Fig. 10 shows the effect of sizing current and time on h , in which the value of h is negatively correlated with time and current. The effect of sizing time on h is less than that of the sizing current. h is 0.6 mm under the interaction of 2200 A and 0 min to 5 min, and it is a maximum in sizing experiments. In each current, the value of h from 20 min to 25 min is both

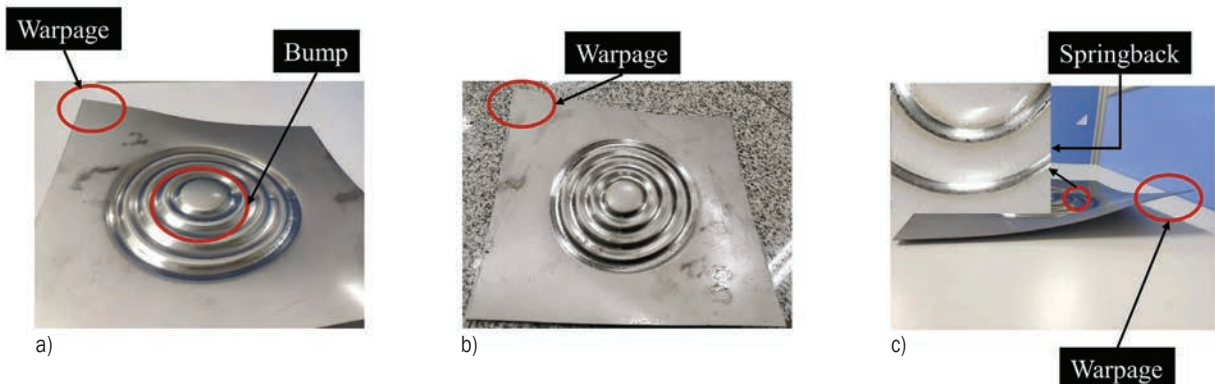


Fig. 8. The effect of feed rates on forming defects; a) 300 mm/min, b) 900 mm/min, c) 1500 mm/min

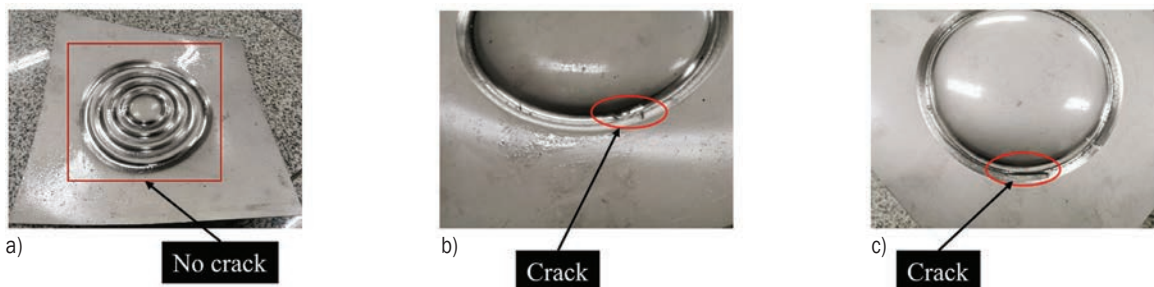


Fig. 9. The effect of step sizes on forming defects; a) 0.2 mm, b) 0.4 mm, c) 0.6 mm

between 3 min and 6 min. Meanwhile, h of 2.1 mm is obtained under the interaction of 300 A and 6 min to 3 min, and the value of h is far less than the blank holder distance (35 mm). According to Saint Venant's principle, the distribution of stresses or displacements in a structure remains nearly unchanged at a sufficiently distant point from the region of interest, as long as the external loads or boundary conditions remain the same. Therefore, an h of 2.1 mm has no influence on the dimensional accuracy of ripple disc according to the above principle. In addition to this, a long heating time can easily lead to the oxidation defect of Ti-6Al-4V titanium alloy. Consequently, the setup of 300 A and 6 min is an optimal combination of sizing parameters, which can significantly eliminate the warpage defect caused by the forming stage.

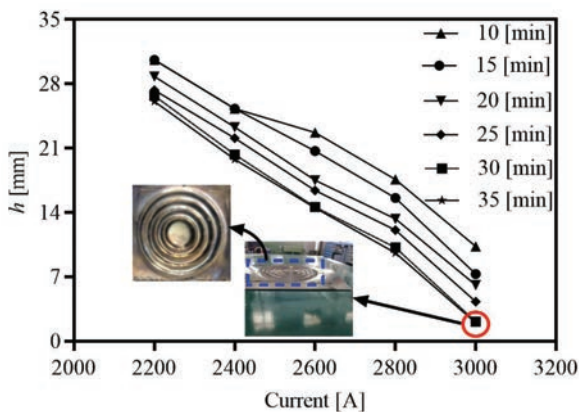


Fig. 10. Difference between different sizing parameters

4 CONCLUSIONS

Aiming to eliminate the forming defect of ripple disc, a novel manufacturing scheme, namely the combination of EHIF and electrically assisted sizing, is proposed to improve fabricating defects, such as crack, bump, and warpage. The crack and the bump are improved through optimizing process parameters in the forming stage, the warpage is an inherent forming defect of Ti-6Al-4V ripple disc, and it is not eliminated through adjusting process parameters. Therefore, an optimal combination of forming process parameters, namely 220 A, 900 mm/min, and 0.2 mm, is selected to fabricate the part according to experimental analysis results. On this basis, the effect of sizing current and time on h is further analysed in detail, and h is negatively correlated with time and current, and the effect of sizing time on h is less than that of the sizing current. Finally, the combination of sizing parameters,

containing 300 A and 6 min, is set to eliminate the warpage defect of ripple disc in the sizing stage.

5 ACKNOWLEDGEMENTS

This work was supported by the National Natural Science Foundation of China (grant No. 5203 and 22220), and the Special Basic Cooperative Research Programs of Yunnan Provincial Undergraduate Universities' Association (grant No. 2020B A00004 26 and 2020B A00004), and the Frontier Research Team of Kunming University 2023 and the Scientific and Technological Research Program of Chongqing Science and Technology Bureau (grant No. cstc2021cyj-msxm2910).

8 REFERENCES

- [1] Bishnoi, P., Chandna, P. (2023). Improved geometric accuracy in single-point incremental forming of aerospace superalloy 625 using Taguchi desirability function analysis. *Aircraft Engineering and Aerospace Technology*, vol. 95, no. 7, p. 0339, DOI:10.1108/AEAT-12-2022-0339.
- [2] Oleksik, V., Trzepieciniski, T., Szpunar, M., Chodola, L., Ficek, D., Szczesny, I. (2021). Single-point incremental forming of titanium and titanium alloy sheets. *Materials*, vol. 14, no. 21, p. 6372, DOI:10.3390/ma14216372.
- [3] Sbayti, M., Ghiotti, A., Bahloul, R., BelhadjSalah, H., Bruschi, S. (2022). Effective strategies of metamodeling and optimization of hot incremental sheet forming process of Ti6Al4V artificial hip joint component. *Journal of Computational Science*, vol. 60, p. 101595, DOI:10.1016/j.jocs.2022.101595.
- [4] Jagtap, R., Kakandikar, G., Dhanawade, A., More, S. (2021). Optimization of wall thickness and geometric accuracy in stretch forming combined with incremental sheet forming using grey relational analysis (GRA). *Materials Today: Proceedings*, vol. 44, p. 4393-4398, DOI:10.1016/j.matpr.2020.10.574.
- [5] Zhu, H., Han, F.C., Liu, Y.B. (2018). The effect of the extrusion direction on the incremental forming quality considering tool deformation. *The International Journal of Advanced Manufacturing Technology*, vol. 97, p. 1835-1846, DOI:10.1007/s00170-018-2069-8.
- [6] Milutinovic, M., Lendjel, R., Balos, S., Zlatanovic, D.L., Sevsek, L., Pepelnjak, T. (2021). Characterisation of geometrical and physical properties of a stainless steel denture framework manufactured by single-point incremental forming. *Journal of Materials Research and Technology*, vol. 10, p. 605-623, DOI:10.1016/j.jmrt.2020.12.014.
- [7] Lu, H.B., Kearney, M., Liu, S., Daniel, W.J.T., Meehan, P.A. (2016). Two directional toolpath correction in single-point incremental forming using model predictive control. *The International Journal of Advanced Manufacturing Technology*, vol. 91, p. 91-106, DOI:10.1007/s00170-016-9672-3.

- [8] Schreiber, R.G., Schaeffer, L. (2019). Manufacture of absorber fins for solar collector using incremental sheet forming. *Journal of Materials Research and Technology*, vol. 8, no. 1, p. 1132-1140, DOI:10.1016/j.jmrt.2018.07.018.
- [9] Li, Z., He, S., An, Z., Gao, Z., Lu, S. (2023). Multi-objective optimization of dimensional accuracy in electric hot incremental sheet forming. *Coatings*, vol. 13, no. 5, p. 923, DOI:10.3390/coatings13050923.
- [10] Ambrogio, G., Palumbo, G., Sgambitterra, E., Guglielmi, P., Piccininni, A., De Napoli, L., Villa, T., Fragomeni, G. (2018). Experimental investigation of the mechanical performances of titanium cranial prostheses manufactured by super plastic forming and single-point incremental forming. *The International Journal of Advanced Manufacturing Technology*, vol. 98, p. 1489-1503, DOI:10.1007/s00170-018-2338-6.
- [11] Ao, D.W., Gao, J., Chu, X.R., Lin, S.X., Lin, J. (2020). Formability and deformation mechanism of Ti-6Al-4V sheet under electropulsing assisted incremental forming. *International Journal of Solids and Structures*, vol. 202, p. 357-367, DOI:10.1016/j.ijsolstr.2020.06.028.
- [12] Saidi, B., Moreau, L.G., Cherouat, A., Nasri, R. (2020). Experimental and numerical study on warm single-point incremental sheet forming (WSPIF) of titanium alloy Ti-6Al-4V, using cartridge heaters. *Journal of the Brazilian Society of Mechanical Sciences and Engineering*, vol. 43, p. 1-15, DOI:10.1007/s40430-020-02632-8.
- [13] Xu, C.X., Li, Y.L., Wang, Z.J., Cheng, Z.N., Liu, F.Y. (2020). The influence of self-lubricating coating during incremental sheet forming of TA1 sheet. *The International Journal of Advanced Manufacturing Technology*, vol. 110, p. 2465-2477, DOI:10.1007/s00170-020-06013-2.
- [14] Mohanraj, R., Elangovan, S. (2020). Thermal modeling and experimental investigation on the influences of the process parameters on warm incremental sheet metal forming of titanium grade 2 using electric heating technique. *The International Journal of Advanced Manufacturing Technology*, vol. 110, p. 255-274, DOI:10.1007/s00170-020-05851-4.
- [15] Wu, R.H., Li, M., Liu, X.M., Cai, S., Chen, J. (2020). Characterization of material flow in friction stir-assisted incremental forming with synchronous bonding of dissimilar sheet metals. *The International Journal of Advanced Manufacturing Technology*, vol. 109, p. 2523-2534, DOI:10.1007/s00170-020-05782-0.
- [16] Ajay, C.V. (2020). Parameter optimization in incremental forming of titanium alloy material. *Transactions of the Indian Institute of Metals*, vol. 73, p. 2403-2413, DOI:10.1007/s12666-020-02044-1.
- [17] Fan, G.P., Gao, L. (2014). Mechanical property of Ti-6Al-4V sheet in one-sided electric hot incremental forming. *The International Journal of Advanced Manufacturing Technology*, vol. 72, p. 989-994, DOI:10.1007/s00170-014-5733-7.
- [18] Ambrogio, G., Filice, L., Gagliardi, F. (2012). Formability of lightweight alloys by hot incremental sheet forming. *Materials & Design*, vol. 34, p. 501-508, DOI:10.1016/j.matdes.2011.08.024.
- [19] Skjoedt, M., Hancock, M.H., Bay, N. (2007). Creating helical tool paths for single point incremental forming. *Key Engineering Materials*, vol. 344, p. 583-590, DOI:10.4028/www.scientific.net/KEM.344.583.
- [20] Shi, X.F., Gao, L., Khalatbari, H., Xu, Y., Wang, H., Jin, L.L. (2013). Electric hot incremental forming of low carbon steel sheet: accuracy improvement. *The International Journal of Advanced Manufacturing Technology*, vol. 68, no. 1, p. 241-247, DOI:10.1007/s00170-013-4724-4.
- [21] Maass F., Hahn M., Tekkaya A.E. (2020). Interaction of Process Parameters, Forming Mechanisms, and Residual Stresses in Single Point Incremental Forming. *Metals*, vol. 10, no. 5, p. 665, DOI:10.3390/met10050656.
- [22] Sevšek, L., Šegota, S.B., Car, Z., Pepelnjak, T. (2023). Determining the influence and correlation for parameters of flexible forming using the random forest method. *Applied Soft Computing*, vol. 144, art. ID 110497, DOI:10.1016/j.asoc.2023.110497.
- [23] Trzepiecinski, T., Szpunar, M., Dzierwa, A., Zaba, K. (2022). Investigation of surface roughness in incremental sheet forming of conical drawpieces from pure titanium sheets. *Materials*, vol. 15, p. 4278, DOI:10.3390/ma15124278.

Roughness Parameters with Statistical Analysis and Modelling Using Artificial Neural Networks After Finish Milling of Magnesium Alloy with Different Edge Helix Angle Tools

Ireneusz Zagórski* – Monika Kulisz² – Anna Szczepaniak¹

¹ Lublin University of Technology, Mechanical Engineering Faculty, Poland

² Lublin University of Technology, Management Faculty, Poland

The paper presents the results of a study investigating the roughness parameters R_q , R_t , R_v , and R_p of finished-milled magnesium alloys AZ91D and AZ31B. Carbide end mills with varying edge helix angles were used in the study. Statistical analysis was additionally performed for selected machining conditions. In addition, modelling of selected roughness parameters on the end face for the AZ91D alloy was carried out using artificial neural networks. Results have shown that the tool with $\lambda_s = 20^\circ$ is more suitable for the finish milling of magnesium alloys because its use leads to a significant reduction in surface roughness parameters with increased cutting speed. Increased feed per tooth leads to increased surface roughness parameters. Both radial and axial depth of cut has an insignificant effect on surface roughness parameters. It has been proven that finish milling is an effective finishing treatment for magnesium alloys. In addition, it was shown that artificial neural networks are a good tool for the prediction of selected surface roughness parameters after finishing milling of the magnesium alloy AZ91D.

Keywords: magnesium alloys, finish milling, roughness, surface quality, statistical analysis, artificial neural networks

Highlights

- Finish milling of magnesium alloys AZ31B and AZ91D is an effective kind of machining method.
- The surface roughness (R_q , R_t , R_v , and R_p) depends on the geometry of the different edge helix angles.
- The tool with $\lambda_s = 20^\circ$ is more suitable for the finish milling of magnesium alloys.
- The change of cutting speed v_c and feed per tooth f_z has a significant influence on the surface roughness parameters during finish milling.
- Both the radial and axial depths of cut (a_e and a_p) have an insignificant effect on surface roughness parameters.
- Artificial neural networks are a good tool for the prediction of selected surface roughness parameters after finishing milling of the magnesium alloy AZ91D.

0 INTRODUCTION

The machinability of a material is described by machinability indices, one of which is surface quality. Geometric structure is defined as the general surface condition, and it is the end result of the technological process for a given workpiece. The geometric structure consists of all surface texture irregularities that are formed due to material wear and machining. The evaluation of the condition of this structure includes considering shape deviations, waviness, and surface roughness.

To compare and verify surface roughness requirements for constructional materials after machining, studies use parameters describing surface conditions in quantitative terms. These include two-dimensional (2D) and \mathbb{D} surface roughness parameters, where 2D measurements are made on the profile, i.e., in the cross-section of a given workpiece, and \mathbb{D} measurements, known as stereometric, are made on the surface.

The fundamental and most widely analysed surface roughness parameter is R_a ; however, surface

roughness evaluation that is based on this parameter only is far from being exhaustive. The R_a parameter is widely used in industry even though it does not provide data about many significant roughness profile features. Therefore, additional parameters must be considered, such as R_q , R_t , R_v , and R_p . The R_q parameter is usually considered together with R_a , with the value of R_q being greater than the value of R_a (by approx. 25 % for random profiles). This relationship for random profiles can be expressed as $R_q \approx 1.25 R_a$ [1].

Another common parameter used for surface quality evaluation is the maximum height of the profile, R_z . Given the fact that single profile peaks and valleys are partly taken into account, this parameter should primarily be analysed for bearing or sliding surfaces and measurement areas [1] and [2]. The R_z parameter is often analysed together with another surface roughness parameter, R_t . These two parameters should also be analysed in combination with other parameters such as R_p (maximum profile peak height) and R_v (maximum profile valley depth). The R_t parameter (total height of profile) may affect

*Corr. Author's Address: University of Technology, Mechanical Engineering Faculty, Department of Production Engineering, Nadbystrzycka 36, 20-618 Lublin, Poland, i.zagorski@pollub.pl

the so-called functional properties of a given surface (e.g., fatigue strength, wear and tear, lubrication etc.) [3]. This parameter is the vertical distance between the maximum profile peak height and the maximum profile valley depth along the evaluation length between (it belongs to the group of so-called amplitude parameters).

The R_p parameter provides information about, e.g., profile shape. Moreover (by analysing the R_p parameter), it is possible to assess the surface in terms of abrasion resistance. A surface with poor abrasion resistance is characterized by high values of R_p compared to R_v . Depending on the values of R_p and R_z and their ratio, it is possible to obtain data about profile shape and, thus the abrasion resistance of the analysed surface. If the R_p/R_z ratio considerably exceeds a value of 0.5 this means that the profile has

sharp peaks and the surface is less abrasion-resistant. The use of the above parameters is recommended for evaluating sliding surfaces, bearings, and pre-coated surfaces, as well as for analysing close fits in terms of shrink behaviour [1] and [3].

Measurements and research of surface roughness parameters are important due to such surface features as friction and wear, lubrication, assembly tolerances, contact deformations, load capacity, contact stresses and other surface features related to the physical or functional properties of a given surface.

Previous studies on the machinability of materials by milling have predominantly investigated the surface roughness parameter R_a . A comparison of machining methods and evaluated roughness parameters used in previous studies is given in Table 1

Table 1. Comparison of machining methods and roughness parameters under evaluation in milling of magnesium alloys

| Machining method | Roughness parameters | Material / Alloy grade | Year | Reference |
|---|--|------------------------|------|-----------|
| milling | $R_a, R_q, R_z, RzDIN, Rt, Ry, RSm$ | AZ91D/HP | 2016 | [4] |
| milling | R_a | Mg-SiC/B4C | 2017 | [5] |
| high-speed dry face milling | R_a | Mg-Ca0.8 | 2010 | [6] |
| dry milling and low plasticity burnishing | R_a | Mg-Ca0.8 | 2011 | [7] |
| milling | R_a | Mg-Ca0.8 | 2018 | [8] |
| milling | R_a | Mg-Ca1.0 | 2017 | [9] |
| dry end milling | R_a | AM60 | 2017 | [10] |
| dry milling and low plasticity burnishing | | Mg-Ca0.8 | 2011 | [11] |
| milling | $R_a, Rt, Rv, Rp, Rku, Rsk, RSm, Sa, Sv, Sp, St, Ssk, Sku$ | AZ91D | 2019 | [12] |
| dry face milling | R_a | ZE41 | 2018 | [13] |
| milling | R_a, Sa, RSm, Ssk, Sku | AZ91D | 2021 | [14] |
| milling | R_a | AZ61 | 2017 | [15] |
| face milling (DRY, MQL) | Sa | AZ61 | 2019 | [16] |
| high speed milling | R_a | AZ91D | 2016 | [17] |
| dry milling by air pressure coolant | R_a | AZ31B | 2010 | [18] |
| milling | R_a | AZ91D | 2016 | [19] |
| precision milling | $R_a, Rv, Rp, Rt, Rvk, Rk, Rpk$ | AZ91D | 2023 | [20] |

Summing up, surface roughness analysis is particularly important in terms of the quality of finished components of machines and devices. Light alloys, including magnesium and aluminium alloys [21] and [22], occupy a special place among construction materials. Surface quality and roughness are even more important when it comes to finishing treatments and operations. Therefore, it seems that the finish milling of light alloys (aluminium and magnesium) is significant not only from the practical and implementation-related points of view but also due to knowledge-related reasons, as there is a lack of comprehensive studies devoted to this problem.

1 METHODS

The objective of this study was to evaluate the surface roughness of two magnesium alloys, AZ91D and AZ31B after milling depending on the value of the technological parameters and tools with variable helix angle. The employed research scheme is shown in Fig. 1 Milling was conducted on the vertical machining centre AVIA VMC80H S with Heidenhain iTNC 640 control and maximum spindle speed of 24000 [rev/min]. In the study, we used two carbide 3 edge end mills with a diameter of 6 mm and a variable helix angle λ_s ($\lambda_s = 20^\circ, \lambda_s = 6^\circ$). Using the ISG 2200

shrink-fit machine from H. Diebold GmbH & CO (Jungingen, Germany), the end mills were mounted in the CELSIO HSK-A63 $\phi 16 \times 95$ tool holder from SCHUNK (Lauffen am Neckar, Germany). According to the ISO 21940-11:2016 standard [23], the tool with the tool holder was balanced to G2.5 (residual unbalance was 0.25 gmm) with a CIMAT RT 6 balancing machine (Bydgoszcz, Poland).

The milling process was conducted using the following ranges of technological parameters: cutting speed $v_c = 400$ m/min to 200 m/min, feed

per tooth $f_z = 0.05$ mm/tooth to 0.3 mm/tooth, axial depth of cut $a_p = 0.1$ mm to 0.5 mm, radial depth of cut $a_e = 0.5$ mm to \mathfrak{F} mm. The following surface roughness parameters were analysed: R_q , R_t , R_v , and R_p . Surface roughness measurements were made on both lateral and end faces with the use of a contact-type roughness tester, HOMMEL TESTER T000, from ITA-K. Pollak, M. Wieczorowski Sp. J. (Poznań, Poland). The measurement parameters were as follows: total measuring length $l_t = 4.8$ mm, sampling length $l_r = 0.8$ mm,



Fig. 1. Research scheme: a) the test set-up, b) the measurement equipment (end mill, milling machine and 2D profilographometer), and c) milling visualization with the roughness measurement model with end face and lateral face on the workpiece surfaces

scanning speed $v_t = 0.5$ mm/s and measuring range/resolution $M = \pm 30 \text{ } \mu\text{m}$ (range) / $0.04 \text{ } \mu\text{m}$ (resolution). Every measurement was repeated five times per each surface.

Data from surface roughness measurements were subjected to statistical verification. The assumed level of significance was $\alpha = 0.05$. There exist several criteria that must be taken into account when selecting a statistical test. In this study, output data were treated as independent quantitative variables. As shown in the scheme, results of the Shapiro-Wilk test for checking the normality of distribution were used to decide whether further tests had to be performed. If the normal distribution was not confirmed, the non-parametric Mann-Whitney U test was performed. If the zero hypothesis saying that “the distributions are not different from the normal distribution in a statistically significant way” was accepted, the significance of differences had to be assessed by one of two parametric tests: Student’s t-test or Cochran’s Q test. The test type was selected by assessing the equality of variances, which was made based on the results of Levene’s test and the Brown and Forsythe test. It should be noted that the selected test type and the end result depended on the p-value. All statistical tests were conducted using Statistica 3 [24] and [25].

Next, the modelling of selected roughness parameters (Rq and Rt) on the face of the magnesium alloy AZ91D after finishing milling was carried out with variable helix angle λ_s ($\lambda_s = 20^\circ, \lambda_s = 6^\circ$) using Matlab software. The input parameters for network learning were machining parameters such as cutting speed $v_c = 400$ m/min to 200 m/min, feed per tooth $f_z = 0.05$ mm/tooth to 0.3 mm/tooth and axial depth of cut $a_p = 0.1$ mm to 0.5 mm. At the output from network learning, the appropriate roughness parameter (Rq, Rt) was obtained for the specified tool ($\lambda_s = 20^\circ, \lambda_s = 6^\circ$).

A shallow neural network with one hidden layer was used for modelling. The learning algorithm Levenberg-Marquardt was used. The number of neurons was selected experimentally in the range of 5 to 10 . The dataset was split in a proportion of $80\% : 20\%$ (for training and validation data, respectively) putting aside the test set due to the small amount of data. Network quality was assessed based on the value of the correlation coefficient R , Mean Squared Error (ME) and root mean square error (RME). The correlation coefficient R that was calculated in accordance with the Eq. (1):

$$R(y', y^*) = \frac{cov(y', y^*)}{\sigma_{y'} \sigma_{y^*}}, \quad (1)$$

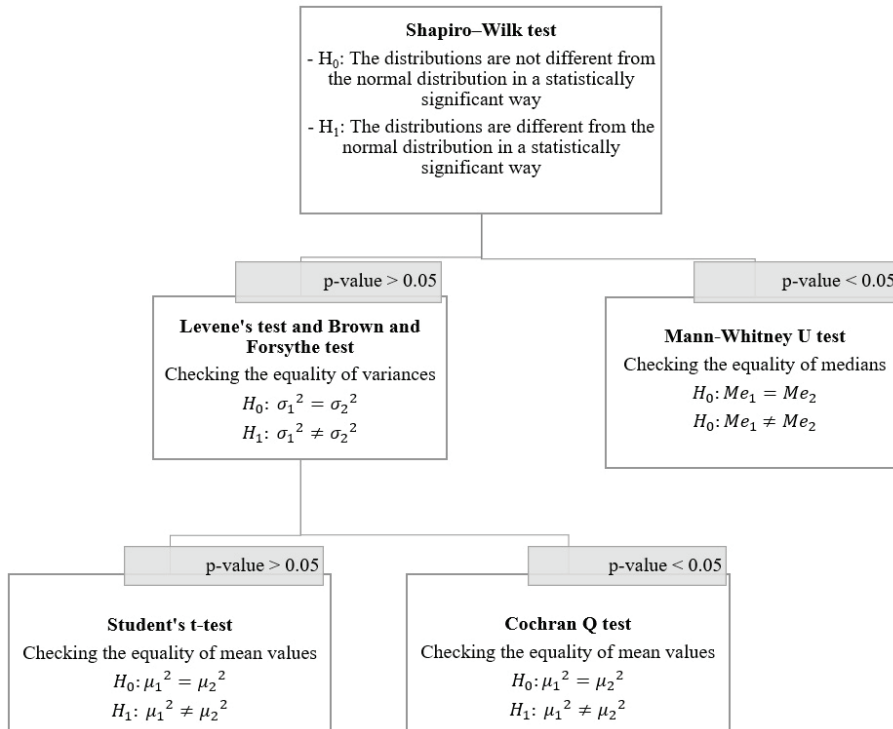


Fig. 2. Statistical test selection scheme [20]

where σ_y is the standard deviation of values of the analysed roughness parameter obtained as a result of experimental tests, σ_{y^*} standard deviation of values obtained as a result of the model predicting the value of the analysed roughness parameter. R is a real number in the interval between 0 and 1

In addition, the value of the MSE, calculated according to Eq. (2), was taken into account:

$$MSE = \frac{1}{n} \sum_{i=1}^n (\hat{y}_i - y_i)^2, \quad (2)$$

as well as RMSE, calculated according to the Eq. (3) :

$$RMSE = \sqrt{\frac{1}{n} \sum_{i=1}^n (\hat{y}_i - y_i)^2}, \quad (3)$$

where y_i is value of the analysed roughness parameter obtained as a result of experimental tests and \hat{y}_i is values obtained as a result of the model predicting the value of the analysed roughness parameter.

2 EXPERIMENTAL RESULTS AND DISCUSSIONS

This section of the paper presents experimental results of surface roughness evaluation for two magnesium alloys: AZ91D and AZ31, obtained with the use of tools with varying helix angles ($\lambda_s = 20^\circ$, $\lambda_s = 6^\circ$). The surface roughness of AZ31 was evaluated for the extreme values of the technological parameters.

Fig. 3 shows the relationship between cutting speed v_c and surface roughness parameters. It can be

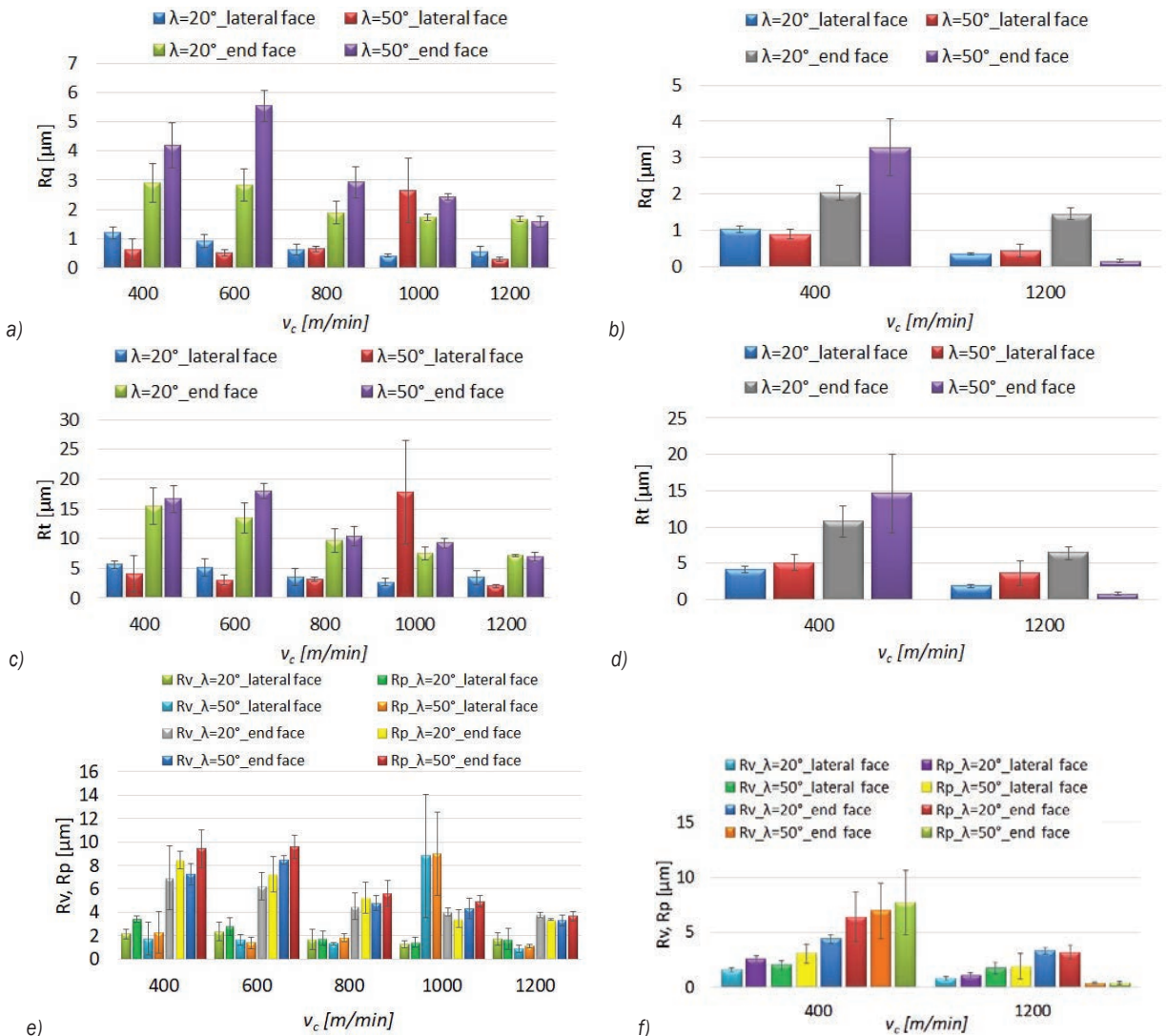


Fig. 3. Cutting speed versus surface roughness parameters: a) R_q of AZ91D, b) R_q of AZ31 c) R_t of AZ91D, d) R_t of AZ31, e) R_v, R_p of AZ91D, f) R_v, R_p of AZ31; $f_z = 0.15$ mm/tooth, lateral face: $a_e = 2$ mm, $a_p = 8$ mm, end face: $a_e = 14$ mm, $a_p = 0.3$ mm

observed that the milling process for AZ91D alloy conducted with the cutting speed v_c ranging from 60 m/min to 1200 m/min results in a clear decrease in the values of Rq and Rt with increasing the cutting speed. The surface roughness parameters only increased on the lateral face after milling with the $\lambda_s = 6^\circ$ tool and increasing the cutting speed value from $v_c = 80$ m/min to 1000 m/min. It should be stressed that the surface roughness parameters are lower on the lateral face. The lowest values of these parameters were obtained with $\lambda_s = 6^\circ$ at $v_c = 100$ m/min ($Rq = 0.29 \mu\text{m}$, $Rt = 2.02 \mu\text{m}$). The lowest values of the parameters were obtained with $\lambda_s = 6^\circ$ on the end face for the milling process conducted with $v_c = 60$ m/min ($Rq = 5.54 \mu\text{m}$, $Rt = 18.04 \mu\text{m}$). The values of

Rv and Rp on the lateral face are similar for all tested cutting speeds and range from $0.89 \mu\text{m}$ to $3.44 \mu\text{m}$. On the end face the parameters Rv and Rp clearly decreased with increasing the cutting speed and their values range $3.29 \mu\text{m}$ to $9.61 \mu\text{m}$.

An increase in cutting speed leads to decreased values of the surface roughness parameters Rq , Rt , Rv and Rp for both AZ91D and AZ31. The greatest differences between these surface parameters can be observed on the end face for the $\lambda_s = 6^\circ$ tool. The parameter Rq value decreased by $3.14 \mu\text{m}$ and that of Rt by $13.87 \mu\text{m}$. Regarding the parameters Rv and Rp , increasing the cutting speed from 400 m/min to 1000 m/min had the greatest impact on these parameter

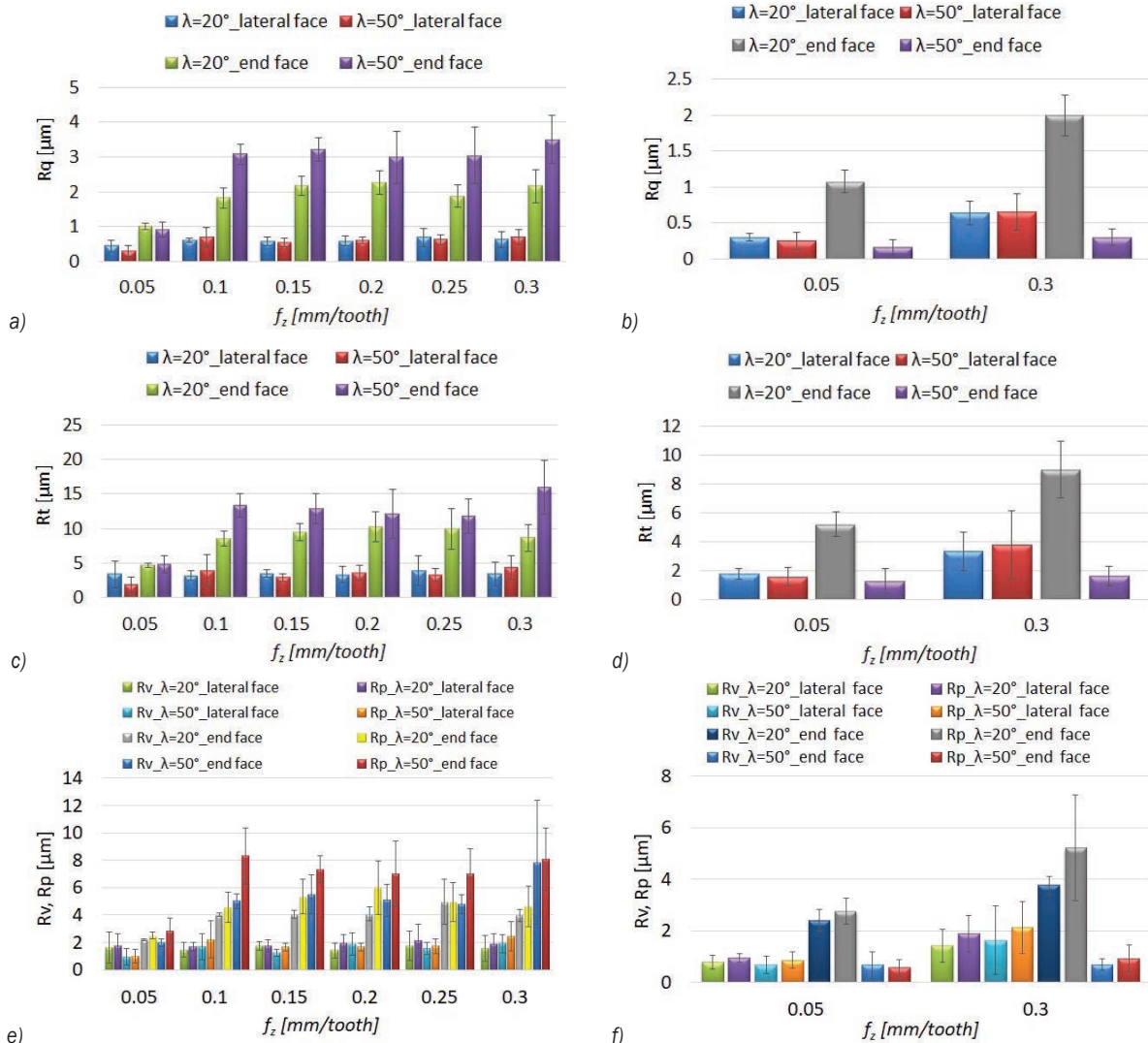


Fig. 4. Feed per tooth f_z versus surface roughness parameters: a) Rq of AZ91D, b) Rq of AZ31, c) Rt of AZ91D, d) Rt of AZ31, e) Rv, Rp of AZ91D, f) Rv, Rp of AZ31; $v_c = 800$ m/min, lateral face: $a_e = 2$ mm, $a_p = 8$ mm, end face: $a_e = 14$ mm, $a_p = 0.3$ mm

values on the end face for the $\lambda_s = 6^\circ$ tool, the value of R_v decreased by $6\ \mu\text{m}$ and that of R_p by $7\ \mu\text{m}$.

Comparing, for example, the machinability of both magnesium alloys for the highest cutting speed value, it can be seen that for the R_q parameter, a lower value roughness was obtained on the end face for the AZ31 alloy ($R_q = 1.45\ \mu\text{m}$), while for the AZ91D alloy ($R_q = 1.67\ \mu\text{m}$).

Fig. 4 shows the relationship between feed per tooth f_z and surface roughness parameters. Regardless of the tool used, increased feed per tooth has no significant effect on the surface roughness parameters on the lateral face of magnesium alloy AZ91D, and the values of these parameters range as follows: R_q $0.3\ \mu\text{m}$ to $0.2\ \mu\text{m}$, R_t $1.95\ \mu\text{m}$ to $4.28\ \mu\text{m}$, R_v $0.96\ \mu\text{m}$ to $1.94\ \mu\text{m}$, R_p $0.99\ \mu\text{m}$ to $2.45\ \mu\text{m}$. However, the roughness parameters show a sudden increase on the end face with increasing the feed per tooth value from $f_z = 0.05\ \text{mm/tooth}$ to $f_z = 0.1\ \text{mm/tooth}$. In the range $f_z = 0.1\ \text{mm/tooth}$ to $-0.3\ \text{mm/tooth}$, the feed per tooth increases. The highest values of the surface roughness parameters were observed for $f_z = 0.3\ \text{mm/tooth}$. The highest values of $R_q = 3.5\ \mu\text{m}$ and $R_t = 15.91\ \mu\text{m}$ are obtained on the end face for $\lambda_s = 6^\circ$ at $f_z = 0.3\ \text{mm/tooth}$. Moreover, for the feed per tooth range $f_z = 0.1\ \text{mm/tooth}$ to $0.25\ \text{mm/tooth}$ ($\lambda_s = 6^\circ$, end face), the values of R_p are higher than those of R_v , which means that the surface has poor abrasion resistance [1].

Regarding magnesium alloy AZ31 increased feed per tooth results in a slight increase in the values of R_q and R_t . The values of R_q and R_t range: R_q $0.17\ \mu\text{m}$ to $0.65\ \mu\text{m}$ and R_t $1.25\ \mu\text{m}$ to $3.77\ \mu\text{m}$. For $\lambda_s = 20^\circ$, the values of the parameters R_q and R_t are higher on the end face, both at $v_c = 400\ \text{m/min}$ ($R_q = 1.08\ \mu\text{m}$, $R_t = 5.18\ \mu\text{m}$) and at $v_c = 200\ \text{m/min}$ ($R_q = 1.99\ \mu\text{m}$, $R_t = 8.96\ \mu\text{m}$). Increasing the feed per tooth value from $0.05\ \text{mm/tooth}$ to $0.3\ \text{mm/tooth}$ also causes an increase in the values of R_v and R_p . The highest values are obtained on the end face with the $\lambda_s = 20^\circ$ tool, both at $f_z = 0.05\ \text{mm/tooth}$ ($R_v = 2.41\ \mu\text{m}$, $R_p = 2.76\ \mu\text{m}$) and at $f_z = 0.3\ \text{mm/tooth}$ ($R_v = 3\ \mu\text{m}$, $R_p = 5.21\ \mu\text{m}$).

Comparing both magnesium alloys on the example of the results for the R_q parameter, it can be seen that at $f_z = 0.3\ \text{mm/tooth}$ (similarly to the cutting speed analysis) a lower value of the R_q parameter was recorded on the end face for the AZ31 alloy ($R_q = 1.99\ \mu\text{m}$), than for AZ91D alloy ($R_q = 2.17\ \mu\text{m}$).

Fig. 5 illustrates the relationship between axial depth of cut and surface roughness parameters. For alloy AZ91D, no significant changes in the parameters R_q , R_t , R_v , R_p are observed in the entire tested axial depth of cut range. The values of the surface

roughness parameters are similar and range as follows: for $\lambda_s = 20^\circ$: R_q ($1.8\ \mu\text{m}$ to $2.13\ \mu\text{m}$), R_t ($8.43\ \mu\text{m}$ to $10.99\ \mu\text{m}$), R_v ($3.97\ \mu\text{m}$ to $4.66\ \mu\text{m}$), R_p ($4.47\ \mu\text{m}$ to $6.53\ \mu\text{m}$), and for $\lambda_s = 6^\circ$: R_q ($1.69\ \mu\text{m}$ to $3.36\ \mu\text{m}$), R_t ($8.56\ \mu\text{m}$ to $12.9\ \mu\text{m}$) R_v ($3.96\ \mu\text{m}$ to $5.57\ \mu\text{m}$), R_p ($4.71\ \mu\text{m}$ to $7.33\ \mu\text{m}$). However, it should be noted that the differences between the values of the above parameters depending on the tool can particularly be observed for $a_p = 0.2\ \text{mm}$ to $0.5\ \text{mm}$. The results demonstrate that the above axial depth of cut range leads to higher values of R_p compared to R_v .

The increased axial depth of cut has no significant effect on the surface roughness parameters of both AZ91D and AZ31. It is noteworthy that the roughness parameters obtained with the $\lambda_s = 6^\circ$ tool are smaller than the values of these parameters obtained after milling with the $\lambda_s = 20^\circ$ tool (AZ31).

An inverse relationship can be observed by analysing the change in the axial depth of cut on the end face, the value of the R_q parameter in the conditions when $a_p = 0.5\ \text{mm}$, for the AZ31 alloy is higher ($R_q = 1.99\ \mu\text{m}$), than for the AZ91D alloy ($R_q = 1.81\ \mu\text{m}$).

Fig. 6 shows the relationship between the radial depth of cut a_e and surface roughness parameters. The results demonstrate that the radial depth of cut has no significant effect on the roughness parameters R_q , R_t , R_v , R_p of both AZ91D ($\lambda_s = 20^\circ$) and AZ31 ($\lambda_s = 20^\circ$ and $\lambda_s = 6^\circ$). The obtained values are similar and range as follows: R_q ($0.53\ \mu\text{m}$ to $0.73\ \mu\text{m}$), R_t ($2.4\ \mu\text{m}$ to $4.24\ \mu\text{m}$), R_v ($1.08\ \mu\text{m}$ to $2.07\ \mu\text{m}$), R_p ($1.5\ \mu\text{m}$ to $2.17\ \mu\text{m}$). In contrast, for the tool with $\lambda_s = 6^\circ$ one can observe a sharp increase in the values of R_q (by $2.56\ \mu\text{m}$) and R_t (by $13.39\ \mu\text{m}$), R_v (by $6.59\ \mu\text{m}$), R_p (by $6.8\ \mu\text{m}$) when the radial depth of cut value is changed from $a_e = 1.5\ \text{mm}$ to $2.5\ \text{mm}$.

Similarly, analysing the radial depth of cut on the end face, it can be seen that for $a_e = 3\ \text{mm}$, the machining results are better (lower value of the R_q parameter) for the AZ91D alloy ($R_q = 0.56\ \mu\text{m}$), while for the AZ31 alloy ($R_q = 0.70\ \mu\text{m}$).

Thus, comparing the results obtained using carbide cutters for roughing and the analysis of the surface of the end face of the workpiece AZ91HP/D [4] and [12], the following conclusions can be drawn:

- when employing a carbide cutter coated with titanium aluminium nitride (TiAlN), higher values of the parameters R_q , R_p , and R_v were recorded, specifically:
 - 1 for the variable parameter v_c , the parameters R_v and R_p range between $6.8\ \mu\text{m}$ to $8.32\ \mu\text{m}$, while the parameter R_t spans from $14.24\ \mu\text{m}$ to $17.72\ \mu\text{m}$;

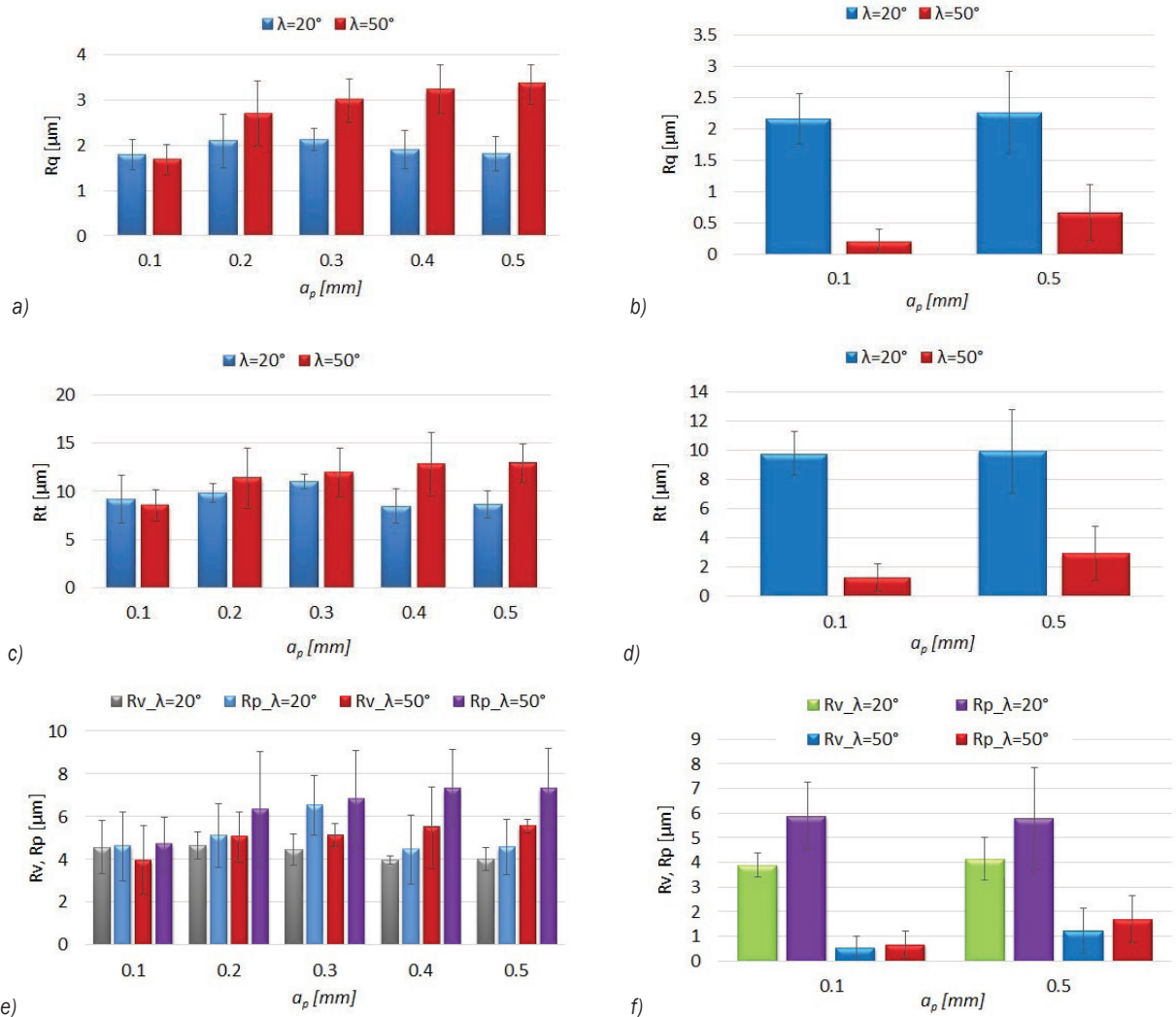


Fig. 5. Axial depth of cut a_p versus surface roughness parameters: a) Rq of AZ91D, b) Rq of AZ31 c) Rt of AZ91D, d) Rt of AZ31, e) Rv, Rp of AZ91D f) Rv, Rp of AZ31; $v_c = 800$ m/min, $f_z = 0.15$ mm/tooth, $a_e = 14$ mm

2. considering the variable parameter f_z , the parameters Rv and Rp lie within the spectrum of 1.94 μm to 15.84 μm , with the parameter Rt standing at 4 μm to 31.04 μm ;
- 3 for the variable parameter a_p , the values of Rv and Rp present remarkable similarity, recorded within the interval of 5.26 μm to 7.78 μm , and for Rt the values range from 12.02 μm to 24.82 μm ;
- in instances of machining with cutters of diverse blade geometry (different rake angles γ), the parameters Rq and Rt were investigated:
 - 1 for the variable parameter v_c , the parameter Rq did not surpass 4 μm , with Rt recorded within the range of 10 μm to 15 μm ,
 2. in relation to the variable parameter f_z , the Rq parameter ascends to a maximum value of

- approximately 3 μm , with the Rt parameter spanning from 10 μm to 15 μm ,
- 3 concerning the variable parameter a_p , the Rq parameter consistently approximates 3 μm , while the value of Rt does not exceed approximately 15 μm .

Therefore, these values are much higher than those observed in the present experiment. This is due to the larger cross-sections of the cutting layer obtained during roughing. However, as the literature lacks a broader analysis of surface roughness parameters, especially after finishing machining while roughing mainly analyses the basic surface roughness parameters (usually mainly Ra), it seems advisable to extend the state of knowledge in this area.

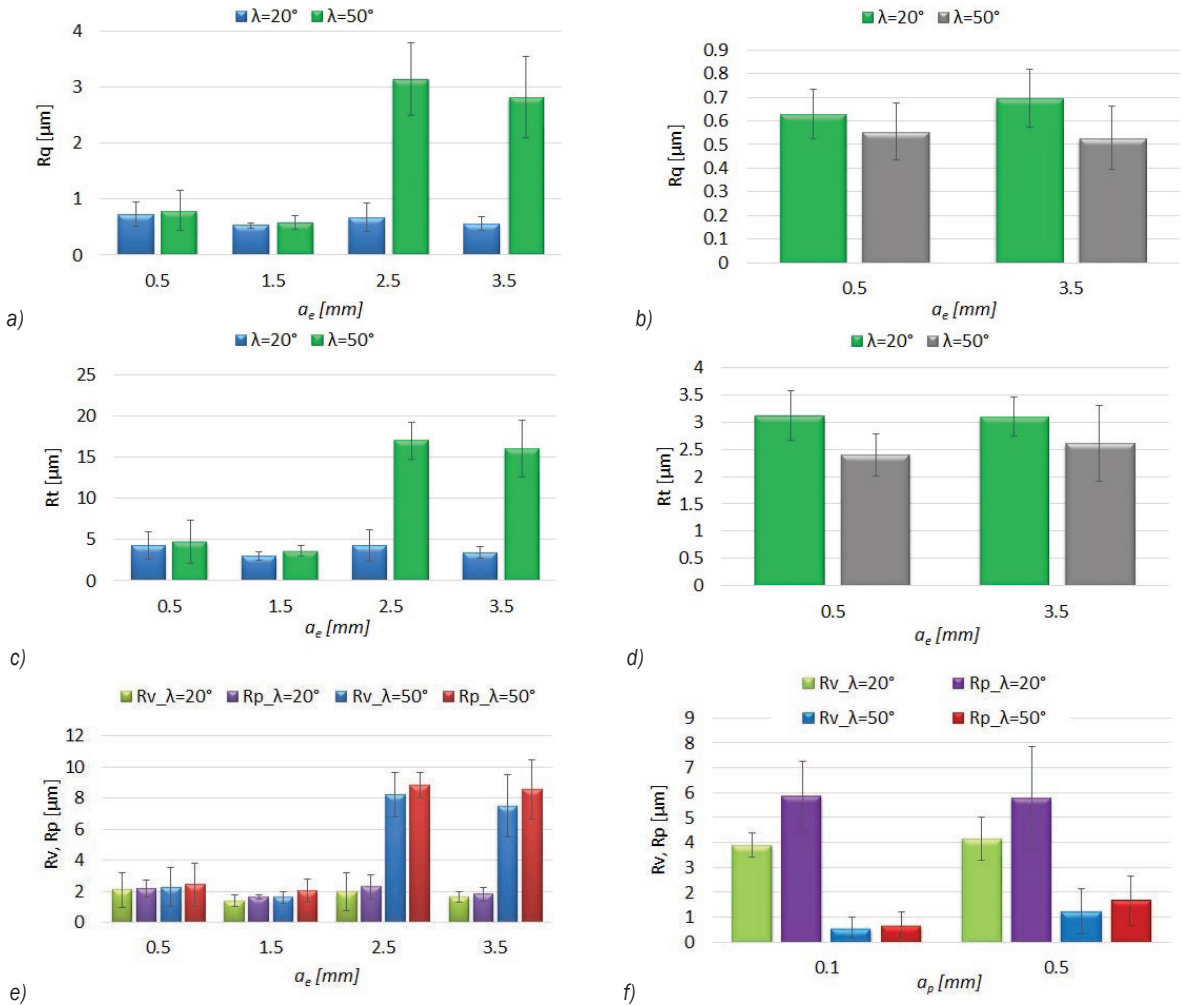


Fig. 6. Radial depth of cut a_e versus surface roughness parameters: a) Rq of AZ91D, b) Rq of AZ31, c) Rt of AZ91D, d) Rt of AZ31, e) Rv, Rp of AZ91D, f) Rv, Rp of AZ31; $v_c = 800$ m/min, $f_z = 0.15$ mm/tooth, $a_p = 8$ mm

3 STATISTICAL ANALYSIS

The experiments were followed by statistical analysis. Significance tests were performed to determine if the following technological parameters: cutting speed v_c , feed per tooth f_z , axial depth of cut a_p and radial depth of cut a_e affected the mean values of surface roughness parameters. The statistical analysis made it possible to determine whether the differences were statistically significant for the assumed level of confidence.

Hypotheses were tested taking account of the extreme values of the technological parameters, i.e., cutting speed $v_c = 400$ m/min, and 100 m/min, feed per tooth $f_z = 0.05$ mm/tooth, and, 0.3 mm/tooth, axial depth of cut $a_p = 0.1$ mm, and 0.5 mm, radial depth of cut $a_e = 0.5$ mm, and 3 mm. In this paper, we report

the final test results, i.e. the median and mean values from the tests.

Fig. 7 shows an example of results obtained by the Student's t-test for the zero hypothesis of normal distribution and the equality of variance hypothesis.

Tables 2 and 3 give the results of the Mann-Whitney U test, Student's t-test, and Cochran's Q test. The results make it possible to statistically assess the significance of differences between the mean and median values obtained for the compared groups.

The statistical analysis results demonstrate that, irrespective of the magnesium alloy grade, for the tool with $\lambda_s = 20^\circ$ increased cutting speed has, in most cases, the greatest impact on the mean and median values of the surface roughness parameters.

Feed per tooth also has a significant impact on the surface roughness parameters for the tool with

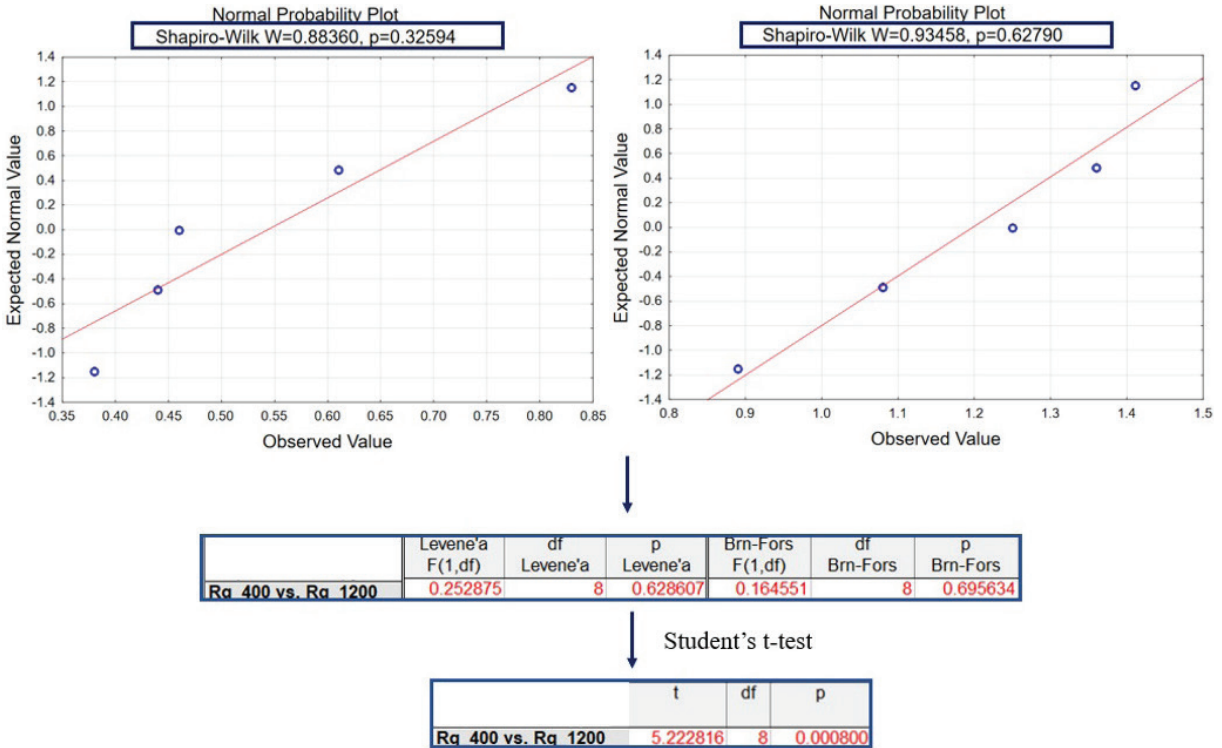


Fig. 7. Student's t-test results

Table 2. Results of Mann-Whitney U test, Student's t-test, Cochran's Q test for the roughness parameters of magnesium alloy AZ91D after milling

| | $\lambda_s = 20^\circ$ | | $\lambda_s = 50^\circ$ | |
|--|-------------------------|---------------------|-------------------------|---------------------|
| | Lateral face p-value | End face p-value | Lateral face p-value | End face p-value |
| v_c [m/min] 400 vs. 1200 | | | | |
| <i>Rq</i> | 0.0008 | 0.01354 | 0.09172 | 0.00124 |
| <i>Rt</i> | 0.00794* | 0.00384 | 0.18904 | 0.00794* |
| <i>Rv</i> | 0.15079* | 0.06089 | 0.22089 | 0.00794* |
| <i>Rp</i> | 0.01587* | 0.00009 | 0.21357 | 0.00794* |
| f_s [mm/tooth] 0.05 vs. 0.3 | | | | |
| <i>Rq</i> | 0.22222* | 0.00466 | 0.03175* | 0.00004 |
| <i>Rt</i> | 1* | 0.00902 | 0.06349* | 0.00028 |
| <i>Rv</i> | 0.84127* | 0.0007 | 0.06349* | 0.00794* |
| <i>Rp</i> | 0.78555 | 0.03114 | 0.03175* | 0.00422 |
| a_e [mm] 0.5 vs. 3.5 0.1 vs. 0.5 0.5 vs. 3.5 0.1 vs. 0.5 | | | | |
| <i>Rq</i> | 0.17048 | 0.95209 | 0.00149 | 0.0001 |
| <i>Rt</i> | 0.35526 | 0.69048* | 0.00103 | 0.00536 |
| <i>Rv</i> | 0.43513 | 0.40148 | 0.00282 | 0.150794* |
| <i>Rp</i> | 0.27617 | 0.97658 | 0.01587* | 0.03102 |

* Mann-Whitney U test for checking the equality of the medians

Table 3. Results of Mann-Whitney U test, Student's t-test, Cochran's Q test for the roughness parameters of magnesium alloy AZ31 after milling

| | $\lambda_s = 20^\circ$ | | $\lambda_s = 50^\circ$ | |
|--|-------------------------|---------------------|-------------------------|---------------------|
| | Lateral face p-value | End face p-value | Lateral face p-value | End face p-value |
| v_c [m/min] 400 vs. 1200 | | | | |
| <i>Rq</i> | 0.00794* | 0.00093 | 0.00362 | 0.00088 |
| <i>Rt</i> | 0.000004 | 0.00287 | 0.159 | 0.00443 |
| <i>Rv</i> | 0.00018 | 0.00126 | 0.35012 | 0.00435 |
| <i>Rp</i> | 0.00003 | 0.02907 | 0.19048* | 0.00507 |
| f_s [mm/tooth] 0.05 vs. 0.3 | | | | |
| <i>Rq</i> | 0.00813 | 0.00022 | 0.01372 | 0.13088 |
| <i>Rt</i> | 0.01587* | 0.00953 | 0.07128 | 0.51158 |
| <i>Rv</i> | 0.05556* | 0.00052 | 0.15926 | 0.966295 |
| <i>Rp</i> | 0.00794* | 0.054187 | 0.02645 | 0.278767 |
| a_e [mm] 0.5 vs. 3.5 0.1 vs. 0.5 0.5 vs. 3.5 0.1 vs. 0.5 | | | | |
| <i>Rq</i> | 0.3862 | 0.77097 | 0.76164 | 0.06349* |
| <i>Rt</i> | 0.84127* | 0.42063* | 0.61483 | 0.12539 |
| <i>Rv</i> | 0.38109 | 0.55077 | 0.94354 | 0.195110 |
| <i>Rp</i> | 0.12928 | 0.92479 | 0.42396 | 0.087671 |

* Mann-Whitney U test for checking the equality of the medians

$\lambda_s = 20^\circ$. The only exception are the results obtained for the lateral end of AZ91D, as they show that changing the feed per tooth value from 0.05 mm/tooth to 0.3 mm/tooth does not result in statistically significant differences between the values of the surface roughness parameters. The opposite can be observed for the tool with $\lambda_s = 6^\circ$, where the p-values are either smaller than the assumed confidence level or verge on the statistically significant limit.

For alloy AZ91D, the differences in the mean and median values of the surface roughness parameters are affected by the radial and axial depth of cut, and depend on the tool.

For alloy AZ31B irrespective of the tool used, the radial and axial depth of cut has no effect on the mean and median values of the surface roughness parameters Rq, Rt, Rv, Rp (on the statistical level).

4 MODELLING OF ARTIFICIAL NEURAL NETWORKS

Artificial neural networks were trained for the magnesium alloy AZ91D in order to build four models showing the relationship between the technological parameters (cutting speed v_c , feed per tooth f_z and axial depth of cut a_p) and the predicted roughness on the face surface of the Rq and Rt parameters, respectively, after machining with the tool with variable helix angle ($\lambda_s = 20^\circ, \lambda_s = 6^\circ$). Approximately 100 networks were trained for each model.

The quality of the obtained models was assessed on the correlation coefficient R , value of ME and RME . Table 4 presents four different models obtained from an artificial neuron network (ANN.)

The best modelling results for the Rq and Rt parameters after machining with a tool with a helix

Table 4. Network parameters

| Model No. | Roughness parameter | Helix angle λ_s | ME | RME | R training data set | R validation data set | R all data set |
|-----------|---------------------|-------------------------|--------|--------|---------------------|-----------------------|----------------|
| 1 | Rq | 20 | 0.0022 | 0.0467 | 0.99999 | 0.99029 | 0.99563 |
| 2 | Rt | | 0.1058 | 0.3252 | 0.99999 | 0.9989 | 0.99358 |
| 3 | Rv | 50 | 0.0193 | 0.1391 | 0.99999 | 0.96648 | 0.99263 |
| 4 | Rp | | 0.3424 | 0.5851 | 0.99999 | 0.95309 | 0.98741 |

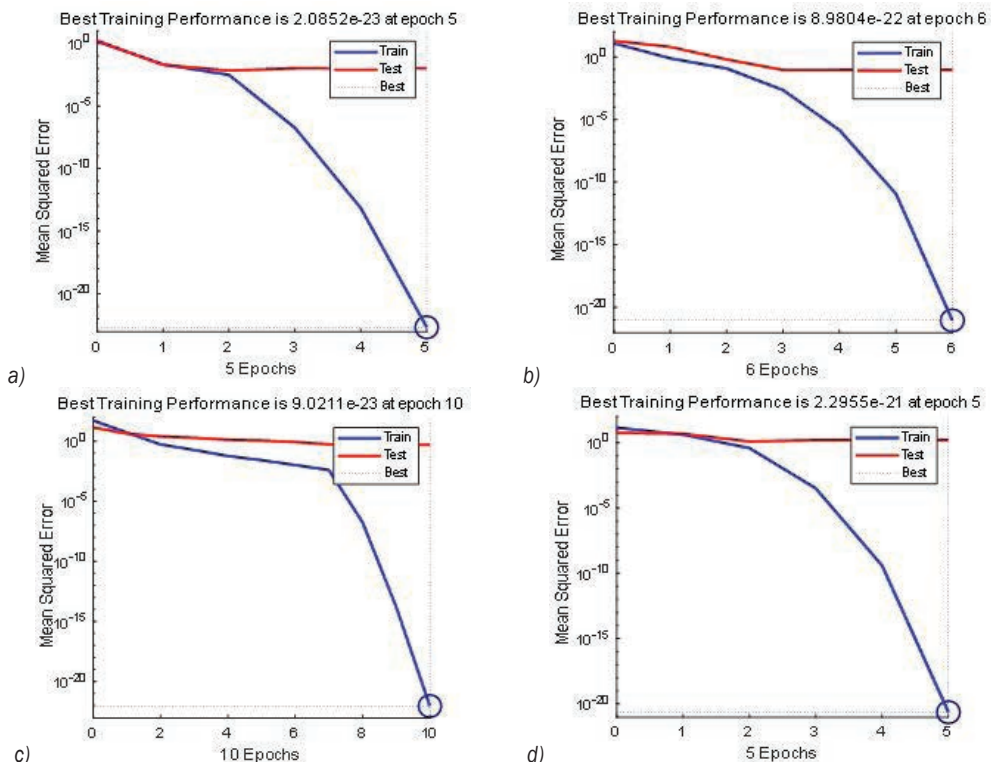


Fig. 8. ANN best training performance for a) parameter $Rq, \lambda_s = 20^\circ$, b) parameter $Rt, \lambda_s = 20^\circ$, c) parameter $Rq, \lambda_s = 50^\circ$, d) parameter $Rt, \lambda_s = 50^\circ$

angle $\lambda_s = 20^\circ$ were obtained for the network with 0 neurons in the hidden layer. The network for the Rq parameter was obtained in five iterations, and for the Rt parameter in ten iterations. In the case of the tool with the helix angle $\lambda_s = 6^\circ$, for the Rq parameter, it was also a network with 0 neurons (obtained in 6 iterations), and for the Rt parameter a network with eight neurons in the hidden layer (obtained in 5 iterations). The best validation performance was obtained respectively for iteration 5 (for Rq parameter when machined with helix angle $\lambda_s = 20^\circ$), which is shown in Fig. 8, for iteration 6 (for Rt parameter when machined with helix angle $\lambda_s = 20^\circ$); Fig. 8, for iteration 0 (for the Rq parameter when machining

with a helix angle $\lambda_s = 6^\circ$); Fig. 8 and for iteration 5 (for the Rt parameter when machining with a helix angle $\lambda_s = 6^\circ$); Fig. 8.

ANN regression statistics for individual sets and the total set was presented in Fig. 9. Respectively for parameter Rq when machining with tool with helix angle $\lambda_s = 20^\circ$; Fig. 9a, for parameter Rt when machining with tool with helix angle $\lambda_s = 20^\circ$; Fig. 9b, for parameter Rq when machining with tool with helix angle $\lambda_s = 50^\circ$; Fig. 9c and for parameter Rt when machining with tool with helix angle $\lambda_s = 50^\circ$; Fig. 9d.

Taking into account the quality of the presented models measured by the level of ME , RME and the R value (R in each case is a value greater than 0.95),

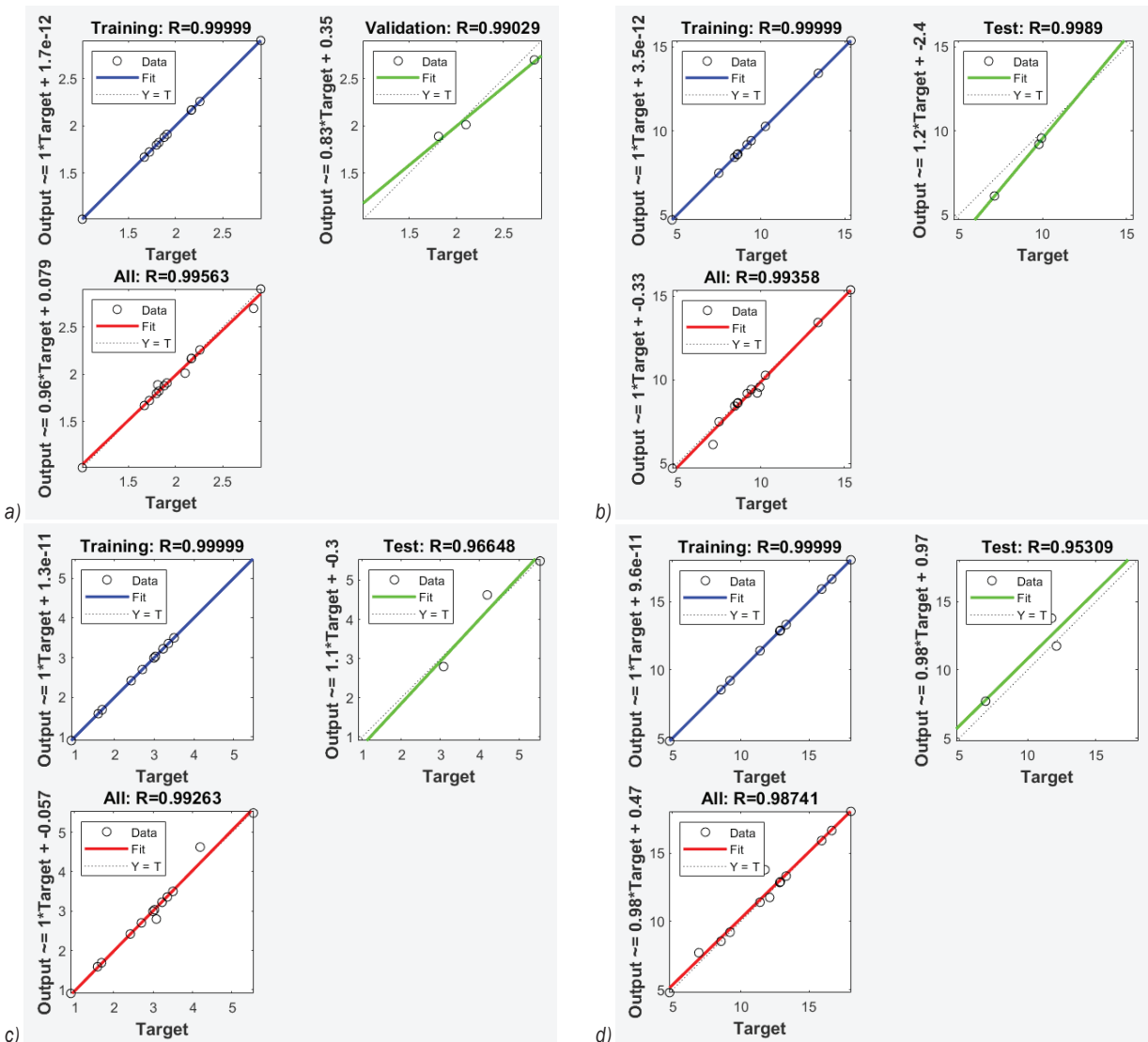


Fig. 9. ANN regression statistics for individual sets and the total set: a) parameter Rq , $\lambda_s = 20^\circ$, b) parameter Rt , $\lambda_s = 20^\circ$, c) parameter Rq , $\lambda_s = 50^\circ$, d) parameter Rt , $\lambda_s = 50^\circ$

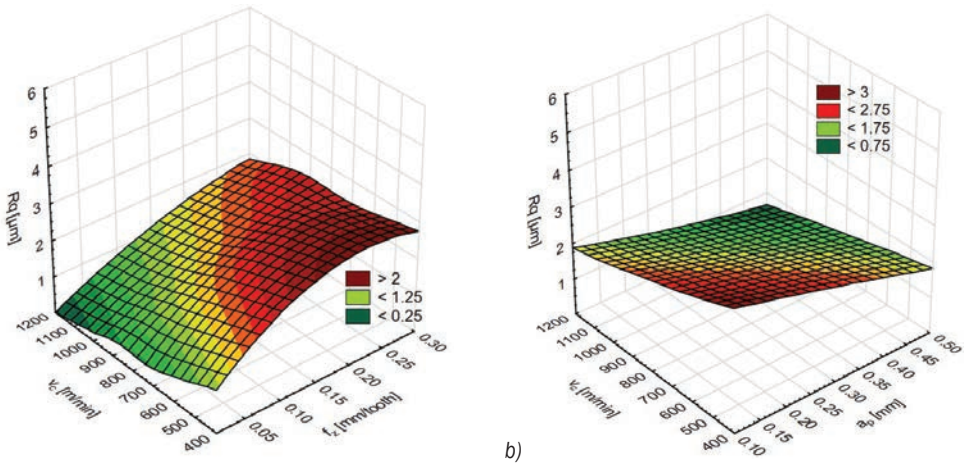


Fig. 10. Simulation results of the R_q surface roughness parameter after machining with tool with helix angle $\lambda_s = 20^\circ$ a) for the v_c and f_z , and b) for the v_c and a_p

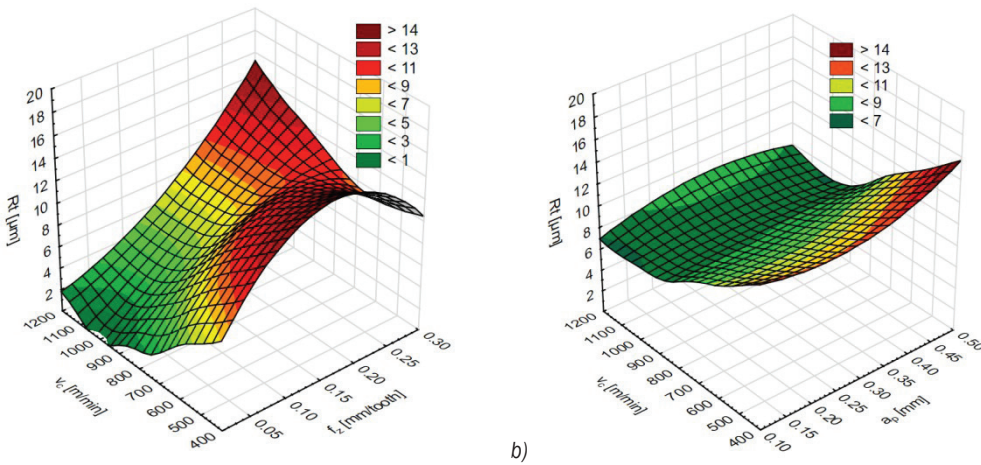


Fig. 11. Simulation results of the R_t surface roughness parameter after machining with tool with helix angle $\lambda_s = 20^\circ$ a) for the v_c and f_z , and b) for the v_c and a_p

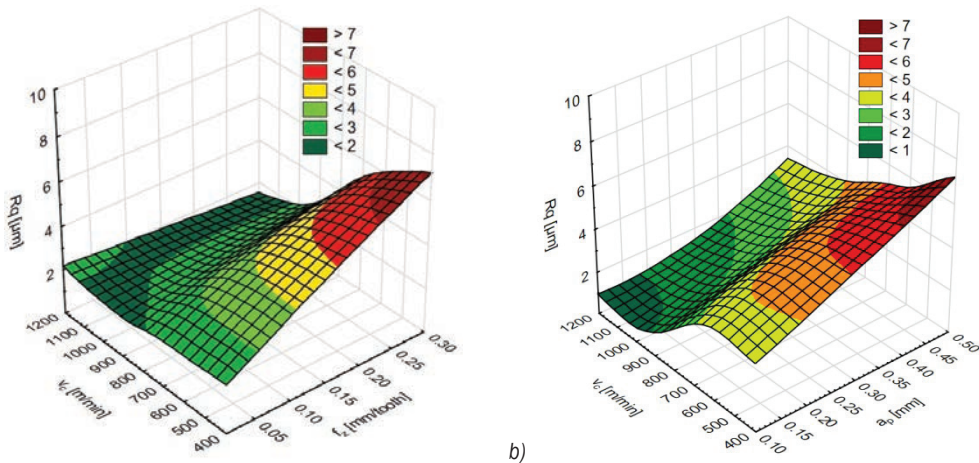


Fig. 12. Simulation results of the R_q surface roughness parameter after machining with tool with helix angle $\lambda_s = 50^\circ$ a) for the v_c and f_z , and b) for the v_c and a_p

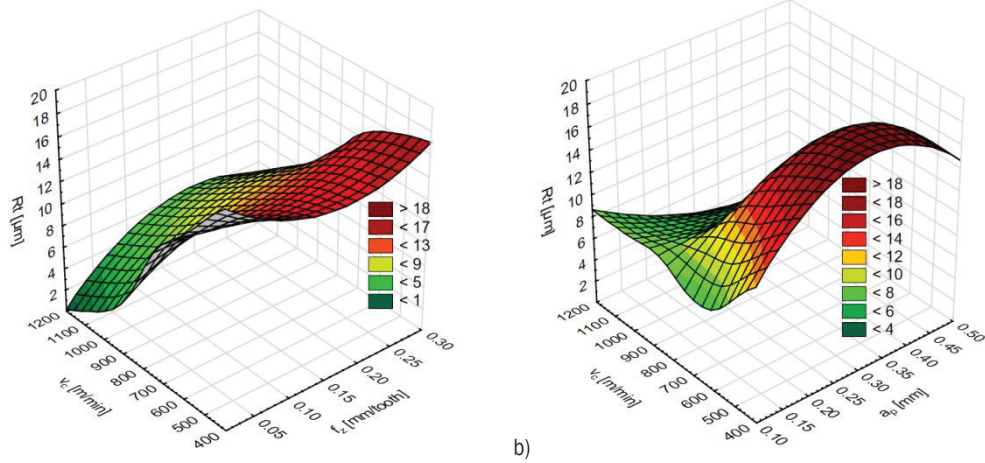


Fig. 13. Simulation results of the Rt surface roughness parameter after machining with tool with helix angle $\lambda_s = 50^\circ$ a) for the v_c and f_z , and b) for the v_c and a_p

it can be concluded that the presented ANN models show an acceptable level of error and can be used to predict approximate values of roughness parameters.

The simulation results of the appropriate roughness parameters Rq/Rt of the AZ91D alloy for the appropriate tool with helix angle $\lambda_s = 20^\circ$, and 60° , for the assumed range of cutting speed v_c , feed per tooth f_z and axial depth of cut a_p parameters are shown in Figs. 0 to 3. The simulation results for each model are presented in two graphs, depending on cutting speed v_c and feed per tooth f_z or cutting speed v_c and axial depth of cut a_p .

5 CONCLUSIONS

The experimental and statistical analysis results of the study leads to the following conclusions:

- for the $\lambda_s = 20^\circ$ tool increased cutting speed leads to a considerable decrease in surface roughness parameters, whereas for the tool with $\lambda_s = 60^\circ$ increased cutting speed has no significant effect on lateral face surface roughness parameters;
- increased feed per tooth leads to increased surface roughness, which was particularly visible when the feed per tooth $f_z = 0.05$ mm/tooth was changed to $f_z = 0.1$ mm/tooth for AZ91D alloy;
- irrespective of the magnesium alloy grade, for the tool with $\lambda_s = 20^\circ$ both axial and radial depth of cut has an insignificant effect on surface roughness parameters;
- the statistical analysis results show that for the tool with $\lambda_s = 20^\circ$ increased cutting speed has, in most cases, the greatest effect on the mean and

median values of the roughness parameters for both AZ91D and AZ31;

- the statistical analysis results for the tool with $\lambda_s = 60^\circ$ show that the roughness parameters of magnesium alloy AZ91D are most affected by varying feed per tooth as well as axial and radial depth of cut;
- as a result of modelling the Rq and Rt parameters after machining with a variable helix angle λ_s tool ($\lambda_s = 20^\circ$, $\lambda_s = 60^\circ$), the best models were obtained primarily for the network with 10 neurons in the hidden layer, only in the case of the Rt parameter with helix angle $\lambda_s = 60^\circ$ the best model had 8 neurons in the hidden layer;
- networks obtained as a result of modelling surface roughness parameters show a satisfactory predictive ability, as evidenced by the obtained regression values R : $Rq_{(\lambda_s=20^\circ)} = 0.99563$, $Rt_{(\lambda_s=20^\circ)} = 0.99358$, $Rq_{(\lambda_s=60^\circ)} = 0.99263$ and $Rt_{(\lambda_s=60^\circ)} = 0.98741$;
- as a result of the conducted modelling of neural networks, it can be concluded that they are an effective tool that can be used to predict surface roughness parameters.

6 ACKNOWLEDGEMENTS

The project/research was financed with FD-20/IM-5 and FD-20/IM-5 06

7 REFERENCES

- [1] Wieczorowski, M., Cellary, A., Chajda, J. (2003). *A Guide to Surface Roughness Measurement, i.e. Roughness and More*. Politechnika Poznańska, Poznań.
- [2] PN-EN ISO 4287:1999. *Part geometry specifications - Surface geometric structure: profile method - Terms, definitions and parameters of surface geometric structure*. International Organization for Standardization, Geneva.
- [3] Grzesik, W. (2015). Effect of the machine parts surface topography features on the machine service. *Mechanik*, vol. 8-9, p. 587-593, DOI:10.17814/mechanik.2015.8-9.493.
- [4] Gziut, O., Kuczmazewski, J., Zagórski, I. (2015). Surface quality assessment following high performance cutting of AZ91HP magnesium alloy. *Management and Production Engineering Review*, vol. 6, no. 1, p. 4-9, DOI:10.1515/MPER-2015-0001.
- [5] Muralidharan, S., Karthikeyan, N., Kumar, A.B., Aatthisugan, I. (2017). A study on machinability characteristic in end milling of magnesium composite. *International Journal of Mechanical Engineering and Technology*, vol. 8, no. 6, p. 455-462.
- [6] Guo, Y.B., Salahshoor, M. (2010). Process mechanics and surface integrity by high-speed dry milling of biodegradable magnesium-calcium implant alloys. *CIRP Annals*, vol. 59, no. 1, p. 151-154, DOI:10.1016/j.cirp.2010.03.051.
- [7] Salahshoor, M., Guo, Y.B. (2011). Surface integrity of magnesium-calcium implants processed by synergistic dry cutting-finish burnishing. *Procedia Engineering*, vol. 19, p. 288-293, DOI:10.1016/j.proeng.2011.11.114.
- [8] Qiao, Y., Wang, S., Guo, P., Yang, X., Wang, Y. (2018). Experimental research on surface roughness of milling medical magnesium alloy. *IOP Conference Series: Materials Science and Engineering*, vol. 397, p. art. ID 012114, DOI:10.1088/1757-899X/397/1/012114.
- [9] Desai, S., Malvade, N., Pawade, R., Warhatkar, H. (2017). Effect of high speed dry machining on surface integrity and biodegradability of Mg-Ca1.0 biodegradable alloy. *Materials Today Proceedings*, vol. 4, no. 6, p. 6817-6727, DOI:10.1016/j.matpr.2017.06.447.
- [10] Sathyamoorthy, V., Deepan, S., Sathya Prasanth, S.P., Prabhu, L. (2017). Optimization of Machining Parameters for Surface Roughness in End Milling of Magnesium AM60 Alloy. *Indian Journal of Science and Technology*, vol. 10, no. 32 p. 1-7. DOI:10.17485/ijst/2017/v10i32/104651.
- [11] Salahshoor, M., Guo, Y.B. (2011). Cutting mechanics in high speed dry machining of biomedical magnesium- calcium alloy using internal state variable plasticity model. *International Journal of Machine Tools and Manufacture*, vol. 51, no. 7-8, p. 579-590, DOI:10.1016/j.ijmactools.2011.04.004.
- [12] Zagórski, I., Korpysa, J. (2019). Surface quality in milling of AZ91D magnesium alloy. *Advances in Science and Technology Research Journal*, vol. 13, no. 2, p. 119-129. DOI:10.12913/22998624/108547.
- [13] Sivam, S.P., Bhat, M.D., Natarajan, S., Chauhan, N. (2018). Analysis of residual stresses, thermal stresses, cutting forces and other output responses of face milling operation on ZE41 magnesium alloy. *International Journal of Modern Manufacturing Technologies*, vol. 10, no. 1, p. 92-101.
- [14] Zagórski, I., Józwiak, J. (2021). Aviation Magnesium Alloys Milling - The Case Study. *IEEE 8th International Workshop on Metrology for AeroSpace (MetroAeroSpace)*, p. 371-375, DOI:10.1109/MetroAeroSpace51421.2021.9511726.
- [15] Alharti, N.H., Bingol, S., Abbas, A.T., Ragab, A.E., El-Danaf, E.A., Alharbi, H.F. (2017). Optimizing cutting conditions and prediction of surface roughness in face milling of AZ61 using regression analysis and artificial neural network. *Advances in Materials Sciences and Engineering*, vol. 2017, art. ID 7560468, DOI:10.1155/2017/7560468.
- [16] Chirita, B., Grigoras, C., Tampu, C., Hergehelegiu, E. (2019). Analysis of cutting forces and surface quality during face milling of a magnesium alloy. *IOP Conference Series: Material. Science Engineering*, vol. 591, art. ID 012006, DOI:10.1088/1757-899X/591/1/012006.
- [17] Ruslan, M.S., Othman, K., Ghani, J.A., Kassim, M.S., Haron, C.H. (2016). Surface roughness of magnesium alloy AZ91D in high speed milling. *Jurnal Teknologi*, vol. 78, p. 115-119. DOI:10.11113/jt.v78.9158.
- [18] Kim, J.D., Lee, K.B. (2010). Surface roughness evaluation in dry-cutting of magnesium alloy by air pressure coolant. *Engineering*, vol. 2, no. 10., p. 788-792, DOI:10.4236/eng.2010.210101.
- [19] Shi, K., Zhang, D., Ren, J., Yao, C., Huang, X. (2016). Effect of cutting parameters on machinability characteristics in milling of magnesium alloy with carbide tool. *Advances in Mechanical Engineering*, vol. 8, no. 1, p. 1-9. DOI:10.1177/1687814016628392.
- [20] Korpysa, J., Kuczmazewski, J., Zagórski, I. (2023). Surface quality of AZ91D magnesium alloy after precision milling with coated tools. *Strojniški vestnik - Journal of Mechanical Engineering*, vol. 69, no. 11-12, p. 497-508, DOI:10.5545/sv-jme.2023.651.
- [21] Natarajanm M.M., (2022). Investigation of Machining Parameters in Thin-Walled Plate Milling Using a Fixture with Cylindrical Support Heads. *Strojniški vestnik - Journal of Mechanical Engineering*, vol. 68, no. 12, p. 746-756. DOI:10.5545/sv-jme.2022.273.
- [22] Kumar, K.P.V., Balasubramanian, M. (2022). Optimization of FSW processing factors on hardness for dissimilar AA6061-T6 and AZ31B O alloys. *Strojniški vestnik - Journal of Mechanical Engineering*, vol. 68, no. 3, p. 166-174, DOI:10.5545/sv-jme.2021.7316.
- [23] ISO 21940-11:2016. *Mechanical vibration. Rotor balancing. Part 11: Procedures and tolerances for rotors with rigid behavior*. International Organization for Standardization, Geneva.
- [24] Watroba, J. (2009). *Data mining, testing of research hypotheses and relationship modeling-examples in Statistica 9*. Statsoft Polska, Kraków, p. 75-86.
- [25] Montgomery, D.C., Runger, G.C. (2003). *Applied Statistics and Probability for Engineers*. John Wiley & Sons, Inc., Hoboken.

Multi-performance Optimization of the Rotary Turning Operation for Environmental and Quality Indicators

Tat-Khoa Doan¹, Trung-Thanh Nguyen¹, An-Le Van^{2,*}

¹ Le Quy Don Technical University, Faculty of Mechanical Engineering, Vietnam

² Nguyen Tat Thanh University, Faculty of Engineering and Technology, Vietnam

In this investigation, two environmental metrics (the comprehensive energy used (TU) and turning noise (TN)) and a quality metric (surface roughness (SR)) of the rotary turning process for the Ti6Al4V were optimized and reduced using the optimal factors (the inclined angle- i , depth of cut- d , feed- f , and turning speed- V). The TU model was proposed comprising the embodied energy of the insert and lubricant. The method based on the removal effects of criteria (MERECE), an improved quantum-behaved particle swarm optimization algorithm (IQPSO), and TOPSIS were applied to select weight values and the best optimal solution. The machining cost (MC) was proposed in terms of process parameters. The outcomes presented that the optimal values of the i , d , f , and V were 35 deg., 0.30 mm, 0.40 mm/rev., and 190 m/min, respectively, while the TU, SR, TN, and MC were saved by 6.7 %, 22.3 %, 23.5 %, and 8.5 %, respectively. The turning responses were primarily affected by the feed rate and turning speed, respectively. The developed turning process could be employed for machining hard-to-cut alloys. The developed approach could be applied to deal with optimization problems for other machining operations.

Keywords: rotary turning, total energy consumption, surface roughness, noise emission, IQPSO

Highlights

- A new rotary turning tool was designed and fabricated.
- Process parameters, including the spindle speed, depth of penetration, feed rate, and inclination angle were optimized.
- The total energy consumption, surface roughness, and turning noise were enhanced.
- An improved quantum-behaved particle swarm optimization algorithm was proposed.

0 INTRODUCTION

The machining operation using rotary inserts is an effective solution to deal with hard-to-cut materials. The cutting temperature, force components, and pressure at the nose are reduced with the support of the rotational motion of the round piece. Additionally, a higher tool life is obtained due to the even distribution of the cutting temperature, leading to higher productivity and quality indicators, as compared to the conventional processes.

Different milling and turning operations having rotary inserts have been developed and optimized by many investigators. Karaguzel et al. [1] indicated that the rotary turning and milling processes provide 10- and 40-times longer tool life than conventional operations. The optimal cutting speed, feed, depth of cut, and inclination angle were selected to decrease the surface roughness and improve the material removal rate [2]. The ultrasonic vibration-based rotary turning was developed to machine decrease the machining forces and average roughness of the turned AA 7075 [3]. The results indicated the tool speed of 98.63 m/min and the feed of 0.08 mm/min were optimal data. A simulation model was developed to predict the tool wear in the rotary turning [4]. The authors stated that the tool wear was effectively decreased due to the

disengagement duration. The energy efficiency and surface roughness were enhanced by 8.9 % and 24.8 %, respectively using the optimal process parameters [5]. Nguyen emphasized that the energy consumption, surface roughness, and material removal rate of the turned SKD11 were affected by the speed, feed, depth of cut, and inclination angle [6]. Umer et al. indicated that an increased speed and/or depth caused a higher temperature of the turned 100 steel [7]. Ahmed et al. stated that surface roughness and tool wear of the turned AISI 440 were decreased by 24.6% and 31.6 %, respectively using optimal process parameters [8].

Nieslony et al. [9] indicated that a higher speed caused a decrease in the surface roughness and a stable turning operation, while an increased depth led to a higher intensity of the vibration. A rotary milling process was developed to machine the titanium alloy, in which a low speed was recommended to reduce the tool wear rate [10]. Ahmed et al. [11] emphasized that low process parameters (speed, feed, and depth of cut) and high inclination angle decreased the temperature of the rotary turning. Similarly, Chen et al. [12] emphasized that the surface roughness produced by the rotary process was lower than the conventional one. A novel simulation model was developed to forecast the temperature of the turned nickel and titanium alloys [13]. The authors stated that low process parameters

(speed, feed, and depth of cut) and high inclination angle decreased the temperature. Umer et al. [14] revealed that a lower depth of cut was recommended to reduce the temperature and forces. The total energy consumed and machining time of the turned SKD6 were decreased by 17 % and 8 %, respectively, using the optimal factors [15]. Additionally, the carbon emission of the rotary turning operation was reduced by 50 % using the PSO [16]. He et al. revealed that the cutting temperature of the turned K47 alloy decreased with a higher inclination angle and cutting speed [17]. However, the shortcomings of the aforementioned works can be expressed as follows.

An efficient self-propelled rotary tool having high stiffness to machine high-hardness steels has not been designed and fabricated to replace the fixed turning one. Low rigidity is a primary drawback of the proposed tools in previous publications.

The noise emission damages the inner ear and causes occupational hearing loss as well as chronic stress; hence, minimizing the sound intensity of the rotary turning operation is a necessary requirement.

Moreover, the optimal process variables have not been determined to make reductions in energy consumed, roughness, and noise emission.

The next section presents the framework. The experimental setting and discussions are then shown. Finally, the obtained findings are drawn.

1 THE CONCEPT OF THE ROTARY TURNING OPERATION

The principle of the rotary turning process to produce external surfaces of hardened materials is presented in Fig. 1. The workpiece is rotated around its axis, while the motion of the round piece is conducted using the friction between the body and specimen. The manufactured tool is shown in Fig. 1b, including the screws, bolts, the round insert, the base, and the holder. The milled grooves on the base are utilized to change the inclination angle. The round insert is conducted self-rotation using two bearings. The round inserts having a rake angle of 11° and a hardness of 92 HRC are utilized for all tests.

2 OPTIMIZATION APPROACH

The *TU* consists of the turning energy (*TE*), embodied energy for the insert (*EI*), and embodied energy for the coolant (*EC*).

$$TU = TE + EI + EC. \quad (1)$$

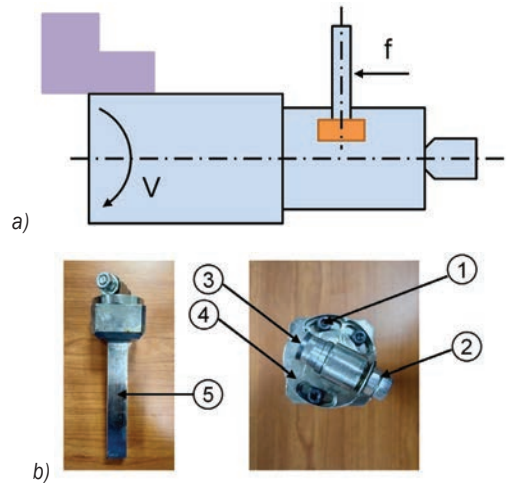


Fig. 1. The concept of the rotary turning process; a) the schematic principle, and b) the fabricated rotary tool (1. the screws; 2. the bolts; 3. the round insert, 4. the base; and 5. the holder)

The *EC* is computed as:

$$TE = E_{st} + E_{sb} + E_m + E_{at} + E_t + E_{tc}. \quad (2)$$

where E_{st} , E_{sb} , E_m , E_{at} , E_t , E_{tc} are energy consumed in the startup, standby, transition, air-turning, turning, and tool change stages (Fig. 2).

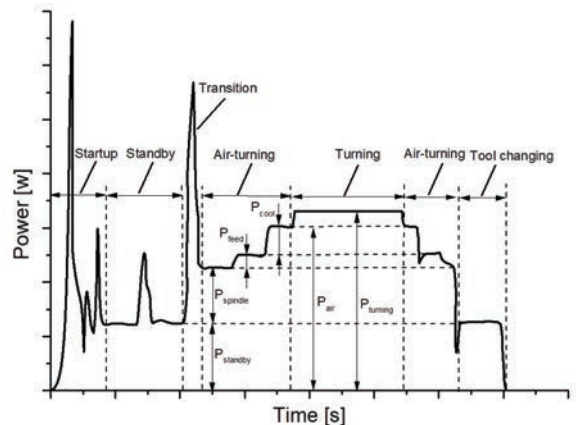


Fig. 2. The machining load of the rotary turning process

The start-up state presents the shortest period for turning on the lathe. The standby state denotes the stable period, which starts with turning on the machine tool and stops with the spindle rotation. The transition state refers to the short period for increasing and decreasing the spindle speed. The air-turning state presents the duration with spindle rotation but no material cutting. The turning state refers to the steady period for material removal.

$$TE = P_o t_o + P_{sb} t_{sb} + aV^2 + bV + c + (P_{st} + c_1 V + c_2) t_a + P_c t_c + P_{st} t_{tc} \left(\frac{t_c}{T_T} \right), \quad (3)$$

where P_o , P_{sb} , and P_c are the power used in the startup, standby, and turning states, respectively. t_o , t_{sb} , t_a , and t_c are the startup, standby, air-cutting, and turning time, respectively. a , b , and c denote the experimental coefficients. t_{tc} and T_T are the tool change time and tool life, respectively. The T_T is expressed as:

$$T_T = \frac{A}{V^\alpha f^\beta d^\gamma}, \quad (4)$$

where A , α , β , and γ are the experimental coefficients. The EI is computed as:

$$EI = \frac{t_c}{T_T} SE_i I_v, \quad (5)$$

where E_i and I_v are the fabricating energy and volume of each insert, respectively.

The EC is computed as:

$$EC = \frac{t_c}{T_L} V_u \eta \rho E_L, \quad (6)$$

where T_L and E_L denote the cycle time and fabricating energy of the lubricant, respectively. V_u is the lubricant volume. ρ and η are the density and concentration of the lubricant, respectively.

The R is computed as:

$$SR = \sum_{i=1}^n \frac{R_{ai}}{n}, \quad (7)$$

where R_{ai} is the average roughness at the i_{th} measured point.

The TN is computed as:

$$TN = \sum_{i=1}^n \frac{TN_i}{n}, \quad (8)$$

where TN_i is the turning noise at the i_{th} measured time.

In this study, the characteristics of the coolant system, cutting piece, and specimen are named as constants. The factors considered and their levels are presented in Table 1. The ranges are determined based on the specifications of the lathe. Moreover, these values are confirmed with the published works related to the rotary turning processes. The optimization issue is presented as:

- Find $X = [i, V, f, \text{ and } d]$.
- Minimizing TU, R , and TN ;
- Constraints: $20 \text{ deg} \leq i \leq 50 \text{ deg}$;
 $0.3 \text{ mm} \leq d \leq 0.7 \text{ mm}$;

$$0.4 \text{ mm/rev} \leq f \leq 0.8 \text{ mm/rev};$$

$$90 \text{ m/min} \leq V \leq 190 \text{ m/min}.$$

Table 1. Process parameters of the rotary turning

| Symbol | Parameters | 1 | 2 | 3 |
|--------|-------------------------|-----|-----|-----|
| i | Inclination angle [deg] | 20 | 35 | 50 |
| d | Turning depth [mm] | 0.3 | 0.5 | 0.7 |
| f | Feed rate [mm/rev] | 0.4 | 0.6 | 0.8 |
| V | Turning speed [m/min] | 90 | 140 | 190 |

3.2 Optimization Framework

The optimizing approach is depicted in Fig. 3

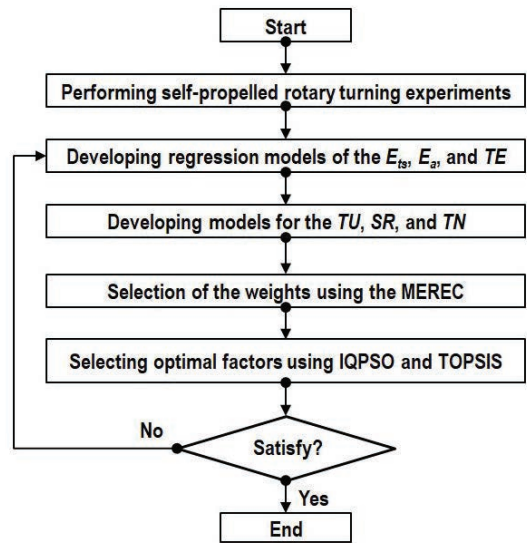


Fig. 3. Systematic optimizing procedure

Step 1: Performing experimental tests using the Box-Behnken design [18] and [19].

The Box-Behnken design requires three levels for each factor, which presents the lowest, middle, and highest ranges. The design points are placed on the middle points of the edge and the centre of the block. The advantages of the Box-Behnken design are the low number of tests and ensuring predictive accuracy. The number of experiments (NE) in the Box-Behnken design is computed as [20]:

$$NE = 2n(n-1) + N_c, \quad (9)$$

where n and N_c are the number of variables and the number of centre points, respectively. In this work, 29 experiments are performed for 4 process parameters and 5 replications.

Step 2: Developing regression models for energy components, R , and TN [21].

Step 3: The MEREC is utilized to compute the weights.

For the maximizing aim, the normalized response (n_{ij}) is computed as:

$$n_{ij} = \frac{\min y_i}{y_i} \quad (10)$$

For the minimizing aim, the n_{ij} is computed as:

$$n_{ij} = \frac{y_i}{\max y_i} \quad (11)$$

The performance of the alternatives S_i is computed as:

$$S_i = \ln \left[1 + \left(\frac{1}{n} \sum_j |\ln(n_{ij})| \right) \right], \quad (12)$$

where n is the number of responses.

The performance of i^{th} alternative is computed as:

$$S'_{ij} = \ln \left[1 + \left(\frac{1}{n} \sum_{k, k \neq j} |\ln(n_{ik})| \right) \right]. \quad (13)$$

The removal effect of the j^{th} response (E_j) is computed as:

$$E_j = \sum_i |S'_{ij} - S_i|. \quad (14)$$

The weight (ω_i) is computed as:

$$\omega_i = \frac{E_j}{\sum_k E_k} \quad (15)$$

Step 4: Generation of the optimality using the IQPSO.

In the QPSO, the updated position of each particle is expressed as: [22] and [23]:

$$x_{i,j}(t+1) = p_{i,j}(t) - \alpha(m_{best\ i,j}(t) - x_{i,j}(t)) \ln\left(\frac{1}{u}\right) \quad \text{If } k \geq 0.5, \quad (16)$$

$$x_{i,j}(t+1) = P_{i,j}(t) + \alpha(m_{best\ i,j}(t) - x_{i,j}(t)) \ln\left(\frac{1}{u}\right) \quad \text{If } k < 0.5, \quad (17)$$

$$p_{i,j}(t+1) = \lambda P_{i,j}(t) + (1 - \lambda)G_j(t), \quad (18)$$

$$m_{best\ i,j}(t) = \frac{1}{N} \sum_{i=1, j=1}^{N, M} P_{i,j}(t). \quad (19)$$

In this work, the IQPSO combining the QPSO and the Cauchy-Lorentz distribution is proposed to expand the perturbation [24]. The probability density function ($f(x)$) of the Cauchy-Lorentz distribution is given as:

$$f(x, x_o, \gamma) = \frac{1}{\pi} \left(\frac{\lambda}{(x - x_o)^2 + \gamma^2} \right), \quad (20)$$

where x_o and γ are the locations of the peak of the distribution and scale parameter, respectively.

In the mutation stage, each vector is added by a Cauchy-Lorentz random value ($D(\cdot)$) and expressed:

$$x' = x + \lambda D(\cdot), \quad (21)$$

where x' is the new location after mutation with random value to x .

The convergence of the QPSO-CL is enhanced with the aid of natural selection, which is expressed as:

$$F(X(t)) = \{F(x_1(t)), \dots, F(x_N(t))\}, \quad (22)$$

where $X(t)$ and $F(X(t))$ are the position vector of particles and fitness function of swarm, respectively. The particles are sorted based on fitness values, which is expressed as:

$$F(X'(t)) = \{F(x'_1(t)) \dots F(x'_N(t))\}, \quad (23)$$

$$X'(t) = \{x'_1(t), \dots, x'_N(t)\}, \quad (23)$$

The operating steps of the IQPSO are illustrated in Fig. 4. Matlab 2019 commercial software entitled is used to conduct the IQPSO.

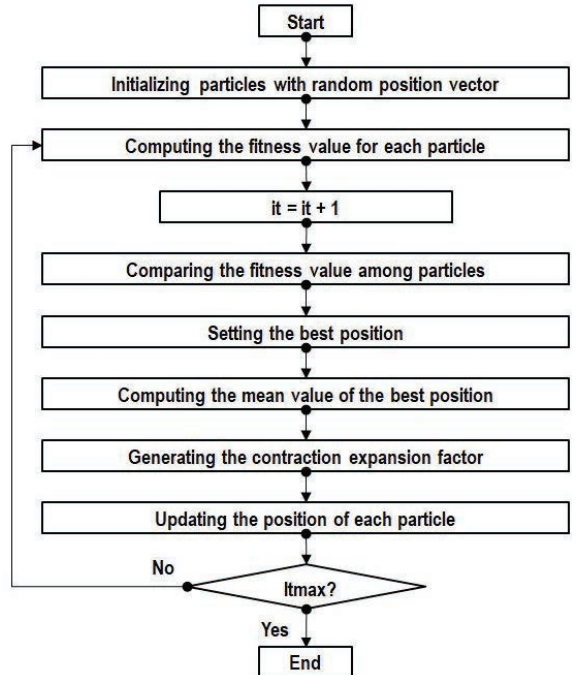


Fig. 4. The operating procedure of the IQPSO

Step 4: The best solution is selected by the TOPSIS.

The normalized value of each alternative (g_{ij}) is computed as:

$$g_{ij} = \frac{e_{ij}}{\sqrt{\sum_{i=1}^m e_{ij}^2}}, \quad (24)$$

where e_{ij} presents the value of the alternative j_{th} .

The positive ideal solution (P^+) and the negative idea solution (N^-) are computed as:

$$P^+ = \sqrt{\sum_{j=1}^m (v_{ij} - v_j^+)^2}, \quad (25)$$

$$N^- = \sqrt{\sum_{j=1}^m (v_{ij} - v_j^-)^2}. \quad (26)$$

The best point is found with the highest selection index (S_i), which is calculated as:

$$S_i = \frac{N^-}{P^+ + N^-}. \quad (27)$$

3 EXPERIMENTAL SETTING

A turning machine entitled EMCOTURN E45 is utilized to execute the turning trials. The Ti6Al4V bar with an outside diameter of ϕ and a length of 400 mm is utilized as the specimen (Fig. 5). The chemical compositions of the Ti6Al4V produced by EDX results are presented in Table 2 and Fig. 6. The outside diameter, inside diameter, and thickness of the round insert are 2 mm, 4.4 mm, and 4.8 mm, respectively.

A KEW65 electrical sensor, Mitutoyo SJ-01 and EXTECH 400 sound meter are employed to obtain the power components, machined roughness, and turning noise.



Fig. 5. The turned specimens

Table 2. Chemical compositions of the Ti6Al4V

| Elements | Al | Ti | V | Fe | C | O | Others |
|----------|------|-------|------|------|------|------|-----------|
| [%] | 6.01 | 83.74 | 3.26 | 0.16 | 0.28 | 5.08 | Allowance |

The representative data of the rotary turning operation are depicted in Fig. 7. Fig. 7a presents the power used at the experimental No. 16 while the roughness profile and SEM image are shown in Figs. 7b and c, respectively. The wear and fracture have not been found on the edges of round inserts, as shown in Fig. 7d. The noise profile is presented in Fig. 7e.

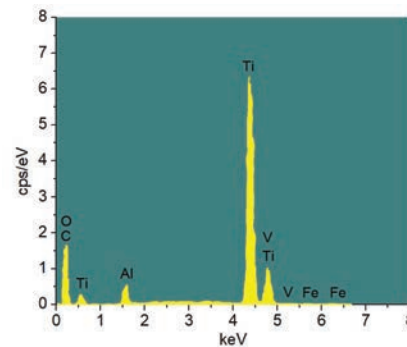


Fig. 6. Investigation of a) the microstructure, and b) chemical compositions of Ti6Al4V; produced by EDX results

Table 3. Regression models of the energy consumed in the transition state and operational power

| No. | Regression model | R^2 | Adjusted R^2 | Predicted R^2 |
|-----|--|--------|----------------|-----------------|
| 1 | $EC_{ts} = 0.000025V^2 - 0.0014V + 0.4682$ | 0.9882 | 0.9794 | 0.9654 |
| 2 | $P_{op} = 0.0025V + 0.03682$ | 0.9924 | 0.9826 | 0.9758 |

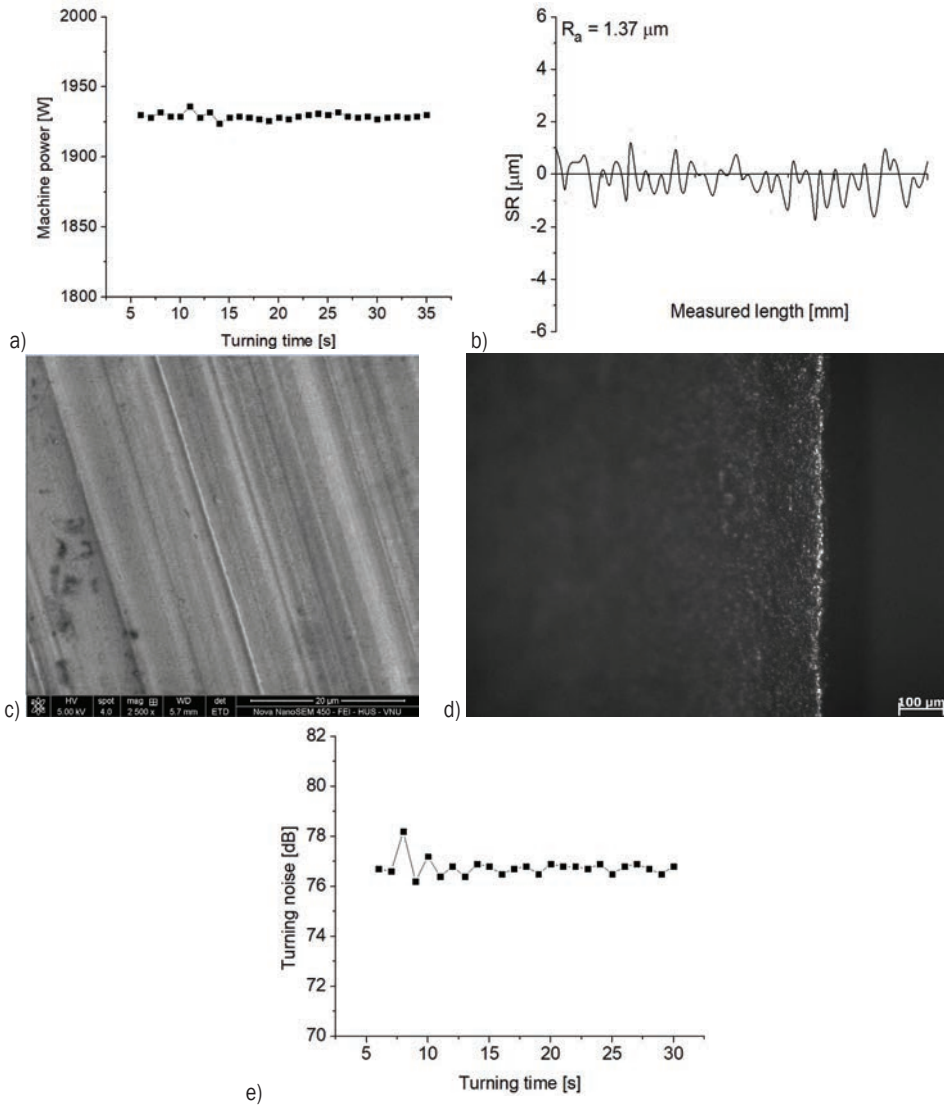


Fig. 7. Representative experiments at experimental No. 16; a) power consumed, b) average roughness, c) the SEM image, d) the SEM image of the round insert, e) turning noise

4 RESULTS AND DISCUSSIONS

4.1 Development of EC_{ts} and P_{op} Models

The EC_{ts} and P_{op} models are shown in Table 3

4.2 Development of E_t , R , and TN models

The obtained data for the E_t , R , and TN are presented in Table 4.

The ANOVA results of the E_t , R , and TN are shown in Tables 5 to 7 respectively. The values of the R^2 , the adjusted R^2 , and the predicted R^2 values

indicate that the E_t , R , and TN correlations are significant.

For the E_t model, the contributions of the i , d , f , and V are 2.11 %, 6.04 %, 22.79 %, and 27.33 %, respectively. The contributions of the if , fd , d^2 , and fV are 1.22 %, 2.44 %, 2.89 %, and 4.23 %, respectively. The contributions of the i^2 , f^2 , and V^2 are 6.89 %, 9.33 %, and 1.22 %, respectively.

For the R model, the contributions of the i , d , f , and V are 6.11 %, 3.11 %, 22.5 %, and 23.3 %, respectively. The contributions of the id , iV , d^2 , and fV are 1.06 %, 2.42 %, 3.34 %, and 2.59 %, respectively. The contributions of the i^2 and d^2 are 12.2 % and 3.3 % respectively.

For the *TN* model, the contributions of the *i*, *d*, *f*, and *V* are 17.37 %, 15.91 %, 16.82 %, and 18.09 %, respectively. The contributions of the *if*, \mathcal{V} , and *fV* are 1.6 %, 1.44 %, and 10.4 %, respectively. The contributions of the *i*², *d*², *f*², and *V*² are 2.23 %, 1.8 %, 1.8 %, and 2.22 % respectively.

The deviations between the actual and predictive values of the *E_t*, *R*, and *TN* change from -0.99 % to 1.26 %, from -0.97 to 0.80, and -1.26 % to -0.47 %, respectively (Table 8). Therefore, the *E_t*, *R*, and *TN* models are significant.

The probability plots of three responses are presented in Fig. 8. It can be stated that observed data are distributed on straight lines, indicating the goodness of the fit of the proposed models.

Table 4. Experimental data for developing the *E_t*, *R*, and *TN* models

| No. | <i>i</i> | <i>d</i> | <i>f</i> | <i>V</i> | <i>E_t</i> | <i>R</i> | <i>TN</i> |
|--|----------|----------|----------|----------|----------------------|----------|-----------|
| Experimental data for developing models | | | | | | | |
| 1 | 50 | 0.5 | 0.6 | 190 | 8.75 | 2.17 | 98.1 |
| 2 | 20 | 0.3 | 0.6 | 140 | 9.69 | 2.04 | 78.2 |
| 3 | 35 | 0.3 | 0.8 | 140 | 7.57 | 2.24 | 78.2 |
| 4 | 20 | 0.5 | 0.8 | 140 | 8.67 | 2.78 | 91.4 |
| 5 | 50 | 0.5 | 0.4 | 140 | 14.90 | 2.16 | 79.4 |
| 6 | 20 | 0.7 | 0.6 | 140 | 10.78 | 2.75 | 92.1 |
| 7 | 50 | 0.5 | 0.6 | 90 | 15.73 | 2.99 | 81.4 |
| 8 | 35 | 0.7 | 0.4 | 140 | 14.24 | 2.19 | 73.3 |
| 9 | 20 | 0.5 | 0.4 | 140 | 13.98 | 1.97 | 77.4 |
| 10 | 35 | 0.5 | 0.6 | 140 | 9.60 | 2.18 | 76.3 |
| 11 | 50 | 0.3 | 0.6 | 140 | 9.99 | 2.31 | 80.1 |
| 12 | 35 | 0.5 | 0.4 | 90 | 19.34 | 2.14 | 59.8 |
| 13 | 20 | 0.5 | 0.6 | 190 | 8.36 | 1.81 | 96.5 |
| 14 | 35 | 0.5 | 0.6 | 140 | 9.62 | 2.16 | 76.8 |
| 15 | 35 | 0.3 | 0.4 | 140 | 12.08 | 1.41 | 58.8 |
| 16 | 35 | 0.5 | 0.4 | 190 | 11.47 | 1.37 | 76.7 |
| 17 | 35 | 0.5 | 0.8 | 190 | 6.52 | 2.11 | 94.9 |
| 18 | 35 | 0.7 | 0.6 | 190 | 8.52 | 2.22 | 93.4 |
| 19 | 50 | 0.5 | 0.8 | 140 | 8.99 | 3.02 | 96.7 |
| 20 | 50 | 0.7 | 0.6 | 140 | 11.29 | 2.94 | 94.2 |
| 21 | 35 | 0.5 | 0.8 | 90 | 12.32 | 3.07 | 75.9 |
| 22 | 35 | 0.3 | 0.6 | 190 | 7.55 | 1.49 | 77.3 |
| 23 | 20 | 0.5 | 0.6 | 90 | 15.09 | 2.81 | 79.2 |
| 24 | 35 | 0.7 | 0.6 | 90 | 15.56 | 2.94 | 74.1 |
| 25 | 35 | 0.7 | 0.8 | 140 | 8.53 | 2.99 | 91.4 |
| 26 | 35 | 0.3 | 0.6 | 90 | 13.18 | 2.46 | 60.9 |
| Experimental data for testing developed models | | | | | | | |
| 27 | 25 | 0.5 | 0.4 | 100 | 17.72 | 2.15 | 65.7 |
| 28 | 30 | 0.4 | 0.5 | 120 | 14.57 | 2.17 | 63.3 |
| 29 | 40 | 0.6 | 0.7 | 140 | 8.95 | 2.63 | 85.7 |
| 30 | 25 | 0.7 | 0.5 | 130 | 13.08 | 2.51 | 80.7 |
| 31 | 40 | 0.5 | 0.7 | 150 | 8.11 | 2.36 | 84.3 |
| 32 | 45 | 0.4 | 0.6 | 160 | 8.73 | 2.06 | 81.9 |

Table 5. ANOVA results for the *E_t* model

| So. | SS | MS | <i>F</i> -value | <i>p</i> -value | Con. [%] |
|---|-------|-------|-----------------|-----------------|----------|
| Mo. | 249.1 | 17.8 | 35.6 | < 0.0001 | |
| <i>i</i> | 37.4 | 37.4 | 74.8 | 0.003 | 2.11 |
| <i>d</i> | 107.1 | 107.1 | 214.1 | < 0.0001 | 6.04 |
| <i>f</i> | 404.0 | 404.0 | 807.9 | < 0.0001 | 22.79 |
| <i>V</i> | 484.4 | 484.4 | 968.9 | < 0.0001 | 27.33 |
| <i>if</i> | 21.6 | 21.6 | 43.2 | 0.007 | 1.22 |
| \mathcal{V} | 51.2 | 51.2 | 102.5 | 0.003 | 2.89 |
| <i>fV</i> | 75.0 | 75.0 | 150.0 | 0.002 | 4.23 |
| <i>i</i> ² | 122.1 | 122.1 | 244.3 | < 0.0001 | 6.89 |
| <i>f</i> ² | 165.4 | 165.4 | 330.8 | < 0.0001 | 9.33 |
| <i>V</i> ² | 234.0 | 234.0 | 467.9 | < 0.0001 | 13.2 |
| Re. | 5.5 | 0.5 | | | |
| To. | 254.6 | | | | |
| <i>R</i> ² = 0.9784; Adj. <i>R</i> ² = 0.9692; Pred. <i>R</i> ² = 0.9578 | | | | | |

Table 6. ANOVA results for the *R* model

| So. | SS | MS | <i>F</i> -value | <i>p</i> -value | Con. [%] |
|---|------|------|-----------------|-----------------|----------|
| Mo. | 6.33 | 0.45 | 38.90 | < 0.0001 | 6.37 |
| <i>i</i> | 0.42 | 0.42 | 154.86 | < 0.0001 | 18.18 |
| <i>d</i> | 1.19 | 1.19 | 441.98 | < 0.0001 | 22.15 |
| <i>f</i> | 1.45 | 1.45 | 538.49 | < 0.0001 | 23.36 |
| <i>V</i> | 1.53 | 1.53 | 567.91 | < 0.0001 | 1.06 |
| <i>id</i> | 0.07 | 0.07 | 25.77 | 0.010 | 6.37 |
| <i>iV</i> | 0.16 | 0.16 | 58.83 | 0.007 | 2.42 |
| \mathcal{V} | 0.22 | 0.22 | 81.20 | 0.009 | 3.34 |
| <i>fV</i> | 0.17 | 0.17 | 62.97 | 0.007 | 2.59 |
| <i>i</i> ² | 1.00 | 1.00 | 370.02 | < 0.0001 | 15.22 |
| <i>d</i> ² | 0.22 | 0.22 | 82.17 | 0.009 | 3.38 |
| Re. | 0.13 | 0.01 | | | |
| To. | 6.45 | | | | |
| <i>R</i> ² = 0.9802; Adj. <i>R</i> ² = 0.9784; pred. <i>R</i> ² = 0.9662 | | | | | |

Table 7. ANOVA results for the *TN* model

| So. | SS | MS | <i>F</i> -value | <i>p</i> -value | Con. [%] |
|---|--------|--------|-----------------|-----------------|----------|
| Mo. | 3168.7 | 226.3 | 44.4 | < 0.0001 | |
| <i>i</i> | 2729.5 | 2729.5 | 535.1 | 0.0010 | 17.37 |
| <i>d</i> | 2500.1 | 2500.1 | 490.1 | < 0.0001 | 15.91 |
| <i>f</i> | 2643.0 | 2643.0 | 518.1 | < 0.0001 | 16.82 |
| <i>V</i> | 2842.6 | 2842.6 | 557.3 | < 0.0001 | 18.09 |
| <i>if</i> | 257.7 | 257.7 | 50.5 | 0.0068 | 1.64 |
| \mathcal{V} | 226.3 | 226.3 | 44.4 | 0.0075 | 1.44 |
| <i>fV</i> | 163.4 | 163.4 | 32.0 | 0.0078 | 1.04 |
| <i>i</i> ² | 3336.0 | 3336.0 | 654.0 | < 0.0001 | 21.23 |
| <i>d</i> ² | 286.0 | 286.0 | 56.1 | 0.0066 | 1.82 |
| <i>f</i> ² | 212.1 | 212.1 | 41.6 | 0.0074 | 1.35 |
| <i>V</i> ² | 348.8 | 348.8 | 68.4 | 0.0062 | 2.22 |
| Re. | 56.1 | 5.1 | | | |
| To. | 3224.8 | | | | |
| <i>R</i> ² = 0.9826; Adj. <i>R</i> ² = 0.9794; pred. <i>R</i> ² = 0.9685 | | | | | |

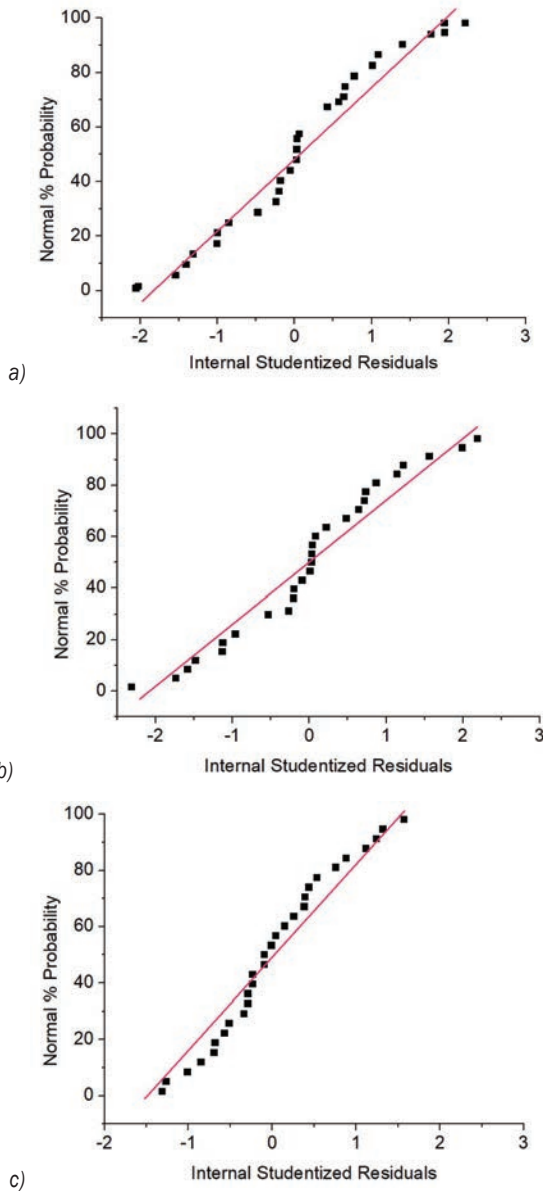


Fig. 8. The probability plots of three responses; a) for E_t model, b) for R model, c) for TN model

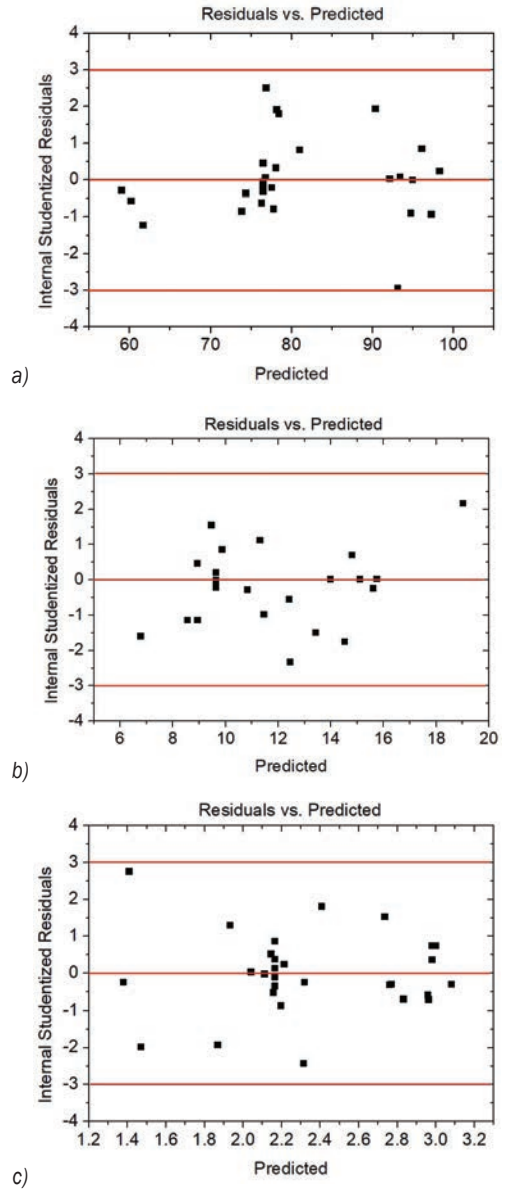


Fig. 9. The residuals versus the observations for three responses; a) for E_t model, b) for R model, c) for TN model

The residuals versus the observations of three responses are presented in Fig. 9. The errors of the responses are systematically distributed, presenting constant errors for each model.

4.3 Parametric Impacts

The E_t is first reduced by 2.8 % with a higher i (Fig. 0a). However, the E_t is increased by 7.9 % with a further i . An increased i causes a reduction in the cutting volume, leading to a decrease in the resistance; hence, the E_t reduces. A higher i increases the cutting

volume due to the perpendicular tool, resulting in higher friction; hence, the E_t increases.

The E_t is increased by 14.9 % with an increment in the d (Fig. 0a). A higher d increases the thickness of the chip; hence, the E_t increases.

The E_t is decreased by 35 % with an increment in the f (Fig. 0b). A higher f reduces the turning time; hence, the E_t increases.

The E_t is decreased by 38.9 % with an increment in the V (Fig. 0b). When the V increases, the turning time reduces; hence, the energy consumption decreases.

Table 8. Confirmations of the precision of the developed models

| No. | E_t [kJ] | | | R [μm] | | | TN [dB] | | |
|-----|------------|-------|-------|-----------------------|-------|-------|-----------|-------|-------|
| | Exp. | Pred. | Err. | Exp. | Pred. | Err. | Exp. | Pred. | Err. |
| 27 | 17.72 | 17.86 | -0.79 | 2.15 | 2.16 | -0.47 | 65.7 | 66.1 | -0.61 |
| 28 | 14.57 | 14.62 | -0.34 | 2.17 | 2.18 | -0.46 | 63.3 | 64.1 | -1.26 |
| 29 | 8.95 | 9.04 | -1.01 | 2.63 | 2.62 | 0.38 | 85.7 | 86.1 | -0.47 |
| 30 | 13.08 | 13.16 | -0.61 | 2.51 | 2.49 | 0.80 | 80.7 | 81.2 | -0.62 |
| 31 | 8.11 | 8.19 | -0.99 | 2.36 | 2.38 | -0.85 | 84.3 | 84.9 | -0.71 |
| 32 | 8.73 | 8.62 | 1.26 | 2.06 | 2.08 | -0.97 | 81.9 | 82.6 | -0.85 |

The R is first decreased by 12 % with an increment in the i (Fig. 11a). However, the R is increased by 21.9 % with a further i . An increased i decreases the turning volume, resulting in a low resistance; hence, a low R is produced. A higher i causes an increased turning volume, leading to a hard turning; hence, a rough surface is generated.

The R is increased by 30.9 % with a higher d (Fig. 11a). A higher d causes an increase in the turning volume, leading to higher resistance; hence, a higher R is produced.

The R is increased by 47 % with an increment in the f (Fig. 11b). A higher f causes an increase in the turning volume, leading to a higher friction; hence, the

SR increases. Moreover, A higher f causes an increase in the turning marks, resulting in a higher roughness.

The R is decreased by 47 % with an increment in the V (Fig. 11b). The cutting temperature increases with an increment in the V , resulting in softer specimen; hence, the R reduces.

The TN is decreased by 8 % with an increment in the i (Fig. 12a). However, the TN is increased by 47 % with further i . A higher i decreases the material removal volume, resulting in low friction between the turning insert and workpiece; hence, the TN decreases. In contrast, a further i increases the material removal volume, leading to greater resistance; hence, the TN increases.

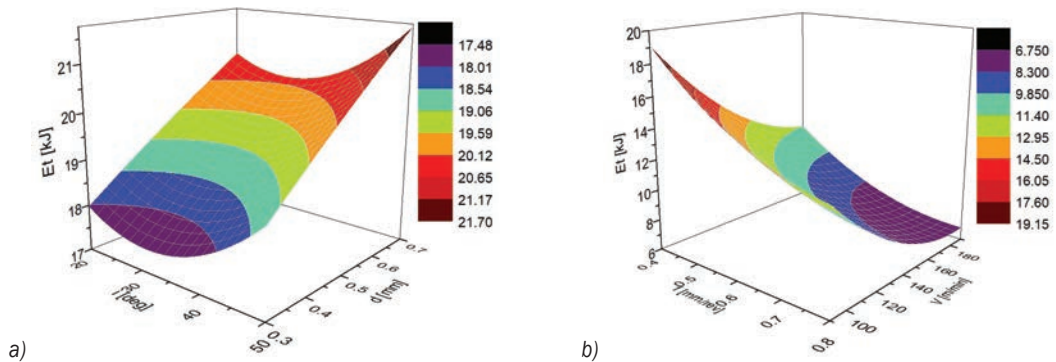


Fig. 10. Interactions of process parameters on the E_t ; a) E_t vs. i and d , b) E_t vs. V and f

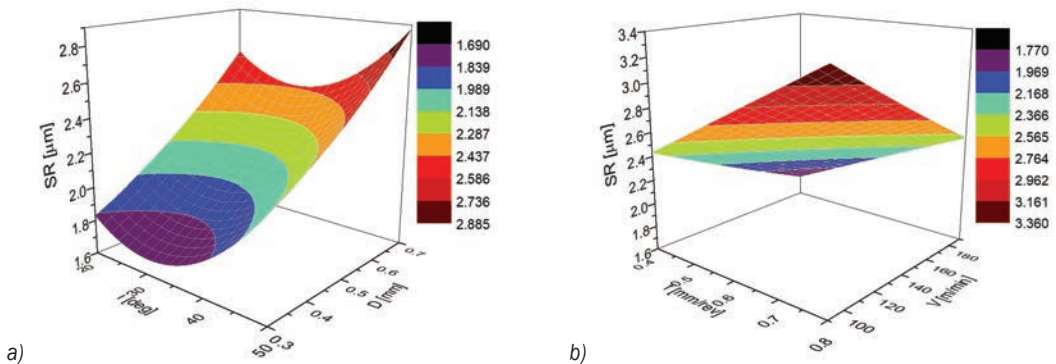


Fig. 11. Interactions of process parameters on the R ; a) R vs. i and d , b) R vs. V and f

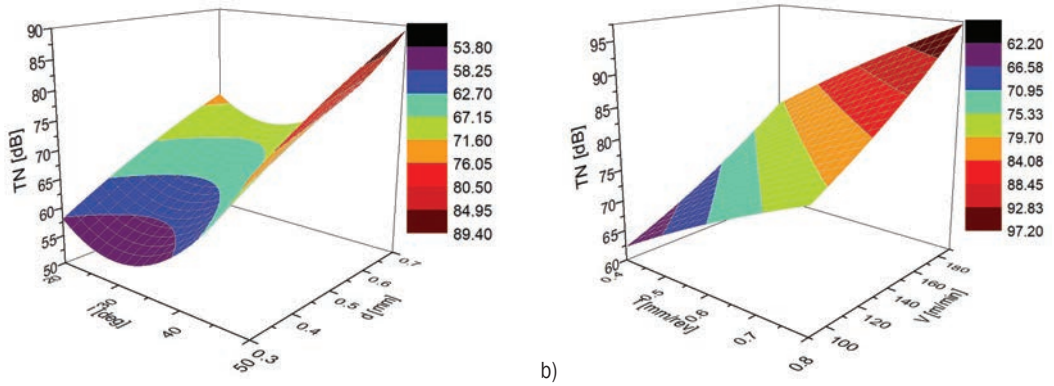


Fig. 12. Interactions of process parameters on the TN; a) TN vs. A and D, b) TN vs. V and f

The TN is increased by 28 % with an increment in the d (Fig. 12a). A higher D increases the material removal to be cut, leading to higher friction; hence, the TN increases. Moreover, a higher d causes greater resistance, resulting in higher turning noise.

The TN is increased by 28 % with an increment in the f (Fig. 12b). An increased f causes higher material removal to be cut, leading to higher friction; hence, the TN increases. Additionally, a higher f increases the machining power of the drive system; hence, a higher TN is produced.

The TN is increased by 29.3 % with an increment in the V (Fig. 12b). A higher V increases the engagement frequency of the spindle system; hence, the TN increases. Additionally, an increased V causes higher material removal to be cut, leading to higher friction; hence, the TN increases.

The E_t , SR , and TN are expressed as:

$$E_t = 0.426 i - 0.218 d + 14.09801d - 49.89973f - 0.23 V + 0.017943id - 0.04979if - 0.00008 iV - 748 df - 0.05 dV + 0.01 f + 0.003 i^2 - 1643 d^2 + 2884 f^2 + 0.0006 V^2 \quad (28)$$

$$R = 3.29271 - 0.08815i - 0.425 d + 2.1 5f - 0.026 V - 0.006 id + 0.0046 if + 0.00006iV - 0.3 fl + 0.0025 dV - 0.0043 fV + 0.0026 i^2 + 8 d^2 - 0.07292f^2 + 0.000005 V^2 \quad (29)$$

$$TN = 604 - 2.8 i + 3051 d + 49.7375f - 0.0091 V + 0.06 id + 0.23 if - 0.0002iV - 825 fl + 0.025 dV + 0.025 fV + 0.0473 i - 22.91667d^2 - 16.97917f^2 + 0.00044V^2 \quad (30)$$

4.4 Optimizing Outcomes Produced by the IQPSO

Table 9 shows the coefficients for turning objectives. The values of the TU , R , and TN are presented in Table 10. The weight values of the TE , R , and TN are 0.430, 0.3 and 0.20, respectively.

The Pareto fronts generated by IQPSO are exhibited in Fig. 3. As a result, turning objectives have contradictory trends. The reduction in the R leads to a higher TU (Fig. 3). Similarly, a decreased TU leads to a higher TN (Fig. 3).

The TOPSIS is utilized to select the best point among feasible solutions. The optimum values of the i , d , f , and V are 5 deg, 0.8 mm, 0.40 mm/rev., and 190 m/min, respectively. The reductions in the TE , R , and TN are 6 %, 22.3 %, and 23 %, respectively in comparison with the initial values (Table 11).

4.5 Comparisons with the Optimization Results Produced by the MOPSO

The optimum findings generated by the MOPSO of the i , d , f , and V are 29 deg, 0.30 mm, 0.40 mm/rev, and 1 m/min, respectively. The reductions in the TU , R , and TN are 6.0 %, 20.9 %, and 23.0 %, respectively, as compared to the initial values. The number of feasible solutions generated by the IQPSO and MOPSO are 426 and 28 respectively. It can be stated that the IQPSO provides better optimization results than the MOPSO.

4.6 Evaluation of the Total Turning Cost

The comprehensive model for the MC is expressed as:

$$MC = k_e TU + k_c \frac{t_c}{T_T} + k_{labor} (t_o + t_{st} + t_a + t_{tc} + t_c) + k_{labor} t_{ch} \frac{t_c}{T_T} + \frac{(k_{fp} + k_{fd})(t_o + t_{st} + t_a + t_{tc} + t_c)V_u}{T_L} + \frac{(k_{md} + k_{mr})(t_o + t_{st} + t_a + t_{tc} + t_c)}{T_m} + \frac{k_n(t_o + t_{st} + t_a + t_{tc} + t_c)}{T_W} \quad (31)$$

Table 9. Experimental coefficients for the rotary turning process

| | | | | | | | | |
|------------|----------------------------|---------------|-----------------------------|-----------------------------|--------------|-----------------------------|-------------|----------------------------|
| p_o [kW] | t_o [s] | P_{st} [kW] | t_{st} [s] | t_a [s] | t_{tc} [s] | A | α | β |
| 0.48 | 4 | 0.72 | 6 | 8 | 8 | 16.2×10^5 | 2.65 | 0.27 |
| γ | U_m [kJ/m ³] | T_L [month] | V_{in} [cm ³] | V_{ad} [cm ³] | H [%] | ρ [g/cm ³] | E_L [J/g] | U_m [kJ/m ³] |
| 0.37 | 9.16×10^3 | 1 | 8.5 | 4.5 | 5 | 0.92 | 422984 | 9.16×10^3 |

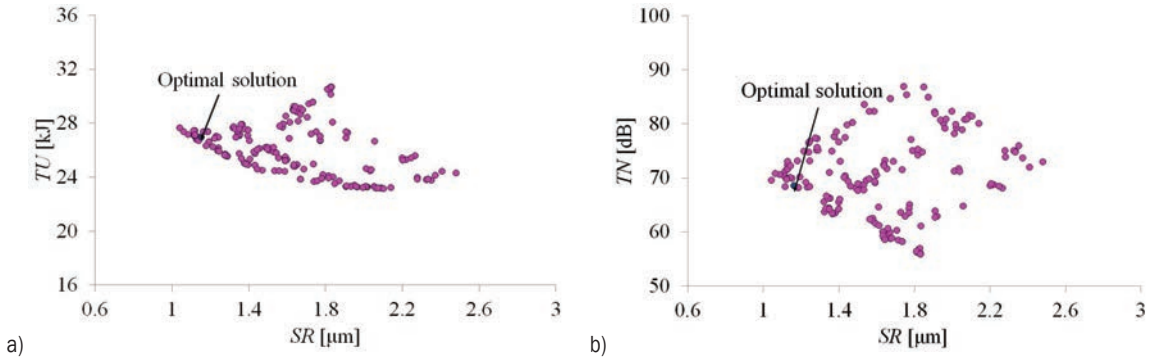


Fig. 13. Pareto fronts generated by IQPSO; a) TE and R , b) TN and R

Table 10. The values of total energy consumption, average roughness, and turning noise

| No. | i [deg] | D [mm] | f [mm/rev] | V [m/min] | TU [kJ] | R [μ m] | TN [dB] |
|-----|-----------|----------|--------------|-------------|-----------|----------------|-----------|
| 1 | 20 | 0.3 | 0.6 | 140 | 25.31 | 2.04 | 73.6 |
| 2 | 50 | 0.3 | 0.6 | 140 | 25.72 | 2.32 | 90.9 |
| 3 | 20 | 0.7 | 0.6 | 140 | 26.69 | 2.76 | 89.5 |
| 4 | 50 | 0.7 | 0.6 | 140 | 27.31 | 2.96 | 107.2 |
| 5 | 35 | 0.5 | 0.4 | 90 | 33.65 | 2.16 | 63.9 |
| 6 | 35 | 0.5 | 0.4 | 190 | 28.52 | 1.38 | 81.3 |
| 7 | 35 | 0.5 | 0.8 | 90 | 27.05 | 3.08 | 79.8 |
| 8 | 35 | 0.5 | 0.8 | 190 | 23.98 | 2.11 | 99.2 |
| 9 | 35 | 0.3 | 0.6 | 90 | 28.05 | 2.41 | 64.3 |
| 10 | 35 | 0.3 | 0.6 | 190 | 24.65 | 1.41 | 81.1 |
| 11 | 35 | 0.7 | 0.6 | 90 | 30.24 | 2.96 | 78.9 |
| 12 | 35 | 0.7 | 0.6 | 190 | 25.43 | 2.21 | 98.5 |
| 13 | 20 | 0.5 | 0.4 | 140 | 29.84 | 1.93 | 74.1 |
| 14 | 20 | 0.5 | 0.8 | 140 | 24.57 | 2.73 | 89.4 |
| 15 | 50 | 0.5 | 0.4 | 140 | 30.66 | 2.14 | 89.9 |
| 16 | 50 | 0.5 | 0.8 | 140 | 24.79 | 3.00 | 108.5 |
| 17 | 35 | 0.3 | 0.4 | 140 | 28.31 | 1.47 | 62.1 |
| 18 | 35 | 0.3 | 0.8 | 140 | 23.33 | 2.31 | 79.7 |
| 19 | 35 | 0.7 | 0.4 | 140 | 30.38 | 2.16 | 78.8 |
| 20 | 35 | 0.7 | 0.8 | 140 | 24.21 | 2.98 | 95.3 |
| 21 | 20 | 0.5 | 0.6 | 90 | 29.73 | 2.83 | 74.3 |
| 22 | 20 | 0.5 | 0.6 | 190 | 25.75 | 1.87 | 92.8 |
| 23 | 50 | 0.5 | 0.6 | 90 | 30.37 | 2.98 | 92.1 |
| 24 | 50 | 0.5 | 0.6 | 190 | 26.14 | 2.20 | 109.9 |
| 25 | 35 | 0.5 | 0.6 | 140 | 25.48 | 2.17 | 80.5 |
| 26 | 35 | 0.3 | 0.4 | 190 | 27.77 | 1.03 | 71.1 |

where k_e, k_c, k_{labr} are the costs of energy, tool, and labour, respectively. V_u is the lubricant volume. k_{fp} and k_{fd} present the cost for the lubricant preparation

and disposal, respectively. $k_{md}, k_{mr},$ and T_m are the cost of the degradation and remanufacturing for the lathe, respectively. T_m is the service life of the machine. k_n

Table 11. The optimality produced by the IQPSO and MOPSO

| Method | i [deg] | d [mm] | f [mm/rev] | V [m/min] | TU [kJ] | R [μ m] | TN [dB] | S_i |
|--------------------------|-----------|----------|--------------|-------------|-----------|----------------|-----------|--------|
| Initial values | 50 | 0.30 | 0.40 | 140 | 28.89 | 1.48 | 89.5 | |
| Optimal values by IQPSO | 35 | 0.30 | 0.40 | 190 | 26.95 | 1.15 | 68.5 | 0.8624 |
| Reductions by IQPSO [%] | | | | | 6.7 | 22.3 | 23.5 | |
| Optimal values by MOPSO | 29 | 0.30 | 0.40 | 172 | 27.08 | 1.17 | 68.9 | |
| Improvement by MOPSO [%] | | | | | 6.0 | 20.9 | 23.0 | |

Table 12. Experimental coefficients for the turning cost model

| k_e [USD/kWh] | k_c [VND/piece] | k_{labour} [USD/h] | V_u [l] | k_{fp} [USD/l] | k_{fd} [USD/l] | T_L [month] | k_{md} [USD] | k_{mr} [USD] | T_m [year] | k_n [USD] |
|-----------------|-------------------|----------------------|-----------|------------------|------------------|---------------|----------------|----------------|--------------|-------------|
| 0.15 | 16.62 | 8.40 | 20 | 0.14 | 0.45 | 1 | 41244.75 | 1649.79 | 14 | 2.68 |

and T_w are the noise tax and working hours per month, respectively.

The empirical coefficients of the MC are shown in Table 2. It can be stated that, the MC is saved by 8% at the selected point (Table 3).

Table 13. Comparative values of the total cost

| Method | Optimization parameters | | | | Response |
|-----------------|-------------------------|----------|--------------|-------------|------------|
| | i [deg] | d [mm] | f [mm/rev] | V [m/min] | MC [USD] |
| Initial values | 50 | 0.30 | 0.40 | 140 | 4.91 |
| Optimal results | 35 | 0.30 | 0.40 | 190 | 4.48 |
| Reduction [%] | | | | | 8.5 |

4.7 The Contribution Analysis

The proposed cutting tool could be used in the practical rotary turning process for other hard-to-cut alloys. The new rotary turning tool could be developed based on the current device.

The empirical correlations of the performance measures could be effectively employed to forecast the total energy, turned roughness, and noise emission.

The optimizing outcomes could be used in the practical operation to improve the technological data.

The proposed turning process could be applied to produce external surfaces for other difficult-to-cut alloys.

The develop optimization approach could be applied to deal with other issues of different machining operations.

The turning expense model could be used to compute total cost.

5 CONCLUSIONS

In the current work, the TU , R , and TN of the rotary turning process were optimized, while optimal inputs

were the i , d , f , and V . The MEREC and IQPSO were utilized to select optimal outcomes. The findings are expressed as below:

- To save the TU , the low data of the i and D were used, while the highest data of the f and V were utilized. To decrease the R , the low d and f were utilized, while the high i and V were employed. For reducing the TN , the lowest process parameters could be applied.
- The TU and R models were primarily affected by the f and V , followed by the d and I , respectively. For the TN model, the V had the highest contribution, followed by the f , i , and d , respectively.
- The optimal i , d , f , and V were 35 deg, 0.30 mm, 0.40 mm/rev, and 190 m/min, respectively. The TU , R , and TN were saved 6.7%, 22.3%, and 23.5%, respectively.
- The IQPSO provided better optimization outcomes for the rotary turning process, as compared to the MOPSO.
- The MC was decreased by 8.5% at the selected point.
- The influences of rotary turning factors on the production rate and carbon emission will be explored in future works.

6 REFERENCES

- Karaguzel, U., Olgun, U., Uysal, E., Budak, E., Bakkal, M. (2015). Increasing tool life in machining of difficult-to-cut materials using nonconventional turning processes. *International Journal of Advanced Manufacturing Technology*, vol. 77, p. 1993-2004, DOI:10.1007/s00170-014-6588-7.
- Rao, T.B., Krishna, A.G., Katta, R.K., Krishna, K.R. (2015). Modeling and multi-response optimization of machining performance while turning hardened steel with self-propelled rotary tool. *Advances in Manufacturing*, vol. 3, p. 84-95, DOI:10.1007/s40436-014-0092-z.
- Teimouri, R., Amini, S., Mohagheghian, N. (2017). Experimental study and empirical analysis on effect of ultrasonic vibration

- during rotary turning of aluminum 7075 aerospace alloy. *Journal of Manufacturing Processes*, vol. 26, p. 1-12, DOI:10.1016/j.jmapro.2016.11.011.
- [4] Mohammad, L., Saeid, A., Mohsen, A. (2018). 3D FEM simulation of tool wear in ultrasonic assisted rotary turning. *Ultrasonics*, vol. 88, p. 106-114, DOI:10.1016/j.ultras.2018.03.013.
- [5] Nguyen, T.T., Duong, Q.D., Mia, M. (2020). Sustainability-based optimization of the rotary turning of the hardened steel. *Metals*, vol. 10, art. ID 939, DOI:10.3390/met10070939.
- [6] Nguyen, T.T. (2020). An energy-efficient optimization of the hard turning using rotary tool. *Neural Computing & Applications*, vol. 33, pp. 2621-2644, DOI:10.1007/s00521-020-05149-2.
- [7] Umer, U., Kishawy, H., Abidi, M.H., Mian, S.H., Moiduddin, K. (2020). Evaluation of self-propelled rotary tool in the machining of hardened steel using finite element models. *Materials*, vol. 13, no. 22, art. ID 5092, DOI:10.3390/ma13225092.
- [8] Ahmed, W., Hegab, H., Mohany, A., Kishawy, H. (2021). Analysis and optimization of machining hardened steel AISI 4140 with self-propelled rotary tools. *Materials*, vol. 14, no. 20, art. ID 6106, DOI:10.3390/ma14206106.
- [9] Nieslony, P., Krolczyk, G., Chudy, R., Wojciechowski, S., Maruda, R., Biłous, P., Lipowczyk, M., Stachowiak, L. (2020). Study on physical and technological effects of precise turning with self-propelled rotary tool. *Precision Engineering*, vol. 66, pp. 62-75, DOI:10.1016/j.precisioneng.2020.06.003.
- [10] Yujiang, L., Tao, C. (2021). Research on cutting performance in high-speed milling of TC11 titanium alloy using self-propelled rotary milling cutters. *International Journal of Advanced Manufacturing Technology*, vol. 116, p. 2125-2135, DOI:10.1007/s00170-021-07592-4.
- [11] Ahmed, W., Hegab, H., Kishawy, H., Mohany, A. (2021). Estimation of temperature in machining with self-propelled rotary tools using finite element method. *Journal of Manufacturing Processes*, vol. 61, p. 100-110, DOI:10.1016/j.jmapro.2020.10.080.
- [12] Chen, T., Wang, Y., Gao, W., Li, R. (2020). Comparative study on the cutting performance of self-propelled rotary cutters and indexable cutters in milling TC11 titanium alloy. *International Journal of Advanced Manufacturing Technology*, vol. 111, p. 2749-2758, DOI:10.1007/s00170-020-06273-y.
- [13] Ahmed, W., Hegab, H., Mohany, A., Kishawy, H. (2021). On machining hardened steel AISI 4140 with self-propelled rotary tools: experimental investigation and analysis. *International Journal of Advanced Manufacturing Technology*, vol. 113, p. 3163-3176, DOI:10.1007/s00170-021-06827-8.
- [14] Umer, U., Mian, S.H., Mohammed, M.K., Abidi, M.H., Moiduddin, K., Kishawy, H. (2022). Self-propelled rotary tools in hard turning: analysis and optimization via finite element models. *Materials*, vol. 15, no. 24, art. ID 8781, DOI:10.3390/ma15248781.
- [15] Nguyen, T.T. (2021). Analytical approach-based optimization of the actively driven rotary turning for environmental and economic metrics considering energy footprint of materials. *Neural Computing & Applications*, vol. 33, p. 11937-11950, DOI:10.1007/s00521-021-05891-1.
- [16] Nguyen, T.T., Duong, Q.D., Mia, M. (2021). Multi-response optimization of the actively driven rotary turning for energy efficiency, carbon emissions, and machining quality. *Proceedings of the Institution of Mechanical Engineers, Part B: Journal of Engineering Manufacture*, vol. 235, no. 13, p. 2155-2173, DOI:10.1177/09544054211001014.
- [17] He, W., Xue, Z., Guo, R., Chen, N., (2023). On machining K417 superalloy with sliding self-propelled rotary tools: simulation and experimental investigation. *International Journal of Advanced Manufacturing Technology*, vol. 126, p. 1669-1680, DOI:10.1007/s00170-023-11218-2.
- [18] Sampath, B., Myilsamy, S. (2021). Experimental Investigation of a cryogenically cooled oxygenmist near-dry wire-cut electrical discharge machining process. *Strojniški vestnik - Journal of Mechanical Engineering*, vol. 67, no. 6, p. 322-330, DOI:10.5545/sv-jme.2021.7161.
- [19] Ning, P., Zhao, J., Ji, S., Li, J., & Dai, H. (2021). Ultra-precision single-point diamond turning of a complex sinusoidal mesh surface using machining accuracy active control. *Strojniški vestnik - Journal of Mechanical Engineering*, vol. 67, no. 7-8, p. 343-351, DOI:10.5545/sv-jme.2021.7172.
- [20] Tzotzis, A., García-Hernández, C., Huertas-Talón, J., Kyratsis, P. (2020). 3D FE modelling of machining forces during AISI 4140 hard turning. *Strojniški vestnik - Journal of Mechanical Engineering*, vol. 66, no. 7-8, p. 467-478, DOI:10.5545/sv-jme.2020.6784.
- [21] Satheesh, C., Sevel, P., Senthil Kumar, R. (2020). Experimental Identification of optimized process parameters for FSW of AZ91Cp Mg Alloy using quadratic regression models. *Strojniški vestnik - Journal of Mechanical Engineering*, vol. 66, no. 12, p. 736-751, DOI:10.5545/sv-jme.2020.6929.
- [22] Ma, M., Xiong, W., Lian, Y., Han, D., Zhao, C., Zhang, J. (2019). Modeling and optimization for laser cladding via multi-objective quantum-behaved particle swarm optimization algorithm. *Surface and Coatings Technology*, vol. 381, art. ID 125129, DOI:10.1016/j.surfcoat.2019.125129.
- [23] Tang, M., Zhu, W., Sun, S., Xin, Y. (2023). Mathematical modeling of resource allocation for cognitive radio sensor health monitoring system using coevolutionary quantum-behaved particle swarm optimization. *Expert Systems with Applications*, vol. 228, art. ID 120388, DOI:10.1016/j.eswa.2023.120388.
- [24] Guo, F., Zhu, J., Huang, L., Li, H., Deng, J., Zhang, X., Wang, K., Liu, H., Hou, X. (2023). A modified BRDF model based on Cauchy-Lorentz distribution theory for metal and coating materials. *Photonics*, vol. 10, no. 7, art. ID 773, DOI:10.3390/photonics10070773.

A New Calculation Method for Instantaneous Efficiency and Torque Fluctuation of Spur Gears

Xin Tian¹ – Guangjian Wang^{1,*} – Yujiang Jiang²

¹ Chongqing University, State Key Laboratory of Mechanical Transmissions, China

² Chongqing University, College of Mechanical and Vehicle Engineering, China

As a critical component of the joint gearbox, spur gear pairs play a crucial role in energy conversion, limiting the performance of a collaborative robot. Accurately assessing their instantaneous efficiency and torque fluctuation is essential for developing high-precision robot joint control models. This study proposes a computational model to predict the instantaneous efficiency and torque fluctuation of spur gears under typical operating conditions. The model incorporates a torque balance model, a load distribution model, and a friction model to reflect the relationship between gear meshing position and efficiency. The instantaneous efficiency and torque fluctuation of gear pairs were compared with the Coulomb friction model with an average friction coefficient and the elastohydrodynamic lubrication model with a time-varying friction coefficient. The effect of gear contact ratio on efficiency is analysed, while the instantaneous efficiency and torque fluctuation of gears are studied under varying operating conditions. The results indicate a maximum efficiency difference of 1.86 % between the two friction coefficient models. Under specific operating conditions, the instantaneous efficiency variation of the gear pair can reach 3.34 %, and the torque fluctuation can reach 5.19 Nm. Finally, this study demonstrates the effectiveness and accuracy of the proposed method through comparative analysis.

Keywords: collaborative robot, instantaneous efficiency, torque fluctuation, friction coefficient, load distribution

Highlights

- A new model to predict instantaneous efficiency and torque fluctuation of spur gears.
- The model includes torque balance, load distribution, and friction models.
- Instantaneous efficiency of gear pairs is examined under different friction coefficient models.
- Torque fluctuation of gear pairs under different friction coefficient models.
- Gear efficiency and torque trends are analysed under varying operating conditions.

0 INTRODUCTION

Collaborative robots are widely used in manufacturing, assembly, rehabilitation, and medical treatment and have become a research hotspot in recent years. To achieve high-precision force/position control of collaborative robots, it is necessary to establish an accurate control model of the joint reducer. However, the commonly used harmonic drive has many disadvantages, such as low efficiency and stiffness, large speed and torque fluctuations, and complex hysteresis characteristics [1] to [3], which directly affect the control precision of collaborative robots. To overcome the limitations of the harmonic drive, many researchers have recently started to study the \mathbb{K} planetary joint reducer with high efficiency and stiffness to meet the high-precision force/position control requirements of collaborative robots [1] and [4] to [6]. However, these studies mainly focus on efficiency optimization design and less on the research of instantaneous efficiency characteristics. The torque fluctuation caused by instantaneous efficiency will directly affect the control performance of collaborative robots. As the basic transmission unit

of the joint reducer, the instantaneous efficiency and torque fluctuation of gear pairs have a direct effect on the stability and lifespan of collaborative robot joints. Therefore, studying the instantaneous efficiency and torque fluctuation characteristics of the gear pair is of great significance for improving the friction characteristics and control model of the joint reducer of collaborative robots.

Energy consumption has drawn much attention in recent years due to the global energy crisis and increasingly stringent environmental regulations. Therefore, improving the efficiency of transmission devices has become an important indicator for evaluating the performance of collaborative robots' joint reducers and other transmission devices in the future [5], and [7] to [9]. In order to accurately evaluate the instantaneous efficiency of planetary gear reducers, it is necessary to study the dynamic changes in the instantaneous efficiency of gear pairs at different meshing positions and contact ratios. As a basic component of planetary transmission systems, the meshing efficiency of gear pairs directly affects the performance of joint reducers in collaborative robots. For example, a 1 % increase in gear meshing

*Corr. Author's Address: Chongqing University, State Key Laboratory of Mechanical Transmissions, Chongqing, 400044, China, gjwang@cqu.edu.cn

efficiency can improve the efficiency of a compound gear train by θ % [10]. The existing literature focuses more on the average efficiency of gears. When calculating the average efficiency of gear pairs, Hön [11] introduced a loss factor based on the Coulomb friction model, considering the influence of gear geometry. Baglioni et al. [12] analysed the effects of different friction coefficient calculation models, transmission ratios, addendum modification coefficients, loads, and speeds on the average efficiency of gear pairs. Pleguezuelos et al. [13] calculated the average efficiency of gear pairs based on a load distribution model and a friction model that remained constant along the contact path and studied the effects of transmission ratio and pressure angle on efficiency. Marques et al. [14] investigated the effects of rigid and elastic load distribution models on the average efficiency of gear pairs while analysing the average power loss of gears under local and constant friction coefficients. Diez-Ibarbia et al. [15] proposed an average efficiency evaluation model for gear pairs that simultaneously considers the Coulomb friction model and load distribution and analysed the effects of addendum modification coefficient, different friction coefficient calculation formulas [16], and tooth profile modification [17] on gear efficiency. Petry-Johnson et al. [18] analysed the changing trends of the average meshing efficiency of gear transmission systems and the average efficiency of gearboxes under different speeds and load torque through experiments.

The instantaneous efficiency of a compound gear train can vary by more than ± 20 % from the average efficiency [19], while there are relatively few studies on the instantaneous efficiency of gear pairs. Cao et al. [20] found that the instantaneous efficiency variation of bevel gears can reach up to 8 %. Li and Kahraman [21] proposed a model for predicting the mechanical power loss related to a load of a gear pair based on the elastohydrodynamic lubrication (EHL) theory. The model predicts the instantaneous mechanical power loss at each tooth contact and the overall power loss at gear engagement based on the pressure and film thickness of the lubricating oil. However, this model is analytically difficult, neglects the load distribution between the teeth, and cannot be used to investigate the torque fluctuation of gear pairs. Xu et al. [22] modelled the time-varying friction coefficient (TFC) at the gear contact point to predict the mechanical power loss caused by gear friction, and analysed the effects of geometric parameters, tooth profile modifications, operating conditions, surface roughness, and lubricant performance on mechanical efficiency loss. However, they only calculated the average efficiency without

delving into the instantaneous efficiency in depth. Wang et al. [19] proposed a method for analysing instantaneous efficiency using a load distribution model. However, this method cannot accurately evaluate the instantaneous efficiency of gears and ignores the relationship between the instantaneous efficiency of gear pairs and torque fluctuation. Therefore, there is an urgent need to propose a calculation model that can accurately evaluate the instantaneous efficiency of gear pairs.

In studying the instantaneous transmission efficiency of gear pairs under constant speed and load, it is generally desirable to have a stable torque for the output side shafting [9]. The strong nonlinearity and time-varying nature of internal friction characteristics in gear pairs cause torque fluctuation not only to vary with the meshing position of the gears but also to be affected by various factors, such as operating temperature [9], [23], and [24], load torque [18], and contact surface roughness [25]. These fluctuations reduce system stability, leading to significant noise and vibration problems [26]. At present, many scholars have carried out modelling and compensation studies on the friction torque of robot harmonic reducers. Lu et al. [27] proposed a method to compensate for the torque fluctuation of a harmonic reducer by using a torque sensor. Tadese et al. [24] used a dynamic friction model that considers temperature fluctuations to predict the joint torque variations of a collaborative robot mechanical arm driven by a harmonic reducer. Although the torque fluctuation and friction model of harmonic reducers have been extensively studied, there are relatively few studies on the torque fluctuation of gear pairs. For collaborative robots employing K planetary transmissions, an in-depth investigation into their friction models and torque fluctuations is crucial for achieving precise force and position control. Therefore, studying the torque fluctuations of gear pairs is essential in enhancing the accuracy and reliability of the system. Accurately assessing torque fluctuations in gear pairs is crucial to improving the accuracy and reliability of a system.

In summary, this paper proposes a computational model for predicting the instantaneous efficiency and torque fluctuation of gear pairs, considering the torque balance at the meshing point, the load distribution between teeth, and the friction coefficient models. The instantaneous efficiency and torque fluctuation of gear pairs under the average friction coefficient (AFC) based on Coulomb friction and the TFC based on EHL are compared. Additionally, the relationship between gear instantaneous efficiency and torque fluctuation is analysed, and the influence of contact ratio on

efficiency is discussed. Compared with existing research, which mainly focuses on the influence of output torque and speed on the average efficiency of gears [12], [15] to [17], and [28], this paper not only considers load and speed conditions but also explores the influence of surface roughness and lubricating oil operating temperature on the instantaneous efficiency and torque fluctuation of gears. Finally, the effectiveness and accuracy of the proposed method were verified through comparative analysis.

The paper is organized as follows. Section 1 develops a model for calculating the instantaneous efficiency of gears based on the torque balance, load distribution model, and friction coefficient model. Section 2 presents a study on the instantaneous efficiency and torque fluctuation of gears under different friction coefficient models with given parameters (geometric parameters and operating conditions). Section 3 discusses the evaluation results of gear efficiency and torque fluctuation under four operating conditions, validating the effectiveness and accuracy of the proposed method. Section 4 is the research conclusion.

1 METHODS

1.1 Instantaneous Efficiency Model of Gears

In gear transmission, it has been found through numerous experiments and numerical analyses that load-dependent power losses are the main cause of changes in system efficiency [11], [16], [18], and [28]. In addition, losses due to sliding friction under adverse load conditions account for approximately 95 % of the losses [17]. Therefore, this paper focuses on the effect of sliding friction on the instantaneous efficiency of gears. To determine the instantaneous efficiency of gears, it is crucial to have a comprehensive understanding of the meshing process; for gears with a contact ratio between 1 and 2, they will sequentially cross the double-tooth meshing area, single-tooth meshing area, and double-tooth meshing area as they mesh in and out along the actual meshing line B_1B_2 . Fig. 1 describes the three key moments of the meshing of a pair of gear wheels with a contact ratio between 1 and 2. There are three pairs of gears involved in the entire meshing process in a single cycle from the in-mesh to the out-mesh. Fig. 1a shows gear pair 2 meshing in the double-tooth meshing area B_1B_{1pstc} while gear pair 3 meshes out in the double-tooth meshing area $B_{hpstc}B_2$. At this time, there are two meshing points on the meshing line B_1B_2 . Fig. 1b shows the situation of gear pair 2 entering the

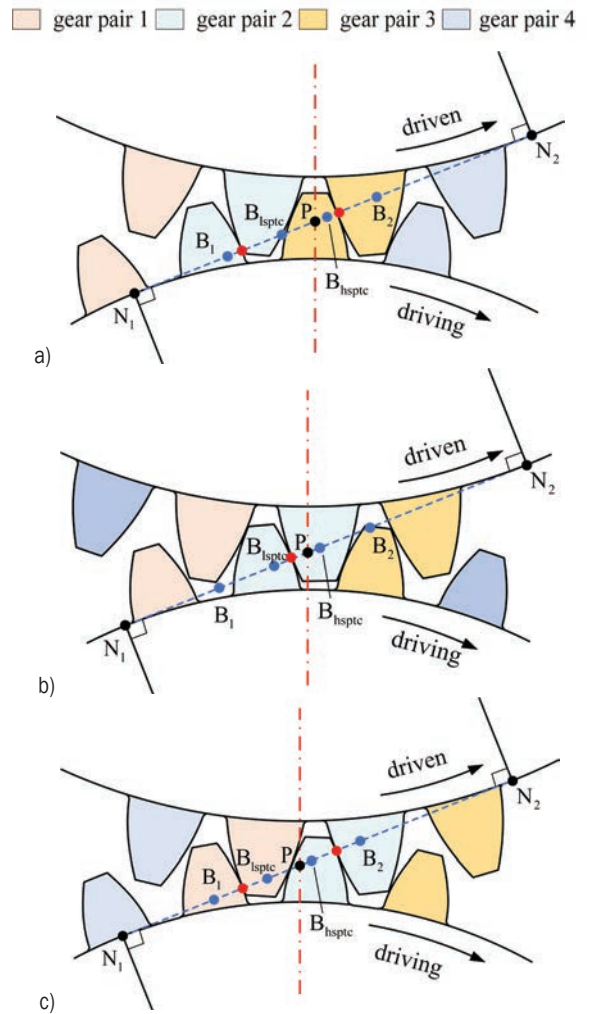


Fig. 1. Gear meshing process; a) MMGP in double-tooth meshing area B_1B_{1pstc} b) MMGP in single-tooth meshing area $B_{1pstc}B_{hpstc}$, and c) MMGP in double-tooth meshing out area $B_{hpstc}B_2$

single-tooth meshing area $B_{1pstc}B_{hpstc}$ from the double-tooth meshing area B_1B_{1pstc} . At this time, there is only one meshing point in the meshing area B_1B_2 . Fig. 1c shows gear pair 2 entering the double-tooth meshing area $B_{hpstc}B_2$ while gear pair 1 meshes in the double-tooth meshing area B_1B_{1pstc} . There are two meshing points on the meshing line B_1B_2 , and gear pair 2 gradually exits the meshing area, completing one gear meshing cycle. For ease of discussion, the gear pair that completes one gear meshing cycle on the meshing line B_1B_2 is defined as the main meshing gear pair (MMGP), such as gear pair 2 mentioned above. When the MMGP is in the double-tooth meshing area, other gear pairs participating in the meshing process are defined as secondary meshing gear pairs (SMGP). It should be noted that there are two gear pairs in the SMGP during

a single gear meshing cycle of the MMGP, such as gear 3 when gear pair 2 appears in B_1B_{1pstc} and gear pair 1 when gear pair 2 appears in $B_{hpstc}B_2$.

When calculating the instantaneous efficiency of the gear pair along the line of contact, the torque balance at different mesh positions, load distribution between teeth, and friction coefficients must be considered. The force analysis of the gear along the contact line is shown in Fig. 2, where P is the meshing node, N_1N_2 is the theoretical contact line, B_1B_2 is the actual contact line, and K_1 and K_2 are the meshing points of the gear profiles of the MMGP and SMGP during the gear transmission process, respectively. The input torque of the driving gear is defined as positive, and the output torque of the driven gear is defined as negative. The gear friction torque is not always in the same direction because the direction of the sliding velocity of the contact point changes up and down at the node, which causes the direction of the friction torque to change. In addition, in the double-tooth meshing area, the parameters such as contact force, sliding velocity, and curvature radius of different meshing points are different, so the friction coefficient and load distribution of each meshing point must be considered separately.

Based on the torque balance model at the meshing point, load distribution between teeth, and friction coefficient, this paper proposes the instantaneous efficiency calculation model for gears. The instantaneous input torque of the gear in the double-tooth meshing area at any moment is expressed as follows:

$$T_{in} = F_n R_{b1} \pm \lambda \mu_1 F_n R_{b1} \tan \alpha_{K1} \mp (1-\lambda) \mu_2 F_n R_{b1} \tan \alpha_{K2}, \quad (1)$$

where F_n is the contact force, R_{b1} is the base circle radius of the driving gear, λ is the load distribution factor (be discussed in a subsequent section), μ_1 and μ_2 are the friction coefficients of MMGP and SMGP, respectively (to be discussed in a subsequent section), α_{K1} and α_{K2} are the instantaneous meshing positions of MMGP and SMGP on the driving gear, respectively.

The output torque of the gear at any instant in the double-tooth meshing area are as follows:

$$T_{out} = -F_n R_{b2} \mp \lambda \mu_1 F_n R_{b2} \tan \beta_{K1} \pm (1-\lambda) \mu_2 F_n R_{b2} \tan \beta_{K2}, \quad (2)$$

where R_{b2} is the base circle radius of the driven wheel, β_{K1} and β_{K2} are the instantaneous meshing positions of MMGP and SMGP on the driven wheel, respectively.

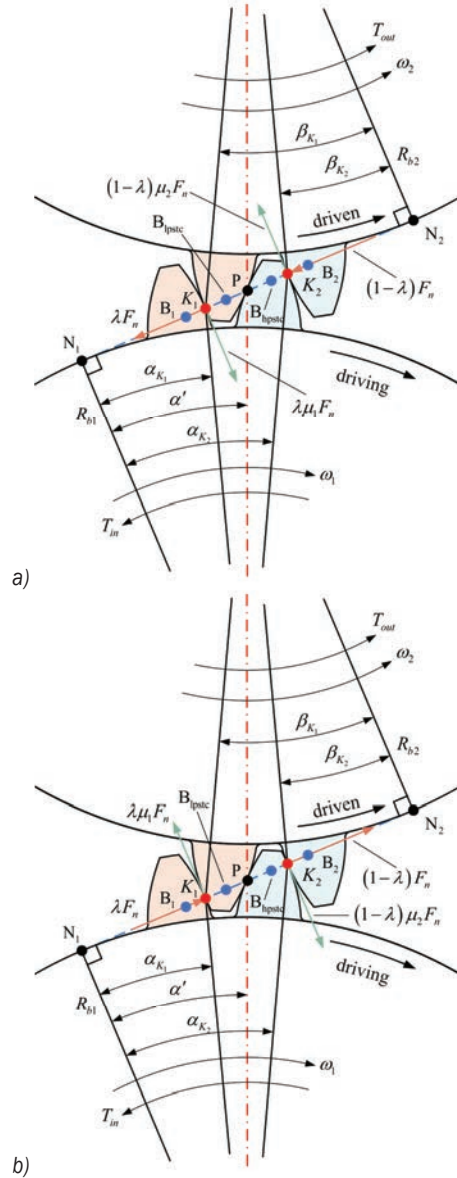


Fig. 2. Gear force analysis; a) forces and friction on a driving gear, and b) forces and friction on a driven wheel

In summary, the instantaneous efficiency calculation model of the gear is Eq. (3) :

$$\eta = -\frac{T_{out} \omega_2}{T_{in} \omega_1} = \begin{cases} \frac{1 - \lambda \mu_1 \tan(\beta_{K1}) + (1-\lambda) \mu_2 \tan(\beta_{K2})}{1 - \lambda \mu_1 \tan(\alpha_{K1}) + (1-\lambda) \mu_2 \tan(\alpha_{K2})}, & \text{when } 0 < B_1 K_1 < B_1 P \\ \frac{1 + \lambda \mu_1 \tan(\beta_{K1}) - (1-\lambda) \mu_2 \tan(\beta_{K2})}{1 + \lambda \mu_1 \tan(\alpha_{K1}) - (1-\lambda) \mu_2 \tan(\alpha_{K2})}, & \text{when } B_1 P < B_1 K_1 < B_1 B_2 \end{cases} \quad (3)$$

where $B_1K_1 = R_{b1} \tan \alpha_{K1} - N_1B_1$, ω_1 and ω_2 are the angular velocity of the driving and driven wheel. When $B_1P < B_1K_1 < B_1B_{hsptc}$, it is the instantaneous efficiency of single-tooth meshing area.

In addition to the above method of using torque balance to obtain the instantaneous efficiency of the gear, the efficiency of the gear can also be obtained through the friction power loss of the gear. The calculation of load-dependent power losses in gear is based on Coulomb friction Eq. (4):

$$F_R = \mu F_N \tag{4}$$

$$P_{loss} = F_R V_g = \mu F_N V_g, \tag{5}$$

where P_{loss} is power loss, μ is coefficient of friction, F_N is normal force, V_g is sliding speed.

Eq. (5) calculates the friction power loss of the gear only for a single-point contact [11], ignoring the alternate meshing process of single and double teeth and leading to an inaccurate evaluation of the power loss over one meshing cycle. Based on the concept presented in this section, this paper modifies Eq. (5) considering the load distribution between gear teeth at the double-tooth meshing position, as well as the friction coefficient and sliding velocity, to obtain the instantaneous friction power loss of the gear is as follows:

$$P_{loss,i} = F_{n,i} \left| \lambda_i \mu_{1,i} v_{s_{1,i}} - (1 - \lambda_i) \mu_{2,i} v_{s_{2,i}} \right|. \tag{6}$$

The calculation model of average friction loss power is as follows:

$$P_{loss} = \frac{F_{n,i}}{B_1 B_2} \left(\int_{B_1}^{B_{hsptc}} \left| \lambda_i \mu_{1,i} v_{s_{1,i}} - (1 - \lambda_i) \mu_{2,i} v_{s_{2,i}} \right| dx + \int_{B_{hsptc}}^{B_2} \left| \lambda_i \mu_{1,i} v_{s_{1,i}} - (1 - \lambda_i) \mu_{2,i} v_{s_{2,i}} \right| dx \right). \tag{7}$$

In this paper, a novel average friction loss calculation model is proposed. Eq. (7) is related not only to the gear parameters themselves but also to the sliding velocity, load, and friction coefficient at the gear meshing point. More importantly, based on the dynamic process of gear on the meshing line, the coupling relationship between different meshing points is considered, and the loss power of single and double teeth meshing is separated. Finally, the gear efficiency is Eq. (8) :

$$\eta = \frac{P_{out}}{P_{out} + P_{loss}}. \tag{8}$$

Combining Eqs. (6) and (8) , the instantaneous efficiency calculated from the equations is consistent

with the result obtained from Eq. (3) , which mutually validates the two proposed models for calculating instantaneous efficiency. To facilitate comparison and highlight the instantaneous fluctuation, the terms “average efficiency $\bar{\eta}$ ” and “efficiency fluctuation $\tilde{\eta}$ ” will be used to represent the instantaneous efficiency variation of the gear in the subsequent text, while the terms “average input torque \bar{T}_{in} ” and “torque fluctuation \tilde{T}_{in} ” will be used to replace the influence of the gear’s instantaneous input torque. Efficiency fluctuations $\tilde{\eta}$ and torque fluctuations \tilde{T}_{in} are defined as follows:

$$\tilde{\eta} = \eta_{max} - \eta_{min}, \tag{9}$$

$$\tilde{T}_{in} = T_{in_max} - T_{in_min}, \tag{10}$$

where η_{max} and T_{in_max} are the maximum value of instantaneous efficiency and instantaneous input torque, η_{min} and T_{in_min} are the minimum value of instantaneous efficiency and instantaneous input torque.

1.2 Load Distribution Coefficient Considering Hertz Contact Stiffness

From Eq. (6) , it can be seen that the factors affecting the instantaneous friction power loss of the gear include the contact force, load distribution coefficient, and friction coefficient. The load distribution between the teeth of spur gears is not distributed evenly but is closely related to the contact stiffness at the contact point. In this paper, the load distribution coefficient adopts a widely accepted simplified linear calculation model proposed in [29], as follows:

$$\lambda = \begin{cases} 0.36 + \frac{0.28}{\varepsilon_\alpha - 1} B_1 K_1, & \text{when } 0 < B_1 K_1 < B_1 B_{hsptc} \\ 1, & \text{when } B_1 B_{hsptc} < B_1 K_1 < B_1 B_{hsptc} \\ 0.36 - \frac{0.28}{\varepsilon_\alpha - 1} (B_1 K_1 - \varepsilon_\alpha), & \text{when } B_1 B_{hsptc} < B_1 K_1 < B_1 B_2 \end{cases}, \tag{11}$$

where ε_α is contact ratio, $1 \leq \varepsilon_\alpha \leq 2$.

This model uses a linear function to represent the relationship between the load distribution coefficient in two double-tooth meshing areas and the displacement of the meshing point, with a simple calculation process, a small amount of computation, and accurate results. The maximum error between the calculation results of this model and the finite element simulation results is within 6% .

1.3 Average Friction Coefficient and Time-Varying Friction Coefficient Models

The friction coefficient is an indispensable factor in evaluating the efficiency of gears, and it is a function of many variables [30], such as normal load, sliding velocity, relative curvature radius, surface roughness, oil viscosity, sliding-to-rolling ratio, and temperature. The selection of the friction coefficient greatly affects the accuracy of the gear efficiency calculation. This section will focus on the average friction coefficient and time-varying friction coefficient used in the calculation of instantaneous efficiency and torque fluctuation.

1.3.1 Method I: Average Friction Coefficient

As the coefficient of friction only changes slightly with the variable operating conditions on the path of contact, it can be assumed to be constant for approximation purposes. In this paper, the most commonly used average friction coefficient in the international standard [31] is as follows:

$$\mu_{AFC} = 0.048 \left(\frac{F_{bt} / b}{v_{\Sigma C} \rho_{redC}} \right)^{0.2} \eta_{oil}^{-0.05} Ra^{0.25} X_L. \quad (2)$$

1.3.2 Method II: Time-varying Coefficient of Friction

The friction coefficient calculation formula proposed by Xu et al. [22] under EHL conditions was adopted in this study. This formula was obtained by performing multivariate linear regression analysis on a large number of EHL predictions under various contact conditions. Compared to traditional methods, this formula is simpler to calculate, and the calculated friction coefficient based on the EHL formula matches well with the measured traction data. The calculation equation is as follows:

$$\mu_{TFC} = e^{f(SR, P_h, v_o, S)} P_h^{b_2} |SR|^{b_3} V_e^{b_6} v_o^{b_7} R^{b_8}, \quad (3)$$

$$f(SR, P_h, v_o, S) = b_1 + b_4 |SR| P_h \log_{10}(v_o) + b_5 e^{-|SR| P_h \log_{10}(v_o)} + b_9 e^S. \quad (4)$$

1.4 Calculation of Gear Contact Force Based on Torque Balance Method

When calculating the gear transmission efficiency under constant speed and load, if the friction effect is ignored, the maximum contact force of the gear can be obtained by Eq. (5). The contact force acts on the

contact point with a constant direction relative to the rotation axis of the meshing gear, the friction force acts on the tangent surface of the meshing tooth flank, and the friction coefficient is a function of the contact force. Therefore, there is a coupling relationship between the friction coefficient and the contact force, and their numerical changes will affect each other. However, Eq. (5) cannot reflect this relationship. Therefore, in efficiency calculation, the gear contact force and friction coefficient are still the focus of discussion [30]. In this paper, the balance between input torque, output torque, and friction torque at the gear meshing point is considered as the entry point. Through the torque balance method, it establishes the relationship expression between output torque, friction coefficient, and contact force, and solves and calculates the contact force of each meshing point of the gear. This is achieved through an iterative process to calculate the torque generated by contact force and friction force and make them equal to the output torque applied to the system.

$$F_{nmax} = \frac{2T_{out}}{d_2}. \quad (5)$$

For the force analysis of the driven gear under constant speed and load conditions, as shown in Fig. 2, after balancing the output torque, the magnitude of the contact force acting on the contact point is derived from Eq. (2):

$$F_n = \frac{T_{out}}{(-1 \mp \lambda \mu_1 \tan \beta_{K_1} \pm (1 - \lambda) \mu_2 \tan \beta_{K_2}) R_{b_2}}. \quad (6)$$

Since the friction coefficient μ_1 and μ_2 are function of the contact force, the contact force F_n during the gear meshing process cannot be directly obtained from this formula when the gear output torque is known. Therefore, this paper uses a numerical iteration method to solve for the contact force F_n and Eq. (6) is set as the initial value of the contact force F_n iteration.

Set the iteration termination condition as follows:

$$\left| F_{n(i+1)} - F_{n(i)} \right| \leq \varepsilon, \quad (7)$$

where $\varepsilon = 0.001$ is the convergence accuracy, and i is the iteration number.

To describe the variation of contact force along the contact line under different friction coefficients visually, the ratio of the contact force for different models to the maximum contact force obtained without considering friction is compared. The ratio of the contact forces obtained from different models after

torque balance is calculated using Eq. (8), and the result is shown in Fig. 5

$$\beta = \frac{F_{ni}}{F_{n\max}} \quad (8)$$

2 CASE OF APPLICATION

The specific calculation process is shown in Fig. 3. The parameters of the spur gear are shown in Table 1 the 75W90-A lubricating oil parameters in reference [32], and the operating conditions are shown in Table 2. Under the same operating conditions, the inter-tooth friction coefficients obtained by considering different friction coefficient calculation models and satisfying the torque balance condition from meshing to disengagement for one cycle of MMGP are shown in Fig. 4. In the single-tooth meshing area $B_{1pstc}B_{hpstc}$, the time-varying friction coefficient in Method II quickly decreases to 0 as MMGP approaches node P and increases as MMGP moves away from node P. This is a clear local variation process, while the average friction coefficient calculated by Method I in this area is almost a straight line and a constant value. In other double-tooth meshing areas, the value of the time-varying friction coefficient is significantly larger than that of the average friction coefficient. The friction coefficient of SMGP only exists in the double-tooth meshing area, which is due to the different gears involved in the meshing and disengagement processes.

Considering the friction and torque balance, the ratio of the contact forces of the MMGP along the actual contact line is shown in Fig. 5 at different meshing positions. In the double-tooth meshing area B_1B_{1pstc} of the SMGR, the contact force is proportional to the meshing distance, while in the double-tooth meshing area $B_{hpstc}B_2$, the change in contact force is opposite to the trend in the B_1B_{1pstc} meshing area and is inversely proportional to the meshing distance. At this time, MMGP is in the meshing-out process, and the load is gradually borne by SMGR. In these two double-tooth meshing areas, the contact force obtained by Method I is greater than the contact force without friction, and the contact force obtained by Method II is greater than that obtained by Method I. These three methods are almost identical in size when entering the double-tooth meshing area, and the difference between them becomes significant as the double-tooth meshing distance increases. At the points B_{1pstc} and B_{hpstc} , the contact force of the gear pair will produce a step change because the gear pair undergoes a single-double tooth meshing transition, which will cause impact and vibration at this moment.

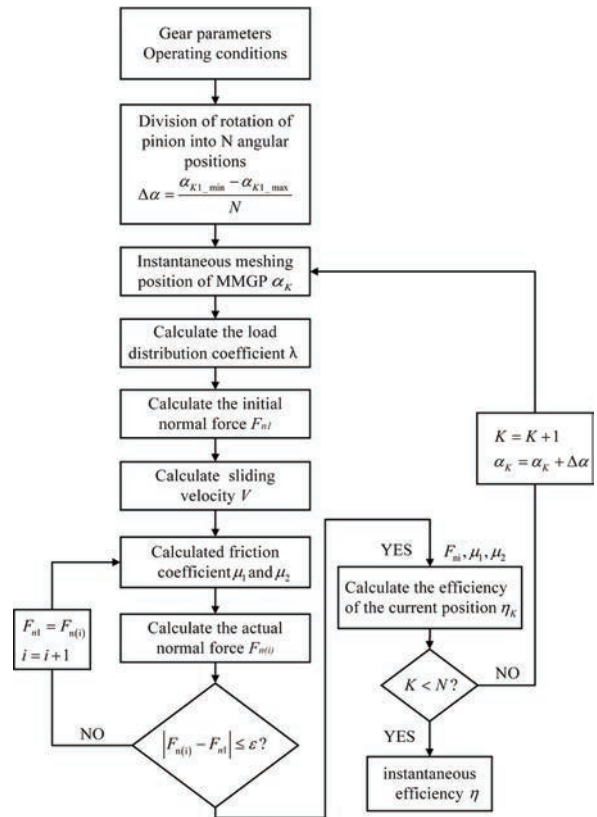


Fig. 3. The calculation flowchart of the mathematical model of the gear instantaneous efficiency model

Table 1. Pinion/gear parameters

| Parameters | |
|--------------------------|------------------------------|
| Teeth number of pinion | $Z_1 = 18$ |
| Teeth number of wheel | $Z_2 = 36$ |
| Pressure angle [°] | $\alpha = 20$ |
| Helix angle [°] | $\beta = 0$ |
| Module [mm] | $m = 3$ |
| Face width [mm] | $b = 26.7$ |
| Centre distance [mm] | $a = 81$ |
| Transverse contact ratio | $\varepsilon_\alpha = 1.611$ |

Table 2. Operating conditions

| Operating conditions | Output torque T_{out} [Nm] | Input speed n_1 [rpm] | Surface roughness Ra [μm] | Lubricant operating temperature θ_{oil} [°C] |
|----------------------|------------------------------|-------------------------|------------------------------------|---|
| case 1 | 159 | 1500 | 0.8 | 55 |
| case 2 | Δ | 1500 | 0.8 | 55 |
| case 3 | 159 | Δ | 0.8 | 55 |
| case 4 | 159 | 1500 | Δ | 55 |
| case 5 | 159 | 1500 | 0.8 | Δ |

Symbol Δ : this value will change in Section 3.

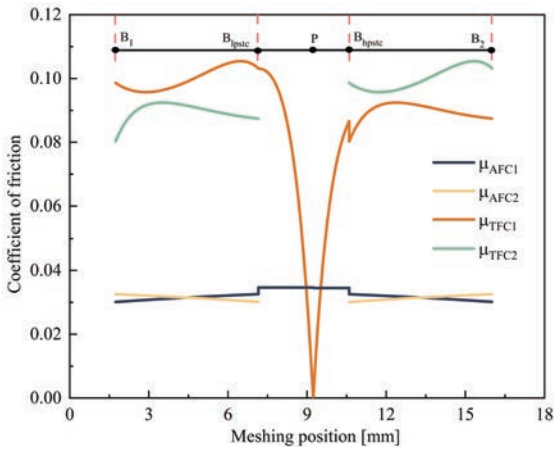


Fig. 4. The friction coefficient of the gear pair at case 1: μ_{AFC1} and μ_{TFC1} are the friction coefficients of MMGP at different meshing positions, μ_{AFC2} and μ_{TFC2} are the friction coefficients of SMGR in the double-tooth meshing area

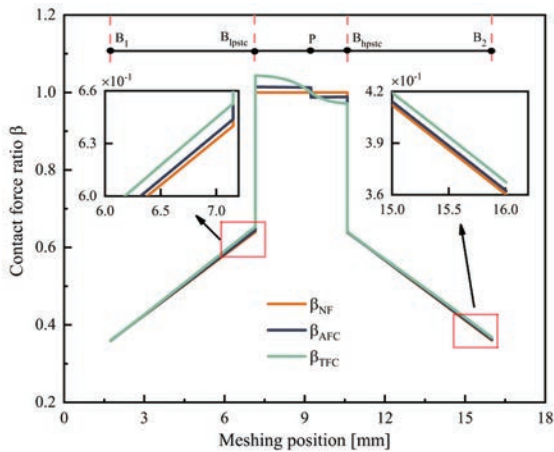


Fig. 5. The ratio of the contact force of the MMPG gear during the engagement cycle at case 1: without friction (β_{NF}), with average friction coefficient (β_{AFC}), and with time-varying friction coefficients (β_{TFC})

In the single-tooth meshing area $B_{1pstc}B_{hpstc}$, the contact force obtained by Method I undergoes a sudden change at node P. The reason for this phenomenon is that the sliding velocity direction of the meshing points on the left and right of node P changes, and the frictional force is related to the sliding velocity which leads to a change in the direction of the frictional torque before and after the node. The contact force obtained by Method II in the single-tooth meshing area will decrease smoothly with the meshing position and will not produce a jump phenomenon. The phenomenon in Fig. 5 is consistent with the previous research [15] to [17]. It can be seen that the size of the tooth surface contact force calculated by different friction coefficient calculation models is different.

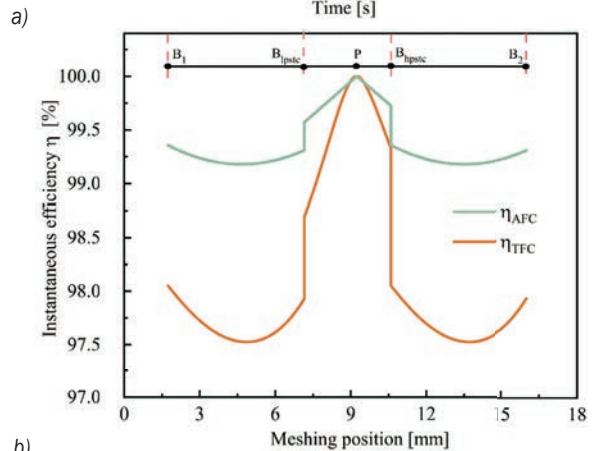
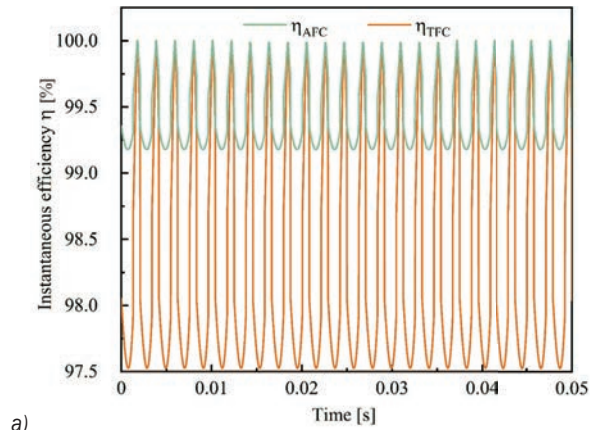


Fig. 6. Gear instantaneous efficiency at case 1: a) The variation of instantaneous efficiency with time in the gear meshing process, b) Instantaneous efficiency at one meshing cycle, η_{AFC} is the instantaneous efficiency obtained by Method I, η_{TFC} is the instantaneous efficiency obtained by Method II

The instantaneous meshing efficiency of the gear under different friction coefficient calculation methods is shown in Fig. 6. Fig. 6 represents the change in the instantaneous efficiency of the gear over time. The instantaneous meshing efficiency obtained by Method I (η_{AFC}) changes from 99.18 % to 100 %, and the fluctuation range of instantaneous efficiency is 0.8 %. The instantaneous meshing efficiency obtained by Method II (η_{TFC}) changes from 97.53 % to 100 %, and the fluctuation range of instantaneous efficiency is 2.47 %. At the same time, the value of η_{TFC} is lower than the value of η_{AFC} at the same meshing position. Fig. 5 can more clearly reflect the instantaneous meshing efficiency of the gear at any meshing point on the meshing line. Regardless of η_{AFC} or η_{TFC} , there will be a significant abrupt change in instantaneous efficiency in the process of single-to-double tooth alternation. At the double-tooth meshing area, the instantaneous efficiency is lower than that in the single-tooth meshing area. This is because the

relative sliding velocity generated by the gear in the double-tooth meshing area is greater than that in the single-tooth meshing area. The instantaneous meshing efficiency at node P is the highest. Although different methods have different friction coefficients at the nodes, the same results can be obtained. For η_{TFC} , there is no relative sliding between the driving and driven wheels at the node, and the friction coefficient is 0, so the efficiency is the highest. For η_{AFC} , although the friction coefficient at the node is not 0, the actual meshing angle at the node is the same, which produces the same result as η_{TFC} . This explains why the numerical values of the different friction coefficient models are different at the node, but their instantaneous efficiency is consistent.

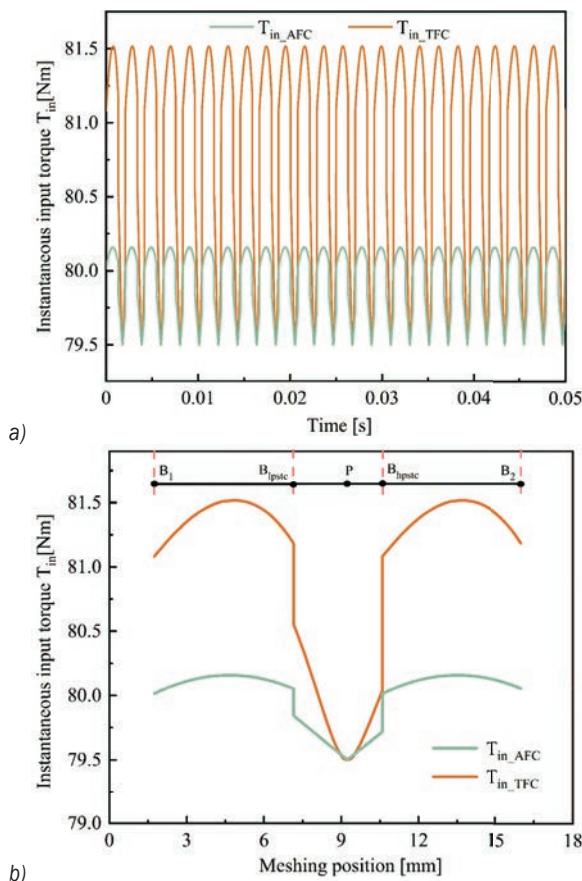


Fig. 7. Gear instantaneous input torque at case 1: a) the variation of instantaneous input torque with time in gear meshing process; b) Instantaneous input torque at one meshing cycle, T_{in_AFC} is the instantaneous input torque obtained by Method I, T_{in_TFC} is the instantaneous input torque obtained by Method II

Under constant speed and load conditions, where a constant output torque is maintained on the driven gear, the instantaneous input torque of the driving gear fluctuates due to the existence of tooth friction

and changes in the meshing position, as shown in Fig. 7. Fig. 7a shows the variation of the instantaneous input torque with time, with T_{in_AFC} changes from 79.50 Nm to 80.16 Nm with a torque fluctuation range of 0.6 Nm, and T_{in_TFC} changes from 79.50 Nm to 80.8 Nm with a torque fluctuation range of 2.02 Nm. Fig. 7b shows the variation of the instantaneous input torque with the meshing position of the gear, where the instantaneous input torque in the double-tooth meshing area is higher than that in the single-tooth meshing area, and T_{in_TFC} is higher than T_{in_AFC} at the same meshing position. Method I has a smaller torque fluctuation than Method II.

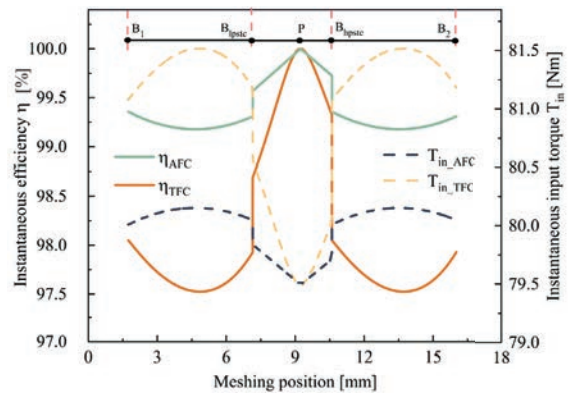


Fig. 8. The instantaneous efficiency and instantaneous input torque of the gear at case 1

Fig. 8 shows that the instantaneous efficiency of the gear decreases as the instantaneous input torque increases. The greater the fluctuation in gear efficiency, the greater the resulting torque fluctuation. The increase in input torque fluctuation not only reduces stability but also creates significant noise and vibration problems, making it difficult to model and compensate for. This also poses a challenge to the original engine. Without changing the gear ratio, increasing the proportion of single-tooth meshing in the actual meshing area, i.e., reducing the contact ratios of the gear, can improve gear transmission efficiency and reduce torque fluctuation. Fig. 9 shows the average efficiency and the efficiency fluctuation of the gear for different contact ratios, showing that decreasing the contact ratio can improve the gear efficiency. However, it should be noted that reducing the gear contact ratio also affects gear transmission capacity, load capacity, and service life. Therefore, in practical applications, a balance and selection should be made based on specific circumstances, ensuring continuous gear transmission while minimizing contact ratio to achieve maximum gear efficiency.

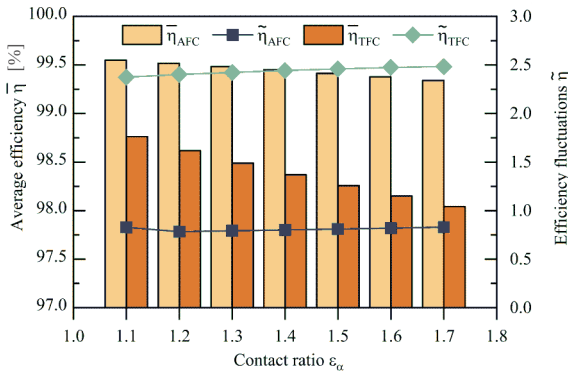


Fig. 9. Influence of gear contact ratio at case 1 on efficiency

3 RESULTS

The efficiency of a gear pair is not only related to factors such as friction coefficient and tooth load distribution but also to operating conditions. Previous research has focused on the effects of friction coefficient calculation models, gear ratios, addendum modification coefficients, loads, and speeds on gear efficiency [12], [15], and [16], neglecting the effects of gear surface roughness and lubricant operating temperature on gear efficiency and lacking exploration of the effects of different operating conditions on torque fluctuations during gear meshing. Improper

design of gear surface roughness and lubricant operating temperature can lead to more friction power loss, reducing gear meshing efficiency and increasing input torque fluctuation. This section focuses on the variability of gear efficiency and torque fluctuations under four different operating conditions: different output torque, input speed, gear surface roughness, and lubricant operating temperature.

3.1 Gear Instantaneous Efficiency under Different Operating Conditions

The meshing efficiency and efficiency fluctuation for gears under different operating conditions are shown in Fig. 10. $\bar{\eta}_{AFC}$ and $\bar{\eta}_{TFC}$ represent the average efficiency under Method I and Method II, respectively. $\tilde{\eta}_{AFC}$ and $\tilde{\eta}_{TFC}$ represent the instantaneous efficiency fluctuation under Method I and Method II, respectively. Fig. 10a shows the influence of different output torques on the average efficiency and efficiency fluctuation. The average efficiency obtained by Method I decreases as the input torque increases, while Method II shows the opposite trend. The difference in the results obtained by the two methods is mainly due to the fact that the friction coefficient calculation formula in Method I increases with the increase of the output torque, causing an increase in

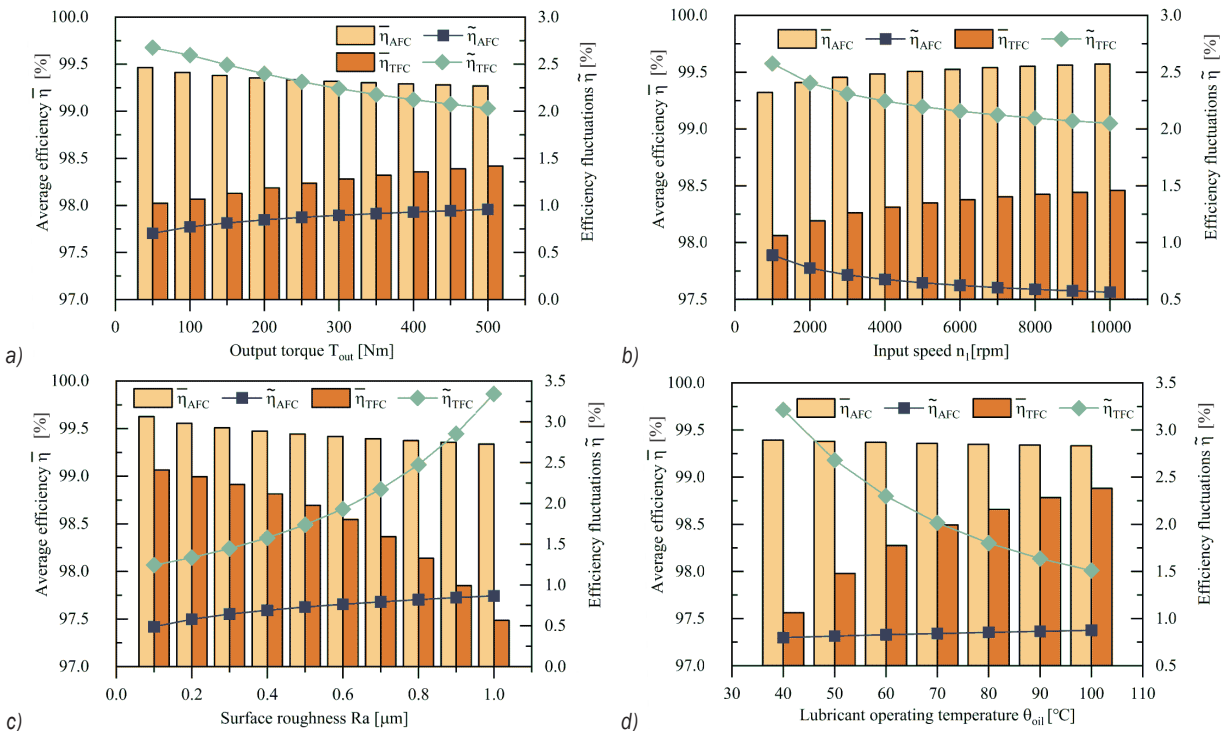


Fig. 10. Efficiency and efficiency fluctuation of gears; a) at case 2, b) at case 3, c) at case 4, and d) at case 5

frictional losses, resulting in a decrease in efficiency. However, the effect of the efficiency decrease is not significant, only 0.19 %. In contrast, the friction coefficient formula in Method II results in a decrease in instantaneous friction coefficient with the increase of the output torque, resulting in a decrease in frictional losses and an increase in efficiency. The amplitude of the efficiency fluctuation is greater than that of the efficiency obtained by Method I. The difference in gear meshing efficiency values obtained by the two methods is at most 144 %. The main reason for the difference in calculation results is that the friction coefficient at each contact point in Method II is a local variable that varies with time, while the friction coefficient in Method I is an average value along the contact line. The effect of input speed on gear efficiency is shown in Fig. 0b. When the speed increases from 000 rpm to 00 00 rpm, the efficiency obtained by both methods increases with the speed. The average efficiency under Method I and Method II increased by 0.25 % and 0.4 %, respectively. From Fig. 0c , gear efficiency decreases with increasing surface roughness, by 0.29 % for Method I and 1.59 % for Method II. This indicates that the TFC is highly sensitive to surface roughness, because as the roughness increases, the formation of the lubricating

oil film in the gear contact area becomes difficult, leading to an increase in friction losses and a decrease in efficiency. From Fig. 0d, with the increase in lubricating oil temperature, the gear efficiency of Method I decreases by 0.06 %, and the gear efficiency of Method II increases by 13 %. The result shows that the AFC is not sensitive to lubricant operating temperature, which is consistent with the results obtained in [33]. When the oil temperature increases, the viscosity of the lubricant decreases, which significantly improves efficiency. However, in Method II, when the oil temperature rises, the viscosity of the lubricant decreases and the efficiency improves significantly. Therefore, in gear design, it is necessary to select a reasonable operating temperature range for the lubricant according to the actual operating conditions, to fully utilize the properties of the lubricant, reduce the frictional power loss of gears, and improve the efficiency of the robot joint reducer.

3.2 Gear Instantaneous Input Torque Under Different Operating Conditions

In this section, the input torque fluctuations due to instantaneous efficiency fluctuations are discussed under constant load torque conditions. Fig. 1a shows

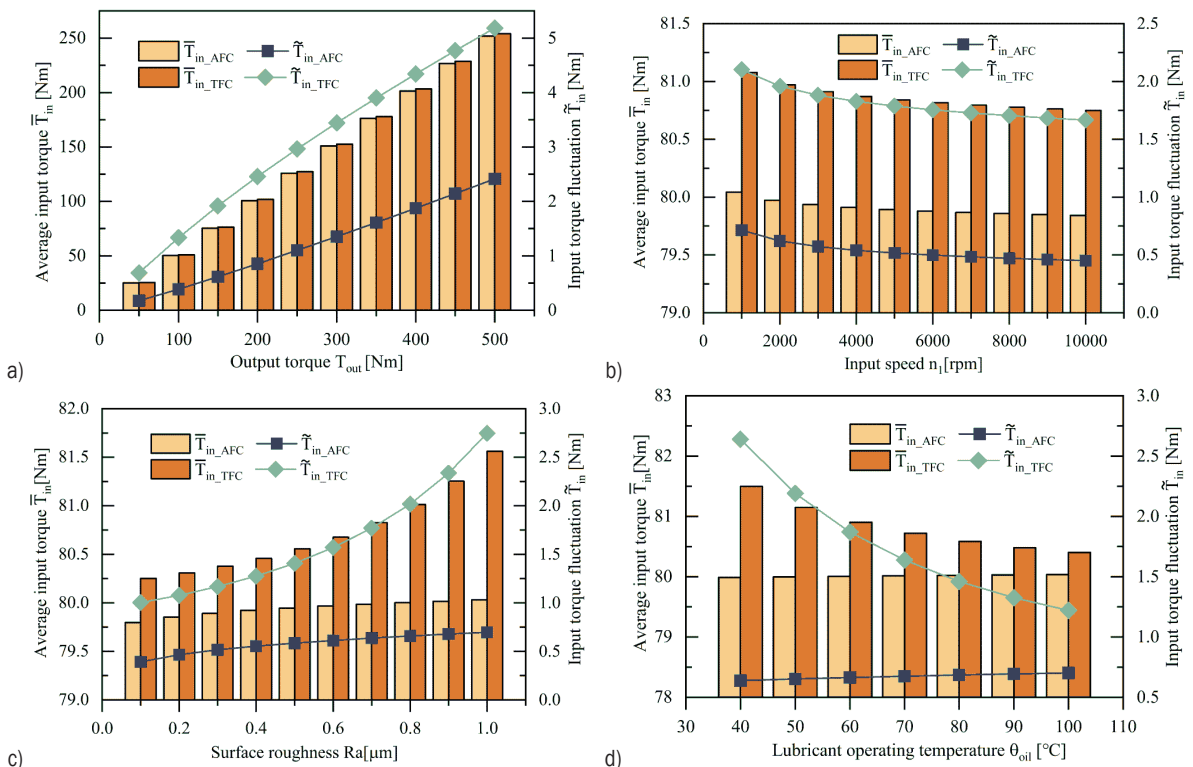


Fig. 11. Input torque and torque fluctuation of gears; a) at case 2, b) at case 3, c) at case 4, and d) at case 5

the influence of different output torques on the input torque fluctuations of the gear. T_{in_AFC} and T_{in_TFC} represent the average input torque under Method I and Method II respectively. \tilde{T}_{in_AFC} and \tilde{T}_{in_TFC} represent the instantaneous torque fluctuation under Method I and Method II, respectively. It can be seen that when the output torque increases, the torque fluctuation will increase with the increase of output torque, whether the AFC or the TFC is used. Therefore, it is necessary to choose a suitable output torque range according to the actual operating conditions in gear design, to reduce the torque power loss and improve the working smoothly of the robot joint reducer. As Fig. 1b shows, increasing the rpm from 000 rpm to 000 rpm reduced torque fluctuation by 3 % and 20 % for Method I and Method II, respectively. Fig. 1d shows that gear input torque fluctuation increases with surface roughness, especially under EHL conditions. Therefore, in design, it is necessary to ensure the smoothness of the gear contact surface as much as possible to promote the formation of oil film on the meshing surface and reduce the torque fluctuation during gear meshing. From Fig. 1d, as the lubricating oil temperature increases from 40 °C to 00 °C, the gear input torque fluctuation of Method I increases from 0.6 Nm to 0.0 Nm, and the gear input torque fluctuation of Method II decreases from 2.3 Nm to 22 Nm. Under EHL conditions, the lubricating oil operating temperature is one of the important factors affecting gear efficiency and torque fluctuation. As the temperature rises, the viscosity of the lubricating oil decreases, which can reduce the viscous resistance of the oil and improve the meshing efficiency of the gear, thereby reducing the input torque fluctuation.

Through the analysis of gear efficiency and torque fluctuation under the same operating conditions in Figs. 0b and 1b, Figs. 0c and 1c, Figs. 0d and 1d, it was found that regardless of using Method I or Method II, the average input torque of the gear will decrease as the average efficiency increases. At the same time, the input torque fluctuation of the gear increases with the increase of efficiency fluctuation. Therefore, studying the laws of gear efficiency and torque fluctuation is conducive to establishing a more accurate friction model and torque fluctuation compensation method for the joint reducer of collaborative robots.

4 DISCUSSION

The gear transmission efficiency and torque fluctuation are influenced by various factors,

including gear output torque, input speed, tooth surface roughness, and temperature, among which the friction coefficient has the greatest impact. In Method I, decreasing the output torque and gear roughness and increasing the input speed can improve gear efficiency, with roughness and speed having the greatest influence on efficiency, while lubricating oil temperature has little effect. In Method II, increasing the output torque, rotational speed, and lubricating oil temperature, and decreasing gear roughness can enhance gear efficiency, with suitable roughness and lubricating oil temperature contributing to around 1.5 % efficiency improvement. The average efficiency calculated by Method I and Method II differs by a maximum of 3 %. Under case 4, the instantaneous efficiency variation of the gear can reach 3 %. Regarding the input torque fluctuation, both Method I and Method II can reduce the torque fluctuation amplitude by lowering the output torque, and the gear surface roughness, and increasing the speed, resulting in smoother gear operation. In addition, in Method II, raising the lubricating oil temperature can reduce torque fluctuation by 3 %. Under case 2, the torque fluctuation of the gear can reach 5.19 Nm. Method I assumes a constant friction coefficient along the meshing line, neglecting the influence of lubricating oil temperature, and is often used to calculate the average efficiency of gears or roughly evaluate gear performance in spur gear transmission design. The friction coefficient of Method II varies along the meshing line and is based on the instantaneous efficiency calculation model presented in this study, so the combination of the two provides a good evaluation of the real-time efficiency at each meshing position in the spur gear pair. For an accurate calculation of the instantaneous efficiency of the gear, the time-varying friction coefficient is recommended in this study.

To evaluate the accuracy of the calculation method proposed in this paper, the numerical results obtained by the present method were compared with those reported in previous studies under the same conditions as described in the reference [15]. Table 3 and Fig. 2 presents the factors considered and the corresponding results from the efficiency calculation models described in the literature. The comparison showed that the average efficiency calculated using the present method I was consistent with the results reported by Hön [11] and Diez-Ibarbia et al. [15], with a difference of only 0.01 %. This can be attributed to the fact that the present study did not treat the friction coefficient as a constant but allowed it to vary with the changing contact conditions at different mesh positions, as shown in Fig. 4. Through comparative

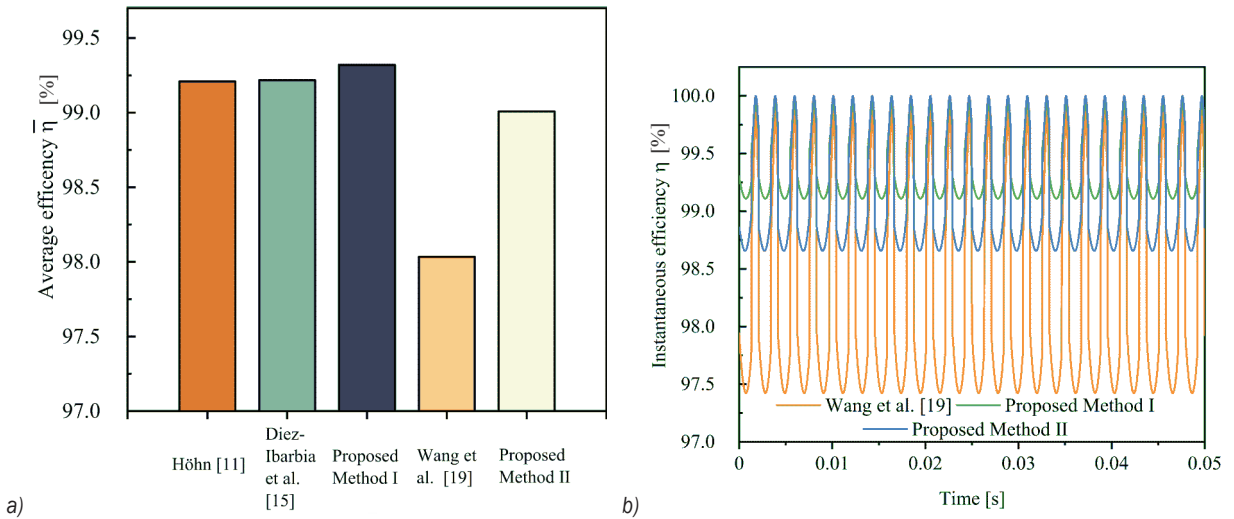


Fig. 12. Gear efficiency comparison; a) average efficiency under different methods, and b) instantaneous efficiency under different methods

Table 3. Comparison of results between different methods under the same conditions

| Method | Instantaneous efficiency | Average efficiency | Method I | Method II | Load distribution | Torque balance | $\bar{\eta}$ [%] |
|--------------------------|--------------------------|--------------------|----------|-----------|-------------------|----------------|------------------|
| Höhn [11] | | ✓ | ✓ | | ✓ | | 99.21 |
| Diez-Ibarbia et al. [15] | | ✓ | ✓ | | ✓ | | 99.22 |
| Proposed Method I | ✓ | | ✓ | | ✓ | ✓ | 99.32 |
| Wang et al. [19] | ✓ | | | | ✓ | | 98.03 |
| Proposed Method II | ✓ | | | ✓ | ✓ | ✓ | 99.01 |

symbol ✓: the method has this characteristic.

analysis, the effectiveness and accuracy of the proposed method in this paper have been verified. This paper proposes a more accurate calculation model for the instantaneous efficiency of gear pairs compared to the model proposed in reference [19], by considering the meshing position, load distribution, and both average and time-varying friction coefficient models of the gear pair.

5 CONCLUSIONS

In this paper, through the analysis of the meshing characteristics of the external meshing gear pair, a numerical calculation model for the instantaneous efficiency of the gear is established under the comprehensive consideration of the friction coefficient model, the load distribution model between the teeth and the torque balance of the meshing point. This model can calculate the instantaneous efficiency of the gear and its corresponding input torque fluctuations. Then, two different friction coefficient models are used to compare the change laws of gear instantaneous efficiency and instantaneous input torque along the meshing position under the same

operating conditions, and also studies the changing law of gear efficiency and efficiency fluctuation, input torque and input torque fluctuation under different load, speed, roughness, and temperature conditions. The following conclusions can be drawn:

- The instantaneous efficiency of gears in the double-tooth meshing area is lower than that in the single-tooth meshing area. Ensuring continuous and stable transmission of gears, the gear transmission efficiency can be improved by reducing the degree of contact ratio.
- Different friction coefficient models have a significant impact on the efficiency and efficiency fluctuation of gears. The efficiency calculated using the time-varying friction coefficient model is lower than that calculated using the average friction coefficient model, and the maximum difference between the two is 1.8 %. In contrast, the value of the torque fluctuation under the average friction coefficient is smaller than that under the time-varying friction coefficient.
- The instantaneous efficiency of the gear increases and the instantaneous input torque decreases under constant load. The gear efficiency

fluctuation increases, and the torque fluctuation at the input end also increases. Under specific operating conditions, the gear pair's instantaneous efficiency variation can reach 3%, and the torque fluctuation can reach 5.19 Nm.

- Increasing the input speed, raising the operating temperature of the lubricating oil, and reducing the surface roughness of the gear can improve the gear transmission efficiency and reduce the torque fluctuation during meshing. In addition, an increase in output torque will increase the torque fluctuation.

This paper presents numerical calculations of the instantaneous efficiency and torque fluctuation of an external meshing gear pair using theoretical analysis. Some of the computed results are consistent with previous studies. However, the presented model only considered the instantaneous efficiency and torque fluctuation of gears under sliding friction, while neglecting the effects of rolling friction losses and non-load-related losses on gear efficiency and torque fluctuation. In addition, the precision and manufacturing errors of gear are also ignored. Therefore, experimental verification of the model is still necessary in future research. Additionally, the development of a model for the instantaneous efficiency and torque fluctuation of a cooperative robot joint reducer composed of gear pairs will be the focus of our future research.

6 ACKNOWLEDGEMENTS

This work is supported by the National Natural Science Foundation of China (Grant No. 92048201). The authors thank the reviewers for their valuable comments on the manuscript.

7 REFERENCES

- [1] Akiyama, N., Fujimoto, Y. (2019). Highly efficient 2K-H compound planetary reduction gearbox using balancer. *45th Annual Conference of the IEEE Industrial Electronics Society*, p. 669-674, DOI:10.1109/IECON.2019.8926722.
- [2] Kanai, Y., Fujimoto, Y. (2019). Performance analysis of torque-sensorless assist control of a powered exoskeleton using highly back-drivable actuators. *IEEE 17th International Conference on Industrial Informatics*, p. 577-582, DOI:10.1109/INDIN41052.2019.8972220.
- [3] Zhang, H., Ahmad, S., Liu, G. (2015). Modeling of torsional compliance and hysteresis behaviors in harmonic drives. *IEEE/ASME Transactions on Mechatronics*, vol. 20, no. 1, p. 178-185, DOI:10.1109/tmech.2014.2311382.
- [4] Matsuki, H., Nagano, K., Fujimoto, Y. (2019). Bilateral drive gear-a highly backdrivable reduction gearbox for robotic actuators. *IEEE/ASME Transactions on Mechatronics*, vol. 24, no. 6, p. 2661-2673, DOI:10.1109/tmech.2019.2946403.
- [5] Brassitos, E., Kong, Q., Mavroidis, C., Weinberg, B. (2014). Design improvements and design methodology for the gear bearing drive: A compact, powerful and cost-effective robotic actuator. *Proceedings of the ASME 2014 International Design Engineering Technical Conferences and Computers and Information in Engineering Conference*, vol. 5B: 38th Mechanisms and Robotics Conference, p. 17-20, DOI:10.1115/DETC2014-35377.
- [6] Kanai, Y., Fujimoto, Y. (2018). Torque-sensorless control for a powered exoskeleton using highly back-drivable actuators. *44th Annual Conference of the IEEE Industrial Electronics Society*, p. 5116-5121, DOI:10.1109/IECON.2018.8591255.
- [7] Pham, A.-D., Ahn, H.-J. (2018). High precision reducers for industrial robots driving 4th industrial revolution: State of arts, analysis, design, performance evaluation and perspective. *International Journal of Precision Engineering and Manufacturing-Green Technology*, vol. 5, p. 519-533, DOI:10.1007/s40684-018-0058-x.
- [8] Kobuse, D., Fujimoto, Y. (2016). Efficiency optimization of high-reduction-ratio planetary gears for very high power density actuators. *IEEE 25th International Symposium on Industrial Electronics*, p. 1240-1245, DOI:10.1109/ISIE.2016.7745072.
- [9] Qiu, Z., Xue, J. (2021). Review of performance testing of high precision reducers for industrial robots. *Measurement*. vol. 183, art. ID 109794, DOI:10.1016/j.measurement.2021.109794.
- [10] Brassitos, E., Jalili, N. (2020). Dynamics of integrated planetary geared bearings. *Journal of Vibration and Control*, vol. 26, no. 7-8, p. 565-580, DOI:10.1177/1077546319889848.
- [11] Höhn, B.-R. (2010). Improvements on noise reduction and efficiency of gears. *Meccanica*, vol. 45, p. 425-437, DOI:10.1007/s11012-009-9251-x.
- [12] Baglioni, S. Cianetti, F., Landi, L. (2012). Influence of the addendum modification on spur gear efficiency. *Mechanism and Machine Theory*, vol. 49, p. 216-233, DOI:10.1016/j.mechmachtheory.2011.10.007.
- [13] Pleguezuelos, M., Pedrero, J.I., Sánchez, M.B. (2013). Analytical expressions of the efficiency of standard and high contact ratio involute spur gears. *Mathematical Problems in Engineering*, vol. 2013, Art. ID 142849, DOI:10.1155/2013/142849.
- [14] Marques, P.M.T., Martins, R.C., Seabra, J.H.O. (2016). Power loss and load distribution models including frictional effects for spur and helical gears. *Mechanism and Machine Theory*, vol. 96, p. 1-25, DOI:10.1016/j.mechmachtheory.2015.09.005.
- [15] Diez-Ibarbia, A., del Rincon, A.F., Iglesias, M., de-Juan, A., Garcia, P., Viadero, F. (2016). Efficiency analysis of spur gears with a shifting profile. *Meccanica*, vol. 51, p. 707-723, DOI:10.1007/s11012-015-0209-x.
- [16] Diez-Ibarbia, A., Fernandez-Del-Rincon, A., Garcia, P., De-Juan, A., Iglesias, M., Viadero, F. (2018). Assessment of load dependent friction coefficients and their influence on spur gears efficiency. *Meccanica*, vol. 53, p. 425-445, DOI:10.1007/s11012-017-0736-8.
- [17] Diez-Ibarbia, A., Fernandez-del-Rincon, A., de-Juan, A., Iglesias, M., Garcia, P., Viadero, F. (2018). Frictional power

- losses on spur gears with tip reliefs. The friction coefficient role. *Mechanism and Machine Theory*, vol. 121, p. 15-27, DOI:10.1016/j.mechmachtheory.2017.10.003.
- [18] Petry-Johnson, T.T., Kahraman, A., Anderson, N.E., Chase, D.R. (2008). An experimental investigation of spur gear efficiency. *Journal of Mechanical Design*, vol. 130, no. 6, art. ID 0626101, DOI:10.1115/1.2898876.
- [19] Wang, A., Gitnes, S., El-Bayoumy, L. (2011). The instantaneous efficiency of epicyclic gears in flight control systems. *Journal of Mechanical Design*, vol. 133, no. 5, art. ID 051008, DOI:10.1115/1.4004001.
- [20] Cao, W., He, T., Pu, W., Xiao, K. (2021). Dynamics of lubricated spiral bevel gears under different contact paths. *Friction*, vol. 10, p. 247-267, DOI: 10.1007/s40544-020-0477-x.
- [21] Li, S., Kahraman, A. (2010). Prediction of spur gear mechanical power losses using a transient elastohydrodynamic lubrication model. *Tribology Transactions*, vol. 53, no. 4, p. 554-563, DOI:10.1080/10402000903502279.
- [22] Xu, H., Kahraman, A., Anderson, N.E., Maddock, D.G. (2007). Prediction of mechanical efficiency of parallel-axis gear pairs. *Journal of Mechanical Design*, vol. 129, no. 1, p. 58-68, DOI:10.1115/1.2359478.
- [23] Raviola, A., Guida, R., De Martin, A., Pastorelli, S., Mauro, S., Sorli, M. (2021). Effects of temperature and mounting configuration on the dynamic parameters identification of industrial robots. *Robotics*, vol. 10, no. 3, art. ID 83, DOI:10.3390/robotics10030083.
- [24] Tadese, M., Pico, N., Seo, S., Moon, H. (2022). A two-step method for dynamic parameter identification of Indy7 collaborative robot manipulator. *Sensors*, vol. 22, no. 24, art. ID 9708, DOI:10.3390/s22249708.
- [25] Okorn, I., Nagode, M., Klemenc, J. (2021). Operating Performance of External Non-Involute Spur and Helical gears: A review. *Strojniški vestnik - Journal of Mechanical Engineering*, vol. 67, no. 5, p. 256-271, DOI:10.5545/sv-jme.2020.7094.
- [26] Piccoli, M., Yim, M. (2016). Anticogging: Torque ripple suppression, modeling, and parameter selection. *The International Journal of Robot.* vol. 35, no. 1-3, p. 148-160. DOI:10.1177/0278364915599045.
- [27] Lu, Y., Lin, S., Hauschild, M., Hirzinger, G. (2012). A torque-ripple compensation scheme for harmonic drive systems. *Electrical Engineering*, vol. 95, p. 357-365, DOI:10.1007/s00202-012-0264-4.
- [28] Fernandes, C.M.C.G., Marques, P.M.T., Martins, R.C., Seabra, J.H.O. (2015). Gearbox power loss. Part II: Friction losses in gears. *Tribology International*, vol. 88, p. 309-316, DOI:10.1016/j.triboint.2014.12.004.
- [29] Sánchez, M.B., Pleguezuelos, M., Pedrero, J.I. (2017). Approximate equations for the meshing stiffness and the load sharing ratio of spur gears including hertzian effects. *Mechanism and Machine Theory*, vol. 109, p. 231-249, DOI:10.1016/j.mechmachtheory.2016.11.014.
- [30] Miler, D., Hoić, M. (2021). Optimisation of cylindrical gear pairs: A review. *Mechanism and Machine Theory*, vol. 156, art. ID 104156, DOI:10.1016/j.mechmachtheory.2020.104156.
- [31] ISO/TR 14179-2:2001. Gears - Thermal capacity - Part 2: Thermal load carrying capacity. International Standard Organization, Geneva
- [32] Hammami, M., Martins, R., Abbes, M.S., Haddar, M., Seabra, J. (2017). Axle gear oils: Tribological characterization under full film lubrication. *Tribology International*, vol. 106, p. 109-122, DOI:10.1016/j.triboint.2016.05.051.
- [33] Fernandes, C.M.C.G., Martins, R.C., Seabra, J.H.O. (2016). Coefficient of friction equation for gears based on a modified Hersey parameter. *Tribology International*, vol. 101, p. 204-217, DOI:10.1016/j.triboint.2016.03.02.

Investigation of the Titanium Alloy Turning Process with Prime A Tools under High-Pressure Cooling Conditions

Grzegorz Struzikiewicz*

AGH University of Science and Technology, Poland

When turning titanium alloys, it is difficult to ensure the required quality with maximum machining efficiency. A typical problem in the turning process of titanium alloys is to achieve effective breaking and removal of chips from the machining zone. The combination of the new construction of cutting tools and machining methods in the machining of titanium alloys increases the efficiency of the machining. For this reason, the use of tools typical for the Prime Turning method in combination with the high-pressure cooling (HPC) method was analysed. The longitudinal turning of the Ti6Al4V ELI titanium alloy was performed using Sandvik Coromant grade 1115 carbide tools. An increase in the pressure of the cutting fluid to $p = 70$ bar was used. Measurements of the components of the total cutting force for finishing machining with variable cutting parameters in the range of: feed rates $f = \langle 0.1; 0.4 \rangle$ mm/rev, cutting depth $a_p = \langle 0.25; 1.0 \rangle$ mm and cutting speed $v_c = \langle 40; 80 \rangle$ m/min were performed. It has been shown that the values of cutting force are mainly dependent on the feed and the depth of cut. An analysis of the forms of chips obtained is presented. The dependence of the applied cutting parameters on the value of the chip breakage coefficient C_{ch} was determined. The method of searching for the maximum efficiency of the turning process was determined, taking into account the desired value of the chip breakage coefficient.

Keywords: turning, titanium alloy, cutting forces, chip form, chip breakage index

Highlights

- Using the carbide cutting insert CP-A1104-L5 and the HPC method is an effective means of improving productivity in the turning process of the Ti6Al4V ELI titanium alloy.
- The cutting parameters have a significant impact on the values of the components of the total cutting force and the chip breakage index.
- It is possible to increase the efficiency of the machining process by maintaining the required chip form.

0 INTRODUCTION

The optimization of existing titanium alloy machining processes and the use of new machining techniques enable the achievement of the expected efficiency and quality of machining at low cost [1]. This is particularly significant for the machining of expensive materials or demanding materials. Titanium alloys, next to nickel alloys and heat-resistant steels, are difficult-to-cut materials. This is due to the specific mechanical and chemical properties that characterize this group of materials [2] and [3].

Due to their high strength, corrosion resistance and inertness, titanium alloys are most often used by the automotive, aerospace, chemical and medical industries [4]. On-going research broadens knowledge in the field of machining titanium alloys. The area of research described in the literature concerns the influence of cutting parameters on the roughness of the machined surface and the determination of the value of forces or temperature in the cutting zone [5]. Another important issue is the process of breaking chips during machining and the use of calculation methods that enable the simulation of cutting processes [6] and [7]. Accelerated wear of cutting tools

due to high temperatures in the cutting zone and stress concentration at the edge of the cutting insert are also frequently analysed issues [1] and [8].

The machinability of titanium alloys can be increased as a result of the use or combination of different techniques and machining methods. For example, the use of various cooling methods in the cutting processes of titanium alloys yields measurable results. The literature describes the results of research on machining under dry cutting conditions, with minimal quantity or high pressure of the cutting fluid, as well as cryo-machining [8] to [12].

Increasing the efficiency of the titanium alloy machining process can be achieved using the high-pressure cooling (HPC) method. Currently, the pressure range recommended by cutting tool manufacturers to work with titanium alloys is 0 bar to 60 bar. This method allows faster heat dissipation and lower temperatures in the cutting zone. Compared to typical cooling, this results in a longer cutting tool life of up to 5 times. HPC machining greatly supports the chip-breaking process and chip removal outside the machining zone [4] and [10]. This is particularly important for turning and drilling processes [13].

In the case of turning titanium alloys under HPC conditions, the selection of tool materials is important. Palanisamy et al. [15] described the results of experimental studies on the machining of inserts made of cemented carbide. The authors showed that HPC machining increases tool life by almost three times compared to conventional cooling. Furthermore, they showed that the mechanical effect of the liquid jet on the chips supports the process of breaking and removing chips from the cutting zone. HPC machining has been shown to produce short, segmented chips. In turn, Ezugwu et al. [16] analysed the machinability of titanium alloys under conventional and high-pressure cooling conditions with tools made of cemented carbides and coated with various coatings. They also demonstrated reduced cutting tool wear under HPC machining conditions. Da Silva et al. [17] analysed the mechanism of tool wear during high-speed machining of titanium alloys. They showed that tool life decreased with increasing cutting speed, and increased productivity was achieved during high-pressure cooling. In turn, Stolf et al. [18] analysed the method of tool wear due to tool-chip contact conditions during HPC machining of the Ti-6Al-4V alloy. They found that the coolant pressure and the maximum wear on the flank surface are inversely proportional. This is due to the effect on the process of abrasion of heat acting on the surface of the cutting tool application. The authors also pointed out that HPC machining has a positive effect on lowering the temperature of the tool and on the chip breakage process. Kaminski and Alvelid [19] showed that high coolant pressure causes fluid to enter the slip zone, reducing friction and temperature. In addition, the high-pressure cutting fluid stream reduces the chip winding radius and shortens the contact time between the tool and the chips.

In turn, Liang et al. [20] performed Ti-6Al-4V surface integrity tests at different cooling pressures and injection positions of cutting fluid. The researchers examined three injection positions, i.e., only injection in the rake face, only in the flank face, and injection in both rake/flank face directions. They observed that compared to dry cutting and HPC conditions, surface roughness parameters were reduced during high-pressure jet-assisted machining. Masek et al. [21] analysed the influence of the direction of liquid supply to the cutting zone during polycrystalline diamond (PCD) machining. Their study showed that double cooling is strongly recommended when machining titanium alloys, both on the rake surface and on the flank surface, and the results showed that the appropriate HPC intensity was around 6 bar. This results in an increase in the efficiency of the chip-

breaking process with reduced tool wear. Çolak [22] optimized the HPC machining process using genetic algorithms due to the desired surface roughness. Surface roughness and chip breaking were selected as optimisation criteria due to their importance for the finishing turning process.

One of the recently developed concepts for increasing the efficiency of the machining process is the so-called Prime Turning method. This concept takes into account the changed geometry of the cutting tool. These cutting inserts have three edges for longitudinal, face and profiling turning. This ensures efficient use of the edges and a longer tool life. Krajčoviech et al. wrote about the use of this type of tool for steel machining [23]. The authors showed that the depth of cut has the most significant impact on the values of cutting forces.

According to a review of the literature presented, researchers investigated various HPC strategies with the common goal of reducing tool wear or increasing process efficiency. However, the impact of machining efficiency of various cutting conditions is connected with different cutting parameter values and tool geometry, methods of cutting liquid delivery, etc. Furthermore, analysis of the quality of the cutting process could be realized from different points of view. In this regard, there are still few analyses that take chip forms into account. Due to the problems described above for obtaining effective machining of titanium alloys, Ti-6Al-4V ELI alloy turning tests were carried out under conditions of feeding the cutting fluid with increased pressure and using Prime A turning tools. The experimental research plan took into account three variables, i.e., feed, depth, and cutting speed. During the experiments, the processes of cutting forces were recorded, microscopic analysis of the chip form was carried out and the chip breakage coefficient was determined. The concept of maximising machining efficiency is presented, taking into account the favourable form of the chips.

1 METHODS

The experimental research plan was developed according to the Taguchi method [24] for three variables, i.e., feed f , depth of cut a_p and cutting speed v_c . The 6 test systems were designated. For statistical analysis, every group of the experimental run was done three times, for a total of 48 trials (16×3 runs). Table 1 shows the assumed ranges of cutting data values. The values of the cutting parameters are within the range of cutting parameters recommended by the tool manufacturer for turning titanium alloys.

Table 1. The variables values in the research plan

| No. | Coded parameter | Real parameter | Value | | | |
|-----|-----------------|----------------|-------|------|------|-----|
| 1 | A | f [mm/rev] | 0.1 | 0.2 | 0.3 | 0.4 |
| 2 | B | a_p [mm] | 0.25 | 0.50 | 0.75 | 1.0 |
| 3 | C | v_c [m/min] | 40 | 80 | | |

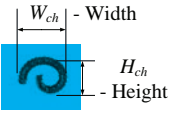
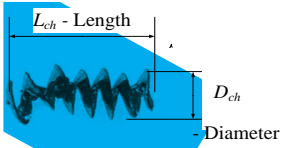
The signal-to-noise (S/N) ratio analysis strategy was adopted as “the lowest-best” according to Eq. (1) [24].

$$S / N = -10 \cdot \log \left(\frac{1}{n} \sum_{i=1}^n y_i^2 \right). \quad (1)$$

A modified classification and characteristics of the chips presented by Fang et al. [25] and Lee et al. [26] were adopted. The aim of the modification was to adapt the classification of chips to practical industrial use. In general, chips can be described using words and numbers. In practice, a typical approach is to characterize chips using language terms such as “good”, “weak”, etc.

The authors of the paper presented a concept in which there are four different types of chip shapes, i.e., arc/bulky, spiral/circular, helical/tubular and ribbon. For each chip type, two main dimensional characteristics of the chips were assigned, which in turn were converted into numerical values. These values can be used to classify and determine the chip breakage coefficient [27]. During the investigation, the analysis of the form of the chips and their classification and evaluation were carried out. Only two forms of chips obtained during machining tests were observed, i.e., arc/bulky and helical/tubular type chips. For these types of chips, the dimensional characteristics were adopted according to Table 2.

Table 2. Dimensional features of chips obtained during cutting tests

| Group | Chip index characterization |
|-----------------|---|
| Arc/Bulky |  |
| Helical/Tubular |  |

Based on the dimensions of the measured chip, the chip breakage coefficient C_{ch} was determined according to Eqs. (2) to (4). In the investigation, a

simplified method of chip classification was adopted, according to which the chip breakage index C_{ch} takes values from 0 to 1 and is described by Eq. (2). Lower C_{ch} values represent better chip breakability.

$$C_{ch} (Dim) = \begin{cases} 0.01 \cdot Dim_{ch} & \text{if } 0 < Dim_{ch} < Dim_{ch_limit2}, \\ 1 & \text{if } Dim_{ch} \geq Dim_{ch_limit2} \end{cases}, (2)$$

where

- $Dim_{chL_imit1} \leq 5$ mm; correct chips ($0 < C_{ch} \leq 0.2$);
- $Dim_{chL_imit1} > 5$ mm and $Dim_{chL_imit2} \leq 20$ mm; acceptable chips ($0.2 < C_{ch} < 1$);
- $Dim_{chL_imit2} > 20$ mm; unfavourable chips ($C_{ch} = \text{const.} = 1$).

Where Dim_{ch} were described for arc/bulky chips by Eq. (3) and for helical/tubular chips by Eq. (4):

$$Dim_{ch} = \overline{W_{ch}} + \overline{H_{ch}}, \quad (3)$$

$$Dim_{ch} = \overline{L_{ch}} + \overline{D_{ch}}. \quad (4)$$

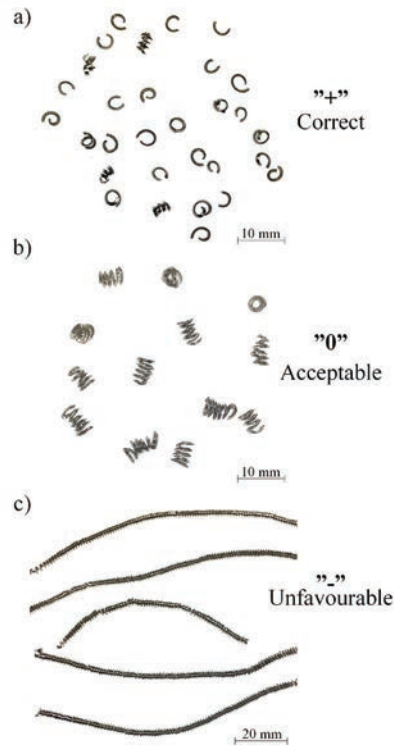


Fig. 1. Sample of chips photographs for parameters: a) $f = 0.4$ mm/rev, $a_p = 0.50$ mm, $v_c = 40$ m/min, b) $f = 0.4$ mm/rev, $a_p = 0.75$ mm, $v_c = 80$ m/min, and c) $f = 0.1$ mm/rev, $a_p = 1.00$ mm, $v_c = 40$ m/min

The main criterion for the assessment of chip form was the chip dimensions, i.e., length and height for arc chips or length and spiral diameters for tubular

chips. A three-stage assessment of the chip form was assumed, i.e., correct chips up to 5 mm, acceptable chips up to 5 mm to 20 mm and incorrect chips over 20 mm. The following markings were adopted when assessing the form of chips: “+” chips correct (good); “-” chips unfavourable (poor); “0” chips acceptable (fair). Example photographs of chips are shown in Fig. 1

2 EXPERIMENTAL

Ti6Al4V-ELI (extra low interstitials) titanium alloy contains less oxygen, nitrogen, carbon, and iron than a typical Ti6Al4V alloy. This improves the ductility and resistance to cracking of the material, which means that this alloy is used in dentistry and medicine, for example, for orthopaedic implants [27]. The material to be processed was a shaft with a diameter of $D_c = 6$ mm. The mechanical properties of the alloy were as follows: tensile strength = 902 MPa, hardness = 29 HRc, elongation 13 %, Yield strength_{0.2%} = 835 MPa. Chemical composition was: Al 6.2 %, V 4.3 %, Fe 0.05 %, O 0.1 %, N 0.01 %, C < 0.01 %, H 0.003 % and Ti remainder.

The longitudinal turning process was analysed under conditions of coolant supply with increased pressure. The cutting fluid was fed to the rake face by the cutting tool through the tool holder nozzle.

In cutting tests, cutting inserts of type Prime A turning (Fig. 2) type CP-A10 4-L5 grade 115 and the tool holder QS-CP-0A R-2020-1C from Sandvik Coromant were used. The value of the corner radius of the cutting insert was $r_c = 0.4$ mm. A new cutting

edge was used in each machining test. The impact of cutting-edge wear was not analysed. A constant cutting liquid pressure of $p = 0$ bar was used, and Blaser's 0 % Blasocut 2000 universal emulsion was used as the cutting fluid. The selected cutting parameters were within the range of finishing titanium alloys. The tests were carried out on a conventional lathe, equipped with a 0 bar pressure high-pressure plunger pump.

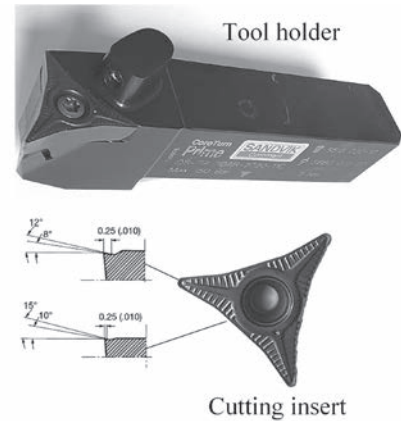


Fig. 2. Cutting tool Prime A

During the research, measurements of the components of the total cutting force and microscopic measurements of the chip dimensions were carried out. To record and analyse the components of the cutting forces, a measuring track system consisting of a 9257B dynamometer and a Kistler 5070B amplifier was used. Chip analysis was carried out using a Keyence VHX-000 type B microscope with dedicated measurement software.

Table 3. Test results for measurements of cutting force F_c and chip breakage coefficient C_{ch}

| No | A | B | C | f [mm/rev] | a_p [mm] | v_c [m/min] | $F_{cm\ ean}$ [N] | S/N_{Fc} | $C_{chm\ ean}$ | S/N_{Cch} |
|----|---|---|---|--------------|------------|---------------|-------------------|------------|----------------|-------------|
| 1 | 1 | 1 | 1 | 0.1 | 1.00 | 40 | 255.4 | -48.2 | 1.00 | 0.0 |
| 2 | 1 | 2 | 1 | 0.1 | 0.75 | 40 | 208.7 | -46.4 | 0.17 | 15.2 |
| 3 | 1 | 3 | 2 | 0.1 | 0.50 | 80 | 140.0 | -42.9 | 0.07 | 22.9 |
| 4 | 1 | 4 | 2 | 0.1 | 0.25 | 80 | 68.2 | -36.7 | 0.05 | 26.6 |
| 5 | 2 | 1 | 1 | 0.2 | 1.00 | 40 | 462.3 | -53.3 | 0.41 | 7.5 |
| 6 | 2 | 2 | 1 | 0.2 | 0.75 | 40 | 395.3 | -52.0 | 0.13 | 17.6 |
| 7 | 2 | 3 | 2 | 0.2 | 0.50 | 80 | 210.6 | -46.5 | 0.07 | 23.2 |
| 8 | 2 | 4 | 2 | 0.2 | 0.25 | 80 | 122.0 | -41.7 | 0.05 | 26.4 |
| 9 | 3 | 1 | 2 | 0.3 | 1.00 | 80 | 610.0 | -55.7 | 0.42 | 7.4 |
| 10 | 3 | 2 | 2 | 0.3 | 0.75 | 80 | 445.9 | -53.0 | 0.14 | 17.2 |
| 11 | 3 | 3 | 1 | 0.3 | 0.50 | 40 | 285.4 | -49.1 | 0.05 | 25.2 |
| 12 | 3 | 4 | 1 | 0.3 | 0.25 | 40 | 152.3 | -43.7 | 0.04 | 27.3 |
| 13 | 4 | 1 | 2 | 0.4 | 1.00 | 80 | 776.0 | -57.8 | 0.20 | 14.0 |
| 14 | 4 | 2 | 2 | 0.4 | 0.75 | 80 | 545.0 | -54.7 | 0.10 | 19.6 |
| 15 | 4 | 3 | 1 | 0.4 | 0.50 | 40 | 351.2 | -50.9 | 0.06 | 24.8 |
| 16 | 4 | 4 | 1 | 0.4 | 0.25 | 40 | 184.1 | -45.3 | 0.05 | 25.9 |

3 RESULTS

In accordance with the adopted research plan, measurements of the components of the total cutting force and geometrical dimensions of the chips obtained were made. The influence of the assumed variables, i.e., feed values f [mm/rev] and depth a_p [mm] and cutting speed v_c [m/min] on the values of components of the total cutting force, i.e., main cutting force F_c [N], feed force F_f [N] and resistive F_p [N] was analysed. Table 3 presents the results of the average values of the cutting force $F_{c_{mean}}$, and the chip breakage coefficient $C_{ch_{mean}}$ and the values of

the N parameter obtained in individual test systems. Tables 4 and 5 present a statistical analysis of the results.

Figs. 3 and 4 show the influence of individual variables on the average value of the main cutting force F_c and the values of the chip breakage coefficient C_{ch} .

4 DISCUSSION

The analysis of the measurement results showed a linear dependence of the values of all components of the total cutting force on the assumed values of the

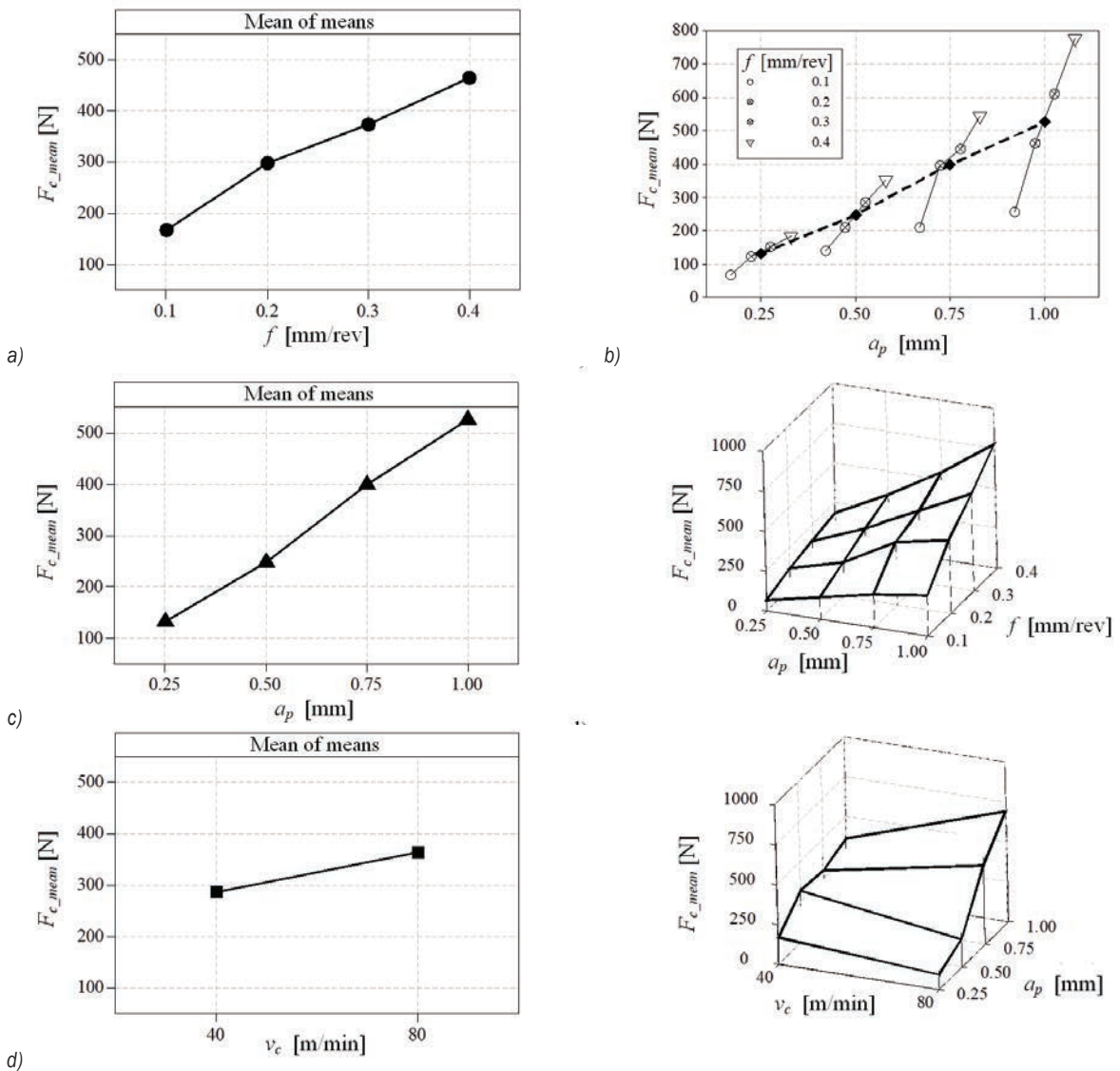


Fig. 3. Influence of the analysed cutting parameters on the mean values of the cutting force F_c :
 a) each parameter in separate graphs: feed f , depth of cut a_p and cutting speed v_c ; b) only depth of cut a_p ;
 c) only depth of cut a_p and feed f ; and d) only cutting speed v_c and feed f

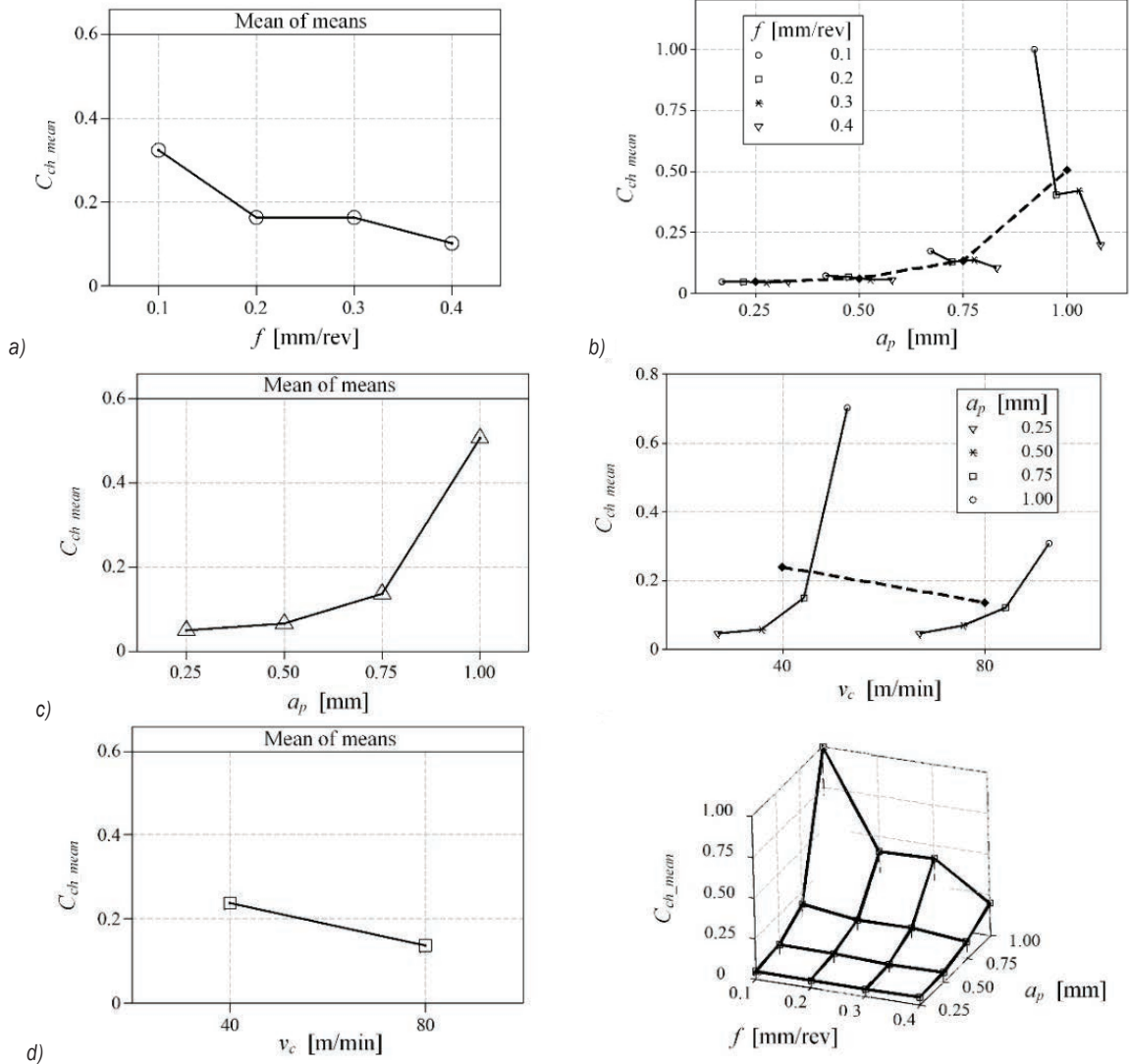


Fig. 4. Influence of the analysed cutting parameters on the mean values of the chip breakability index C_{ch} ; a) each parameter in separate graphs: feed f , depth of cut a_p and cutting speed v_c ; b) only depth of cut a_p ; and c) only cutting speed v_c ; and d) only feed f and depth of cut a_p

cutting parameters during the HPC turning of the titanium alloy Ti6Al4V ELI.

The most significant factors (Fig. 3) on the value of the cutting force F_c were depth of cut a_p and feed f . The depth of cut contributed 8 % and the feed rate contributed 8 % in the F_c response of the cutting force during the machining of the alloy. This was due to the increase in the cross section of the cut layer, which required the cutting process to use higher cutting forces. A fourfold increase in feed value or cutting depth results in about a fourfold increase in the average cutting force. In turn, a twofold increase in cutting speed, that is, from $v_c = 40$ m/min to $v_c = 80$ m/

min, resulted in an increase (by about 6 N) in the average cutting force F_c . For cutting speed $v_c = 80$ m/min, an increase in the intensity of increase in cutting forces was observed, both as a function of depth of cut a_p and feed f (Fig. 3 and d).

The analysis of the data obtained showed that the chip form and average values of the chip breakage coefficient in the longitudinal turning process are significantly influenced by the tested cutting parameters (Fig. 4a), with the cutting depth a_p most significantly. The depth of cut contributed 0 % in chip breakage coefficient C_{ch} responses during the turning of the tested alloy. The cutting speed v_c and

Table 4. Analysis of variance for mean values for cutting force F_c

| Source | DF | SeqSS | AdjSS | AdjMS | F | P | % Contribution |
|----------------|----|--------|--------|--------|-------|-------|----------------|
| f | 3 | 188287 | 188287 | 62762 | 18.96 | 0.001 | 30 |
| a_p | 3 | 357200 | 357200 | 119067 | 35.96 | 0.000 | 58 |
| v_c | 1 | 24255 | 24255 | 24255 | 7.33 | 0.027 | 12 |
| Residual Error | 8 | 26486 | 26486 | 3311 | | | |
| Total | 15 | 596228 | | | | | |

Table 5. Analysis of variance for mean values for chip breakability index C_{ch}

| Source | DF | SeqSS | AdjSS | AdjMS | F | P | % Contribution |
|----------------|----|-------|-------|-------|------|-------|----------------|
| f | 3 | 0.107 | 0.107 | 0.036 | 1.36 | 0.323 | 14 |
| a_p | 3 | 0.558 | 0.558 | 0.186 | 7.09 | 0.012 | 70 |
| v_c | 1 | 0.042 | 0.042 | 0.042 | 1.61 | 0.240 | 16 |
| Residual Error | 8 | 0.210 | 0.210 | 0.026 | | | |
| Total | 15 | 0.917 | | | | | |

the feed rate f contributed, respectively, 6 % and 4 %.

In this case, the correct and acceptable form of chips results from the simultaneous action of the pressure of the cutting fluid and the shape of the chip groove on the rake surface of the insert. For increasing depth of cut and feed values, the chip groove is filled with the chip material to a greater degree. The chip winding radius is also reduced (more short arc chips). The pressure of the cutting fluid additionally supports the process of chip winding and cracking. The chip-cracking process may also be supported by the impact of the chip formed against the unfinished surface of the workpiece or the flank surface of the cutting insert.

In contrast, increasing values of depth of cut cause a much faster increase in the average values of the chip breakage coefficient C_{ch} (Fig. 4b). An increase in the depth of cut value causes an increase in the width of the created chip. The chip strength are increased. The pressure of the cutting fluid may not be sufficient to initiate the chip cracking process.

The determined regression equations $F_c(f, a_p, v_c)$ and $C_{ch}(f, a_p, v_c)$ are shown below.

$$F_c(f, a_p, v_c) = -366 + 964 \cdot f + 534 \cdot a_p + 1.95 \cdot v_c, \quad (5)$$

$$C_{ch}(f, a_p, v_c) = 0.711 - 1.899 \cdot f - 1.192 \cdot a_p - 0.00257 \cdot v_c + 2.479 \cdot f^2 + 1.418 \cdot a_p^2, \quad (6)$$

A confirmatory test was performed to verify the predicted values compared to the experimental values. The results obtained (Table 6) showed a good precision of the predicted cutting force values and the classification of chips based on the chip breakability index C_{ch} .

It was also observed that for the cutting speed $v_c = 8$ m/min, lower values of the C_{ch} coefficient and thus a more correct form of chips were obtained (Fig. 4c). The unacceptable form of chips (Fig. 4d) was obtained for low feed values (e.g., $f = 0.1$ mm/min) and large depth of cut values (e.g., $a_p = 10$ mm). It is a prerequisite to look for an increase in the efficiency of the machining process, taking into account the correct form of the chips. This is particularly important for the finishing machining titanium alloys.

Analysing the results obtained, it can be concluded that increased machining efficiency should be sought by selecting higher values of depth or cutting speed. It is well-known that the feed value has a significant and negative effect on the surface roughness. Therefore, for finishing machining, it may be difficult to increase productivity by increasing feed value.

An example illustrating the method is shown in Fig. 5. In the analysed case, $F_c \leq 200$ N and $C_{ch} \leq 0.2$ (correct form of chips) were adopted as limiting criteria to not exceed the cutting force value. The cutting force diagrams F_c and C_{ch} were determined on the basis of the regression equations presented in Eqs. (5) and (6). The material removal rate Q_v was established according to Eq. (7):

$$Q_v(f, a_p, v_c) = f \cdot a_p \cdot v_c \quad [\text{cm}^3/\text{min}]. \quad (7)$$

Taking into account the limiting criteria, it can be noted that the adoption of a higher cutting speed value (i.e., $v_c = 8$ m/min) results in an increase in the material removal rate, from $Q_v = 4$ cm³/min to $Q_v = 6$ cm³/min, which is an increase of more than 50 % in efficiency. Despite the reduction in depth of

Table 6. Results for confirmation test

| No | F_c mean [N] | F_c anticipated [N] | F_c percent age error [%] | C_{ch} mean | Chips class. | C_{ch} mean anticipated | Anticip. chips class. |
|----|----------------|-----------------------|-----------------------------|---------------|--------------|---------------------------|-----------------------|
| 1 | 255.4 | 342.4 | 34.1 | 1.00 | unfavo. | 0.67 | accept.. |
| 2 | 208.7 | 208.9 | 0.1 | 0.17 | correct | 0.35 | accept. |
| 3 | 140.0 | 153.4 | 9.6 | 0.07 | correct | 0.10 | correct |
| 4 | 68.2 | 19.9 | 70.8 | 0.05 | correct | 0.13 | correct |
| 5 | 462.3 | 438.8 | 5.1 | 0.41 | accept. | 0.55 | accept. |
| 6 | 395.3 | 305.3 | 22.8 | 0.13 | correct | 0.23 | accept. |
| 7 | 210.6 | 249.8 | 18.6 | 0.07 | correct | 0.00 | correct |
| 8 | 122.0 | 116.3 | 4.7 | 0.05 | correct | 0.02 | correct |
| 9 | 610.0 | 613.2 | 0.5 | 0.42 | accept. | 0.38 | accept. |
| 10 | 445.9 | 479.7 | 7.6 | 0.14 | correct | 0.06 | correct |
| 11 | 285.4 | 268.2 | 6.0 | 0.05 | correct | 0.02 | correct |
| 12 | 152.3 | 134.7 | 11.6 | 0.04 | correct | 0.05 | correct |
| 13 | 776.0 | 709.6 | 8.6 | 0.20 | correct | 0.37 | accept. |
| 14 | 545.0 | 576.1 | 5.7 | 0.10 | correct | 0.05 | correct |
| 15 | 351.2 | 364.6 | 3.8 | 0.06 | correct | 0.00 | correct |
| 16 | 184.1 | 231.1 | 25.5 | 0.05 | correct | 0.04 | correct |

cut a_p resulting from the limitation of the permissible value of the cutting force F_c .

It should be noted that an increase in the cutting speed may accelerate the wear of the cutting tools. This may result in higher manufacturing costs. The presented method does not take into account the tool life of the cutting edge.

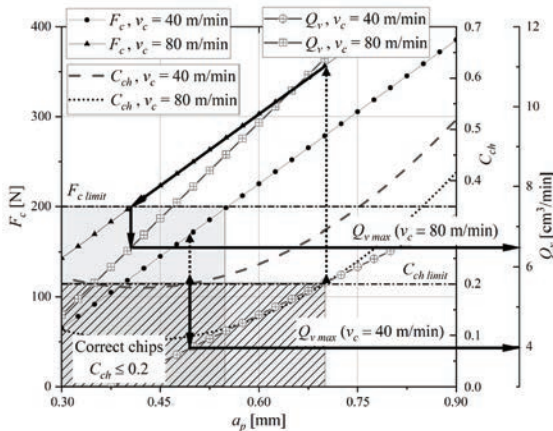


Fig. 5. Method of searching for an increase in material removal rate Q_v .

5 CONCLUSIONS

The purpose of the experimental research was to analyse the machinability of the Ti6Al4V titanium alloy with Prime A turning tools made of

cemented carbides under machining conditions with increased pressure of the cutting fluid. The main area of analysis was to determine the influence of the cutting parameters (f , a_p , v_c) on the values of the cutting forces, as well as the chip breakage coefficient C_{ch} and the form of the chips. The results of the analysis showed that:

- the values of the cutting force F_c depend linearly on the cutting parameters adopted. According to the statistical analysis, the cutting depth a_p was the most significant parameter, followed by feed f , which affects the cutting force. The cutting speed v_c affected the mean cutting force to a much lesser extent.
- the cutting depth a_p was the most significant parameter which affects the chip breakability index C_{ch} . The obtained form of chips (correct, acceptable, and incorrect) depends on the range of cutting parameters used. On average, for the tested ranges of cutting parameter values, a correct chip form was obtained for: $a_p \leq 0.75$ mm, $f \geq 0.2$ mm/rev. A higher cutting speed value, that is, for $v_c = 80$ m/min, reduced the chip breakage coefficient value.
- obtaining a correct form of chips in the finishing turning of titanium alloy Ti6Al4V under HPC machining conditions depends on the synergistic impact of factors such as the values of cutting parameters, the shape and degree of filling of the chip breaker on the rake face, as well as the pressure of the cutting fluid. Under these

conditions, it is possible to increase the machining efficiency by selecting the cutting speed. In the case presented, the increase in the material removal rate Q_v of the machining was more than 6 % .

8 REFERENCES

- [1] Saini, A., Pabla, B.S., Dhama, S.S. (2016). Developments in cutting tool technology in improving machinability of Ti6Al4V alloy: A review. *Proceedings of the Institution of Mechanical Engineers, Part B: Journal of Engineering Manufacture*, vol. 230, no. 11, p. 1977-1989, DOI:10.1177/0954405416640176.
- [2] Kramar, D., Kopač, J. (2009). high pressure cooling in the machining of hard-to-machine materials, *Strojniški vestnik - Journal of Mechanical Engineering*, vol. 55, no. 11, p. 685-694.
- [3] Hourmand, M., Sarhan, A.A.D., Sayuti, M., Hamdi, M. (2021). A comprehensive review on machining of titanium alloys. *Arabian Journal for Science and Engineering*, vol. 46, p. 7087-7123, DOI:10.1007/s13369-021-05420-1.
- [4] Pimenov, D.Y., Mia, M., Gupta, M.K., Machado, A.R., Tomaz, I.V., Sarikaya, M., Wojciechowski, S., Mikołajczyk, T., Kapłonek, W. (2021). Improvement of machinability of Ti and its alloys using cooling-lubrication techniques: a review and future prospect. *Journal of Materials Research and Technology*, vol. 11, p. 719-753, DOI:10.1016/j.jmrt.2021.01.031.
- [5] Davim, J.P. (2014). *Machining of Titanium Alloys*. Springer Berlin, Heidelberg, DOI:10.1007/978-3-662-43902-9.
- [6] Moaz, H.A., Ansari, M.N.M., Khidhir, B.A., Bashir, M., Oshkour, A.A. (2014). Simulation machining of titanium alloy (Ti-6Al-4V) based on the finite element modeling. *Journal of the Brazilian Society of Mechanical Sciences and Engineering*, vol. 36, p. 315-324, DOI:10.1007/s40430-013-0084-0.
- [7] Gao, Y., Wang, G., Liu, B. (2016). Chip formation characteristics in the machining of titanium alloys: a review. *International Journal of Machining and Machinability of Materials*, vol. 18, no. 1-2, p. 155-184, DOI:10.1504/IJMMM.2016.075467.
- [8] Khanna, N., Agrawal, C., Pimenov, D.Y., Singla, A.K., Machado, A.R., da Silva, L.R.R., Gupta, M.K., Sarikaya, M., Krolczyk, G.M. (2021). Review on design and development of cryogenic machining setups for heat resistant alloys and composites. *Journal of Manufacturing Processes*, vol. 68, p. 398-422, DOI:10.1016/j.jmapro.2021.05.053.
- [9] Singh, J., Gill, S.S., Dogra M., Singh, R., Singh, M., Sharma, S., Singh, G., Li, C., Rajkumar, S. (2022) State of the art review on the sustainable dry machining of advanced materials for multifaceted engineering applications: progressive advancements and directions for future prospects, *Materials Research Express*, vol. 9, no. 6, art. ID 064003, DOI:10.1088/2053-1591/ac6fba.
- [10] Hosokawa, A., Kosugi, K., Ueda, T. (2022). Turning characteristics of titanium alloy Ti-6Al-4V with high-pressure cutting fluid. *CIRP Annals*, vol. 71, no. 1, p. 81-84, DOI:10.1016/j.cirp.2022.04.064.
- [11] Singh, J., Gill, S.S., Dogra, M., Singh, R. (2021). A review on cutting fluids used in machining processes. *Engineering Research Express*, vol. 3, no. 1, art. ID 012002, DOI:10.1088/2631-8695/abeca0.
- [12] Singh, J., Gill, S.S., Dogra, M., Sharma, S., Singh, M., Dwivedi, S.P., Li, C., Singh, S., Muhammad, S., Salah, B., Shamseldin, M.A. (2022). Effect of Ranque-Hilsch vortex tube cooling to enhance the surface-topography and tool-wear in sustainable turning of Al-5.6Zn-2.5Mg-1.6Cu-0.23Cr-T6 aerospace alloy. *Materials*, vol. 15, no. 16, art. ID 5681, DOI:10.3390/ma15165681.
- [13] Coelho, W.A., Pereira, R.B.D., Lauro, C.H., Brandão, L.C., Davim, J.P. (2023). Comparative study of deep drilling in the Ti-6Al-4 V ELI titanium alloy using standard and high-feed rate. *The International Journal of Advanced Manufacturing Technology*, vol. 126, p. 4157-4170, DOI:10.1007/s00170-023-11351-y.
- [14] Singh, J., Gill, S.S., Mahajan, A. (2023). Experimental investigation and optimizing of turning parameters for machining of al7075-t6 aerospace alloy for reducing the tool wear and surface roughness. *Journal of Materials Engineering and Performance*, DOI:10.1007/s11665-023-08584-z.
- [15] Palanisamy, S., McDonald, S.D., Dargush, M.S. (2009). Effects of coolant pressure on chip formation while turning Ti6AlV alloy. *International Journal of Machine Tools and Manufacture*, vol. 49, no. 9, p. 739-743, DOI:10.1016/j.ijmactools.2009.02.010.
- [16] Ezugwu, E.O., Bonney, J., Da Silva, R.B., Machado, A.R., Ugwoha, E. (2009). High productivity rough turning of Ti-6Al-4V alloy with flood and high-pressure cooling. *Tribology Transactions*, vol. 52, no. 3, p. 395-400, DOI:10.1080/10402000802687866.
- [17] Da Silva, R.B., Machado, Á.R., Ezugwu, E.O., Bonney, J., Sales, W.F. (2013). Tool life and wear mechanisms in high speed machining of Ti-6Al-4V alloy with PCD tools under various coolant pressures. *Journal of Materials Processing Technology*, vol. 213, no. 8, p. 1459-1464, DOI:10.1016/j.jmatprotec.2013.03.008.
- [18] Stolf, P., Paiva, J.M., Ahmed, Y.S., Endrino, J.L., Goel, S., Veldhuis, S.C. (2019). The role of high-pressure coolant in the wear characteristics of WC-Co tools during the cutting of Ti-6Al-4V, *Wear*, vol. 440-441, art. ID 203090, DOI:10.1016/j.wear.2019.203090.
- [19] Kaminski, J., Alvelid, B. (2000). Temperature reduction in water-jet assisted turning. *Journal of Materials Processing Technology*, vol. 106, no. 1-3, p. 68-73, DOI:10.1016/S0924-0136(00)00640-3.
- [20] Liang, X., Liu, Z., Liu, W., Wang, B., Yao, G. (2019). Surface integrity analysis for high-pressure jet assisted machined Ti-6Al-4V considering cooling pressures and injection positions. *Journal of Manufacturing Processes*, vol. 40, p. 149-159, DOI:10.1016/j.jmapro.2019.03.020.
- [21] Masek, P., Maly, J., Zeman, P., Heinrich, P., Alagan, N.T. (2022). Turning of titanium alloy with PCD tool and high-pressure cooling. *Journal of Manufacturing Processes*, vol. 84, p. 871-885, DOI:10.1016/j.jmapro.2022.10.034.
- [22] Çolak, O. (2014). Optimization of machining performance in high-pressure assisted turning of Ti6Al4V alloy. *Strojniški vestnik - Journal of Mechanical Engineering*, vol. 60, no. 10, p. 675-681, DOI:10.5545/sv-jme.2013.1079.

- [23] Krajčoviech, S., Holubjak, J., Richtarik, M., Czánová, T. (2021). Identification of process Prime A turning when machining steel C56E2 and monitoring of cutting forces. *Transportation Research Procedia*, vol. 55, p. 605-612, DOI:10.1016/j.trpro.2021.07.027.
- [24] Mitra, A. (2011). The Taguchi method. *WIRES Computational Statistics*, vol. 3, no. 5, p. 472-480, DOI:10.1002/wics.169.
- [25] Fang, X.D., Fei, J., Jawahir, I.S. (1996). A hybrid algorithm for predicting chip form/chip breakability in machining. *International Journal of Machine Tools and Manufacture*, vol. 36, no. 10, p. 1093-1107, DOI:10.1016/0890-6955(96)00002-8.
- [26] Lee, Y.M., Yang, S.H., Chang, S.I. (2006). Assessment of chip-breaking characteristics using new chip-breaking index. *Journal of Materials Processing Technology*, vol. 173, no. 2, p. 166-171, DOI:10.1016/j.matprotec.2005.05.057.
- [27] Festas, A., Ramos, A., Davim, J.P. (2021). Machining of titanium alloys for medical application - a review. *Proceedings of the Institution of Mechanical Engineers, Part B: Journal of Engineering Manufacture*, vol. 236, no. 4, p. 309-318, DOI:10.1177/09544054211028531.

A Modified Approach to the Rack Generation of Beveloid Gears

Berat Gürcan Şentürk^{1*} – Mahmut Cüneyt Fetvacı²

¹Dogus University, Turkey

²Istanbul University-Cerrahpasa, Turkey

The purpose of this paper is to present an easier and more efficient method for the determination of the geometry of a bevelled gear tooth. Based on a method that provides an easier way for the rack generation of involute helical gears, the mathematical model of a beveloid gear is studied. The mathematical procedure for developing two-dimensional cross-sections has been extended to three-dimensional gear models. A computer programme is developed to obtain generating and generated surfaces. The proposed algorithm is compared with the previous studies for verification and validation. The results demonstrate that the coordinates obtained from the given method are nearly the same on the start and end points of the main gear parts, such as the involute and root fillets regions. Also, between the limits, the values can be considered acceptable. A coordinate deviation of the gear profile has been observed in the mathematical model, because of the profile shift. Modifications have been developed in the equations to eliminate these cases. The main advantage of the proposed method is to obtain mathematical models without carrying out some of the calculation steps used in previous studies. Eventually, this feature will provide an easier and faster method to develop computer-aided models of the beveloid gear types.

Keywords: beveloid gears, mathematical modelling, rack-type cutters, parametric modelling, involute profile

Highlights

- An extended mathematical model for involute gears generated by rack-type cutters.
- Implementation differences between the given method and the previous methods have been compared.
- Avoiding the deviation of the profile caused by the profile shift.
- Coordinates of the critical points on the roots are analysed.

0 INTRODUCTION

Gear wheels, which are widely used in power transmission, have a wide range of applications from watches to automobiles, from printers to helicopters. In applications requiring high reliability, high strength, and low weight, simulating the physical behaviour of gear wheels in operating conditions before manufacturing saves time and material in the product development stage.

Numerical tools, such as the finite element method, are widely used to calculate the bending strength, contact stress, and transmission error of gear wheels. An accurate representation of the gear tooth geometry is essential for a reliable numerical analysis.

Rack-type cutters are widely used in the mass production of involute gears. A rack cutter is composed of three generating sections: involute, tip fillet, and top land. The corresponding generated surfaces of a gear are the involute flank, trochoidal root fillet, and root bottom land [1] and [2]. The mathematical equations of a gear tooth profile can be obtained based on the profile of the generating cutter, the manufacturing process, and gear meshing theory [3].

There are many studies on the mathematical modelling of gear wheels manufactured by rack

cutters in the literature [3], [4] and [5]. To mention some other studies as rack cutter modelling examples, Yang et al. have proposed a mathematical model for helical gears with asymmetric teeth [6]. Element construction and dynamic analysis have been made by Huang et al. for involute spur and helical gears [7]. Figliolini and Rea proposed a general algorithm for the kinematic synthesis of spur and helical gears and analysed the effects of the design parameters on the undercutting [8].

An approach for a mathematical model and contact analysis of helical gears was developed by Zeyin et al. [9]. Another parameterized approach to establish a high precision three-dimension finite element model of involute helical gears is proposed by Liu et al. [10]. In that study, a refinement methodology of the elements has been developed to improve the mesh quality and accuracy. A new tooth surface modelling method for beveloid gears has been proposed, and influences of the design parameters on the contact behaviours of parallel beveloid gears have been studied by Sun et al. [11]. Şentürk and Fetvacı have developed a mathematical method to prevent undercutting on the beveloid gear models [12]. Mesh stiffness is also a frequently studied topic for computerized gear modeling. A potential energy-based method was proposed by Song et al. to calculate the

mesh stiffness for straight beveloid gears with parallel axes. The effects of parameters, such as the pressure angle, pitch cone angle, and profile shift coefficient on the mesh stiffness were investigated [13]. Another mesh stiffness model has been generated by Zhou et al., which considers the direction variation of the tooth friction and wear influence on single gear–rack tooth pair mesh stiffness [14].

In another significant study, a calculation method of tooth profile modification for tooth contact analysis technology is proposed by Wang et al. [15]. In all the studies mentioned, the rack cutter generating method has been used in the modelling of gear geometries.

Litvin's Vector Approach, which also takes into account functional or production-required modifications, is widely used in the mathematical modelling of gear wheels. This approach also can be extended to all gear wheel modifications such as concave, crowning [16], parabolic modifications [17] and [18], non-circular gears [19] and cylindrical gears [20]. The mathematical model of the concave beveloid gears given, and contact simulations have been performed in [21]. Concave beveloid gears are also modelled and analysed in [22], [23] and [24]. The research on gear tooth modifications continues, such as the research on the external non-involute gear profiles. A review is made on this topic by Okorn et al. [25]. Also, experimental research investigates the characteristics and increases the performance of the gear systems, such as the electrical control anti backlash method proposed by Wang et al. [26] and the experimental study and numerical analysis on aviation spiral bevel gear made by Li et.al. [27].

By generalizing the mathematical model for parallel axis gears, a model including spur, helical, straight beveloid, and helical beveloid gears can be obtained [4], [5] and [7]. A beveloid gear can be generated by a basic rack whose pitch plane intersects with the axis of the gear and forms an angle equal to the generating cone angle [4].

In the computer simulation of gear wheels, the vector representation of the generating tool is first established. Usually, equations are expressed in the normal section. Coordinate transformation is performed in the case of helical and/or conical geometries. Then, the cutter geometry at the transverse section is expressed in the coordinate system of the gear to be manufactured. The next step is to establish the equation of meshing by using differential geometry and gear theory. Thus, the mathematical model of the gear wheel is obtained.

In the publications mentioned above, the coordinate systems used for determining the tool geometries may be oriented differently. The right-hand type of a cartesian coordinate system is preferred. Analytical description of the rack tooth geometry and intervals of curvilinear parameters may change due to the orientation of the coordinate system attached to the generating cutter. In most of the papers engineering approach to differential geometry proposed by Litvin is used to establish the equation of meshing. In Batista's study [28], the origin of the coordinate system, unlike with other researchers, is located at the point where the pitch line intersects the involute edge, as illustrated in Fig. 1 compared to other studies, Batista did not use the directional cosines of the cutter surface vector in the determination of the equation of meshing. The steps followed in modelling provide ease of computer programming.

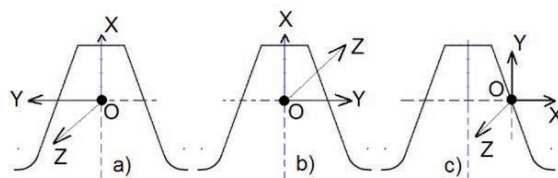


Fig. 1. Different coordinate systems for normal section of rack cutter

The mathematical models of beveloid gears generated by rack-type cutters are studied in various research works [7], [11] and [12]. The aim of this study is to extend the mathematical model proposed by Batista to beveloid (involute conical) gearing. This way, when compared to the previous studies, the gear tooth geometry can be expressed in a much simpler form, depending on the roll angle. Also, the gear simulation process will be less time consuming by shortening the modelling algorithm.

In scope of this work, the design steps of the proposed modelling method are given clearly, by showing the mathematical equations of the design parameters, including the modifications for the conical and beveloid gear geometries. Gear tooth profiles drawn by the previous studies and the present method are compared, and finally, the modelling algorithms are shown.

1 METHODS

According to one of the previous methods proposed by Liu et.al. [4], a beveloid gear can be modelled by defining the rack cutter geometry and simulating the translation and rotation of the cutter around the global

$$y_L = \begin{cases} u & -\frac{m_n \pi}{4} \leq x_L \leq -u \tan(\alpha_{n1,2}) \\ -\frac{x_L}{\tan(\alpha_{n1,2})} & -u \tan(\alpha_{n1,2}) \leq x_L \leq m_n \tan(\alpha_{n1,2}) \\ y_{L0} - \sqrt{(\rho_{1,2})^2 - (x_{L0} - x_L)^2} & m_n \tan(\alpha_{n1,2}) \leq x_L \leq x_{L0} \\ -m_n - c_n & x_{L0} \leq x_L \leq \frac{m_n \pi}{4} \end{cases}, \quad (1)$$

coordinate system origin, S_C . Dimensions of the rack cutter design parameters are given in Fig. 2. Also, the figure shows the asymmetrical state, in which both tapered and helical hobbing conditions exist in the gear model.

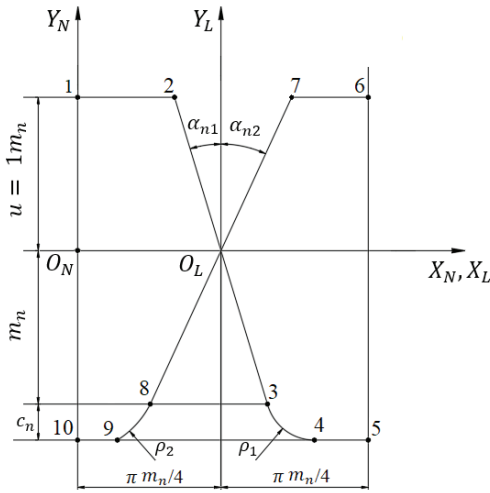


Fig. 2. The configuration of rack cutter and reference coordinate system

In Eq. (1), the equations that define the beveloid tooth profile can be simplified according to the position of this chosen coordinate system. Because of this orientation, intervals of the design parameters can be changed when compared to previous studies [4], [6], [12].

Fig. 2 shows that the rack cutter coordinate system is placed over the involute section. The angles β and δ are the helical and cone angles of the gear tooth, respectively.

From Fig. 2, the coordinates can be defined analytically by Eq. (1).

Here, the radius of the root fillets ρ_1 and ρ_2 and the origin coordinates x_{L0} and y_{L0} of the rack coordinate system S_L can be expressed as:

$$\begin{aligned} \rho_{1,2} &= \frac{c_n}{1 - \sin(\alpha_{n1,2})}, \\ x_{L0} &= m_n \tan(\alpha_{n1,2}) + \rho_{1,2} \cos(\alpha_{n1,2}), \\ y_{L0} &= -m_n + \rho_{1,2} \sin(\alpha_{n1,2}). \end{aligned} \quad (2)$$

For plotting, we can define the tool geometry in the global cartesian coordinate system S_0 , as written in Eq. (3).

$$\begin{bmatrix} x_N \\ y_N \end{bmatrix} = \begin{bmatrix} x_L \\ y_L \end{bmatrix} + \begin{bmatrix} \mp 0.25 m_n \pi \\ 0 \end{bmatrix}. \quad (3)$$

On Eq. (3), the + and - signs are for the left and right side of the rack, respectively.

Eq. (3) draws only one of the rack cutter profiles for the zero position in 2D. The rack cutter cross-section is translated by $r_i \varphi$ and rolled by an angle which is one of the major design parameters φ . After the translation and rotation processes, two-dimensional cross-section of the beveloid gear, which has an asymmetrical profile due to the helix and cone angles, is drawn by the imaginary motion of the inclined rack cutter cross-sections (see Fig. 3).

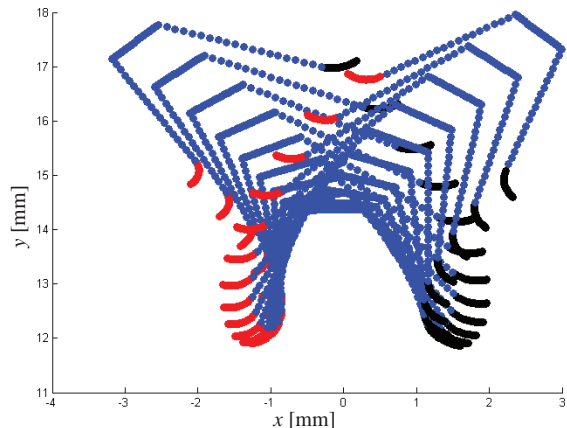


Fig. 3. The rack cutter generation process for beveloid gears

Because of the helix and cone angles, the position of the rack cutter should be turned around the horizontal and vertical axis X_N and Y_N , by the amount of δ and β , respectively. The rotation matrices are given in Eq. (4).

$$\mathbf{M}_{CP} = \begin{bmatrix} 1 & 0 & 0 & 0 \\ 0 & \cos(\delta) & -\sin(\delta) & 0 \\ 0 & \sin(\delta) & \cos(\delta) & 0 \\ 0 & 0 & 0 & 1 \end{bmatrix},$$

$$\mathbf{M}_{PN} = \begin{bmatrix} \cos(\beta) & 0 & -\sin(\beta) & \lambda \sin(\beta) \\ 0 & 1 & 0 & 0 \\ \sin(\beta) & 0 & \cos(\beta) & -\lambda \cos(\beta) \\ 0 & 0 & 0 & 1 \end{bmatrix}. \quad (4)$$

$$\mathbf{R}_C = \begin{bmatrix} x_C \\ y_C \\ z_C \end{bmatrix} =$$

$$\begin{bmatrix} x_N \cos(\beta) - \lambda \sin(\beta) \\ -x_N \sin(\delta) \sin(\beta) + y_N \cos(\delta) - \lambda \sin(\delta) \cos(\beta) \\ -y_N \sin(\delta) - x_N \cos(\delta) \sin(\beta) + \lambda \cos(\delta) \cos(\beta) \end{bmatrix}. \quad (5)$$

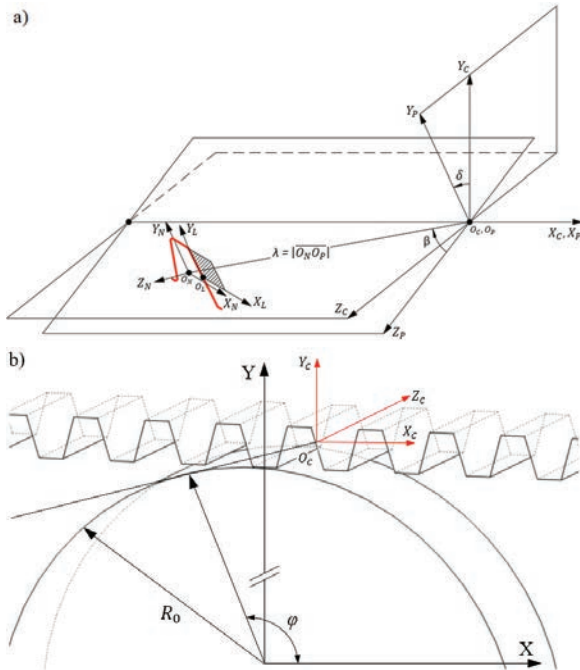


Fig. 4. Relations among the coordinate systems

By applying these coordinate transformations, we can obtain tooth geometry in the S_C coordinate system.

The term λ states the translation of the origin O_c and is integrated into the matrix \mathbf{M}_{PN} .

If the third row of Eq. (5) is rearranged for $z_C = z$, the parameter λ can be calculated as in Eq. (6). With the help of this parameter, a two-dimensional cross-section of the rack can be defined.

$$\lambda = \frac{z + y_N \sin(\delta) + x_N \cos(\delta) \sin(\beta)}{\cos(\beta) \cos(\delta)}. \quad (6)$$

On the analytical definitions, different from the formulations given in the previous studies, normal vectors are not used. Instead, the meshing condition is simulated with the help of partial derivatives. Finally, the parametric equations for the geometric positions of the rack cutter have been derived.

As explained earlier, the global and rack coordinate systems are defined and can be seen in Fig. 4. The relation between these systems can be expressed as:

$$X = X_0 + x_N \sin(\varphi) + y_N \cos(\varphi), \quad (7)$$

$$Y = Y_0 - x_N \cos(\varphi) + y_N \sin(\varphi). \quad (8)$$

The involute of the circle, which described by the origin of the rack coordinate system S_0 , can be defined as:

$$X_0 = R_0 \cos(\varphi) + R_0 \varphi \sin(\varphi), \quad (9)$$

$$Y_0 = R_0 \sin(\varphi) - R_0 \varphi \cos(\varphi). \quad (10)$$

The vertical position of the rack cutter should be redefined due to the profile shift e . The equation of the generated gear tooth surface at the transverse section can be explained by Eq. (11).

$$y_N \rightarrow y_N + e, \quad (11)$$

$$X = (R_0 + e + y_C) \cos(\varphi) + (R_0 \varphi + x_C) \sin(\varphi), \quad (12)$$

$$Y = (R_0 + e + y_C) \sin(\varphi) - (R_0 \varphi + x_C) \cos(\varphi). \quad (13)$$

In Eqs. (11) to (13), parameters x_C and y_C can be defined as $x_C = x_C(s)$ and $y_C = y_C(s)$. Here s is defined as an arbitrary continuous parameter.

To be able to calculate the roll angle φ , the condition during the meshing of the gears in contact can be written as in Eq. (14),

$$\frac{\delta X}{\delta \varphi} \frac{\delta Y}{\delta s} - \frac{\delta Y}{\delta \varphi} \frac{\delta X}{\delta s} = 0. \quad (14)$$

After the parameters in Eqs. (12) and (13) are differentiated, and plugged, in Eq. (14) the roll angle φ can be calculated as,

$$\varphi(x_c) = -\frac{1}{R_0} [x_c + e + y_c] \frac{dy_c}{dx_L} \quad (5)$$

Here, the value for the derivative $\frac{dy_c}{dx_L}$ can be written as in Eq. (6) :

$$\frac{dy_c}{dx_L} = \begin{cases} 0 \\ \pm \frac{1}{\tan(\alpha_{r1,2})} \\ \frac{x_{L0} - x_L}{\sqrt{(\rho_{1,2})^2 - (x_{L0} - x_L)^2}} \tan(\alpha_{n1,2}) \\ 0 \end{cases}, \quad (6)$$

By using Eqs. (5), (6), (2), (3), (5) and (6), we can obtain generated gear geometry in the plane of rotation (in transverse section).

In this manner, a three-dimensional beveloid gear tooth can be modelled with the help of changed cross-sections with respect to coordinate z .

In Eq. (6), α_{rD} is included in the formulation to state the pressure angle on the transverse plane. If not, because of the helical and conical properties, this condition will cause geometric irregularities on the involute section and the root fillets. This modification is one of the major changes made in the mathematical models proposed by Batista [28].

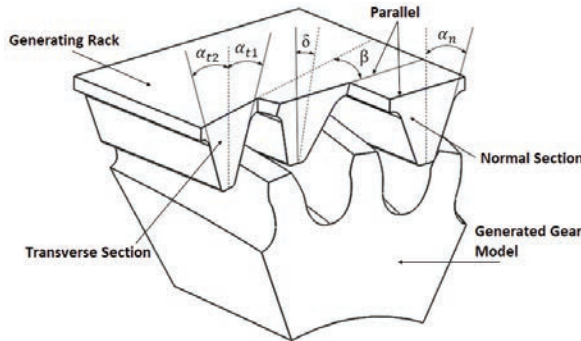


Fig. 5. Generating rack and generated gear in mesh

$$\alpha_{r1} = (\tan)^{-1} \left(\frac{\cos(\delta) \sin(\alpha_{n1}) - \cos(\alpha_{n1}) \sin(\beta) \sin(\delta)}{\cos(\alpha_{n1}) \cos(\beta)} \right), \quad (7)$$

$$\alpha_{r2} = (\tan)^{-1} \left(\frac{\cos(\delta) \sin(\alpha_{n2}) + \cos(\alpha_{n2}) \sin(\beta) \sin(\delta)}{\cos(\alpha_{n2}) \cos(\beta)} \right). \quad (8)$$

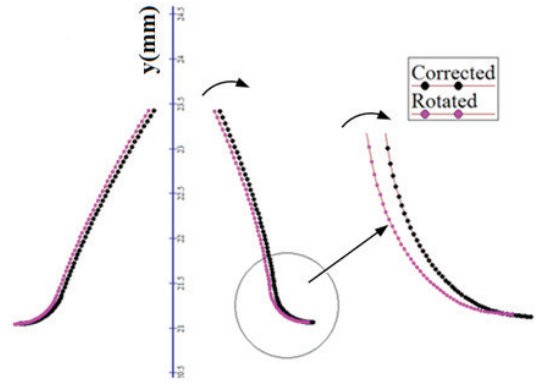


Fig. 6. Generating rack and generated gear in mesh

This relationship can be seen in Fig. 5. The equations of “ α_{rD} ” on each side of the rack can be written as in Eqs. (17) and (8). These expressions are proposed on the previous works by Liu and Tsay [4].

It has been observed in the present mathematical model that the conventional profile shift causes coordinate deviation of the generated helical beveloid gear. To compensate for this deviation, gear blank is re-rotated by the angle γ .

$$e = \frac{e_n}{\cos(\delta)}, \quad (19)$$

$$\gamma = e \tan(\beta) \frac{\sin(\delta)}{R_0} \text{ or } \gamma = e_n \tan(\beta) \frac{\tan(\delta)}{R}. \quad (20)$$

Fig. 6 shows this effect for the parameters, $m_n = 1 \text{ mm}$, $z = 40$, $\delta = 4^\circ$, $\beta = 24^\circ$, $e_n = 0.5 m_n$. For this case, the deflection is $2.37 \times 10^{-3} \text{ rad}$ (0.4363°).

$$R_0 = \frac{m_n z}{2} \cos(\beta). \quad (21)$$

After defining the deflection angle, the correction can be made by following

$$\mathbf{R}_G = \begin{bmatrix} X_G \\ Y_G \\ Z_G \end{bmatrix} = \begin{bmatrix} \cos(\gamma) & \sin(\gamma) & 0 \\ -\sin(\gamma) & \cos(\gamma) & 0 \\ 0 & 0 & 1 \end{bmatrix} \begin{bmatrix} X_c \\ Y_c \\ Z_c \end{bmatrix}. \quad (22)$$

After multiplying the gear profile coordinates by the correction matrix in Eq. (22), gear coordinates with the profile shift, X_G , Y_G and Z_G can be obtained.

1.1 Gear Generation

After generating the tooth profiles in two dimensions, cross-section geometries can be combined using

geometric methods offered by computer-aided design (CAD) software. After modelling the single gear tooth, the \mathcal{B} geometries can be duplicated.

Fig. 7 displays the change in geometry through the tooth width. By using these cross-section geometries, solid models of beveloid gears can be built. Consecutive cross-sections form the tooth surfaces as seen in Figs. 7b and in c the complete model is seen.

Fig. 8 displays the geometric parameters of the designed beveloid gear pair, such as the centre distance, tip and root diameters and the tooth thickness. The design parameters are: $m_n = 3$ mm,

$z = 24$, $\alpha_{n1} = \alpha_{n2} = 20^\circ$, $\delta = 5^\circ$, $\beta = 5^\circ$ for both pinion and gear.

The \mathcal{B} models of the gear geometries has been produced by 3D printer using, fused deposition modelling (FDM) technique. It can be seen on Figs. 8b and c that the tooth thickness is becoming smaller, and undercutting can start to occur on the side where the height of the root region is the greatest and becoming larger on the other side where the root height is the smallest. Gear geometries in both Figs. 8b and c are the same, but the gears are flipped.

Fig. 9 displays the generation algorithms of previous studies in Fig. 9a and the proposed method

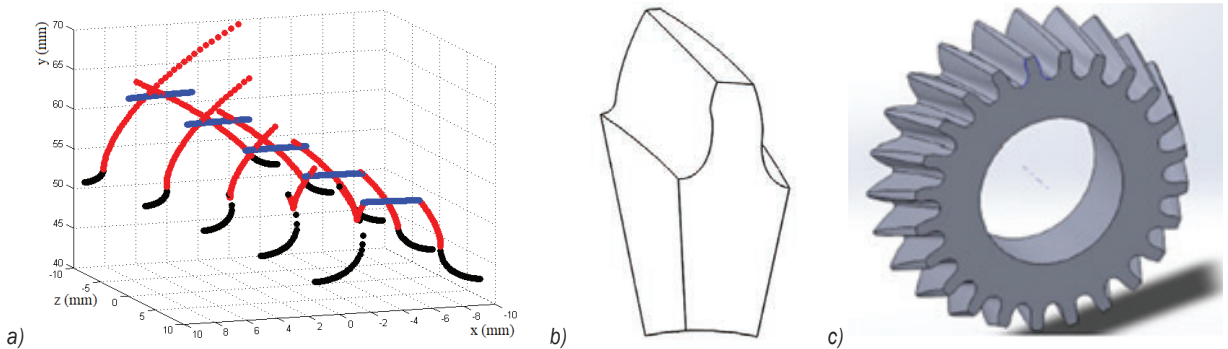


Fig. 7. Beveloid gear generation steps

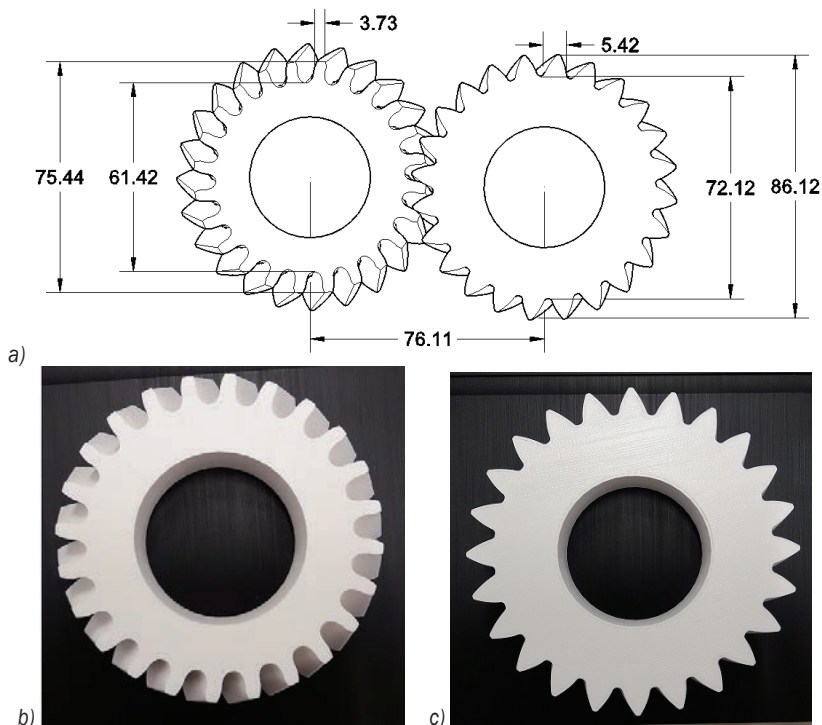


Fig. 8. Geometric parameters of the gear pair and generated beveloid gears;

a) beveloid gear pair on parallel axes, b) and c) views form the front and back sides of the beveloid gear model respectively

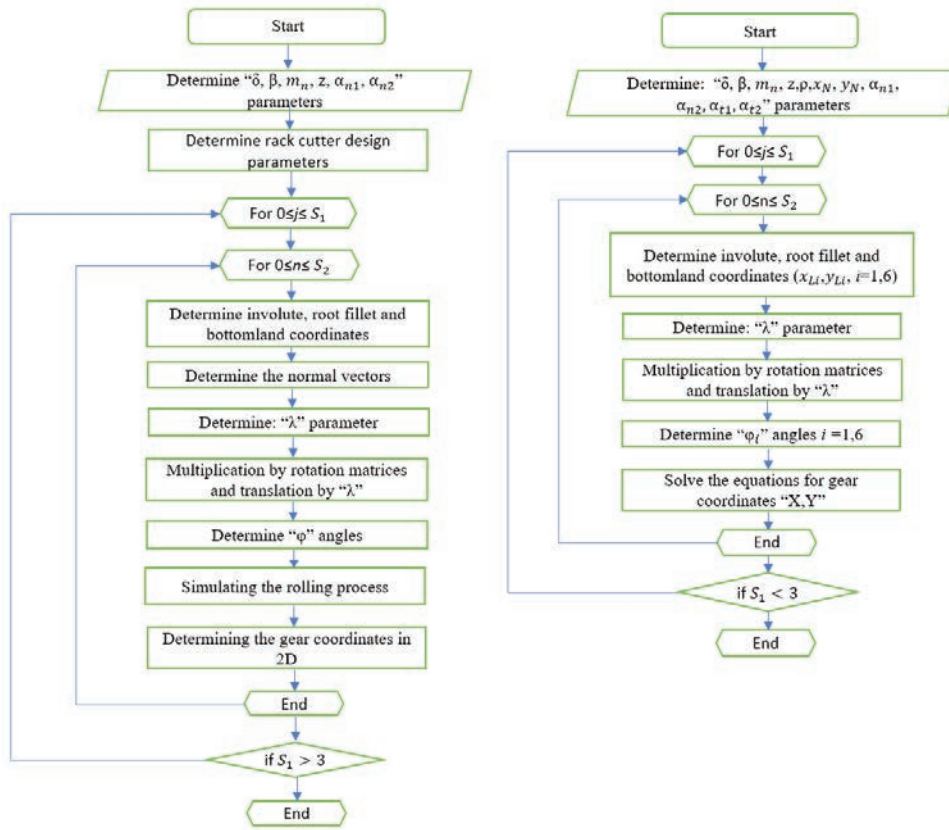


Fig. 9. Gear generation algorithms a) previous studies, b) proposed method

in Fig. 9b. It has seen that the calculating algorithm is shortened. For this reason, the modelling process for the proposed model becomes much simpler and less time consuming. For the cross-section generation, values for the roll angle “ φ_i ” is calculated by meshing equation Eq. (15). In this manner, the definition of normal vectors will not be necessary. As seen in Eq. (A8) the normal vector equation is a function of both the “ l_R ” and “ λ ” parameters. The symbolic definition of a normal vector becomes large and hard to calculate after the cross multiplication operations. With the help of the new proposed method, gear cross-sections can be drawn directly from coordinate definitions “ X and Y ” as in Eqs. (5) and (6).

2 RESULTS

Based on the proposed mathematical model, a program is developed to obtain generating and generated surfaces.

Fig. 10 displays cross-section geometries of beveloid gears for design parameters ... $m_n = 4$ mm, z

$= 25$ $\alpha_{n1} = \alpha_{n2} = 20^\circ$, $\delta = 20^\circ$, $\beta = 0^\circ$ for Fig. 10a and $\delta = 20^\circ$, $\beta = 20^\circ$ for Fig. 10b.

The same parameters are also used in Figs. 11 to 13

Fig. 11 shows the comparison of the gear tooth geometries drawn by the previous and the new proposed method. It is clearly seen that the position coordinates are nearly the same. Here, the helical and cone angles are the same as in Fig. 10b.

After the mathematical model for the two-dimensional cross-sections has been completed, the involute and root fillet regions are compared with the previous models. Figs. 11 and 12 show the change in the root fillets due to tooth width and cone angle δ respectively.

As seen in Fig. 12, the distance between the position coordinates of the root fillet regions is sensitive to the excessive undercut cases. These situations can occur either with the increase in the cone angle or the change in the tooth width through undercut sections. Mathematically, this inconsistency is caused by the square root terms in the root fillet definitions of the proposed model.

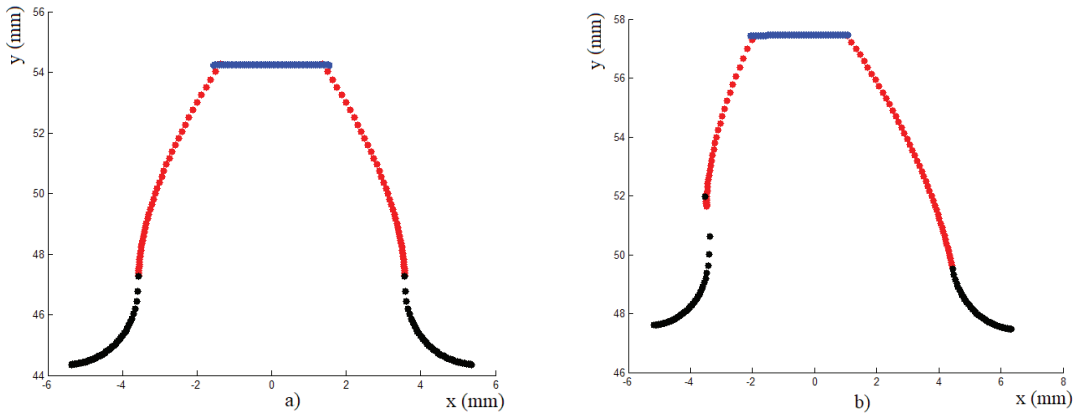


Fig. 10. 2D cross-sections of conical and beveloid gear models; a) non-helical, b) helical beveloid gear models

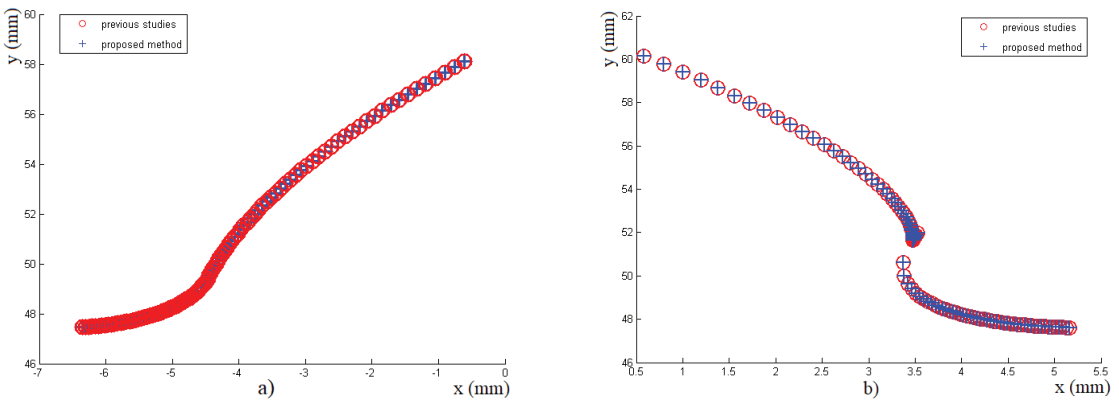


Fig. 11. Comparison of conventional method and the method proposed by Batista [28] in 2D; a) the side with no undercut, and b) undercut side

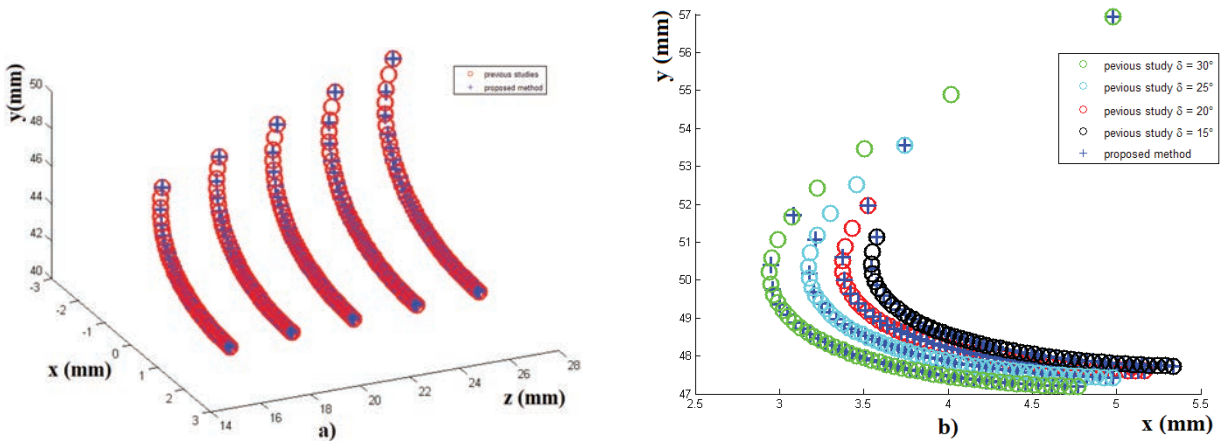


Fig. 12. The root fillet coordinates of 2D beveloid gear models generated by previous and new developed methods; a) $\delta = 10^\circ$, $\beta = 10^\circ$ and $z = 15$ mm to 25 mm, and b) $\delta = 15^\circ$ to 30° , $\beta = 20^\circ$

Fig. 13 indicates the same result, by comparing the radius values R , which is the square root of sum of square values of horizontal and vertical position coordinates. The coordinate values are chosen from

the regions where the root fillets are connected to the involute sections.

At high cone angle values, undercutting starts to occur. The patterns do not follow the geometric

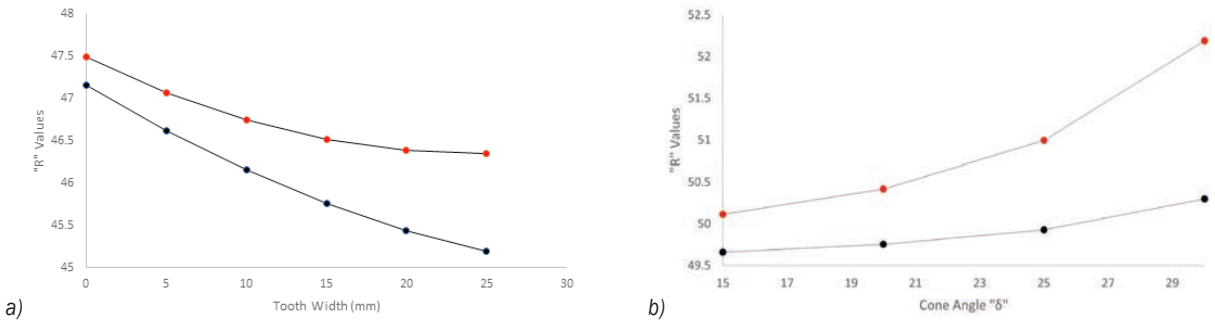


Fig. 13. The change in radius values R based on the change in a) tooth width, and b) cone angle δ

contour around the undercut regions of the models drawn by previous methods. Nevertheless, the two-dimensional geometries are compatible with the previous ones on the end points of the root fillets. In general applications, cone angles are not selected as high values to cause undercutting problems (mostly up to 30°). Because of that, deviation cases do not cause serious modelling errors.

Consequently, the variation between the calculation algorithms cause a relatively small difference in the coordinates when undercutting status is concerned. This condition can be fixed by practical geometric techniques offered by CAD programs. Also, the results shows that the differences between the coordinate values are within acceptable limits.

3 CONCLUSION

In this study, Batista’s mathematical model for rack generation [28] has been extended to beveloid gears. That model was developed for 2D cross-sections; the modified equations in the proposed method allows for model gear geometries in three dimensions by changing the cross-section accurately, considering the effect of the cone angle.

The mathematical equations are given briefly, and the modelling algorithms are compared with the previous method proposed by Liu and Tsay [4]. It has seen that the gear tooth profiles generated by the two methods overlap very closely with each other.

Also, while adapting of the equations, it has been observed that the profile shift parameters cause the cross-sections to rotate by a small angle around the tooth width axis for beveloid geometries. To avoid that, a modification angle has been developed and included in the equations.

The detailed investigation on the root fillet regions for helical and conical cases showed that the change in the position coordinates is within acceptable limits.

It is obvious that the modelling technique proposed by Batista [28] makes it easier to define the gear cross-section geometries and enables the designers to avoid time-consuming techniques.

In this way, especially for the computer simulations of gears, modelling the point clouds and tooth surfaces of the involute, root fillet, bottom land, and tip regions of the beveloid gears will be easier and less time-consuming.

The mathematical model proposed in this study, can be extended to different gear geometries such as non-circular, cylindrical gears, and curvilinear gear teeth [19], [20] and [29], and internal gears [30]. Also parabolic modification [17] and [18] and generating cutter can be considered [31] to [33].

4 NOMENCLATURES

- δ cone angle, [°]
- β helix angle, [°]
- ρ_D root fillet radius, [mm]
- c_n clearance, [mm]
- u addendum, [mm]
- m_n normal module, [mm]
- α_{nD} pressure angle on normal plane, [°]
- α_{tD} pressure angle on transverse plane, [°]
- z gear tooth width, [mm]
- φ roll angle, [°]
- e profile shift in transverse section, [mm]
- e_n profile shift in normal section, [mm]
- γ deflection angle, [°]
- R_0 pitch circle radius, [mm]

5 REFERENCES

[1] Jelaska, D. (2012). Gears and Gear Drives. John Wiley & Sons, Chichester, DOI:10.1002/9781118392393.
 [2] Vullo, V. (2020). Gears. Springer, Cham, DOI:10.1007/978-3-030-40164-1.

- [3] Litvin, F.L., Fuentes, A. (2004). *Gear Geometry and Applied Theory*. Cambridge University Press, Cambridge, DOI:10.1017/CB09780511547126.
- [4] Liu, C.-C., Tsay, C.-B. (2001). Tooth undercutting of beveloid gears. *Journal of Mechanical Design*, vol. 123, no. 4, p. 569-576, DOI:10.1115/1.1414128.
- [5] Brauer, J. (2004). A general finite element model of involute gears. *Finite Elements in Analysis and Design*, vol. 40, no. 13-14, p. 1857-1872, DOI:10.1016/j.finel.2004.02.002.
- [6] Yang, S.-C.. (2005). Mathematical model of a helical gear with asymmetric involute teeth and its analysis. *The International Journal of Advanced Manufacturing Technology*, vol. 26, p. 448-456, DOI:10.1007/s00170-003-2033-z.
- [7] Huang, K.J., Wei Su, H.. (2010). Approaches to parametric element constructions and dynamic analyses of spur/helical gears including modifications and undercutting. *Finite Elements in Analysis and Design*, vol. 46, no. 12, p. 1106-1113, DOI:10.1016/j.finel.2010.08.002.
- [8] Figliolini, G., Rea, P. (2014). Effects of the design parameters of involute gears generated by rack-cutters. *International Gear Conference*, p. 294-302, DOI:10.1533/9781782421955.294.
- [9] He, Z., Lin, T., Luo, T., Deng., T., Hu, Q. (2016). Parametric modeling and contact analysis of helical gears with modifications. *Journal of Mechanical Science and Technology*, vol. 30, p. 4859-4867, DOI:10.1007/s12206-016-1004-x.
- [10] Liu, Y., Zhao, Y., Liu, M., Sun, X. (2019). Parameterized high-precision finite element modelling method of 3D helical gears with contact zone refinement. *Shock and Vibration*, vol. 2019, art ID 5809164, DOI:10.1155/2019/5809164.
- [11] Sun, R., Song, C., Zhu, C., Liu, S., Wei, C. (2020). Tooth surface modelling and mesh behaviors for paralleled beveloid gears. *Journal of Mechanical Design*, vol. 142, no. 5, art. ID 054501, DOI:10.1115/1.4045141.
- [12] Şentürk, B.G., Fetvacı, M.C. (2020). Modelling and undercutting analysis of beveloid gears. *Journal of the Faculty of Engineering and Architecture of Gazi University*, vol. 35, no. 2, p. 901-916, DOI:10.17341/gazimmfd.544038. (in Turkish)
- [13] Song, C., Zhou, S., Zhu, C., Yang, X., Li, Z., Sun, R. (2018). Modeling and analysis of mesh stiffness for straight beveloid gear with parallel axes based on potential energy method. *Journal of Advanced Mechanical Design, Systems, and Manufacturing*, vol. 12, no. 7, (2018): art. ID JAMDMS0122, DOI:10.1299/jamdsm.2018jamdsm0122.
- [14] Zhou, C., Dong, X., Wang, H., Liu, Z. (2022). Time-varying mesh stiffness model of a modified gear-rack drive with tooth friction and wear. *Journal of the Brazilian Society of Mechanical Sciences and Engineering*, vol. 44art. ID 213, DOI:10.1007/s40430-022-03517-8.
- [15] Wang, C. Wang, S., Wang, G. (2018). A calculation method of tooth profile modification for tooth contact analysis technology. *Journal of the Brazilian Society of Mechanical Sciences and Engineering*, vol. 40 art. ID 341, DOI:10.1007/s40430-018-1268-4.
- [16] Wang, H., Zhou, C., Hu, B., Liu, Z. (2019). Tooth wear prediction of crowned helical gears in point contact. *Proceedings of the Institution of Mechanical Engineers, Part J: Journal of Engineering Tribology*, vol. 234, no. 6, p. 947-963, DOI:10.1177/1350650119896467.
- [17] Chen, Y.-J., Yang, H.-C., Pai, P.F. (2016). Design and kinematics evaluation of a gear pair with asymmetric parabolic teeth. *Mechanism and Machine Theory*, vol. 101, p. 140-157, DOI: 10.1016/j.mechmachtheory.2016.03.008.
- [18] Ni, G., Zhu, C., Song, C., Du, X., Zhou, Y. (2017). Tooth contact analysis of crossed beveloid gear transmission with parabolic modification. *Mechanism and Machine Theory*, vol. 113, p. 40-52, DOI:10.1016/j.mechmachtheory.2017.03.004.
- [19] Wu, L., Han, J., Zhu, Y., Tian, X., Xia, L.. (2017). Non-circular gear continuous generating machining interpolation method and experimental research. *Journal of the Brazilian Society of Mechanical Sciences and Engineering*, vol. 39, p. 5171-5180, DOI:10.1007/s40430-017-0873-y.
- [20] Jia, K., Guo, J., Zheng, S., Hong, J. (2019). A general mathematical model for two-parameter generating machining of involute cylindrical gears. *Applied Mathematical Modelling*, vol. 75, p. 37-51, DOI:10.1016/j.apm.2019.05.021.
- [21] Liu, C.-C., Tsay, C.-B. (2002). Mathematical models and contact simulations of concave beveloid gears. *Journal of Mechanical Design*, vol. 124, no. 4, p. 753-760, DOI:10.1115/1.1517563.
- [22] Liu, S., Song, C., Zhu, C., Fan, Q. (2018). Concave modifications of tooth surfaces of beveloid gears with crossed axes. *Proceedings of the Institution of Mechanical Engineers, Part C: Journal of Mechanical Engineering Science*, vol. 233, no. 4, p. 1411-1425, DOI:10.1177/0954406218768842.
- [23] Liu, C.-C., Chen, Y.-C., Lin, S.-H. (2010). Contact stress analysis of straight concave conical involute gear pairs with small intersected angles. *Proceedings of the International MultiConference of Engineers and Computer Scientists*, vol. 3.
- [24] Liu, C.-C., Chen, Y.-C., Peng, Y.-L. (2015). Contact pattern simulation and stress analysis of intersected concave conical involute gear pairs generated by shaper cutters. *Proceedings of the 14th IFToMM World Congress*, DOI:10.6567/IFTToMM.14TH.WC.PS6.007.
- [25] Okorn, I., Nagode, M., Klemenc, J. (2021). Operating performance of external non-involute spur and helical gears: A Review. *Journal of Mechanical Engineering - Strojniški vestnik*, vol. 67, no. 5, p. 256-271, DOI:10.5545/sv-jme.2020.7094.
- [26] Wang, G., Zhu, D., Zou, S., Jiang, Y., Tian, X. (2022). Simulation and experimental research on electrical control anti-backlash based on a novel type of variable tooth thickness involute gear pair. *Strojniški vestnik - Journal of Mechanical Engineering*, vol. 68, no. 2, p. 126-140, DOI:10.5545/sv-jme.2021.7452.
- [27] Li, L., Wang, S. (2023). Experimental study and numerical analysis on windage power loss characteristics of aviation spiral bevel gear with oil injection lubrication. *Strojniški vestnik-Journal of Mechanical Engineering*, vol. 69, no. 5-6, p. 235-247, DOI:10.5545/sv-jme.2023.558.
- [28] Batista, M. (2021). Analytical treatment of the geometry of involute gears. *ResearchGate*, DOI:10.13140/RG.2.2.31057.66404.
- [29] Tseng, R.-T., Tsay, C.-B. (2004). Contact characteristics of cylindrical gears with curvilinear shaped teeth. *Mechanism and Machine Theory*, vol. 39, no. 9, p. 905-919, DOI:10.1016/j.mechmachtheory.2004.04.006.
- [30] Yan, G., Song, C., Zhu, F., Cui, Z., Deng, Z. (2022). The analysis of contact ratio of involute internal beveloid gears with small tooth difference. *Journal of Advanced Mechanical*

Design, Systems, and Manufacturing, vol. 16, no. 1, art. IDJAMDSM0017, DOI:10.1299/jamdsm.2022jamdsm0017.

- [31] Lai, C.-H., Yang, H.-C. (2016). Theoretical investigation of a planar rack cutter with variable diametral pitch. *Arabian Journal for Science and Engineering*, vol. 41, p. 1585-1594, DOI:10.1007/s13369-015-1856-x.
- [32] Yang, S.-C. (2006). A study on using deviation function method to reshape a rack cutter. *The International Journal of Advanced Manufacturing Technology*, vol. 30, p. 385-394, DOI:10.1007/s00170-005-0089-7.
- [33] Cao, B., Li, G. (2021). Computerized design of plunge shaving tool for beveloid gears and plunge shaving characteristic analysis. *Mechanism and Machine Theory*, vol. 161, art. ID 104325, DOI:10.1016/j.mechmachtheory.2021.104325.

6 APPENDIX

Comparison of Mathematical Models

The calculation process due to the generation method proposed by Liu and Tsay [4] is explained in detail.

The coordinates of the involute section is:

$$\mathbf{R}_n^R = \begin{bmatrix} x_n^R \\ y_n^R \\ z_n^R \end{bmatrix} = \begin{bmatrix} b_c - l_R \sin(\alpha_{n1}) + c_y \pi m_n \\ l_R \cos(\alpha_{n1}) \\ 0 \end{bmatrix}. \quad (A1)$$

Here l_R is the coordinates of the involute section of the rack, where:

$$\frac{-a_c}{\cos(\alpha_{n1})} \leq l_R \leq \frac{a_t}{\cos(\alpha_{n1})}, \quad (A2)$$

where a_c and a_t are addendum and dedendum values respectively and equal to normal module m_n and $b_c = 0.25 \pi m_n$.

The value c_y can be determined as 0, 1, 2, ... so that the rack cutter and generated gear can be modeled with desired number of teeth.

The rotation matrices for the cone and helix angles can be written as:

$$\mathbf{M}_{cp} = \begin{bmatrix} 1 & 0 & 0 & 0 \\ 0 & \cos(\delta) & -\sin(\delta) & 0 \\ 0 & \sin(\delta) & \cos(\delta) & 0 \\ 0 & 0 & 0 & 1 \end{bmatrix}, \quad (A3)$$

$$\mathbf{M}_{pn} = \begin{bmatrix} \cos(\beta) & 0 & -\sin(\beta) & \lambda \sin(\beta) \\ 0 & 1 & 0 & 0 \\ \sin(\beta) & 0 & \cos(\beta) & -\lambda \cos(\beta) \\ 0 & 0 & 0 & 1 \end{bmatrix}. \quad (A4)$$

By multiplying \mathbf{M}_{cp} with \mathbf{M}_{pn} , \mathbf{M}_{cn} can be written as:

$$\mathbf{M}_{cn} = \begin{bmatrix} \cos(\beta) & 0 & -\sin(\beta) & \lambda \sin(\beta) \\ -\sin(\beta) \sin(\delta) & \cos(\delta) & -\cos(\beta) \sin(\delta) & \lambda \cos(\beta) \sin(\delta) \\ \cos(\delta) \sin(\beta) & \sin(\delta) & \cos(\beta) \cos(\delta) & -\lambda \cos(\beta) \cos(\delta) \\ 0 & 0 & 0 & 1 \end{bmatrix}. \quad (A5)$$

The position vector \mathbf{R}_c^i can be obtained as:

$$\mathbf{R}_c^i = [\mathbf{M}_{cn}] \mathbf{R}_n^i, \quad (A6)$$

The components of the vector are:

$$\begin{aligned} x_c^i &= x_n^i \cos(\beta) + \lambda \sin(\beta), \\ y_c^i &= y_n^i \cos(\delta) + \lambda \cos(\beta) \sin(\delta) \\ &\quad - x_n^i \sin(\delta) \sin(\beta), \\ z_c^i &= y_n^i \sin(\delta) - \lambda \cos(\beta) \cos(\delta) \\ &\quad + x_n^i \cos(\delta) \sin(\beta). \end{aligned} \quad (A7)$$

Here, λ is the same offset parameter which is given in Eq. (6). In this way, coordinates of the 2D gear cross-sections can be calculated for an arbitrary value of tooth thickness in the axis of z . In the next step, the normal vectors of the cutting tool surfaces n_c^i should be calculated as:

$$n_c^i = \frac{\frac{\partial R_c^i}{\partial l_R} \times \frac{\partial R_c^i}{\partial \lambda_1}}{\left| \frac{\partial R_c^i}{\partial l_R} \times \frac{\partial R_c^i}{\partial \lambda_1} \right|}. \quad (A8)$$

Considering the rolling process, the relation between the rack cutter and the generated gear can be specified with the matrix \mathbf{M}_t .

$$\mathbf{M}_{tc} = \begin{bmatrix} \cos(\varphi_1) & \sin(\varphi_1) & 0 & r_1(\sin(\varphi_1) - \varphi_1 \cos(\varphi_1)) \\ -\sin(\varphi_1) & \cos(\varphi_1) & 0 & r_1(\cos(\varphi_1) + \varphi_1 \sin(\varphi_1)) \\ 0 & 0 & 1 & 0 \\ 0 & 0 & 0 & 1 \end{bmatrix}. \quad (A9)$$

The roll angle of the generated gear φ_1 can be calculated by considering the fundamental law of gearing.

$$\frac{X_c^i - x_c^i}{n_{xc}^i} = \frac{Y_c^i - y_c^i}{n_{yc}^i} = \frac{Z_c^i - z_c^i}{n_{zc}^i}, \quad (A10)$$

where X_c^i , Y_c^i and Z_c^i are the coordinates of an arbitrary point on the instant center of rotation $I-I$. Detailed explanation is given in [6]. Here, n_{xc}^i , n_{yc}^i and n_{zc}^i are the direction cosines of the unit normal

n_c^i . Using this relation, the angle ϕ_1 can be obtained as:

$$\phi_1 = \frac{(y_c^i n_{xc}^i - x_c^i n_{yc}^i)}{r_p^i n_{xc}^i}. \quad (\text{A11})$$

After calculating the related parameters as specified, coordinates of the generated gear can be obtained by calculating the coordinate vector \mathbf{R}_1^i .

$$\mathbf{R}_1^i = [\mathbf{M}_{1c}] \mathbf{R}_c^i. \quad (\text{A12})$$

The calculation steps shows that, the position vector can not be obtained without calculating the roll angle ϕ_1 . Eq. (A11) requires the calculation of the unit normal n_c^i . The proposed mathematical method in this study, enables to complete the process without this calculation. The roll angle ϕ can be calculated directly by Eq. (4) and the gear coordinates can be obtained by Eq. (2).

Investigation on the Application of ~~W~~ n Cutting Tool Inserts as Burnishing Tools

Oktay Adıyaman*

¹Batman University, Besiri Organized Industrial Zone Vocational School, Turkey

The amount of wear in cutting tools used in all machining processes is around 1 % to 2 % evaluation of the non-wearing areas of the inserts is economically beneficial. This study aims to test the usability of the non-wearing regions of the waste tungsten carbide (WC), cubic boron nitride (CBN) and ceramic inserts as a rolling tool in the deep rolling method and to observe their performance. The turned workpieces were deep rolled with three different types of waste-cutting tools (WC, CBN and ceramic) in different machining parameters (rolling force, number of passes, and feed rate). As a result, surface roughness and microhardness values obtained in deep rolling operations with these inserts were similar to those in deep rolling operations with other rolling tools. It has been determined that ceramic inserts perform better in deep rolling processes in terms of microhardness, and WC inserts perform better in terms of surface roughness. Thus, it has been determined that waste WC, CBN and ceramic inserts can be used in the deep rolling method.

Keywords: deep rolling, ball burnishing, microhardness, tribology, surface roughness

Highlights

- Deep rolling process is a surface treatment process that has been studied in recent years.
- The inserts (WC, ceramic, CBN, etc.) used in machining processes have areas that are largely ($\approx 98\%$ to 99%) non-worn after use.
- The use of non-worn areas of these tools is very valuable from economic and environmental points of view.
- The use of these waste inserts in deep rolling processes is an alternative.

0 INTRODUCTION

The cutting insert wear occurs at a rate of 1 % to 2 % in machining applications, and after this damage, they are junked [1], which is a great loss in terms of economy and environment. Recycled WC makes up nearly 20 % and 8 % of the total production according to statistics. Retrieving tungsten carbide decreases the raw material cost between 5 % and 6 % [2]. All these reasons make the studies related to re-evaluation of these cutting tools that have become wasted very significant. The increasing metal demand throughout the world has encouraged intensive studies for extracting metals from low grade ores and/or from secondary sources [3]. Among these metals, the main raw materials of cutting tools such as tungsten carbide (WC), cubic boron nitride (CBN) and ceramic, are the most important materials in industrial applications [3]. Since the production of cutting inserts is a very costly process, regaining these inserts through recycling makes the process more important [4]. Besides the benefit that recycling studies bring together with them [5], it is an expensive process, which encourages seeking different alternatives. This makes the reuse of waste-cutting inserts important.

The deep rolling process is a surface treatment process. Deep rolling that Ford Company first applied to axle shafts dates back to the 1930s [6]. The basic

mechanism in this method is the surface pressure effect created between a workpiece and a spherical ball end in the contacted area, as explained through Hertzian theory [7]. As a result of this surface pressure, residual tensions and micro structural deformations (hardening/ softening) occur since the yield force of the material is exceeded [8], [9], and [6]. Studies about deep rolling are still continuing in various ways, such as simulation works about deep rolling [10], deep rolling analysis through finite elements method [11], and [12], trials of deep rolling in different work conditions (for example: cryogenic) [13], and deep rolling analysis through regression methods etc.. It is seen that hardness, corrosion resistance and fatigue life have been obtained as a result of press residual stress formed on the surfaces by deep rolling [14]. The good surface quality obtained and the spreading possibility of fatigue cracks are counteracted by residual press stresses [14]. Deep rolling nitration, similar to that of induction hardening and hardening with laser processes, has effects on the surface of the workpiece at values close to the values of surface penetration depth [6].

The cutting tools used in machining processes have areas that are largely ($\approx 98\%$ to 99%) non-worn after use. Except for the studies on recycling cutting tools, no studies were found in the literature on the evaluation of unused surfaces of inserts. In order to

achieve this aim, the non-worn insert areas on the surfaces of cutting tools were used as the crushing edge in the deep rolling method, and thus, it was recovered again. In this context, three different cutting insert types (WC, CBN and ceramic) that had become waste were selected and processed by a deep-rolling method with different processing parameters of AISI 1045 steel. Thus, the applicability of the deep rolling method in the recycling of these inserts was investigated. The performances of the inserts used were compared in terms of microhardness, surface roughness (R_a) and the resulting surface appearance. The aim of this article is not to analyse deep rolling, but to detail whether the waste inserts achieve the results in deep rolling or not.

1 MATERIALS AND METHODS

A SMARC brand CAK6030 X 200 model computer numerical control (CNC) lathe was used in all turning operations (Fig. 1a). In the cutting process in general turning operations, the upper surface of the cutting tool is aligned with the workpiece axis. In this study, in the deep rolling process, the middle region of the used and worn cutting edge was aligned in the same direction of the workpiece axis (Fig. 1b). Henceforth, the used waste insert will be called the roll insert. The roll insert was mounted on the CNC lathe turret with a specially designed tool holder (Fig. 1c).

In order to adjust the pressure force of the cutting tool and the tool holder, the pressure force was adjusted by changing the spring length as a result of the connection apparatus that was specially designed and connected to the turret. Three different clamping force values adjusted according to the spring pressure lengths in the spring catalogue [15] were selected (Fig. 1d). The pressure forces were not separately measured during the experiment, yet the table values were taken as reference.

Here, the basic aim is to investigate and measure the effects according to force increase rather than measuring the forces. In all deep rolling processes, three different roll inserts were used. The inserts were chosen from different types of each group, such as the PVD-coated M10 series (WC) (8 % WC + 5 % titanium carbide (TiC) + 0 % Co), (CBN) and ceramic. All cutting inserts chosen were previously used and became waste materials (Fig. 2).

AISI 1045 steel (20 mm diameter and 70 mm long) was used in the experiments. The work piece with an 8 mm diameter was primarily finish applied material. The average hardness of the material before rolling was measured as 220 HV0.5 to 240 HV0.5

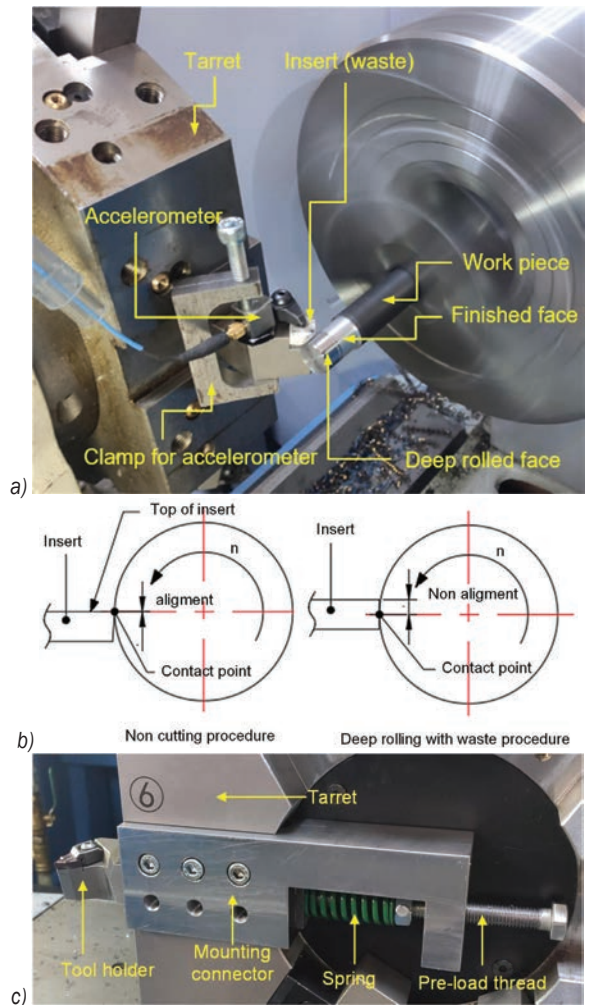


Fig. 1. Schematic representation of conducting deep rolling and aligning waste cutting tool with workpiece a) All operations b) tool alignment c) tool holder

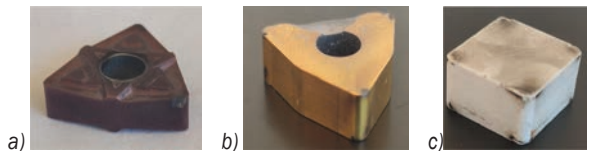


Fig. 2. Different waste inserts a) WC, b) CBN, and c) ceramic

In the experiments, three pressure forces (43 N, 80 N and 495 N), three passes (1, 2 and 3) and three feed rate values (0.04 mm/rev, 0.08 mm/rev and 0.2 mm/rev) were selected. Thus, for each inserts, 27 experiments (Table 1), 81 experiments in total were performed for all inserts.

No cooling was used in the experiments. Variance analysis was performed to examine the effect of process parameters on the results for both microhardness and R_a .

Table 1. The design matrix for the experiments

| Exp. No | Insert | Number of passes | Feed rate [mm/rev] | Force [N] |
|---------|-----------------|------------------|--------------------|-----------|
| 1 | WC -CBN-Ceramic | 1 | 0.04 | 143 |
| 2 | | 1 | 0.08 | 143 |
| 3 | | 1 | 0.12 | 143 |
| 4 | | 2 | 0.04 | 143 |
| 5 | | 2 | 0.08 | 143 |
| 6 | | 2 | 0.12 | 143 |
| 7 | | 3 | 0.04 | 143 |
| 8 | | 3 | 0.08 | 143 |
| 9 | | 3 | 0.12 | 143 |
| 10 | | 1 | 0.04 | 330 |
| 11 | | 1 | 0.08 | 330 |
| 12 | | 1 | 0.12 | 330 |
| 13 | | 2 | 0.04 | 330 |
| 14 | | 2 | 0.08 | 330 |
| 15 | | 2 | 0.12 | 330 |
| 16 | | 3 | 0.04 | 330 |
| 17 | | 3 | 0.08 | 330 |
| 18 | | 3 | 0.12 | 330 |
| 19 | 1 | 0.04 | 495 | |
| 20 | 1 | 0.08 | 495 | |
| 21 | 1 | 0.12 | 495 | |
| 22 | 2 | 0.04 | 495 | |
| 23 | 2 | 0.08 | 495 | |
| 24 | 2 | 0.12 | 495 | |
| 25 | 3 | 0.04 | 495 | |
| 26 | 3 | 0.08 | 495 | |
| 27 | 3 | 0.12 | 495 | |

27 for each insert, 81 total experiments

For each pass, an equal 0.04 mm depth of pass was applied. For the microhardness, 27 pieces from the parts with a feed rate of 0.08 mm/rev were selected. Microhardness was measured from at three different points of the cylindrical surface of each selected part and was assigned by calculating the arithmetic average of the three values measured. For the face microhardness, the microhardness was measured as \emptyset values by shifting $\emptyset \mu\text{m}$ from the edge to the axis of the part. For the surface roughness, the arithmetic mean of Ra values measured from three different areas of each cylindrical surface was accepted as the surface Ra of the experiment sample.

2 RESULTS AND DISCUSSION

2.1 Tool Wear

The purpose of the study to re-evaluate waste-cutting tools by using them in the rolling process. The

damages occurring in the nose part of the cutting tools are shown in Fig. 3

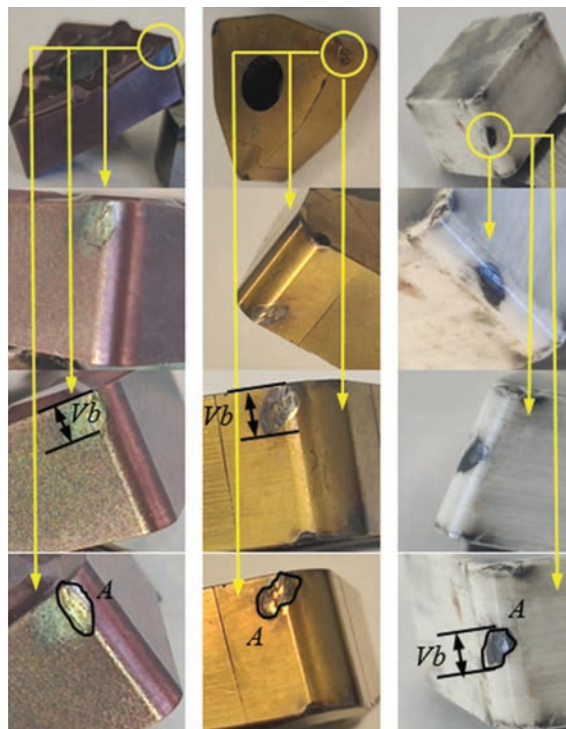


Fig. 3. The worn areas in inserts

Three different types of roll inserts shown in Fig. 6 were calculated as both insert wear length (Vb_{ax}) and the worn area (A), and the results are shown in Table 2.

Table 2. Worn area values

| Tool type | Vb_{ax} [mm] | Area, A [mm ²] |
|-----------|----------------|------------------------------|
| WC insert | 1.1525 | 1.059 |
| CBN | 1.236 | 0.910 |
| Ceramic | 1.339 | 0.758 |

In the observations, no significant wear was observed on the surface of all three insert types. In the WNMG and CBN insert types, it was observed that the coating layer was erased, but no trace of abrasion was formed on the surface (Fig. 6 and b). Only a black zone has formed due to heat and abrasion. Of the insert types used, the ceramic tip is uncoated. As seen in Fig. 6 group, there was no significant wear-related damage on this insert type; only a black area was caused by heat and dirt. What is expressed as Vb_{ax} here is not actually the wear value in the real sense but is expressed only as the dimensional length of the trace formed. From the results obtained, it is

possible to say that every insert type can be used in deep rolling. Considering Table 2 data, it is seen that the dimensional lengths of the traces (here as the edge wear length ($V_{h\text{ ax}}$)) are close to each other. When the sizes of the areas formed by the traces are examined, it is seen that the largest area is with the WC-type insert, and the smallest area is with the ceramic-type insert.

2.2 Microhardness

Microhardness measurements were carried out to examine the number of passes in the radial direction on the face surface of the samples, and the microhardness values graph of values from cylindrical surfaces are seen in Fig. 4a. When the graph of Fig. 4a is examined, it is seen that there is an increase in the hardness caused by deep rolling on the surface of the workpiece. This situation presents parallelism with the results of many studies in the literature [16] to [18].

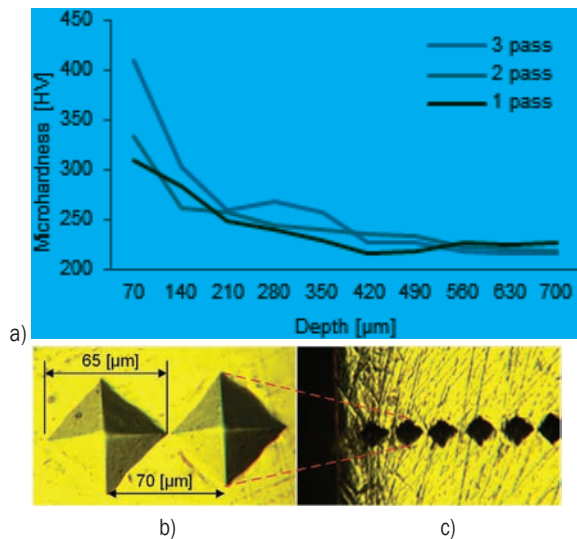


Fig. 4. a) Microhardness graph in radial direction, b) status of traces, and c) surface distribution of traces

It was also stated that the highest hardness occurred on the surface and the hardness decreased from the surface to the centre [12], [14], [18] and [19]. Abrão et al. [20] stated that for AISI 0 6 steel, with the increase of rolling pressure and the number of passes, the intensity of the plastic stress under the surface increased, resulting in an increase in both the microhardness value and the depth of the affected zone. Loh et al. [21] found that the surface hardness of medium carbon steel increased by an average of 5 % after deep rolling with tungsten carbide balls. Also, rolling pressure and feed rate were found to be

the most important factors in microhardness [22]. As can be seen in Fig. 4a, the highest hardness value was obtained in the experiment with three passes, and the lowest value was obtained in one pass.

There is a difference in surface hardness up to 60 μm below the surface. Studies on deep rolling show that the depth of the affected area varies between 60 μm to -1 μm [13], [16] and [20]. This depth varies according to material type, process parameters and application environment (cryogenic, etc.).

When each insert type was analysed according to the values, the graphic in Fig. 5 were obtained.

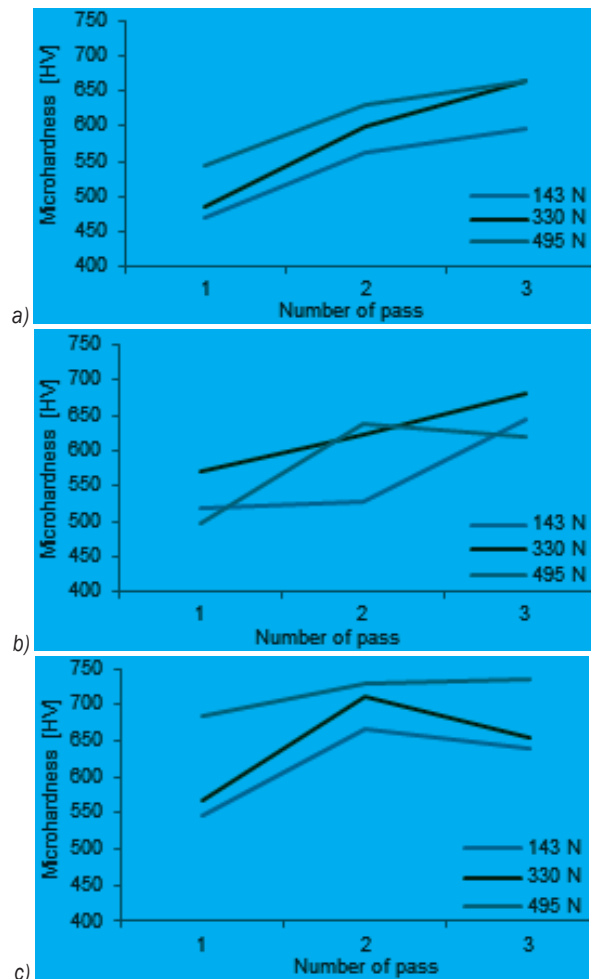


Fig. 5. Microhardness graphs according to insert types; a) WC, b) ceramic, and c) CBN

This effect is also seen in other studies [12]. Parallel to this, the increase in the number of passes at all inserts also causes an increase in hardness.

It is seen that the highest hardness values are obtained with the ceramic insert, and the lowest hardness values are obtained with the WC insert.

When the values in Fig. 5 are evaluated, it can be said that the use of ceramic inserts in deep rolling is more convenient in terms of microhardness. In applications for which hardness is required, ceramic inserts and high pass numbers are recommended. In general, it is seen from the graphs that instabilities in the CBN inserts occur with the increase in the pressing force. It is estimated that these instabilities are due to the instabilities on the surface of the work piece. In general terms, it is possible to say that the hardness increases in both the surface and radial directions in the deep rolling method for all inserts. This did not change in the use of waste inserts. It should also be noted that compared to previous studies, hardness values can be quite misleading in evaluating the hardening state because increases in hardness values are also induced by compressive residual stresses [23].

When Fig. 5 is examined, it is seen that the hardness of all inserts increases with the increase of the pressure force. Depending on the material, deep rolling can result in the formation of dislocation cell structures [24], nanocrystals [9] and [25], twinning [18] or martensitic transformations [18].

When the surfaces with microhardness values are examined, it is seen that quite different structures are formed within the same region (Fig. 6). In deep rolling, temperature is one of the most important criteria. The main source of formations on the surface is temperature [13] and [19]. As a result of plastic deformation of the surface (with changes in parameters such as feed rate, number of passes etc.), increases in temperature occur. Also, with effects such as a high feed rate, more force (partially converted to heat in the ball-work piece contact zone) is required for rolling [12]. In addition, the increased heat from the wear mechanism causes the structure to transform from ferrite to perlite or martensite. Accordingly, it is observed that carbide bands are formed (Fig. 6).

Maximov expresses the work obtained in the thermodynamic explanation of the tool and workpiece in the deep rolling process in Eq. (1) [19].

$$\overline{dA}^e = dA_Q^e + |dA_{el}| + |dA_{pl}| \quad (1)$$

Here \overline{dA}^e the external (input) work, dA_Q^e the work converted into heat and $|dA_{el}| + |dA_{pl}|$ are the elementary works of the external and the internal surface forces for the elastic and plastic deformation of the workpiece, respectively. Accordingly, the rise in temperature is an important parameter of the work achieved in deep rolling. Temperature increases on the workpiece thermodynamically have an improving effect on the work obtained. In the graphs in Fig. 8 it

is seen that the hardest structure is the ceramic tip, followed by the CBN and WC tips, respectively. Since the thermal conductivity of WC-type and CBN-type inserts (6 W/(m K) to 8 W/(m K)) is higher than the thermal conductivity of ceramic inserts (0 W/(m K) to 20 W/(m K)) [26], WC and CBN inserts take most of the heat generated on themselves and do not transfer it to the material surface. Unlike WC and CBN inserts, since ceramic inserts have

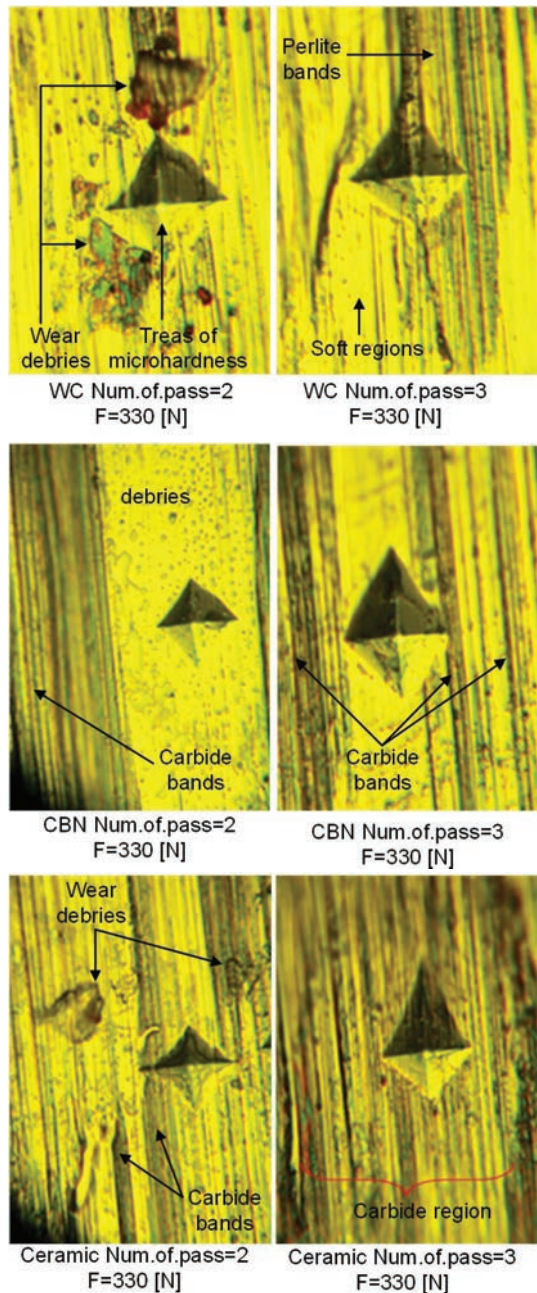


Fig. 6. Images of structures on surfaces

lower thermal conductivity, most of the heat generated in deep rolling is transferred to the workpiece. It is thought that [19] phase transformations occur thermodynamically as a result of the heat staying more on the workpiece, and as a result, the hardness increases. It is thought that the reason for the high hardness values in deep rolling with ceramic-type inserts is in this direction. Similar to this idea, in their study of carbon steels, Abrão et al. and other researches [17], [20] and [27] stated that partial annealing, full annealing or quenching and tempering occur on AISI 1006 steel material. In particular, it was stated that the pressure force and the number of passes significantly increase the hardness [20]. In contrast, since the ferrite layers are transformed into perlite in the heat transfer, it was observed that the microhardness increases accordingly [19].

The results in Table 3 were obtained as a result of the ANOVA analysis performed to investigate to what extent the process parameters affected the microhardness. When the variance analysis table is examined, the values under the column shown with the *P*-value indicate whether the independent variables are statistically significant on the dependent variables. The fact that the *P*-value is less than 0.05 indicates that this value is statistically significant. In this regard, it can be seen that the insert type, force, and number of pass parameters on microhardness are statistically significant. It is the “Contribution” value that shows the effect of independent variables on dependent variables. Accordingly, it can be seen that the number of passes, insert type, and force are effective on microhardness by 44.7 %, 23.0 % and 18.3 %, respectively. This shows that deep rolling of

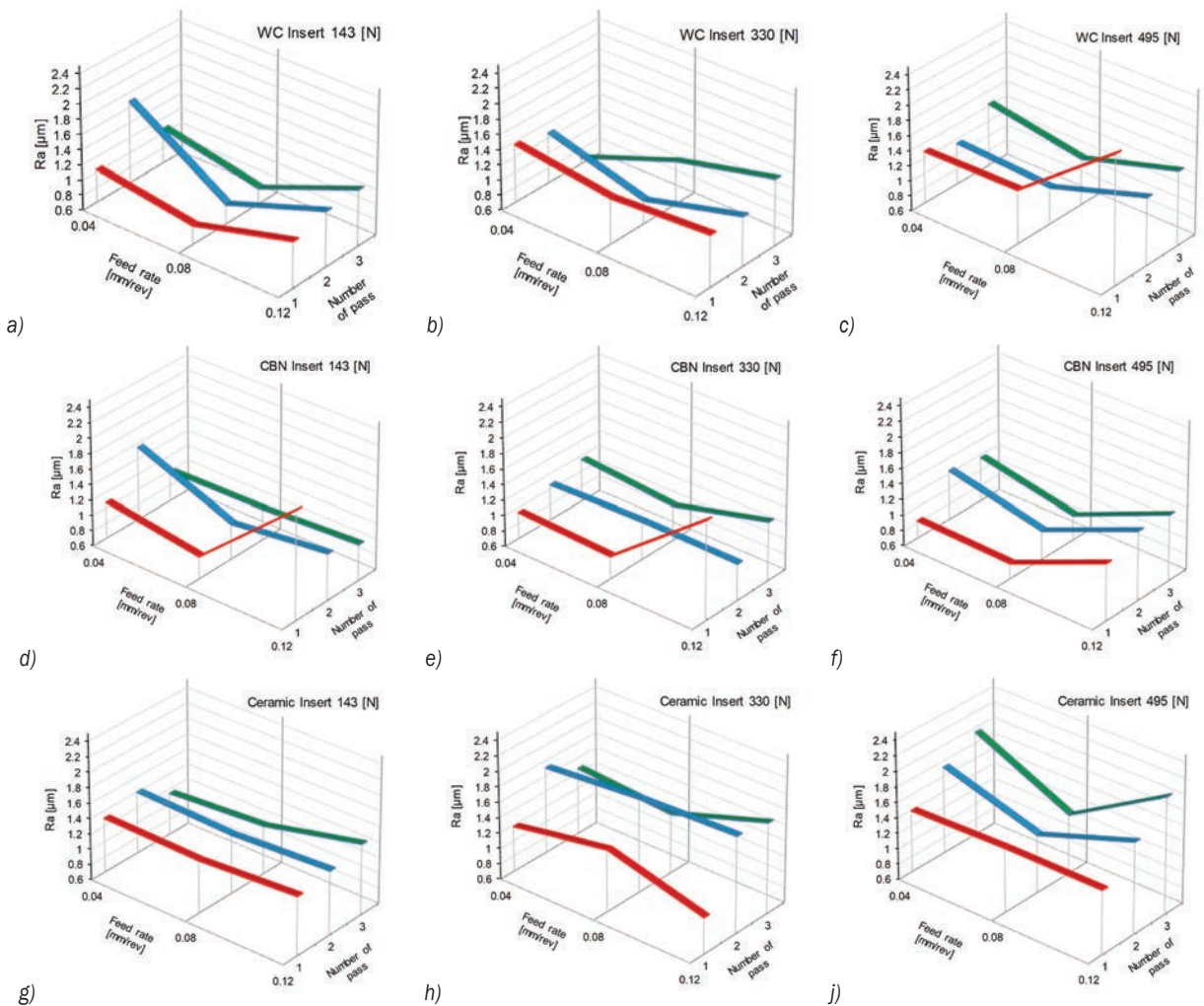


Fig. 7. R_a values measured according to feed rate and number of passes

Table 3. ANOVA for microhardness

| Source | DF | Seq SS | Contribution [%] | Adj SS | Adj MS | F-value | P-value |
|------------------|----|--------|------------------|--------|--------|---------|---------|
| Insert type | 2 | 33670 | 23.70 | 33670 | 16835 | 13.16 | 0.000 |
| Force [N] | 2 | 19218 | 13.53 | 19218 | 9609 | 7.51 | 0.004 |
| Number of passes | 2 | 63616 | 44.77 | 63616 | 31808 | 24.87 | 0.000 |
| Error | 20 | 25578 | 18.00 | 25578 | 1279 | | |
| Total | 26 | 142081 | 100.00 | | | | |

waste insert inserts produces a result parallel to the literature [17], [19] and [28].

When the graphs in Fig. 5 and the images in Fig. 6 are evaluated together with variance analysis, it is seen that the insert type is also effective as the number of passes increases. Each pass causes more deformation on the surface, resulting in a tougher structure and more carbide formation on the material surface, which is observed as an increase in microhardness. With each pass, the peaks on the surface fill into the valleys on the surface. If more passes are applied after a certain stage, a mechanism similar to sliding-rubbing occurs between the material and the crushing tip. This situation causes the formation of debris and carbide bands similar to the one in Fig. 6. The number of passes having the greatest impact here is perhaps due to the filling of the valleys on the surface after the 1st or 2nd pass and the burnishing turning into sliding-rubbing after this stage. Therefore, more work is needed to obtain optimum values. When an excessive number of passes or rolling force is applied, the surface turns into a mechanism similar to ploughing, as in the grinding process.

The fact that some of the slopes in Fig. 5 do not occur linearly or logarithmically can be defined as a result of the unstable structures formed.

2.3 Surface Roughness

Each insert was separately examined according to Ra values and relevant rolling force obtained, and the results are shown in Fig. 7. When Fig. 7 is examined, it is seen that the lowest Ra values are obtained when $f = 0.08$ mm/rev according to the different feed values selected. Low and high feed rates have a negative effect on Ra . This shows that optimum feed rates must be achieved in deep rolling.

Data showing a direct relationship between progress and Ra could not be obtained from the graphs in Fig. 7. Prabhu et al. found the coefficient effect of progress on Ra very low in their regression and ANOVA analysis in deep rolling of AISI 440 steel [29].

In deep rolling, the surface of the workpiece is exposed to more heat as the time to reach the maximum temperature increases with the decrease of the feed value. In Figs. 7, h and j graphs, higher Ra values were obtained in ceramic inserts. Here too, we believe that the temperature factor is effective. It is thought that the surface structure deteriorates due to the heat accumulated on the surface formed at the ceramic inserts, and as a result, increases in Ra values occur.

Similarly, in another study, it is stated that the decrease in feed causes the deformation of the surface layers near the roll insert, resulting in higher workpiece temperatures. It is stated that at higher feed rates, more power (partially converted to heat in the ball-work piece contact area) is required for deep rolling [12].

The low and high progress therefore, causes negative effects on the surface in terms of Ra . From all this, we are of the opinion that optimum values should be applied for progress rather than low or high. In all graphs in Fig. 7 the Ra value was mostly obtained at 0.08 mm/rev as the optimum value. Considering the situations where the rolling force is low, it is seen that lower Ra values are obtained in WC inserts than in CBN inserts (Figs. 7, a, and d). However, when the rolling force is increased (Figs. 7, b, c, d, and e), it is seen that CBN inserts have a more positive effect on Ra .

Here, it can be concluded that the best Ra values are obtained in WC inserts with low rolling forces and in CBN inserts with high rolling forces. In addition, according to these results, it can be said that the use of ceramic inserts in deep rolling applications where Ra values are intended to be low is not appropriate compared to other insert types. It is observed that Ra values generally increase with the increase in the number of passes in the WC insert (Figs. 7, a, b, and c). However, the same trend cannot be said for CBN (Figs. 7, d, e, and f) and ceramic (Figs. 7, h, and j) inserts. In this respect, it can be said that the insert type, which is parallel to the literature in terms of Ra values to be obtained, is WC-type inserts. Studies show that Ra values decrease with the increase in the

number of passes [28] and [29] and the most effective parameter on Ra is the number of passes [29].

The graphs obtained in order that the effect of the rolling force in connection with feed rate on Ra can be better understood are presented in Fig. 8. Although it is said that the increase in the rolling force causes an increase in Ra [20] and [29], there are also studies indicating that the increase in the rolling force leads to worse surface quality [28]. While interpreting this situation, some studies stated that when the rolling force exceeds a certain value, deterioration occurs as a result of overloading the material. Abrão et al.

found that for AISI 06 steel, high-pressure values produced higher Ra values than more moderate-pressure values [28].

In deep rolling, the surface of the workpiece is exposed to more heat [12] and [29] as the time to reach the maximum temperature increases with the decrease of the feed rate value. This causes unstable Ra values to occur in WC-type inserts at a low feed rate, depending on the rolling force and the number of passes (Fig. 8). At higher feed rates, a more balanced distribution and an increase in Ra values are observed with the increase in rolling force (Figs. 8, a and c).

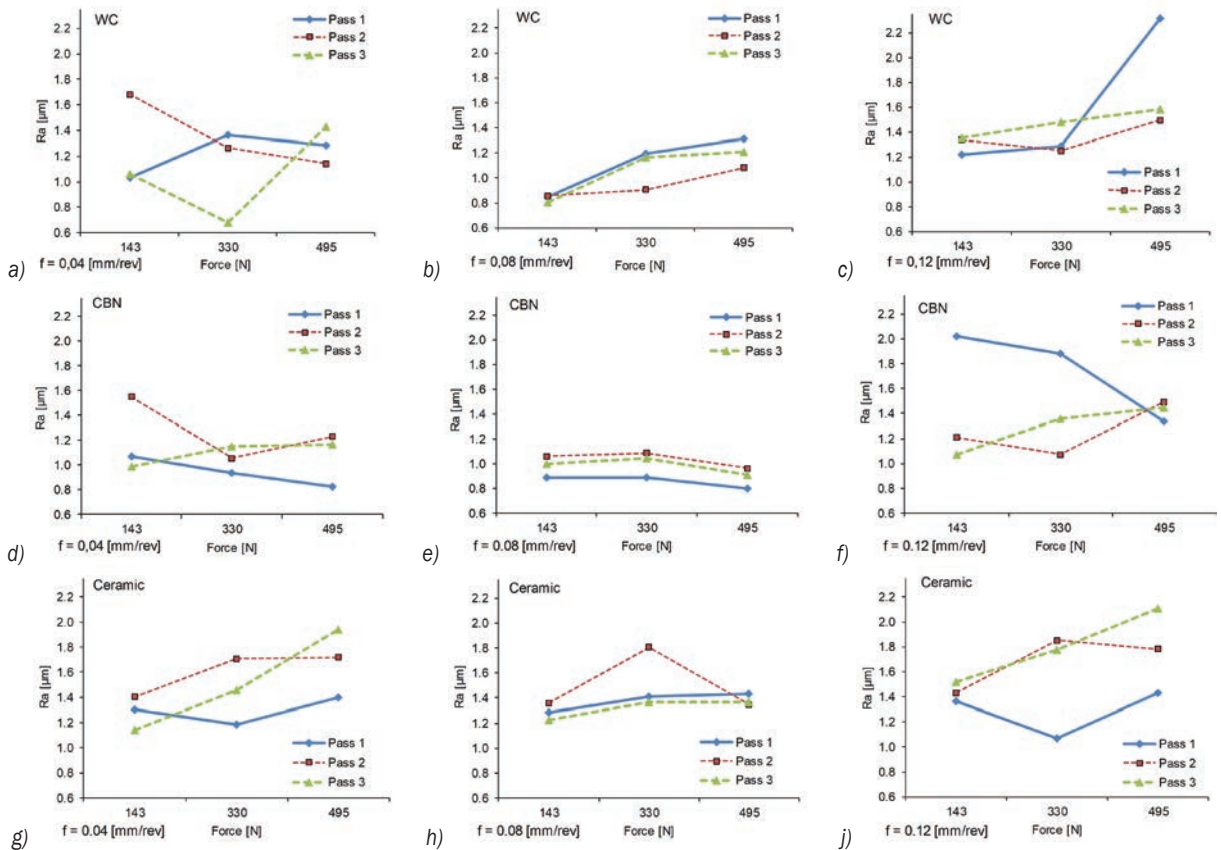


Fig. 8. Display of the relation between rolling force and feed rate values according to inserts a,b and c) WC, d, e and f) CBN, and g, h and j) ceramic inserts

Table 4. ANOVA for surface roughness (Ra)

| Source | DF | Seq SS | Contribution [%] | Adj SS | Adj MS | F-value | P-value |
|--------------------|----|---------|------------------|---------|---------|---------|---------|
| Insert type | 2 | 1.50865 | 18.23 | 1.50865 | 0.75433 | 12.18 | 0.000 |
| Force [N] | 2 | 0.37534 | 4.54 | 0.37534 | 0.18767 | 3.03 | 0.054 |
| Number of passes | 2 | 0.06379 | 0.77 | 0.06379 | 0.03189 | 0.52 | 0.600 |
| Feed rate [mm/rev] | 2 | 1.87061 | 22.60 | 1.87061 | 0.93531 | 15.11 | 0.000 |
| Error | 72 | 4.45776 | 53.86 | 4.45776 | 0.06191 | | |
| Total | 80 | 8.27616 | 100.00 | | | | |

When Figs. 8, b and c are examined, it is seen that the lowest Ra values are $f = 0.08$ mm/rev for WC-type inserts, and Ra values close to each other are obtained when the number of passes is two and three. Abrão et al. [28] stated that there is a decrease in Ra value after 6 bar pressure value, and deterioration occurs after 10 bar for AISI 1045 steel. They stated that the reason for this is the deterioration and spalling in the plastic flow. In Figs. 8 and c, it is understood that the compression value of 43 N for AISI 1045 steel is the most appropriate rolling force value for low Ra values in WC-type inserts.

Looking at the CBN insert type, it is seen that the most stable and ideal feed is $f = 0.08$ mm/rev, similar to the WC insert type (Fig. 8e). However, here, unlike the WC insert type, Ra values decrease with increasing rolling force (Fig. 8). In this insert type, it is understood that the most unstable and highest Ra values are $f = 0.1$ mm/rev (Fig. 8f). Ra values at low ($f = 0.04$ mm/rev) and medium feeds ($f = 0.08$ mm/rev) are quite low for this insert type (Figs. 8, and e). In this type of insert, the ideal conditions for Ra are low pass number, medium feed value ($f = 0.08$ mm/rev) and high rolling force values.

When looking at the ceramic insert type, it is seen that higher Ra values occur in all cases compared to WC and CBN insert types (Figs. 8, h and j). In this insert type, an increase in Ra values is observed with an increase in rolling force. As explained, it was concluded that the formed high temperature remains on the workpiece due to the low thermal conductivity coefficient of the ceramic insert, and as a result, both instability and surface deterioration occur. It is seen that the ideal feed rate is $f = 0.08$ mm/rev in the ceramic insert type as in the other insert types (Fig. 8). When this type of insert is used, low rolling force, low pass number and medium feed values should be chosen.

Variance analysis was performed to see the interaction of Ra and process parameters, to determine the effect rate of the parameters on Ra , and to examine the issue statistically. As a result of the variance analysis, the values in Table 4 were obtained.

When the variance analysis table (Table 4) for Ra is examined, it is seen that the insert type and feed rate values on surface roughness are statistically significant. When the "Contribution" values, which reveal the effect of independent variables on the dependent variable Ra , are examined, it is seen that the most effective parameter on Ra is the feed rate. The effect ranking on the dependent variable Ra was obtained as 22.60 %, 23 %, 4.5 % and 0.7 % for feed rate, insert type, force and number of passes,

respectively. The fact that the effect percentage rates here are not significantly different from each other prevents reaching a very clear conclusion for federate and insert types, which have a significant effect on Ra . Even in the research referenced in the evaluations made for Fig. 8 above, no definite conclusions in machining could be reached. In this respect, more studies are needed to form certain opinions and formulations on deep rolling.

3 CONCLUSIONS and SUGGESTIONS

The following conclusions and suggestions have been listed for WC, CBN and ceramic inserts used in the deep rolling process in order to have wasted cutting tools regained:

- In the deep rolling process with waste inserts, good results are obtained with WC and CBN type inserts in terms of surface roughness, and ceramic inserts in terms of microhardness.
- When the rolling force and pass numbers increased, it was seen that the microhardness in all types of inserts increased. The increase in microhardness is due to the increase in subsurface plastic stress intensity as a result of the increase in pressing force and number of passes.
- It was observed that the highest hardness values were obtained from ceramic inserts, while the lowest values were obtained from WC inserts. This situation is explained by the higher temperature increase on the surface due to the low thermal conductivity of ceramic tips.
- Medium feed rates are suitable for all insert types for AISI 1045 steel, and in this study, this value was established as $f = 0.08$ mm/rev. In WC cutting inserts, unstable Ra values formed with regard to rolling force and number of passes in low feed rates. It is thought that the high thermal conductivity of this insert type and the temperature increase on the surface at low feed are the sources of the unstable structure formed.
- In ceramic type insert, it was seen that in general, Ra values increased with the increase in rolling force. Thus, when this type of insert is used, low rolling force, pass numbers, and medium feed should be chosen.
- In CBN-type inserts, it was seen that Ra values decreased with the increase in rolling force. For this type of insert, the ideal conditions for Ra values occur at low pass numbers, medium feed value ($f = 0.08$ mm/rev) and high rolling force.
- It was determined that the 43 N rolling value for AISI 1045 steel was the most suitable rolling force

for low Ra values in WC-type cutting inserts. WC inserts give good results in low rolling forces. This is due to reduced surface deterioration combined with lower heat generation.

In all conditions, optimum values of process parameters must be obtained in terms of surface deformation, temperature, and stress.

8 REFERENCES

- [1] Ustel, F., Turk, A., Yildiz, K., Kurt, A.O. (2022). Recovery of carbide cutting tools with pyrometallurgical method, from <https://search.trdizin.gov.tr/tr/yayin/detay/612820/>, accessed on 2024-01-13
- [2] Karayazgan, N. (2022). Electrolytic recovery of WC - CO based cutting tools, from <https://acikbilim.yok.gov.tr/handle/20.500.12812/655102>, accessed on 2024-01-13.
- [3] Gürmen, S. (2005). Recovery of nano-sized cobalt powder from cemented carbide scrap. *Turkish Journal of Engineering and Environmental Sciences*, vol. 29, no. 6, p. 343-350.
- [4] Srivastava, R. R., Lee, J. C., Bae, M., Kumar, V. (2019). Reclamation of tungsten from carbide scraps and spent materials. *Journal of Materials Science*, vol. 54, no.1, p. 83-107, DOI:10.1007/s10853-018-2876-1.
- [5] Sandvik (2022). Recycling of carbide cutting tools, from <https://www.sandvik.coromant.com/tr-tr/services/pages/recycling.aspx>, accessed on 2022-08-15.
- [6] Altenberger, I., Scholtes, B. (2000). Recent developments in mechanical surface optimization. *Materials Science Forum*. Trans Tech Publications Ltd, vol. 347, p. 382-398, <https://doi.org/10.4028/www.scientific.net/MSF.347-349.382>, accessed on 2022-08-15..
- [7] Broszeit, E. (1984). Grundlagen der schwingfestigkeitssteigerung durch fest- und glattwalzen. *Materialwissenschaft und Werkstofftechnik*, vol. 15, no. 12, p. 416-420, DOI:10.1002/mawe.19840151204.
- [8] Berstein, G., Fuchsbauer, B., (1982). Deep rolling and fatigue strength. *Z. Werkstofftech*, vol. 13, no. 3, p. 103-109, DOI:10.1002/mawe.19820130309.
- [9] Altenberger, I. (2003). Alternative mechanical surface treatments: microstructures, residual stresses & fatigue behavior. *Shot Peening*, p. 419-434, DOI:10.1002/3527606580.ch54.
- [10] Maiß, O., Röttger, K. (2022). Monitoring the surface quality for various deep rolling processes-limits and experimental results. *Procedia CIRP*, vol. 108, p. 857-862, DOI:10.1016/j.procir.2022.05.199.
- [11] Kinner-Becker, T., Hettig, M., Sölter, J., Meyer, D., (2021). Analysis of internal material loads and process signature components in deep rolling. *CIRP Journal of Manufacturing Science and Technology*, vol. 35, p. 400-409, DOI:10.1016/j.cirpj.2021.06.024.
- [12] Martins, A., M., Leal, C., A., Campidelli, A., F., Abrão, A., M., Rodrigues, P., C., Magalhães, F., C., Meyer, K. (2022). Assessment of the temperature distribution in deep rolling of hardened AISI 4140 steel. *Journal of Manufacturing Processes*, vol. 73, p. 686-694, DOI:10.1016/j.jmapro.2021.11.052.
- [13] Oevermann, T., Wegener, T., Liehr, A., Hübner, L., Niendorf, T. (2021). Evolution of residual stress, microstructure and cyclic performance of the equiatomic high-entropy alloy CoCrFeMnNi after deep rolling. *International Journal of Fatigue*, vol. 153: p. 106-513, DOI:10.1016/j.ijfatigue.2021.106513.
- [14] Scholtes, B. (1997). *Assessment of Residual Stresses, Structural and Residual Stress Analysis by Non-Destructive Methods*. Elsevier, Amsterdam, p. 590-632, DOI:10.1016/B978-044482476-9/50020-7.
- [15] Yuceteknik (2022). Mechanic mould springs, from <https://www.yuceteknik.com/Mekanik-Kalip-Yaylari-Yesil-Yay,PR-1779.html>, accessed on 22-08-27.
- [16] Meyer, D., Brinksmeier, E., Hoffmann, F. (2011). Surface hardening by cryogenic deep rolling. *Procedia Engineering*, vol. 19, p. 258-263, DOI:10.1016/j.proeng.2011.11.109.
- [17] Abrão, A.M., Denkena, B., Köhler, J., Breidenstein, B., Mörke, T. (2014). The influence of deep rolling on the surface integrity of AISI 1060 high carbon steel. *Procedia CIRP*, vol. 13, p. 31-36, DOI:10.1016/j.procir.2014.04.006.
- [18] Noster, U., Altenberger, I., Scholtes, B. (2001). Combined mechanical and thermal surface treatment of magnesium wrought alloy AZ31. *WIT Transactions on Engineering Sciences*, DOI:10.1002/3527607552.ch49.
- [19] Maximov, J.T., Duncheva, G.V., Anchev, A.P., Dunchev, V.P. (2020). Slide burnishing versus deep rolling-a comparative analysis. *The International Journal of Advanced Manufacturing Technology*, vol. 110, no. 7, p. 1923-1939, DOI:10.1007/s00170-020-05950-2.
- [20] Abrão, A.M., Denkena, B., Köhler, J., Breidenstein, B., Mörke, T., Rodrigues, P.C.M. (2014). The influence of heat treatment and deep rolling on the mechanical properties and integrity of AISI 1060 steel. *Journal of Materials Processing Technology*, vol. 214, p. 3020-3030, DOI:10.1016/j.jmatprotec.2014.07.013.
- [21] Loh, N.H., Tam, S.C., Miyazawa, S. (1990). Surface hardening by ball burnishing. *Tribology International*, vol. 23, no. 6, p. 413-417, DOI:10.1016/0301-679X(90)90057-V.
- [22] Loh, N.H., Tam, S.C., Miyazawa, S. (1989). Statistical analyses of the effects of ball burnishing parameters on surface hardness. *Wear*, vol. 129, no. 2, p. 235-243, DOI: 10.1016/0043-1648(89)90261-5.
- [23] Zöltzer, G., Altenberger, I., Scholtes, B. (2001). Einfluss von eigenspannungen auf die mikrohärteverteilung in elastisch-plastisch gebogenen stäben aus C80. *HTM. Härterei-Technische Mitteilungen*, vol. 56, no. 5, p. 347-352, DOI:10.1515/htm-2001-560514.
- [24] Altenberger, I., Scholtes, B., Martin, U., Oettel, H. (1998). Mikrostruktur und wechselverformungsverhalten des mechanisch randschichtverfestigten Stahls Ck 45. *HTM. Härterei Technische Mitteilungen*, vol. 53, no. 6, p. 395-406, DOI:10.1515/htm-1998-530613.
- [25] Altenberger, I., Scholtes, B., Martin, U., Oettel, H., (1999). Cyclic deformation and near surface microstructures of shot peened or deep rolled austenitic stainless steel AISI 304. *Materials Science and Engineering A*, vol. 264, no. 1-2, p. 1-16, DOI:10.1016/S0921-5093(98)01121-6.
- [26] Doğan, B., Hüsametdin, T.A.N. (2018). Investigation of thermal conductivity of ceramic cutting edge based sialon- Si3N4.

Journal of Polytechnic, vol. 21, no. 1, p. 7-12, DOI:10.2339/politeknik.389237.

- [27] Abrão, A.M., Denkena, B., Breidenstein, B. (2014). Surface and subsurface alterations induced by deep rolling of hardened AISI 1060 steel. *Production Engineering*, vol. 8, p. 551-558. DOI:10.1007/s 11740-014-0539-x.
- [28] Abrão, A., M., Denkena, B., Koehler, J., Breidenstein, B., Moerke, T. (2015). The inducement of residual stress through deep rolling of AISI 1060 steel and its subsequent

relaxation under cyclic loading. *International Journal of Advanced Manufacturing Technology*, vol. 79, p. 1939-1947.

- DOI:10.1007/s00170-015-6946-0.
- [29] Prabhu, P.R., Kulkarni, S.M., Sharma, S.S. (2011). An experimental investigation on the effect of deep cold rolling parameters on surface roughness and hardness of AISI 4140 steel. *International Journal of Mechanical and Mechatronics Engineering*, vol. 5, no. 12, p. 2632-2637.

List of reviewers who reviewed manuscripts in 2023

- Husam Jawad Abdulsamad, Iraq
Alexandre M. Abrão, Brasil
Abuzer Açıkgoz, Turkey
Paulo Sergio Afonso, Portugal
Hassan Afshari, Iran
Siddique Akbar, Austria
Marwan Alakhras, UK
Salman Aldriasawi, Iraq
Jorge Enrique Araque Isidro, Italy
Mohammad Arefi, Iran
Muhammad Usman Asad, Canada
- Frank Baginski, USA
Jani Barle, Croatia
Anmol Bathia, India
Michał Batsch, Poland
Hedi Belhadjsalah, Tunisia
Jure Berce, Slovenia
Anton Bergant, Slovenia
Tomaž Berlec, Slovenia
Cristina Biris, Romania
Miha Boltežar, Slovenia
Andrej Bombač, Slovenia
Éd Claudio Bordinassi, Brasil
Marek Boryga, Poland
Rajmohan Bose, India
Jarosław Brodny, Poland
Tomasz Bulzak, Poland
- Michele Calì, Italy
Bing Cao, China
Caterina Capponi, Italy
George Carutasu, Romania
Gregor Cepon, Slovenia
Ferdinand Cerbe, Germany
Himadri Chatopadhyay, India
Alfredo Chávez, Mexico
Peng Cheng, US
Bogdan Chirita, Romania
Filippo Cianetti, Italy
Marco Cirelli, Italy
Marco Cocconcelli, Italy
Franco Concli, Italy
- Martin Česnik, Slovenia
- Omar Dávalos, Mexico
J. Paulo Davim, Poland
Luis de Lacalle Marcaide, Spain
Krisztián Deák, Hungary
Hamed Aghajani Derazkola, Spain
Željko V. Despotović, Serbia
Jiang Ding, China
Ján Dižo, Slovakia
Changbin Dong, China
David B. Dooner, Puerto Rico
Mateja Dovjak, Slovenia
Xing Du, China
Nguyen Dinh Duc, Vietnam
L. Canan Dli ger, Turkey
Paweł Dunaj, Poland
- Radomir Đokić, Serbia
- Rune Elvik, Norway
Igor Emri, Slovenia
Kaan Emre Engin, Turkey
- Mohammad A. Faraj, Iraq
Hamed Farzaneh, Iran
Cuneyt Fetvacı, Turkey
Grzegorz Filo, Poland
Jii gen Fleischer, Germany
Alexey Fomin, Russia
Paolo Franceschi, Italy
Frederico Miguel Freire Rodrigues, Portugal
- Juan Carlos García, Mexico
Rok Gašperšič, Slovenia
Jabbar Gattmah, Turkey
Vijay Gautam, India
Srečko Glodež, Slovenia
Adam Glowacz, Poland
F. Gómez-Silva, Spain
Domen Gorjup, Slovenia
Christoph Greb, Germany
Damir Grguraš, Slovenia
Alec Groysman, Israel
- Tarahom Mesri Gundoshmian, Iran
Leo Gusel, Slovenia
Hamid Haghshenas Gorgani, Iran
- Ali Hajnayeb, Canada
R Halicioglu, Turkey
Miroslav Halilović, Slovenia
Patricia Habib Hallak, Brasil
Anis Hamza, Tunisia
Boštjan Harl, Slovenia
Mikihito Hirohata, Japan
Sergej Hloch, Slovakia
Zbigniew Humienny, Poland
Zbigniew Humienny, Poland
Soichi Ibaraki, Japan
Musa Alhaji Ibrahim, Nigeria
Jamshed Iqbal, Pakistan
Hajro Ismar, Bosnia and Herzegovina
Špiro Ivošević, Montenegro
- Adam Jacso, Hungary
Goran Janjić, Bosnia and Herzegovina
Juliana Javorova, Bolgarij
Boris Jerman, Slovenia
Matija Jezeršek, Slovenia
Hongxiang Jiang, China
Jihailiu Jihai, China
- Nikolaos Karkalos, Grece
Masashi Kashiwagi, Japan
Zdenka Keran, Croatia
Nicole Kessissoglou, Australia
Mohammed-El-Amine Khodja, Algeria
Kyo-Seon Kim, South Korea
Pino Koc, Slovenia
Borut Kosec, Slovenia
Robert Kosturek, Poland
Nataša Kovač, Montenegro
Győ gy Kovács, Hungary
Grzegorz Krolczyk, Poland
Vivek Kumar, India

- Robert Kunc, Slovenia
Amanendra K. Kushwaha, USA
Janez Kušar, Slovenia
- Marzena Lachowicz, Poland
Andrej Lebar, Slovenia
Stanislaw Legutko, Poland
Hirpa Lemu, Norway
Changhe Li, China
Xin Liao, China
Mathias Liewald, Germany
Edgar López, Mexico
Darko Lovrec, Slovenia
- Liteng Ma, China
Miloš Madić, Serbia
Olasumbo Makinde, South Africa
Petr Masek, Czech Republic
Nicolae Medan, Romania
Marc Medrano, Spain
N. Muthu Mekala, India
Giovanni Meneghetti, Italy
Andrijana Milinović, Croatia
Mladomir Milutinović, Serbia
Sergey Mironov, Russia
Ava Mohammed, Iraq
R. Mohanraj, India
Nikolaj Mole, Slovenia
Gonzalo Moreno, Brasil
Essam B. Moustafa, Saudi Arabia
Manuel Moya, Spain
Matic Može, Slovenia
Jacek Mucha, Poland
Andrzej Myśliński, Poland
- Balazs Nemeth, Hungary
Trung-Thanh Nguyen, Vietnam
Johann Nicolics, Austria
Anatolij Nikonov, Slovenia
- Milosav Ognjanović, Serbia
Ivan Okorn, Slovenia
Simon Oman, Slovenia
Ashraf Omar, Maroko
S. Omprakasam, India
Sabri Ozturk, Turkey
- Srinivasa P. Pai, India
Massimiliano Palmieri, Italy
Chandan Pandey, India
Branislav Panić, Slovenia
- Parth Sarathi Panigrahy, USA
Yong-Hwa Park, South Korea
Ji Pei, China
Tomaž Pepelnjak, Slovenia
Tomas Petr, Czech Republic
Igor Petrović, Slovenia
Vu Ngoc Pi, Vietnam
Miha Pipan, Slovenia
Bojan Podgornik, Slovenia
Pavel Polach, Czech Republic
Marko Polajnar, Slovenia
Milton Luiz Polli, Brasil
Antonio Posa, USA
Radu-Emil Precup, Romania
Chand R. Prem, India
Franci Pušavec, Slovenia
- Riad Ramadani, Kosovo
Matjaž Ramšak, Slovenia
Dunja Ravnikar, Slovenia
Sunil Raykar, India
Dragan Rodic, Serbia
Andreas Rosenkranz, Chile
Michal Ruzek, France
- Mohammad Reza Safaei, Saudi Arabia
serdar şahin, Turkey
Rafael Sanchez Crespo, UK
Manel Sbayti, Tunisia
Dieter Schuöcker, Austria
Sathish Kumar Selvaperumal, Malesia
V. Serbezov, Bolgaria
Huseyin Sevinc, Turkey
Yujie Shen, China
Xia Sheng, China
Krzysztof Siczek, Poland
Silvio Simani, Italy
Vilmos Simon, Hungary
Noan Tonini Simonassi, Brasil
Rabesh kumar Singh, India
Jasjeevan Singh, India
Lidija Slemenik Perše, Slovenia
Luigi Solazzi, Italy
Fikret Sömez, Turkey
Mohsen Soori, Turkey
Marco Sortino, Italy
Uroš Stritih, Slovenia
Idawu Yakubu Suleiman, Nigeria
Wenjing Sun, China
- S. Suresh, India
Rbert Szabolcsi, Hungary
- Domen Šeruga, Slovenia
Tatjana Šibalija, Serbia
Marko Šimic, Slovenia
Graciela Šterpin Valić, Croatia
Roman Šturm, Slovenia
Titus Thankachan, India
Stefano Tornincasa, Italy
Xuan Bo Tran, Vietnam
Anastasios Tzotzis, Greece
- Cuneyt Uysal, Turkey
Çağrı Uzay, Turkey
Erdem Uzunsoy, Turkey
- Wim Van Helden, Austria
J. A. Velasco-Parra, Colombia
Aleksandar Vencel, Serbia
Simone Venturini, Italy
Arkady Voloshin, USA
Goran Vorotovic, Serbia
Rok Vrabič, Slovenia
Željko Vukelić, Slovenia
- Zhenshuai Wan, China
Zhenqian Wang, China
Xuhao Wang, China
Yueyong Wang, China
Shunli Wang, China
Chenxue Wang, China
Jürgen Weber, Germany
Jerzy Adam Winczek, Poland
Hongwei Yan, China
- Yuewei Yu, China
Yang Yu, Australia
- Daniel Zabek, UK
Binglong Zhang, China
Wanjie Zhang, China
Xiaohong Zhang, China
Wei Zhao, China
Bo Zhou, China
Youhang Zhou, China
Shuaidong Zou, China
Samo Zupan, Slovenia
- Uroš Župerl, Slovenia

The Editorial would like to thank all the reviewers in participating in reviewing process.
We appreciate the time and effort and greatly value the assistance as a manuscript reviewer for
Strojniški vestnik – Journal of Mechanical Engineering.

Vsebina

Strojniški vestnik - Journal of Mechanical Engineering
letnik 70, (2024), številka 1 2
Ljubljana, januar-februar 2024
ISSN 0039-2480

Izhaja dvomesečno

Razširjeni povzetki (extended abstracts)

| | |
|--|-------|
| Samo Zupan, Robert Kunc: Pregled načel in pravil za geometrijske specifikacije izdelkov v skladu z aktualnimi ISO standardi | SI 3 |
| Zhengfang Li, Xudong Di, Zhengyuan Gao, Zhiguo An, Ling Chen, Yuhang Zhang, Shihong Lu: Izboljšanje dimenzijske točnosti valovitega diska iz materiala Ti-6Al-4V po električnem inkrementalnem preoblikovanju pločevine v vročem | SI 4 |
| Ireneusz Zagórski, Monika Kulisz, Anna Szczepaniak: Uporaba statistične analize in modeliranja za določitev parametrov hrapavosti po končni obdelavi magnezijevih zlitin z orodji z variabilnim kotom vijačnice | SI 5 |
| Tat-Khoa Doan, Trung-Thanh Nguyen, An-Le Van: Večkriterijska optimizacija procesa struženja z gnanim orodjem glede na okoljske in kakovostne kazalnike | SI 6 |
| Xin Tian, Guangjian Wang, Yujiang Jiang: Nova metoda za računanje trenutnega izkoristka in nihanj momenta pri čelnih zobniških gonilih | SI 7 |
| Grzegorz Struzikiewicz: Raziskava struženja titanovih zlitin z orodji Prime A v pogojih visokotlačnega hlajenja | SI 8 |
| Berat Gürçan Şentürk, Mahmut Cüneyt Fetvacı: Prilagojen pristop h generiranju zobnic za beveloidne zobnike | SI 9 |
| Oktay Adıyaman: Študija možnosti uporabe izrabljenih rezalnih ploščic za gladilno valjanje | SI 10 |

Pregled načel in pravil za geometrijske specifikacije izdelkov v skladu z aktualnimi ISO standardi

Samo Zupan*– Robert Kunc

Univerza v Ljubljani, Fakulteta za strojništvo, Slovenija

V članku smo pregledali filozofijo načel in pravil v ozadju serije ISO standardov za področje geometrijskih specifikacij proizvodov (GPS), ki so ob materialnih specifikacijah ključna sestavina posredovanih informacij pri učinkovitem načrtovanju in izdelavi mehanskih izdelkov ter tudi pri komunikacijah med partnerji, ki sodelujejo v teh procesih. Področje GPS, za katerega skrbi ISO tehnični komite št. 213, vključuje številne standarde (trenutno 44), ki opisujejo zahtevano natančnost geometrijskih značilnosti »velikosti« (tolerance mer) in geometrijskih toleranc, ki se uporabljajo za zagotavljanje natančnosti oblike, orientacije in lokacije geometrijskih značilnosti v 3D prostoru. Opravljen je pregled temeljnih načel in pravil, ki jih določajo aktualni standardi ISO GPS. Opisana je organizacija sistema ISO GPS standardov in povzetek vsebine bolj relevantnih standardov, ki so nedavno doživeli več revizij ali so povsem novi. Standardi ISO GPS temeljijo na načelu dvojnosti: geometrijskim specifikacijam neizogibno sledijo ustrezni postopki verifikacije. V tem prispevku smo se osredotočili predvsem na steber geometrijskih specifikacij, izpustili pa smo celotni vzporedni steber verifikacije, ki v skladu z modelom matrice ISO GPS standardov vsebuje še večje število dokumentov (standardov o merjenju oziroma preverjanju). Področje GPS je torej zelo obsežno in v stebru specifikacij zajema poglavja toleranc kotiranih mer, geometrijske tolerance ter definicije in omejitve stanja površin (nov standard ISO 21920:2021) in robov (čemer smo se v tem prispevku prav tako izognili).

Načela in osnovna pravila za jasen in nedvoumen zapis vseh zahtev za geometrijske značilnosti izdelkov so razdeljena v skupine temeljnih, splošnih in dopolnilnih standardov ISO GPS. Organizacija standardov je prikazana s pomočjo matrice GPS, ki je definirana v temeljnem ISO 14638:2015 standardu. Glavna načela področja so dana večinoma v ISO 8015:2011 in v drugih temeljnih standardih, ki podajajo osnovne definicije. Načela in pravila za praktično rabo pri določanju in uporabi toleranc mer linearnih velikosti zunanjih in notranjih oblik (premeri oz. širine čepov in lukenj) so podrobno določena v seriji ISO 14405 standardov (trije deli). Standardi prinašajo številne nove definicije pomena linearne (1. del) in kotne (3. del) velikosti čepov in lukenj, kjer so mnoge specifikacije povezane z novimi tehnologijami in metodami verifikacije. Definicije velikosti geometrijske značilnosti čisto temeljijo na matematičnem obravnavanju izmerkov v oblaku točk podanih z absolutnimi prostorskimi koordinatami. Bistvena novost so definicije velikosti s pomočjo statističnih cenilk, ki jih pogosto uporabljamo pri statističnem nadzoru procesov (SPC). Hkrati ISO 14405-2 definira kotirane mere, ki ne predstavljajo značilnih velikosti čepov in lukenj in predlaga, da vse take značilnosti toleriramo dosledno z uporabo geometrijskih toleranc oblike, orientacije, lege in teka v skladu s povezanimi pravili (več standardov).

Najbolj obsežnemu poglavju geometrijskih toleranc (GT) so posvečeni številni ISO GPS standardi in večina jih je bila v zadnjem obdobju pomembno posodobljena in nadgrajena. V članku so ključni aktualni standardi naštetih v virih. Temeljni standard za geometrijske tolerance je ISO 101 207, ki pa ne vsebuje vsega potrebnega za obvladovanje področja. Pomembne vsebine imajo tudi drugi ISO standardi za GT (definicije toleranc oblike, profila, teka, materialni pogoji (ključni npr. za izdelavo kalibrov), reference oziroma baze itd. Članek daje pregled in glavne povzetke o teh ISO GT standardih ter daje nekaj primerov, ki prikazujejo tudi najbolj opazne novosti pri grafičnem simbolnem jeziku. ISO 16792:2021 definira načela in pravila v skladu z sodobnimi potrebami in filozofijo »Model Based Definitions« (MBD) posredovanja vseh geometrijskih informacij o izdelkih že s prostorskimi virtualnimi (3D CAD) modeli. Obsežen standard vsebuje vsa potrebna načela in pravila, po katerih lahko geometrijske definicije in zahteve z uporabo ISO simbolov vnesemo bodisi v 3D virtualne model izdelkov in po enakih načelih in pravilih se ti lahko dedujejo tudi na 2D delavniške risbe. Dalje članek obravnava tudi pomembno GPS načelo, po katerem je na delavniških risbah možno in potrebno podati vse zahteve o tolerancah na splošen ali na izrecen način, pravila o tem pa so urejena v več ISO standardih glede na tehnologijo izdelave izdelkov.

Ker gre za pomembne osnove tehnične komunikacije, bi morali uporabniki (inženirji) dobro poznati te standarde. Pogosto pa ni tako, saj gre za obsežno tematiko s pogostimi spremembami in novostmi, kar povzroča znaten napor in s tem težave praktičnim uporabnikom pri usposabljanju. Zaradi velikega obsega standardov inženirji pri delu v praksi težko sledijo tej dinamiki, težava pa je tudi v dostopnosti standardov za uporabnike, saj je ta pogosto povezana z znatnimi stroški. To povzroča številne težave v praksi, saj komunikacija med partnerji (naročniki in dobavitelji in tudi v podjetju) pogosto ne poteka na istih izhodiščih.

Ključne besede: ISO standard, geometrijske specifikacije proizvodov, GPS, geometrijske tolerance, načela, pravila, velikost, toleranca, verifikacija

Izboljšanje dimenzijske točnosti valovitega diska iz materiala Ti-6Al-4V po električnem inkrementalnem preoblikovanju pločevine v vročem

Zhengfang Li¹ – Xudong Di² – Zhengyuan Gao^{3*} – Zhiguo An³ – Ling Chen⁴ – Yuhang Zhang¹ – Shihong Lu⁵

¹ Univerza Kunming, Šola za strojništvo in elektrotehniko, Kitajska

² Jianghuai Automobile Group Co., Ltd., Raziskovalni inštitut za tehnologijo osebnih vozil, Kitajska

³ Univerza Chongqing Jiaotong, Šola za mehatroniko in avtomobilsko tehniko, Kitajska

⁴ Univerza Kunming, Oddelek za znanost in tehnologijo, Kitajska

⁵ Univerza za aeronavtiliko in astronavtiliko v Nanjingu, Kolidž za strojništvo in elektrotehniko, Kitajska

Veganje robov predstavlja veliko težavo pri električnem inkrementalnem preoblikovanju valovitih diskov iz materiala Ti-6Al-4V v vročem in lahko privede do znatnih dimenzijskih napak. V članku je zato predstavljen predlog novega postopka za odpravo napak pri preoblikovanju valovitih diskov iz materiala Ti-6Al-4V, ki kombinira električno inkrementalno preoblikovanje v vročem z električno podprtim kalibriranjem.

Predstavljen je tudi eksperimentalen proizvodni postopek za analizo vpliva parametrov preoblikovalnega procesa in kalibriranja na dimenzijsko točnost diska. Veganje na robu izdelka kot ciljni parameter (h) je bilo izmerjeno z inštrumentom za meritve višine. Valoviti disk je bil izdelan na numerično krmiljenem stroju, uporabljena pa sta bila tudi izvor enosmernega toka (od 0 A do 3000 A) za segrevanje in termovizijska kamera (proizvajalec: Shenzhen Ce-temp Technology Co., Ltd; tip: PI1M-PI80x; merilno območje: $-20\text{ }^{\circ}\text{C}$ do $1500\text{ }^{\circ}\text{C}$; napaka: $\pm 0,1\text{ }^{\circ}\text{C}$) za meritve temperature v coni preoblikovanja.

Disk je bil izdelan v dveh korakih. Prva pot preoblikovalnega orodja je bila uporabljena za izdelavo bočne stene valovitega diska, nasprotna stena pa je bila izdelana z drugo potjo. Za analizo kakovosti preoblikovanja valovitega diska po metodi kontrolnih spremenljivk so bili izbrani procesni parametri tok, podajalna hitrost in velikost koraka. Referenčna temperatura žarjenja titanove zlitine Ti-6Al-4V glede na mehanizem popuščenja napetosti je $600\text{ }^{\circ}\text{C}$ do $650\text{ }^{\circ}\text{C}$. Izbranih je bilo pet vrednosti toka (2200 A, 2400 A, 2600 A, 2800 A in 3000 A) ustrezno tradicionalnim postopkom žarjenja. Ustrezne temperature znašajo $563,7\text{ }^{\circ}\text{C}$, $593,6\text{ }^{\circ}\text{C}$, $623,5\text{ }^{\circ}\text{C}$, $652,3\text{ }^{\circ}\text{C}$ in $684,1\text{ }^{\circ}\text{C}$. Uporabljeni so bili časi 10 min, 15 min, 20 min, 25 min, 30 min in 35 min za analizo sprememb ciljne vrednosti ob upoštevanju napak zaradi visokotemperaturne oksidacije titanove zlitine Ti-6Al-4V. Članek obravnava tematsko področje preoblikovanja pločevine.

Eksperimenti so pokazali, da je izdelani valoviti disk brez razpok in izboklin pri kombinaciji parametrov 2200 A, 900 mm/min in 0,2 mm. Vrednosti 3000 A in 30 min sta optimalni za kalibriranje, pri katerem so v veliki meri odpravljene napake veganja iz faze preoblikovanja.

Ciljna vrednost pri optimalnih procesnih parametrih še vedno znaša 2,1 mm, nadaljnje zmanjšanje višine pa bo lahko predmet prihodnjih raziskav.

V članku je predstavljen predlog novega postopka za odpravo napak pri preoblikovanju valovitih diskov iz materiala Ti-6Al-4V, ki kombinira električno inkrementalno preoblikovanje v vročem z električno podprtim kalibriranjem. Podrobno je preučen vpliv parametrov procesa na nastanek razpok med preoblikovanjem in določena je optimalna kombinacija parametrov za uspešno preoblikovanje valovitega diska iz materiala Ti-6Al-4V. Na tej podlagi sta bila ločeno izbrana in analizirana naprava za kalibriranje in vrednost el. toka za odpravo napak veganja. Eksperimenti so dokazali uporabnost predlaganega izdelovalnega postopka. Rezultati raziskave bodo uporabni za hitro izdelavo valovitih diskov v letalski in vesoljski industriji, postopek pa bo z dopolnitvami uporaben tudi za avtomobilsko industrijo, biomedicino, industrijo tirnih vozil idr.

Ključne besede: inkrementalno preoblikovanje pločevine, električno preoblikovanje v vročem, električno podprto kalibriranje, veganje robov, valoviti disk, optimizacija velikosti

Uporaba statistične analize in modeliranja za določitev parametrov hrapavosti po končni obdelavi magnezijevih zlitin z orodji z variabilnim kotom vijačnice

Ireneusz Zagórski^{*} – Monika Kulisz² – Anna Szczepaniak¹

¹ Tehniška univerza v Lublinu, Fakulteta za strojništvo, Poljska

² Tehniška univerza v Lublinu, Fakulteta za management, Poljska

Obstaja pomanjkanje objav na področju analize končnih obdelav magnezijevih zlitin, zlasti z rezkanjem. Cilj raziskave je bila zato analiza procesa končne obdelave magnezijevih zlitin AZ91D in AZ31 z rezkanjem. Analiziran je bil vpliv sprememb tehnoloških parametrov rezkanja na 2D-parametre površinske hrapavosti, kot so Rq , Rt , Rv in Rp , kakor tudi vpliv spremembe variabilnega kota vijačnice steblastega rezkarja λ_s ($\lambda_s = 20^\circ$, $\lambda_s = 50^\circ$). Opravljene so bile statistične analize in numerične simulacije s pomočjo umetnih nevronske mreže.

Definicija problema: obravnavani problem je izbira ustreznih tehnoloških parametrov končne obdelave, ki bo zagotavljal visoko kakovost končne površine obdelovancev. Uporabljena je bila enofaktorska metoda načrtovanja eksperimentov.

Rezkanje je bilo opravljeno na vertikalnem obdelovalnem centru AVIA VMC80H S. Uporabljena sta bila dva trdokovinska steblasta rezkarja s tremi rezalnimi robi premera 16 mm in variabilnim kotom vijačnice λ_s ($\lambda_s = 20^\circ$, $\lambda_s = 50^\circ$). Za vpenjanje steblastih rezkarjev v orodno držalo je bila uporabljena naprava za nakrčevanje. Orodje v držalu je bilo na ustreznem stroju centrirano do preostale neuravnoteženosti 0,25 g mm (G2.5). Nato je bilo opravljeno rezkanje v naslednjem razponu tehnoloških parametrov: rezalna hitrost $v_c = 400$ m/min do 200 m/min, podajanje na zob $f_z = 0,05$ mm/zob do 0,3 mm/zob, aksialna globina reza $a_p = 0,1$ mm do 0,5 mm, radialna globina reza $a_e = 0,5$ mm do 3,5 mm. Meritve površinske hrapavosti so bile izvedene na bočnih in čelnih površinah s kontaktnim merilnikom hrapavosti HOMMEL TESTER T1000. Opravljene so bile tudi statistične analize (s paketom Statistica 13) in numerične simulacije s pomočjo umetnih nevronske mreže (s paketom Matlab).

Na hrapavost obdelane površine vplivajo tako sprememba kota vijačnice kakor tudi izbrani tehnološki parametri rezkanja. Najboljše modele je dalo omrežje z 10 nevroni v skitem sloju. Mreže, ustvarjene z modeliranjem parametrov površinske hrapavosti, imajo glede na izračunane vrednosti regresijskih parametrov zadovoljivo prediktivno zmogljivost. Rezultati modeliranja z nevronske mreže kažejo, da so le-te učinkovito orodje za napovedovanje parametrov površinske hrapavosti.

Možnosti za prihodnje raziskave in identificirane omejitve pri raziskavi: nadaljevanje raziskav na področju končne in precizne obdelave magnezijevih zlitin, edina potencialna omejitev je nagnjenost manjših odrezkov k vžigu med obdelavo.

Analiza površinske hrapavosti je še posebej pomembna za kakovost obdelanih komponent strojev in naprav. Kakovost in hrapavost površin sta še pomembnejši v kontekstu končnih obdelav. Končna obdelava lahkih zlitin (aluminija in magnezija) je pomembna s praktičnega vidika, obstaja pa pomanjkanje celovitih študij omenjene tematike.

Ključne besede: magnezijeve zlitine, končna obdelava, hrapavost, kakovost površin, statistična analiza, umetne nevronske mreže

Večkriterijska optimizacija procesa struženja z gnanim orodjem glede na okoljske in kakovostne kazalnike

Tat-Khoa Doan¹, Trung-Thanh Nguyen¹, An-Le Van^{2,*}

¹ Tehniška univerza Le Quy Don, Fakulteta za strojništvo, Ha Noi, Vietnam

² Univerza Nguyen Tat Thanh, Tehniška fakulteta, Ho Chi Minh, Vietnam

Cilj predstavljene študije je optimizacija parametrov procesa struženja materiala Ti6Al4V z gnanim orodjem – nagibni kot, globina reza, hitrost podajanja in vrtilna frekvenca – za zmanjšanje skupne rabe energije, hrupa med obdelavo in površinske hrapavosti.

Učinkovita gnana rotacijska orodja z visoko togostjo za obdelavo trdih jekel še niso bila zasnovana in izdelana, da bi lahko zamenjala fiksna stružna orodja. Glavna slabost orodij, ki so predstavljena v obstoječi literaturi, je majhna togost. Glasen hrup lahko povzroči okvare sluha in kroničen stres, zato mora biti pri struženju z gnanimi orodji poskrbljeno za zmanjšanje obremenitve s prahom. Prav tako še niso bili opredeljeni optimalni parametri procesa za zmanjšanje rabe energije, hrapavosti in emisij hrupa.

Prediktivni modeli so bili postavljeni na podlagi regresijske metode. Pri izbiri vrednosti uteži in optimalnih rešitev so bili uporabljeni metoda na podlagi vpliva odstranitve kriterijev, izboljššan optimizacijski algoritem z rojem delcev s kvantnim vedenjem in TOPSIS.

Glavni rezultati:

- Raba energije, površinska hrapavost, hrup med struženjem in celotni stroški so se zmanjšali za 6,7 %, 22,3 %, 2,3% oz. 8% .
- Na odziv pri struženju sta vplivali predvsem podajalna hitrost in vrtilna frekvenca.

Vpliv dejavnikov struženja z gnanim orodjem na zmogljivost proizvodnje in ogljični odtis bo raziskan v prihodnje.

Predstavljeno rezalno orodje je primerno tudi za obdelavo drugih zlitin, ki so zahtevne za odrezavanje. Iz trenutne izvedbe bi bilo mogoče razviti nova stružna orodja.

Z empiričnimi korelacijami kriterijev zmogljivosti je mogoče napovedovati rabo energije, hrapavost po struženju in emisijo hrupa.

Rezultate optimizacije je mogoče uveljaviti za izboljšanje tehnoloških parametrov v praksi.

Predstavljeni stružni proces je mogoče uporabiti tudi za obdelavo zunanjih površin izdelkov iz drugih zlitin, ki so težavne za odrezavanje.

Opisani pristop k optimizaciji je poleg tega primeren za odpravo težav pri drugih obdelovalnih postopkih.

Za izračun celotnih stroškov je mogoče uporabiti model stroškov struženja.

Ključne besede: struženje z gnanim rotacijskim orodjem, celotna raba energije, površinska hrapavost, emisija hrupa, IQPSO

Nova metoda za računanje trenutnega izkoristka in nihanj momenta pri čelnih zobniških gonilih

Xin Tian² – Guangjian Wang^{2,*} – Yujiang Jiang²

1

² Univerza v Čongčingu, Kolidž za strojništvo in avtomobilsko tehniko, Kitajska

Kolaborativni roboti so pomembni za sodobno industrijo, ozko grlo pri uporabi teh robotov pa predstavlja izkoristek sklepnih reduktorjev. Trenutna nihanja izkoristka in momenta pri čelnih zobniških dvojicah v sklepnih reduktorjih neposredno vplivajo na njihovo zmogljivost pomika in točnost. V članku je predstavljen računski model za napovedovanje trenutnega izkoristka in nihanj momenta pri zobniških dvojicah ob upoštevanju ravnovesja momentov v točki ubiranja, porazdelitve sil med zobmi in modelov količnika trenja. Nihanja momenta pri zobniških dvojicah do sedaj še niso bila obravnavana v znanstveni literaturi. Predstavljena je primerjava trenutnega izkoristka in nihanj momenta pri zobniških dvojicah ob upoštevanju povprečnega količnika trenja (AFC) na podlagi Coulombovega trenja in časovno spremenljivega količnika trenja (TFC) na podlagi elastohidrodinamičnega mazanja. Analizirana je odvisnost med trenutnim izkoristkom in nihanjem momenta gonila in obravnavan je vpliv kontaktnega razmerja na izkoristek. Za razliko od obstoječih raziskav, ki se osredotočajo predvsem na vpliv izhodnega momenta in hitrosti na povprečni izkoristek zobniških gonil, ta članek preučuje tako obremenitvene in hitrostne razmere kakor tudi vpliv površinske hrapavosti in delovne temperature mazalnega olja na trenutni izkoristek in nihanja momenta. Učinkovitost in točnost predlagane metode v danih obratovalnih pogojih je bila potrjena s primerjavo s tehnikami za računanje izkoristka iz literature.

Rezultati kažejo, da je trenutni izkoristek zobniškega gonila v območju ubiranja dveh zob manjši kot v območju ubiranja enega zoba. Izkoristek je za neprekinjen in stabilen prenos mogoče izboljšati z zmanjšanjem kontaktnega razmerja. Različni modeli količnika trenja signifikantno vplivajo na izkoristek in nihanja izkoristka zobniških gonil. Izkoristek, izračunan po modelu časovno spremenljivega količnika trenja, je manjši od izkoristka, izračunanega po modelu povprečnega količnika trenja, največja razlika med obema pa znaša 1,86 %. Vrednost nihanja momenta pri povprečnem količniku trenja je manjša kot pri časovno spremenljivem količniku trenja. Trenutni izkoristek zobniškega gonila in trenutni vhodni moment se zmanjšata pod konstantno obremenitvijo. Nihanje izkoristka se poveča, prav tako pa se poveča nihanje vhodnega momenta. Variabilnost trenutnega izkoristka zobniškega gonila v danih obratovalnih pogojih lahko doseže 3,34 %, nihanja momenta pa 5,19 Nm. Ob porastu hitrosti na vhodu se poviša obratovalna temperatura mazalnega olja, zmanjšanje površinske hrapavosti zobniškega gonila pa lahko izboljša izkoristek prenosa in zmanjša nihanja momenta med ubiranjem. Povečanje izhodnega momenta poveča nihanja momenta.

Raziskava tako izpolnjuje vrzel na področju nihanja momenta pri zobniških dvojicah ter predstavlja nov prediktivni in računski model za trenutni izkoristek in nihanja momenta pri zobniških dvojicah. Model zagotavlja solidno podporo raziskavam in aplikacijam sklepnih reduktorjev kolaborativnih robotov ter prinaša nove zamisli in metode za preučevanje trenutnega izkoristka in nihanj momenta. V članku je predstavljena metoda za numerično računanje takojšnjega izkoristka in nihanj momenta pri zobniških dvojicah z zunanjim ubiranjem na podlagi teoretične analize. Nekateri rezultati izračunov se ujemajo s predhodnimi študijami. Predstavljeni model upošteva samo trenutni izkoristek in nihanja momenta pri zobniških gonilih v pogojih drsnega trenja, ne zajema pa vpliva izgub zaradi kotalnega trenja in izgub, ki niso povezane z obremenitvijo. Prezrte so tudi natančnost in napake v izdelavi zobniških gonil, zato bo v prihodnje potrebna eksperimentalna verifikacija modela. Prihodnje raziskave bodo usmerjene v razvoj modela trenutnega izkoristka in nihanj momenta v sklepnih reduktorjih kolaborativnih robotov, sestavljenih iz zobniških dvojic.

Ključne besede: kolaborativni robot, trenutni izkoristek, nihanje momenta, količnik trenja, porazdelitev obremenitev

Raziskava struženja titanovih zlitin z orodji Prime A v pogojih visokotlačnega hlajenja

Grzegorz Struzikiewicz*

Znanstveno-tehniška univerza AGH, Fakulteta za strojništvo in robotiko, Poljska

Na področju strojne obdelave poteka stalen razvoj novih metod za izboljšanje kakovosti in učinkovitosti obdelovalnih postopkov. Glavna motivacija za pripravo pričujočega članka je bilo zagotavljanje zahtevane kakovosti procesa struženja titanove zlitine z največjo učinkovitostjo ob upoštevanju oblike odrezkov. Značilna težava pri struženju titanovih zlitin je učinkovitost lomljenja in odstranjevanja odrezkov iz cone obdelave. Novost v predstavljeni raziskavi je kombinacija nove zasnove rezalnega orodja in postopkov za obdelavo titanovih zlitin, ki izboljšuje učinkovitost obdelave. V ta namen je bila analizirana uporaba značilnih stružnih orodij tipa Prime v kombinaciji z visokotlačnim hlajenjem (HPC).

Glavna tema analize je bila opredelitev vpliva rezalnih parametrov (f , a_p , v_c) na vrednosti rezalnih sil, kakor tudi količnika lomljenja odrezkov C_{ch} in oblike odrezkov. Za vzdolžno struženje titanove zlitine Ti6Al4V ELI so bila uporabljena trdokovinska orodja Sandvik Coromant kvalitete 115. Uporabljen je bil povišan tlak hladilno-mazalne tekočine $p = 70$ bar. Izmerjene so bile komponente skupne rezalne sile pri končni obdelavi z variabilnimi rezalnimi parametri v naslednjih razponih: podajalna hitrost $f = 0,1$ mm/vrt do $0,4$ mm/vrt, globina rezanja $a_p = 0,25$ mm do $1,0$ mm in rezalna hitrost $v_c = 40$ m/min do 80 m/min. Izkazalo se je, da je rezalna sila odvisna predvsem od podajanja in od globine reza. Predstavljena je analiza oblike ustvarjenih odrezkov in opredeljena je odvisnost vrednosti količnika lomljenja odrezkov C_{ch} od rezalnih parametrov. Opredeljena je tudi metoda za iskanje največje učinkovitosti procesa struženja ob upoštevanju želene vrednosti količnika lomljenja odrezkov.

Rezultati analize so predstavljeni v nadaljevanju.

- Rezalna sila F_c je v linearni povezavi z obravnavanimi rezalnimi parametri. Statistično najbolj signifikanten parameter pri tem je globina reza a_p , sledi pa ji podajanje f . Vpliv rezalne hitrosti v_c na srednjo rezalno silo je bistveno manjši.
- Globina reza a_p je najpomembnejši dejavnik, ki vpliva na količnik lomljivosti odrezkov C_{ch} . Oblika nastalih odrezkov (pravilna, sprejemljiva in nepravilna) je odvisna od razpona rezalnih parametrov. Odrezki prave oblike so bili v preizkušenem razponu rezalnih parametrov v povprečju doseženi pri vrednostih $a_p \leq 0,75$ mm, $f \geq 0,2$ mm/vrt. Pri višji vrednosti rezalne hitrosti $v_c = 80$ m/min se je zmanjšal količnik lomljenja odrezkov.
- Doseganje prave oblike odrezkov pri končni obdelavi titanove zlitine Ti6Al4V v pogojih obdelave HPC je odvisna od sinergije med dejavniki, kot so vrednosti rezalnih parametrov, oblika in stopnja izpolnitve lomilca odrezkov na cepilni ploskvi ter tlak hladilno-mazalne tekočine. V opisanih pogojih je mogoče izboljšati učinkovitost obdelave z izbiro rezalne hitrosti.

V nadaljevanju bo mogoče nadaljevati z razvojem in simulacijo procesa struženja zlitine Ti6Al4V z orodji tipa Prime ter raziskati obrabljanje teh orodij pri obdelavi materialov, ki so zahtevni za odrezavanje.

Ključne besede: struženje, orodja Prime A, titanova zlitina, Ti6Al4V, rezalne sile, oblika odrezka, indeks lomljenja odrezkov

Prilagojen pristop h generiranju zobnic za beveloidne zobnike

Berat Gürçan Şentürk* – Mahmut Cüneyt Fetvacı²

¹Univerza Dogus, Turčija

²Univerza v Istanbulu Cerrahpasa, Turčija

Namen pričujoče študije je predstavitev poenostavljene in učinkovite metode za opredelitev geometrije ozboja beveloidnih zobnikov. Avtorji so med pregledom literature odkrili metodo Milana Batiste, ki omogoča preprostejšo matematično opredelitev geometrije ravnih in spiralnih zob v dveh razsežnostih. Cilj je razširitev njegovih formul na beveloidne zobnike v treh razsežnostih in nova metoda tako vključuje risanje različnih 2D-prerezov po globini zoba, ki sestavljeni oblikujejo \mathcal{B} -model zoba.

Za beveloidne zobnike je predstavljena tehnika modeliranja z orodji v obliki zobnice, ki namesto na metodi avtorja Liu temelji na Batistinem modelu. Vrednosti kotalnega kota pri generiranju prerezov so izračunane z enačbo ubiranja.

Predstavljena je primerjava geometrij zob, ustvarjenih s prejšnjo in novo metodo. Razvidne so manjše razlike v vrednostih koordinat. Prototipni zobniki so bili izdelani z dodajalno tehnologijo ciljnega nalaganja (FDM) in nato sestavljeni.

Ugotovljeno je bilo odstopanje koordinat zaradi profilnega pomika, ki se kompenzira z zasukom surovca za določen kot.

Kot je navedeno v razdelku Rezultati in ugotovitve, so pri nekaterih vrednostih parametrov zobnika možna odstopanja koordinat v korenu. To je značilno za modele s kotom stožca, ki presega 15° , in lahko predstavlja omejitve uporabnosti predlagane metode. Kot stožca pri izdelanih prototipih je znašal 15° .

V prihodnje bo mogoče prilagoditi formule, ki opredeljujejo ovojnično krivuljo. Matematični model bo prav tako mogoče razširiti na druge vrste zobnikov, kot so eliptični ali neokrogli zobniki, ter na geometrije zobnikov s paraboličnimi, konkavnimi, konveksnimi ali kronskimi modifikacijami. Predlagana nova metoda omogoča generiranje evolvente, korena in medzobne vrzeli, tehnike za modifikacijo zob pa je mogoče prilagoditi formulam.

Matematični model, ki ga je predstavil Batista za dvorazsežnostne prereze, je bil v pričujoči študiji razširjen na trirazsežnostne modele beveloidnih zobnikov. Predlagani modelirni algoritem je krajši, generirani zobniški profili pa se tesno prekrivajo.

Pri prilagajanju enačb je bilo ugotovljeno, da parametri profilnega pomika pri beveloidnih geometrijah povzročijo zasuk prerezov po širini osi zoba za manjši kot. V izogib temu je bil izpeljan prilagoditveni kot, ki je vključen v enačbah. V rezultatih so prikazani zobni profili z odstopanji in korigirani zobni profili.

Opravljen je bila podrobna analiza področja zaokrožitve korena zoba za spiralne in konične zobnike. Podana je primerjava položajnih koordinat za različne kote stožca in širine zoba. Rezultati so pokazali, da so spremembe položajnih koordinat v sprejemljivih mejah.

Predstavljena tehnika modeliranja tako poenostavlja opredelitev geometrije v prerezu, konstruktorjem pa so pripravljene zamudne tehnike, saj formule ne zahtevajo računanja normalnih vektorjev.

Ključne besede: beveloidni zobniki, matematično modeliranje, orodja v obliki zobnice, parametrično modeliranje, evolventni profil, analiza spodrezanja

Študija možnosti uporabe izrabljenih rezalnih ploščic za gladilno valjanje

Oktay Adıyaman*
Univerza Batman, Turčija

Namen pričujoče študije je preveriti uporabnost in zmogljivost neobrabljenih delov odsluženih rezalnih ploščic iz materialov WC, CBN in keramike v funkciji orodja za globoko valjanje.

Rezalna orodja za strojno obdelavo (iz karbidne trdine, CBN, keramike itd.) so ključnega pomena v industriji, narejena pa so iz dragocenih kovin. Rezalne ploščice se običajno zavržejo, ko dosežejo stopnjo obrabe 1 % do 2 %, kar je povezano s stroški in obremenitvijo za okolje. Po statističnih podatkih se reciklira med 20 % in 30 % WC. Recikliranje je sicer koristen, vendar tudi drag postopek. Zato obstaja potreba po iskanju alternativ in v tem kontekstu je pomembna ponovna uporaba izrabljenih rezalnih ploščic.

Neobrabljeni deli rezalnih ploščic (iz WC, CBN in keramike) so bili preizkušeni pri gladilnem valjanju jekla AISI 1050 po metodi globokega valjanja z različnimi parametri. Na ta način so bile preučene možnosti za ponovno uporabo omenjenih ploščic za globoko valjanje. Zmogljivost ploščic je bila ovrednotena na podlagi mikrotrdote, hrapavosti (R_a) in videza nastalih površin. Za eksperimente brez hlajenja so bile izbrane tri sile valjanja (43 N, 330 N in 495 N), tri števila prehodov (1, 2 in 3) in tri podajalne hitrosti (0,04 mm/vrt, 0,08 mm/vrt in 0,12 mm/vrt). Opravljenih je bilo torej 27 eksperimentov z vsako ploščico, skupaj 81 eksperimentov. Vpliv procesnih parametrov na vrednosti mikrotrdote in R_a je bil določen z analizo variance.

Po globokem valjanju ni bilo mogoče opaziti signifikantne obrabe na površini nobene od rezalnih ploščic. Pri ploščicah iz materialov WC in CBN je bilo ugotovljeno, da je sicer izginila prevleka, na površini pa ni bilo sledov abrazije. Zaradi toplote in abrazije se je oblikovala le črna cona.

Proces globokega valjanja je povzročil porast mikrotrdote. Trdota je največja na površini in od tam pada proti sredini. Največja vrednost trdote je bila izmerjena po eksperimentih s tremi prehodi, najmanjša pa po enem prehodu. Trdota je bila največja pri keramični ploščici in najmanjša pri ploščici iz materiala WC. Analiza variance je pokazala, da so statistično signifikantni dejavniki za mikrotrdoto tip ploščice, sila in število prehodov. Prispevek števila prehodov, vrste ploščic in sile k mikrotrdoti znaša 44,77 %, 23,70 % oz. 13,53 %.

Nizke in visoke vrednosti podajanja negativno vplivajo na hrapavost površine (vrednost R_a), podajanje pa naj bi zagotovilo optimalne vrednosti R_a . V razmerah z manjšo silo valjanja so bile pri ploščicah iz WC dosežene nižje vrednosti R_a kot pri ploščicah iz CBN. Pri večjih silah valjanja ima material CBN bolj pozitiven vpliv na R_a . Najboljše vrednosti R_a so bile dosežene pri ploščicah iz WC pri majhnih silah, pri ploščicah iz materiala CBN pa pri velikih silah valjanja. Vrednost R_a pri ploščicah iz materiala WC na splošno narašča s številom prehodov. Dosežene vrednosti R_a pri ploščici iz materiala WC se ujemajo s podatki iz literature. Glede na analizo variance imata statistično signifikanten vpliv na R_a tip ploščice in hitrost podajanja. Največji vpliv na vrednost R_a ima podajanje, sledijo pa mu vrsta ploščice, sila in število prehodov s prispevki 22,60 %, 18,23 %, 4,54 % oz. 0,77 %.

V literaturi je mogoče najti študije na temo recikliranja rezalnih orodij, medtem ko izkoriščanje neizrabljenih površin rezalnih ploščic še ni bilo obravnavano. Pričujoča študija predstavlja alternativo za ponovno uporabo odpadnih (izrabljenih) ploščic v funkciji orodja za globoko gladilno valjanje, s čimer je bilo odprto tudi novo raziskovalno področje.

Ključne besede: globoko valjanje, gladilno valjanje s kroglo, mikrotrdota, tribologija, površinska hrapavost, integriteta površine

Guide for Authors

All manuscripts must be in English. Pages should be numbered sequentially. The manuscript should be composed in accordance with the Article Template given above. The suggested length of contributions is 10 to 20 pages. Longer contributions will only be accepted if authors provide justification in a cover letter. For full instructions see the Information for Authors section on the journal's website: <http://en.sv-jme.eu>.

SUBMISSION:

Submission to SV-JME is made with the implicit understanding that neither the manuscript nor the essence of its content has been published previously either in whole or in part and that it is not being considered for publication elsewhere. All the listed authors should have agreed on the content and the corresponding (submitting) author is responsible for having ensured that this agreement has been reached. The acceptance of an article is based entirely on its scientific merit, as judged by peer review. Scientific articles comprising simulations only will not be accepted for publication; simulations must be accompanied by experimental results carried out to confirm or deny the accuracy of the simulation. Every manuscript submitted to the SV-JME undergoes a peer-review process.

The authors are kindly invited to submit the paper through our web site: <http://ojs.sv-jme.eu>. The Author is able to track the submission through the editorial process - as well as participate in the copyediting and proofreading of submissions accepted for publication - by logging in, and using the username and password provided.

SUBMISSION CONTENT:

The typical submission material consists of:

- A **manuscript** (A PDF file, with title, all authors with affiliations, abstract, keywords, highlights, inserted figures and tables and references),
- Supplementary files:
 - a **manuscript** in a WORD file format
 - a **cover letter** (please see instructions for composing the cover letter)
 - a ZIP file containing **figures** in high resolution in one of the graphical formats (please see instructions for preparing the figure files)
 - possible **appendices** (optional), cover materials, video materials, etc.

Incomplete or improperly prepared submissions will be rejected with explanatory comments provided. In this case we will kindly ask the authors to carefully read the Information for Authors and to resubmit their manuscripts taking into consideration our comments.

COVER LETTER INSTRUCTIONS:

Please add a **cover letter** stating the following information about the submitted paper:

1. Paper **title**, list of **authors** and their **affiliations**. **One** corresponding author should be provided.
2. **Type of paper**: original scientific paper (1.01), review scientific paper (1.02) or short scientific paper (1.03).
3. A **declaration** that neither the manuscript nor the essence of its content has been published in whole or in part previously and that it is not being considered for publication elsewhere.
4. State the **value of the paper** or its practical, theoretical and scientific implications. What is new in the paper with respect to the state-of-the-art in the published papers? Do not repeat the content of your abstract for this purpose.
5. We kindly ask you to suggest at least two **reviewers** for your paper and give us their names, their full affiliation and contact information, and their scientific research interest. The suggested reviewers should have at least two relevant references (with an impact factor) to the scientific field concerned; they should not be from the same country as the authors and should have no close connection with the authors.
6. Please confirm that authors are willing/able to pay the Open Access **publication fee** as indicated in the Guide for Authors under Publication Fee, available at <https://www.sv-jme.eu/guide-for-authors-online/>.

FORMAT OF THE MANUSCRIPT:

The manuscript should be composed in accordance with the Article Template. The manuscript should be written in the following format:

- A **Title** that adequately describes the content of the manuscript.
- A list of **Authors** and their **affiliations**.
- An **Abstract** that should not exceed 250 words. The Abstract should state the principal objectives and the scope of the investigation, as well as the methodology employed. It should summarize the results and state the principal conclusions.
- 4 to 6 significant **key words** should follow the abstract to aid indexing.
- 4 to 6 **highlights**; a short collection of bullet points that convey the core findings and provide readers with a quick textual overview of the article. These four to six bullet points should describe the essence of the research (e.g. results or conclusions) and highlight what is distinctive about it.
- An **Introduction** that should provide a review of recent literature and sufficient background information to allow the results of the article to be understood and evaluated.
- A **Methods** section detailing the theoretical or experimental methods used.
- An **Experimental section** that should provide details of the experimental set-up and the methods used to obtain the results.
- A **Results** section that should clearly and concisely present the data, using figures and tables where appropriate.
- A **Discussion** section that should describe the relationships and generalizations shown by the results and discuss the significance of the results, making comparisons with previously published work. (It may be appropriate to combine the Results and Discussion sections into a single section to improve clarity.)
- A **Conclusions** section that should present one or more conclusions drawn from the results and subsequent discussion and should not duplicate the Abstract.
- **Acknowledgement** (optional) of collaboration or preparation assistance may be included. Please note the source of funding for the research.
- **Nomenclature** (optional). Papers with many symbols should have a nomenclature that defines all symbols with units, inserted above the references. If one is used, it must contain all the symbols used in the manuscript and the definitions should not be repeated in the text. In all cases, identify the symbols used if they are not widely recognized in the profession. Define acronyms in the text, not in the nomenclature.
- **References** must be cited consecutively in the text using square brackets [1] and collected together in a reference list at the end of the manuscript.
- **Appendix(-ices)** if any.

SPECIAL NOTES

Units: The SI system of units for nomenclature, symbols and abbreviations should be followed closely. Symbols for physical quantities in the text should be written in italics (e.g. v , T , n , etc.). Symbols for units that consist of letters should be in plain text (e.g. ms^{-1} , K, min, mm, etc.). Please also see: <http://physics.nist.gov/cuu/pdf/sp811.pdf>.

Abbreviations should be spelt out in full on first appearance followed by the abbreviation in parentheses, e.g. variable time geometry (VTG). The meaning of symbols and units belonging to symbols should be explained in each case or cited in a **nomenclature** section at the end of the manuscript before the References.

Figures (figures, graphs, illustrations digital images, photographs) must be cited in consecutive numerical order in the text and referred to in both the text and the captions as Fig. 1, Fig. 2, etc. Figures should be prepared without borders and on white grounding and should be sent separately in their original formats. If a figure is composed of several parts, please mark each part with a), b), c), etc. and provide an explanation for each part in Figure caption. The caption should be self-explanatory. Letters and numbers should be readable (Arial or Times New Roman, min 6 pt with equal sizes and fonts in all figures). Graphics (submitted as supplementary files) may be exported in resolution good enough for printing (min. 300 dpi) in any common format, e.g. TIFF, BMP or JPG, PDF and should be named Fig1.jpg, Fig2.tif, etc. However, graphs and line drawings should be prepared as vector images, e.g. CDR, AI. Multi-curve graphs should have individual curves marked with a symbol or otherwise provide distinguishing differences using, for example, different thicknesses or dashing.

Tables should carry separate titles and must be numbered in consecutive numerical order in the text and referred to in both the text and the captions as Table 1, Table 2, etc. In addition to the physical quantities, such as t (in italics), the units [s] (normal text) should be added in square brackets. Tables should not duplicate data found elsewhere in the manuscript. Tables should be prepared using a table editor and not inserted as a graphic.

REFERENCES:

A reference list must be included using the following information as a guide. Only cited text references are to be included. Each reference is to be referred to in the text by a number enclosed in a square bracket (i.e. [3] or [2] to [4] for more references; do not combine more than 3 references, explain each). No reference to the author is necessary.

References must be numbered and ordered according to where they are first mentioned in the paper, not alphabetically. All references must be complete and accurate. Please add DOI code when available. Examples follow.

Journal Papers:

Surname 1, Initials, Surname 2, Initials (year). Title. *Journal*, volume, number, pages, DOI code.

- [1] Hackenschmidt, R., Alber-Laukant, B., Rieg, F. (2010). Simulating nonlinear materials under centrifugal forces by using intelligent cross-linked simulations. *Strojniški vestnik - Journal of Mechanical Engineering*, vol. 57, no. 7-8, p. 531-538, DOI:10.5545/sv-jme.2011.013.

Journal titles should not be abbreviated. Note that journal title is set in italics.

Books:

Surname 1, Initials, Surname 2, Initials (year). Title. Publisher, place of publication.

- [2] Groover, M.P. (2007). *Fundamentals of Modern Manufacturing*. John Wiley & Sons, Hoboken.

Note that the title of the book is italicized.

Chapters in Books:

Surname 1, Initials, Surname 2, Initials (year). Chapter title. Editor(s) of book, book title. Publisher, place of publication, pages.

- [3] Carbone, G., Ceccarelli, M. (2005). Legged robotic systems. Kordić, V., Lazinica, A., Merdan, M. (Eds.), *Cutting Edge Robotics*. Pro literatur Verlag, Mammendorf, p. 553-576.

Proceedings Papers:

Surname 1, Initials, Surname 2, Initials (year). Paper title. Proceedings title, pages.

- [4] Štefanič, N., Martinčević-Mikić, S., Tošanović, N. (2009). Applied lean system in process industry. *MOTSP Conference Proceedings*, p. 422-427.

Standards:

Standard-Code (year). Title. Organisation. Place.

- [5] ISO/DIS 16000-6:2002. *Indoor Air - Part 6: Determination of Volatile Organic Compounds in Indoor and Chamber Air by Active Sampling on TENAX TA Sorbent, Thermal Desorption and Gas Chromatography using MSD/FID*. International Organization for Standardization. Geneva.

WWW pages:

Surname, Initials or Company name. Title, from <http://address>, date of access.

- [6] Rockwell Automation. Arena, from <http://www.arenasimulation.com>, accessed on 2009-09-07.

EXTENDED ABSTRACT:

When the paper is accepted for publishing, the authors will be requested to send an **extended abstract** (approx. one A4 page or 3500 to 4000 characters or approx. 600 words). The instruction for composing the extended abstract are published on-line: <http://www.sv-jme.eu/information-for-authors/>.

COPYRIGHT:

Authors submitting a manuscript do so on the understanding that the work has not been published before, is not being considered for publication elsewhere and has been read and approved by all authors. The submission of the manuscript by the authors means that the authors automatically agree to publish the paper under CC-BY 4.0 Int. or CC-BY-NC 4.0 Int. when the manuscript is accepted for publication. All accepted manuscripts must be accompanied by a Copyright Agreement, which should be sent to the editor. The work should be original work by the authors and not be published elsewhere in any language without the written consent of the publisher. The proof will be sent to the author showing the final layout of the article. Proof correction must be minimal and executed quickly. Thus it is essential that manuscripts are accurate when submitted. Authors can track the status of their accepted articles on <https://en.sv-jme.eu>.

PUBLICATION FEE:

Authors will be asked to pay a publication fee for each article prior to the article appearing in the journal. However, this fee only needs to be paid after the article has been accepted for publishing. The fee is 380 EUR (for articles with maximum of 6 pages), 470 EUR (for articles with maximum of 10 pages), plus 50 EUR for each additional page. The additional cost for a color page is 90.00 EUR (only for a journal hard copy; optional upon author's request). These fees do not include tax.



<http://www.sv-jme.eu>

Contents

Papers

- 3 Samo Zupan, Robert Kunc:
Overview of Principles and Rules of Geometrical Product Specifications According to the Current ISO Standards
- 20 Zhengfang Li, Xudong Di, Zhengyuan Gao, Zhiguo An, Ling Chen, Yuhang Zhang, Shihong Lu:
Improvement of the Dimensional Accuracy of a Ti-6Al-4V Ripple Disc During Electric Hot Incremental Sheet Forming
- 27 Ireneusz Zagórski, Monika Kulisz, Anna Szczepaniak:
Roughness Parameters with Statistical Analysis and Modelling Using Artificial Neural Networks After Finish Milling of Magnesium Alloys with Different Edge Helix Angle Tools
- 42 Tat-Khoa Doan, Trung-Thanh Nguyen, An-Le Van:
Multi-performance Optimization of the Rotary Turning Operation for Environmental and Quality Indicators
- 55 Xin Tian, Guangjian Wang, Yujiang Jiang:
A New Calculation Method for Instantaneous Efficiency and Torque Fluctuation of Spur Gears
- 70 Grzegorz Struzikiewicz:
Investigation of the Titanium Alloy Turning Process with Prime A Tools under High-Pressure Cooling Conditions
- 80 Berat Gürçan Şentürk, Mahmut Cüneyt Fetvacı:
A Modified Approach to the Rack Generation of Beveloid Gears
- 92 Oktay Adıyaman:
Investigation on the Application of Worn Cutting Tool Inserts as Burnishing Tools